



Universiteit
Leiden
The Netherlands

The evolution of radio-loud active galactic nuclei

Vries, N. de

Citation

Vries, N. de. (2009, November 25). *The evolution of radio-loud active galactic nuclei*. Retrieved from <https://hdl.handle.net/1887/14440>

Version: Corrected Publisher's Version

License: [Licence agreement concerning inclusion of doctoral thesis in the Institutional Repository of the University of Leiden](#)

Downloaded from: <https://hdl.handle.net/1887/14440>

Note: To cite this publication please use the final published version (if applicable).

The
Evolution
of
Radio-Loud
Active Galactic Nuclei

The
Evolution
of
Radio-Loud
Active Galactic Nuclei

Proefschrift

ter verkrijging van
de graad van Doctor aan de Universiteit Leiden,
op gezag van de Rector Magnificus prof. mr. P.F. van der Heijden,
volgens besluit van het College voor Promoties
te verdedigen op woensdag 25 november 2009
klokke 11.15 uur

door

Nathan de Vries

geboren te Haarlem
in 1982

Promotiecommissie

Promotor:	Prof. dr. R. T. Schilizzi	(SKA Project Development Office, Manchester, UK)
Co-promotores:	Dr. I. A. G. Snellen Prof. dr. H. J. A. Röttgering	
Overige leden:	Prof. dr. K. H. Kuijken Prof. dr. G. K. Miley Dr. R. Morganti Dr. M. N. Lehnert	(ASTRON, Dwingeloo) (Observatoire de Paris)

Voor mijn Kleine Beer en mijn Grote Beer

Omslag: *Kayhan*¹
door Robbin Heyker

Achterzijde: *Astronaut eet banaan*²
door Jisk de Vries, 6 jaar

¹Kayhan is Afghaans voor 'heelal'.

²Op de achtergrond een gedeelte van de *Spitzer* Deep, Wide-Field Survey (SDWFS), met in rood contouren van de Very Large Array (VLA) radiokaart. Deze gegevens zijn gebruikt in hoofdstuk 5 van dit proefschrift.

Table of contents

	Page
Chapter 1. Introduction	1
1.1 Active galaxies	1
1.2 Radio-loud AGN	4
1.3 Young radio sources	6
1.4 Highlights of this thesis	7
Chapter 2. Complete identification of the Parkes half-Jansky sample of GHz peaked spectrum radio galaxies	11
2.1 The Parkes half-Jansky sample of GPS galaxies	13
2.2 Observations	13
2.2.1 VLT-FORS1 spectroscopy	13
2.2.2 ESO 3.6m observations	14
2.2.3 Additional near-infrared photometry	15
2.3 Results and discussion	15
2.3.1 R-band Hubble diagram	17
2.3.2 Absolute magnitudes	19
2.4 Appendix	23
2.4.1 Comments on selected sources	23
2.4.2 Tables and figures	28
Chapter 3. VLBI observations of the CORALZ sample: young radio sources at low redshift	35
3.1 Observations and data reduction	38
3.2 Data analysis	41
3.2.1 Source structure and angular sizes	41
3.2.2 Morphological classification	41
3.2.3 Expansion velocity	42
3.3 Results and discussion	43
3.3.1 Source structure	44
3.3.2 Radio morphology	45
3.3.3 Spectral turnover and angular size	45

3.3.4 Expansion velocity and radio power	50
3.4 Conclusions	52
3.5 Appendix	56
3.5.1 Radio source evolution modelling	56
3.5.2 Observations and radio maps	58
Chapter 4. The dynamical ages of two low-luminosity young radio sources	77
4.1 Observations and data reduction	80
4.2 Data analysis	80
4.3 Results and discussion	81
4.3.1 CORALZ J083139+460800	81
4.3.2 CORALZ J131739+411545	82
4.3.3 Expansion velocity and radio power	84
4.4 Conclusions	88
Chapter 5. Infrared properties of radio sources in the Boötes field: evidence for evolution of the dust-torus over AGN-lifetime	91
5.1 Surveys in the Boötes field	94
5.1.1 Radio observations	94
5.1.2 Optical and near-infrared surveys	95
5.1.3 Mid-infrared survey	95
5.2 Properties of the radio sources	96
5.2.1 Visual examination	96
5.2.2 Angular size	97
5.2.3 Radio positions	100
5.2.4 Host galaxies	100
5.2.5 Photometric redshifts and stellar masses	102
5.2.6 Radio luminosities and physical sizes	105
5.3 Sample selection	106
5.4 Results	107
5.4.1 Evolution of 24 μm emission	108
5.4.2 Evolution of 8.0 μm emission	108
5.4.3 IRAC colors	111
5.5 Discussion	112
5.5.1 AGN unification	112
5.5.2 Evolution of mid-infrared emission	115

5.5.3 IRAC colors	116
5.6 Conclusions	117
5.7 Appendix	120
5.7.1 Overlays	120
Chapter 6. Survival rates of young radio-loud AGN and their environments	133
6.1 CORALZ sample	135
6.2 Mock radio source populations	136
6.2.1 Radio source evolution model	137
6.2.2 Default model parameters	138
6.2.3 Randomly assigned radio source properties	139
6.2.4 Generating mock radio source populations	140
6.2.5 Normalization to the radio luminosity function	140
6.3 Results	141
6.3.1 Predicted CORALZ sample sizes	141
6.3.2 Distributions of radio source properties	143
6.4 Discussion	147
6.5 Conclusions	148
Nederlandse samenvatting	151
Curriculum vitae	163
Nawoord	165

Chapter 1

Introduction



ALAXIES, vast collections of stars orbiting their common center of gravity, are amongst the most beautiful objects in the universe. Although four galaxies can actually be seen from the earth with the naked eye, it was only after Heber D. Curtis discovered that the Andromeda nebula was an ‘island universe’ (a separate galaxy located outside the Milky Way; Curtis 1917), that it was realized that many nebulae were actually galaxies, consisting of huge numbers of stars. By means of the telescope, which celebrates its 400th birthday this year, astronomers have discovered billions of galaxies more, each comprising a few tens of millions up to trillions of stars.

Stars are not the only constituent of galaxies though. In between the stars reside large amounts of gas and dust, from which new stars may be formed. Furthermore, in the very center of virtually all massive galaxies a supermassive black hole (SMBH) is hidden (Magorrian et al. 1998; Kormendy & Gebhardt 2001). Usually this SMBH is dormant, but from time to time this greedy monster is fed with fresh gas, which is accompanied with highly energetic phenomena, a state astronomers call ‘active’.

1.1 Active galaxies

Active galaxies can have a wide range of observational characteristics. All these phenomena originate in a very small region, called the active galactic nucleus (AGN), which surrounds the SMBH at the center of the galaxy (Fig. 1.1). Narrow emission lines are seen in the optical spectra of most AGN, with line widths corresponding to random velocities of a few hundred kilometers per second. Some AGN also show broad emission lines, with widths of a few thousand kilometers per second. The brightest active galaxies, quasars, show optical continuum emis-

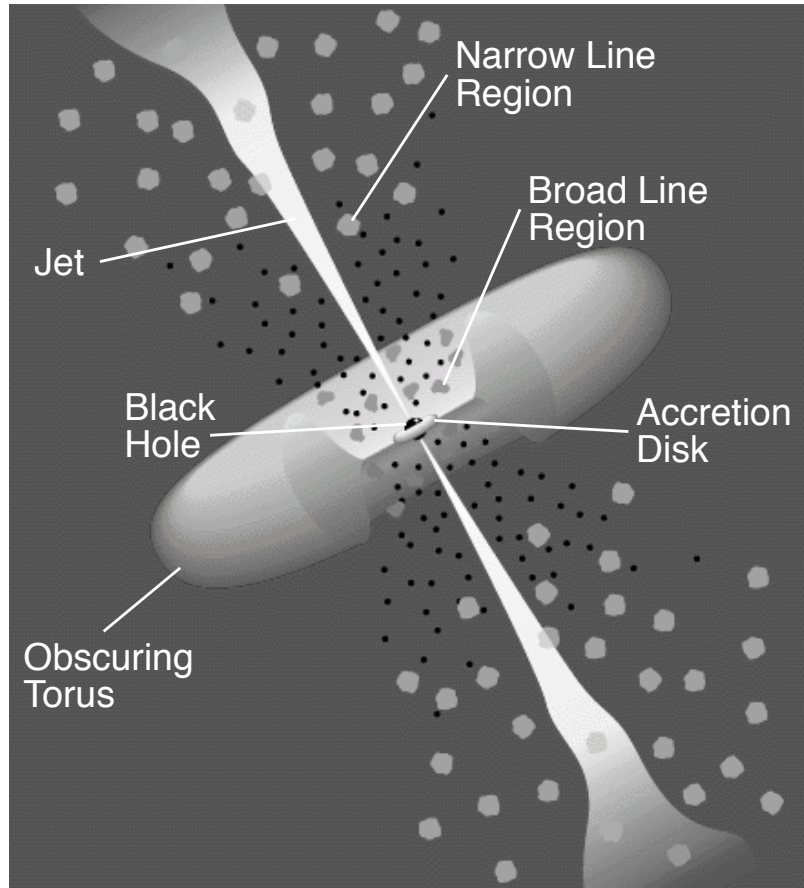


Figure 1.1: — The standard unified model of AGN (not to scale). The central black hole and surrounding accretion disk are indicated. The broad line region lies close to the black hole and, depending on the orientation of the AGN with respect to the line of sight, is sometimes hidden from view by the obscuring torus. The narrow line region lies further from the black hole, in particular above the torus, and is visible from any viewing angle. Perpendicular to the accretion disk and torus, a bidirectional jet may emerge from very near the black hole. Credit: C. M. Urry & P. Padovani (1995).

sion from the nucleus often outshining the stellar light of the entire host galaxy. This luminous emission is radiated by matter falling towards the supermassive black hole, forming an accretion disk which heats itself through frictional forces. AGN in general can have continuum emission basically over the whole electromagnetic spectrum.

While the AGN itself is usually unresolvable by current means, radio emission from AGN often extends to large scales, even beyond the outskirts of the host galaxy. This radio emission is produced by electrons spiraling around magnetic field lines with relativistic velocities, causing them to emit synchrotron radiation. These electrons are sent out to these dazzling distances via bidirectional jets emerging from the nucleus. Some radio jets have turbulent structures and become fainter

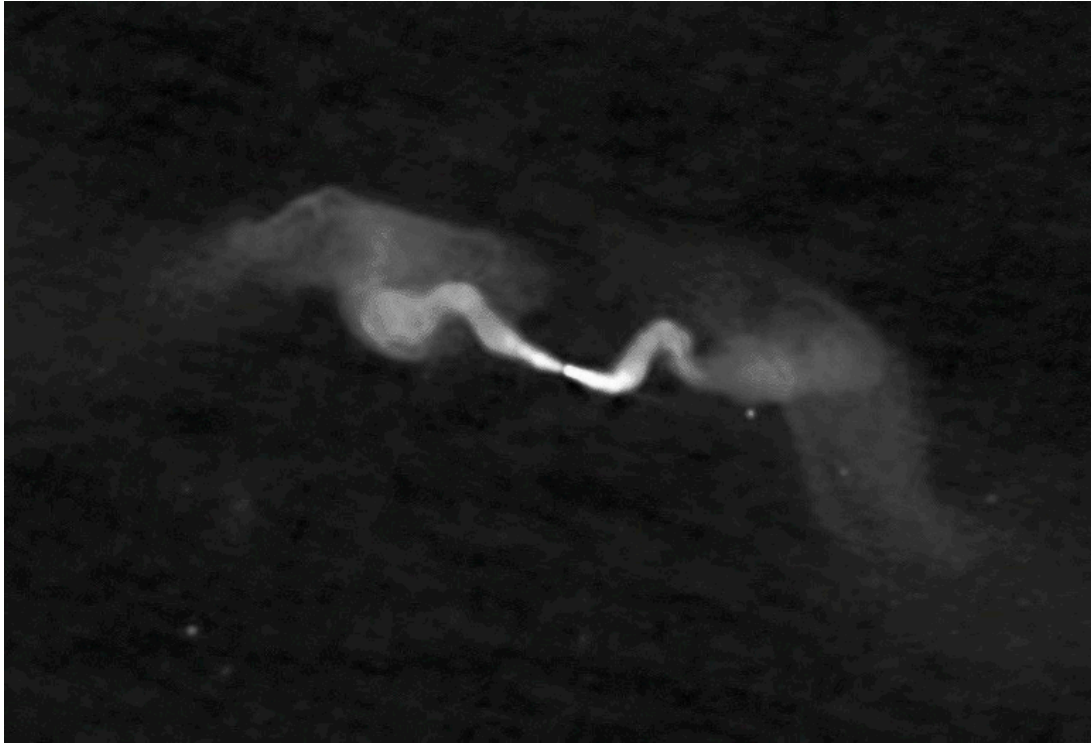


Figure 1.2: — Very Large Array (VLA) radio map of 3C31, a typical FR I radio source. The turbulent jets wiggle and become fainter with distance from the center. 3C31 has a total extent of ~ 400 kpc. Credit: NRAO.

with distance from the nucleus (FR I; Fanaroff & Riley 1974). Others remain laminar up to the hotspots (FR II), where the jets strongly interact with the interstellar medium of the host galaxy or with the intragalactic medium. The relativistic plasma produced in this collision, fills giant lobes behind the shock front. In Fig. 1.2 and Fig. 1.3 typical examples of FR I and FR II type radio sources are shown. These radio-loud AGN are almost exclusively hosted by massive elliptical galaxies. On the other hand, many AGN, especially those hosted by (less massive) spiral galaxies, do not show jets or strong radio emission.

Over the years this diversity of observational characteristics has led to the definition of a large number of AGN classes. Since it is generally accepted that all AGN are powered by the same physical mechanism - the accretion of matter onto a black hole, it is remarkable that AGN classes appear so different. The first attempts to link in this wide range of observational phenomena into a single model, involved the orientation of the AGN. Orientation-based unified schemes are based on a spherically asymmetric AGN model, where the central object is surrounded by a

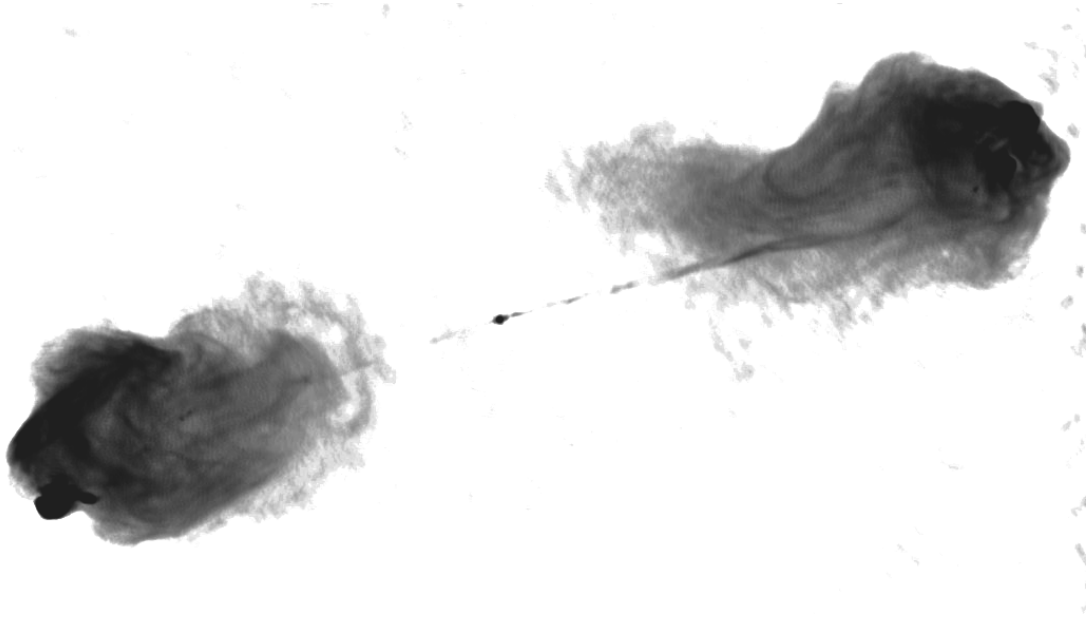


Figure 1.3: — Cygnus A, the first extragalactic radio source to be discovered. It has a typical double lobed FR II morphology, with two large lobes behind the hotspots. A radio core in the center is also visible, as well as two highly collimated jets. Cygnus A has a size similar to 3C31 in Fig. 1.2. Credit: NRAO.

torus of gas and dust (Fig. 1.1). When viewed from the side, this torus blocks off the most central part of the AGN, which would be visible from other viewing angles (Antonucci 1984; Barthel 1989). Despite the success of this unification theory many issues remain unresolved. For example it fails to explain why some AGN produce powerful radio emission, while others do not.

1.2 Radio-loud AGN

The study of radio-loud AGN has its origins in the serendipitous discovery of Karl Jansky (1933). He was investigating static in ‘short wave’ (>14 m) radio communication signals (see Fig. 1.4), and found a source of radio static that recurred every sidereal day, which he later identified with the Milky Way center. Twenty years later Baade and Minkowski (1954) discovered the first extragalactic radio source, Cygnus A, by identifying this bright radio source with a merging galaxy pair. After this discovery extragalactic radio astronomy quickly developed, resulting in the publication of the 3C radio catalog and subsequent revisions (Edge et al. 1959; Bennett 1962; Laing et al. 1983). Soon it was discovered that the

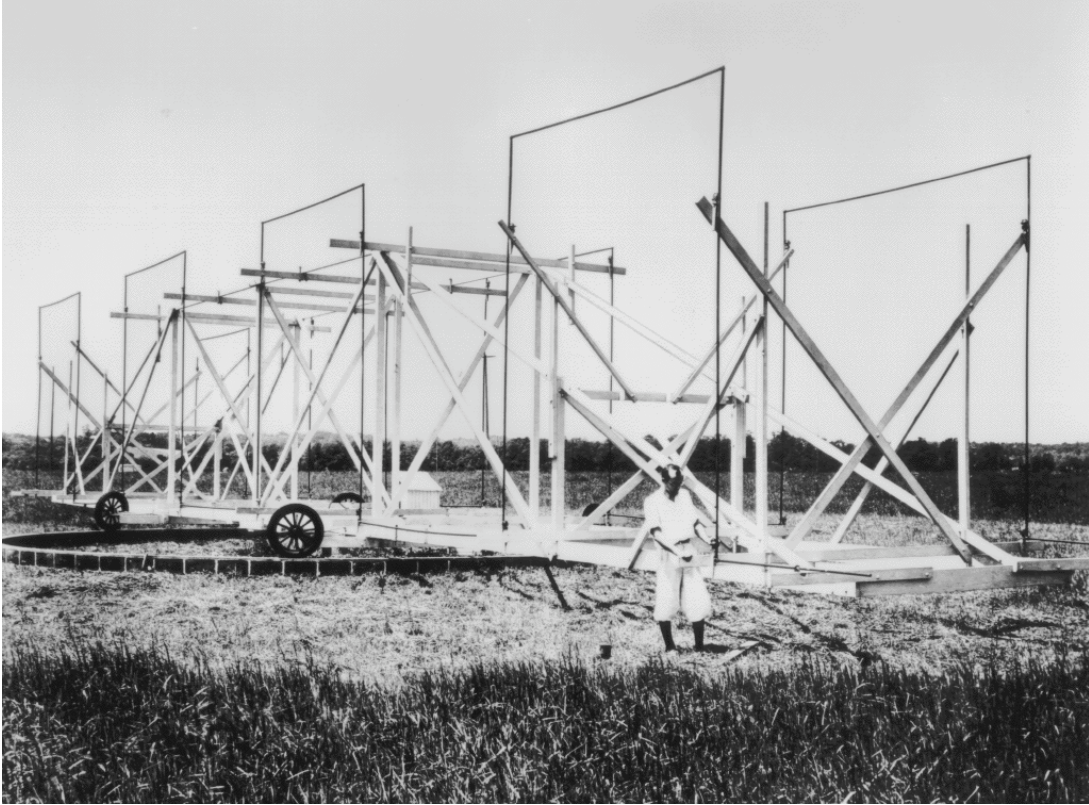


Figure 1.4: — Karl Jansky in front of his radio antenna, with which he discovered radio waves coming from the Milky Way center in 1933. Credit: NRAO.

majority of these bright radio sources had large, mostly double, structures (Allen, Hanbury Brown & Palmer 1962), often exceeding the size of their host galaxy. The unresolved ($\lesssim 1''$) radio sources were classified on the basis of their radio spectra, leading to the discoveries of compact steep spectrum (CSS; Conway, Kellermann & Long 1963) and gigahertz peaked spectrum (GPS; Bolton, Gardener & Mackey 1963) radio sources. Later on it became possible to resolve these compact radio-loud AGN, employing the technique of very long baseline interferometry (VLBI). With this technique the signals of several radio telescopes are correlated to synthesize a radio telescope aperture with the size of the largest baseline between the separate dishes, tremendously enhancing the angular resolution. The structures of GPS and CSS radio sources proved to be very similar to those of extended double radio sources, but at a much smaller angular scale (Fig. 1.5) with corresponding physical sizes of $\lesssim 20$ kpc and $\lesssim 1$ kpc (e.g. O'Dea 1998) for CSS and GPS radio sources, respectively.

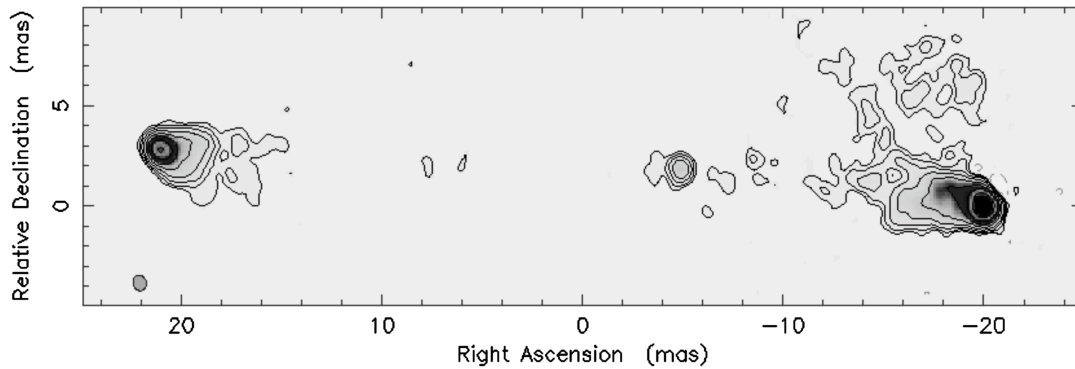


Figure 1.5: — The GPS radio source 1943+546, for which an age of ~ 1000 years has been determined (Polatidis et al. 1999). It has a size of only ~ 160 pc. Note the similarity to Cygnus A in Fig. 1.3. Credit: Polatidis et al. (1999).

1.3 Young radio sources

More detailed studies on CSS and GPS radio sources only began during the early 1980s, when observations at higher frequencies became available. At 2.7 GHz and 5 GHz these compact sources start to make up a significant fraction ($\sim 30\%$ for CSS, and $\sim 10\%$ for GPS radio sources) of the bright flux density-selected samples (Kapahi 1981; Peacock & Wall 1982). To explain the relatively small sizes of these sources two scenarios were proposed, (1) that GPS radio sources are very young radio-loud AGN which grow and evolve into CSS sources and subsequently become extended FR I/II radio sources, or (2) that they are ‘frustrated’ radio sources, millions of years old, but confined by a dense interstellar medium (Baum et al. 1990). At the turn of the millennium compelling evidence accumulated in favour of the youth scenario. VLBI monitoring of the archetype GPS sources, that began in the early 1980s, showed these sources expand in size, implying source ages of $10^2\text{--}3$ years only (Owsianik et al. 1998; Owsianik & Conway 1998; Tschager et al. 2000; Polatidis & Conway 2003), in good agreement with spectral age estimates (Murgia 2003).

Now that it has been established that GPS and CSS radio sources are indeed young, it is clear that they play a key role in understanding radio-loud AGN. In this thesis samples of young radio-loud AGN are studied, with the aim to determine:

- the triggering mechanism of radio-loud AGN: *Why are some AGN radio-loud, while others are not?*

- how radio-loud AGN evolve over their lifetime: *Does the obscuring torus remain, or is it consumed during the lifetime of the AGN?*
- the typical lifetime of radio-loud AGN: *Do all radio-loud AGN grow old, or does a significant fraction suffer an untimely death?*
- the effects of radio-loud nuclear activity on the host galaxies: *Do radio-loud AGN control the star formation of their host galaxy?*

1.4 Highlights of this thesis

Chapter 2

(*de Vries et al. 2007, A&A, 464, 879*)

In this chapter we study the Parkes half-Jansky sample of GPS radio galaxies as selected by Snellen et al. (2002). We identify the host galaxies of all radio sources and determine redshifts for most of them (80%). From a comparison of their absolute magnitudes with stellar evolution models we find that these massive elliptical galaxies are overluminous in the restframe UV. This UV excess can be attributed to a small population of young stars, or AGN induced emission.

Chapter 3

(*de Vries et al. 2009, A&A, 498, 641*)

This chapter presents a global VLBI study of the CORALZ sample of compact radio sources at low redshift. Sources in the CORALZ sample typically have relatively low luminosities compared to previously studied samples of young radio-loud AGN. We present high resolution radio maps of all sources, and determine angular sizes and morphologies. The relationship between angular size, spectral peak frequency, and flux density of the (low-luminosity) CORALZ sample provides further strong evidence that the turnover in spectra of young radio-loud AGN is caused by synchrotron self-absorption.

Chapter 4

(*de Vries et al. 2009, A&A, accepted*)

We for the first time detect expansion for a low-luminosity GPS radio source, and strongly constrain the speed of a second one. The expansion speed of $0.095 \pm 0.020h^{-1}c$ for CORALZ J083139+460800 corresponds to a dynamical age of 245 ± 55 years, confirming that this radio-loud AGN is indeed very young. However, the expansion speed is significantly

lower than expected from studies of high-luminosity GPS sources, indicating a correlation between expansion speed and radio luminosity.

Chapter 5

(*de Vries et al. 2009, to be submitted to A&A*)

We investigate the trigger and evolution of radio-loud AGN in the context of current unification theories. For this purpose we exploited the large data sets available for the 9 deg^2 Boötes field, in particular deep optical, near-infrared, mid-infrared, and radio surveys. For a complete sample of 334 radio sources down to a radio flux of $S_{325 \text{ MHz}} > 0.75 \text{ mJy}$ the photometric redshifts, stellar masses, (projected) linear radio source sizes, and the mid-infrared properties were determined. We detect a significant decrease of $24 \text{ }\mu\text{m}$ detection rate with linear source size, while a similar but weaker trend is seen at $8 \text{ }\mu\text{m}$. We suggest this fits an evolution scenario, in which young radio-loud AGN contain a circumnuclear torus, while older AGN consumed most of the circumnuclear material, contradicting the hypothesis that radio-loud AGN are fueled through Bondi accretion (Bondi 1952). We argue that radio-loud AGN may still be powered through cooling flows, but with the accreted material probably settling in a (standard unification theory) disk, and not being continuously replenished.

Chapter 6

(*de Vries et al. 2009, to be submitted to A&A*)

We investigate the common assumption that *all* young radio sources eventually evolve into extended FR II and/or FR I radio sources, by comparing the observed characteristics of the CORALZ core sample with mock populations of radio sources. The simulations are based on the analytic radio source models of Kaiser & Best (2007), fully taking into account size and luminosity evolution. We find that the size distribution of the CORALZ core sample is significantly different from the simulated radio sources, and strongly favors a steep density profile of the external medium. In order to explain the size distribution of the CORALZ core sample, a significant fraction of the *most compact* CORALZ sources must shut down and fade before they could evolve into extended radio sources. However, not a large fraction of the *total* number of CORALZ sources is allowed to suffer an early death, as derived from a comparison

with the predicted sample sizes, otherwise implying an unreasonably long lifetime for typical radio-loud AGN activity.

References

- Allen, L. R., Hanbury Brown, R., & Palmer, H. P. 1962, MNRAS, 125, 57
Antonucci, R. R. J. 1984, ApJ, 278, 499
Baade, W., & Minkowski, R. 1954, ApJ, 119, 206
Barthel, P. D. 1989, ApJ, 336, 606
Baum S.A., O'Dea C.P., Murphy D.W., de Bruyn A.G., 1990, A&A, 232, 19
Bennett, A. S. 1962, MNRAS, 125, 75
Bolton, J. G., Gardner, F. F., & Mackey, M. B. 1963, Nature, 199, 682
Bondi, H. 1952, MNRAS, 112, 195
Conway, R. G., Kellermann, K. I., & Long, R. J. 1963, MNRAS, 125, 261
Curtis, H. D. 1917, PASP, 29, 206
de Vries, N., Snellen, I. A. G., Schilizzi, R. T., Lehnert, M. D., & Bremer, M. N. 2007, A&A, 464, 879, Chapter 2
de Vries, N., Snellen, I. A. G., Schilizzi, R. T., Mack, K.-H., & Kaiser, C. R. 2009, A&A, 498, 641, Chapter 3
de Vries, N., Snellen, I. A. G., Schilizzi, R. T., & Mack, K.-H. 2009, A&A, accepted, Chapter 4
Edge, D. O., Shakeshaft, J. R., McAdam, W. B., Baldwin, J. E., & Archer, S. 1959, MmRAS, 68, 37
Fanaroff, B. L., & Riley, J. M. 1974, MNRAS, 167, 31P
Jansky, K. G. 1933, Nature, 132, 66
Kaiser, C. R., & Best, P. N. 2007, MNRAS, 381, 1548
Kapahi, V. K. 1981, A&AS, 43, 381
Kormendy, J., & Gebhardt, K. 2001, 20th Texas Symposium on relativistic astrophysics, 586, 363
Laing, R. A., Riley, J. M., & Longair, M. S. 1983, MNRAS, 204, 151
Magorrian, J., et al. 1998, AJ, 115, 2285
Murgia M., 2003, PASA, 20, 19M
O'Dea, C. P. 1998, PASP, 110, 493
Owsianik I., Conway J.E., 1998, A&A, 337, 69
Owsianik I., Conway J.E., Polatidis A.G., 1998, A&A, 336, L37
Peacock, J. A., & Wall, J. V. 1982, MNRAS, 198, 843
Polatidis, A., Wilkinson, P. N., Xu, W., Readhead, A. C. S., Pearson, T. J., Taylor, G. B., & Vermeulen, R. C. 1999, New Astronomy Review, 43, 657
Polatidis A.G., Conway J.E., 2003, PASA, 20, 69P
Snellen, I. A. G., Lehnert, M. D., Bremer, M. N., & Schilizzi, R. T. 2002, MNRAS, 337, 981
Tschager W., Schilizzi R.T., Röttgering H.J.A., Snellen I.A.G., Miley G.K., 2000, A&A, 360, 887
Urry, C. M., & Padovani, P. 1995, PASP, 107, 803

Chapter 2

Complete identification of the Parkes half-Jansky sample of GHz peaked spectrum radio galaxies

Abstract. Gigahertz Peaked Spectrum (GPS) radio galaxies are generally thought to be the young counterparts of classical extended radio sources. Statistically complete samples of GPS sources are vital for studying the early evolution of radio-loud AGN and the trigger of their nuclear activity. The ‘Parkes half-Jansky’ sample of GPS radio galaxies is such a sample, representing the southern counterpart of the 1998 Stanghellini sample of bright GPS sources. As a first step of the investigation of the sample, the host galaxies need to be identified and their redshifts determined. Deep R -band VLT-FORS1 and ESO 3.6m EFOSC II images and long slit spectra have been taken for the unidentified sources in the sample. We have identified all twelve previously unknown host galaxies of the radio sources in the sample. Eleven have host galaxies in the range $21.0 < R_C < 23.0$, while one object, PKS J0210+0419, is identified in the near infrared with a galaxy with $K_s = 18.3$. The redshifts of 21 host galaxies have been determined in the range $0.474 < z < 1.539$, bringing the total number of redshifts to 39 (80%). Analysis of the absolute magnitudes of the GPS host galaxies show that at $z > 1$ they are on average a magnitude fainter than classical 3C radio galaxies, as found in earlier studies. However their restframe UV luminosities indicate that there is an extra light contribution from the AGN, or from a population of young stars.

N. de Vries, I. A. G. Snellen, R. T. Schilizzi, M. D. Lehnert, and M. N. Bremer
Astronomy & Astrophysics, **464**, 879 (2007)

Complete identification of the Parkes half-Jansky sample of GHz peaked spectrum radio galaxies



GAHERTZ Peaked Spectrum (GPS) radio sources are among the brightest radio sources in the sky. They are compact objects characterized by a turnover in their radio spectra at about 1 GHz in frequency. Their radio morphologies are small-scale versions of the well known extended Fanaroff & Riley (FR) I/II radio sources, but with a physical extent of only 10-100 pc, well within the central regions of their host galaxies (Stanghellini et al. 1999). To explain the compactness of these sources two scenarios were proposed: (1) these objects are very young radio-loud active galaxies which may evolve into kpc-sized Compact Steep Spectrum (CSS) sources and eventually grow to become FR I/IIs, (2) they are ‘frustrated’ radio sources, millions of years old, but confined by a dense interstellar medium (Baum et al. 1990). In recent years compelling evidence has accumulated in favour of the youth scenario. VLBI monitoring of the archetype GPS sources, that began in the early 1980s, has now conclusively shown these sources expand in size, implying source ages of 10^{2-3} years only (Owsianik et al. 1998; Owsianik & Conway 1998; Tschager et al. 2000; Polatidis & Conway 2003), in good agreement with spectral age estimates (Murgia 2003). Recently Vink et al. (2006) have shown that their optical line emission is relatively underluminous, exhibiting a possible trend with radio source age. This is consistent with the fact that the Strömgren sphere should still be expanding in these objects, and that we are witnessing the birth of their narrow emission line regions. If indeed GPS galaxies are young, as now seems to be very likely, they form the key objects to study the early evolution of powerful radio-loud AGN, and the trigger of nuclear activity. In this chapter we present new optical observations of a sample of GPS galaxies, aimed at identifying all host galaxies and determining their redshifts. Section 2.1 defines this sample, section 2.2 describes the observations, and the results are presented and

discussed in Sect. 2.3.

2.1 The Parkes half-Jansky sample of GPS galaxies

Snellen et al. (2002) have defined a sample of bright GPS sources in the southern/equatorial sky, representing the counterpart of the sample of Stanghellini et al. (1998), although somewhat deeper. High flux density GPS sources are rare and therefore all sky coverage is needed in order to obtain a statistically significant number of sources. Furthermore, access to large optical telescopes is better for the southern hemisphere, at least for European astronomers. The selection criteria of the sample are described in detail in a previous paper (Snellen et al. 2002). Summarizing, it consists of 49 sources selected from the Parkes multifrequency survey (PKSCAT90, Wright & Otrupcek 1990), with $-40^\circ < \delta < +15^\circ$, $|b| > 20^\circ$ and $S_{2.7\text{GHz}} > 0.5\text{Jy}$. The sample only consists of GPS radio sources associated with galaxies since GPS quasars do not seem to be related to GPS galaxies, despite having similar radio characteristics, and may not be young (e.g. Snellen et al. 1999). Before the current work, 75% of the radio sources had been optically identified with a host galaxy and 40% had known redshifts.

2.2 Observations

2.2.1 VLT-FORS1 spectroscopy

Optical long slit spectroscopy was performed on objects in the sample using the European Southern Observatory (ESO) Very Large Telescope (VLT) at Paranal, in Chile, from March to September 2004. All observations were obtained in service mode with the visual and near UV Focal Reducer and low dispersion Spectrograph (FORS1), using exposure times of 1800 s with the grism GRIS-300V (ESO # 10) in combination with the order separation filter GG 435. The FORS1 has a Tektronix 2048×2048 CCD detector with $24\mu\text{m}$ pixels, resulting in a scale of $0.2''/\text{pixel}$ (with the Standard Resolution collimator) and a slit length of $6.8'$. The grism results in a dispersion of $2.69 \text{ \AA}/\text{pixel}$ and a total wavelength coverage of $4450 - 8650 \text{ \AA}$. The spectra were taken using a slit width of $1.0''$, resulting in a spectral resolution of $\text{FWHM} = 5 \text{ pixels}$

(13 Å). Usually the slit was oriented near the parallactic angle, unless a second interesting object was located near the GPS galaxy (e.g. a possibly associated companion galaxy). The data reduction was carried out in a standard way using NOAO's IRAF reduction software. One dimensional spectra were extracted by summing in the spatial direction over an aperture as large as the spatial extent of the continuum or the brightest emission line. Acquisition images were taken to center the slit and in addition, for a few sources, to determine their R -band magnitude.

2.2.2 ESO 3.6m observations

Optical CCD imaging and spectroscopy were also performed using the ESO 3.6m Telescope at La Silla, in Chile, on March 23 and 24, 2004. For all observations we used the ESO Faint Object Spectrograph and Camera (EFOSC II), which has a 2048×2048 CCD detector with $15\mu\text{m}$ pixels resulting in a scale of $0.157''/\text{pixel}$ and a field size of $5.4' \times 5.4'$. Spectroscopic observations were carried out in long slit mode with a slit width of $1.2''$, using the EFOSC grism #6, which has a wavelength coverage of 3860 - 8070 Å and a dispersion of 137 Å/mm or 2.06 Å/pixel . The slit was always oriented near the parallactic angle. The reduction of the spectra was carried out in a similar way to the VLT data.

Photometric observations were carried out in Gunn r -band (EFOSC filter $r\#786$). The reduction of the images was carried out in a standard way using NOAO's IRAF reduction software. Astrometry was performed using data from the USNO-B1.0 Catalog, extracted with the VizieR catalogue access tool. For each image, catalogued positions of at least ten stars were used. With the IRAF procedure CCMAP, the equatorial coordinates were determined with errors always well within one pixel. Optical identifications were found, within the $1-\sigma$ uncertainty ellipse, for all seven radio sources. Photometry was carried out using the IDL procedure APER with the aperture diameter set to $2.51''$ (16 pixels). The magnitude scale was calibrated using Landolt standard stars, with their Cousins R_C magnitudes converted to Gunn r using the conversion formula from Schombert et al. (1990):

$$r = R_C + 0.280 + 0.038(R_C - I_C) \quad (2.1)$$

For better comparison with the rest of the sample, we also calculated

Cousins R_C magnitudes of the sources by using the unconverted Cousins R_C magnitudes of the standard stars to calibrate our Gunn r data. Since the colors of the sources are unknown, this conversion introduces extra uncertainties. However, these were always found to be small compared to the photometric errors.

2.2.3 Additional near-infrared photometry

Earlier optical observations of the GPS source PKS J0210+0419 (Snellen et al. 2002), did not result in an identification, with a lower limit of $m_R > 24.1$. We therefore observed this source in K_s -band using the SOFI near-infrared camera on ESO's New Technology Telescope (NTT). SOFI is equipped with a Rockwell 1024×1024 detector that provides images with a pixel scale of $0.288''/\text{pixel}$, and a field of view of about $4.9' \times 4.9'$ (Large Field imaging mode). The SOFI K_s filter has a central wavelength of $2.162 \mu\text{m}$ and a width of $0.275 \mu\text{m}$. Details of the K_s -band observations of PKS J0210+0419 and of other sources in the sample will be published in a following paper, however we present the K_s -band identification and magnitude of PKS J0210+0419 ($K_s = 18.3$) here for completeness.

2.3 Results and discussion

In total, eleven previously unidentified sources in the sample have been observed in R -band with the ESO 3.6m and VLT telescopes. All were optically identified, with $21.0 < R_C < 23.0$. Including the one identification in K -band (PKS J0210+0419), this means that the Parkes half-Jansky sample of GPS galaxies is now *completely* identified. Note that we have left one source (PKS J1600–0037) out of our statistical sample, because it is located too close to a 12^{th} magnitude star to make an optical identification possible. Since this is a random occurrence, it does not introduce any selection effects, so the sample will remain statistically complete. The results of the photometric observations are given in Table 2.1; in column 1 the source name, in column 2 the exposure time, in column 3 the observed Gunn r -band magnitude with its error, and in column 4 the observed or deduced Cousins R_C -band magnitude.

We have also taken deep spectra of 24 objects in total. These have resulted in twenty secure redshifts, based on two or more emission or

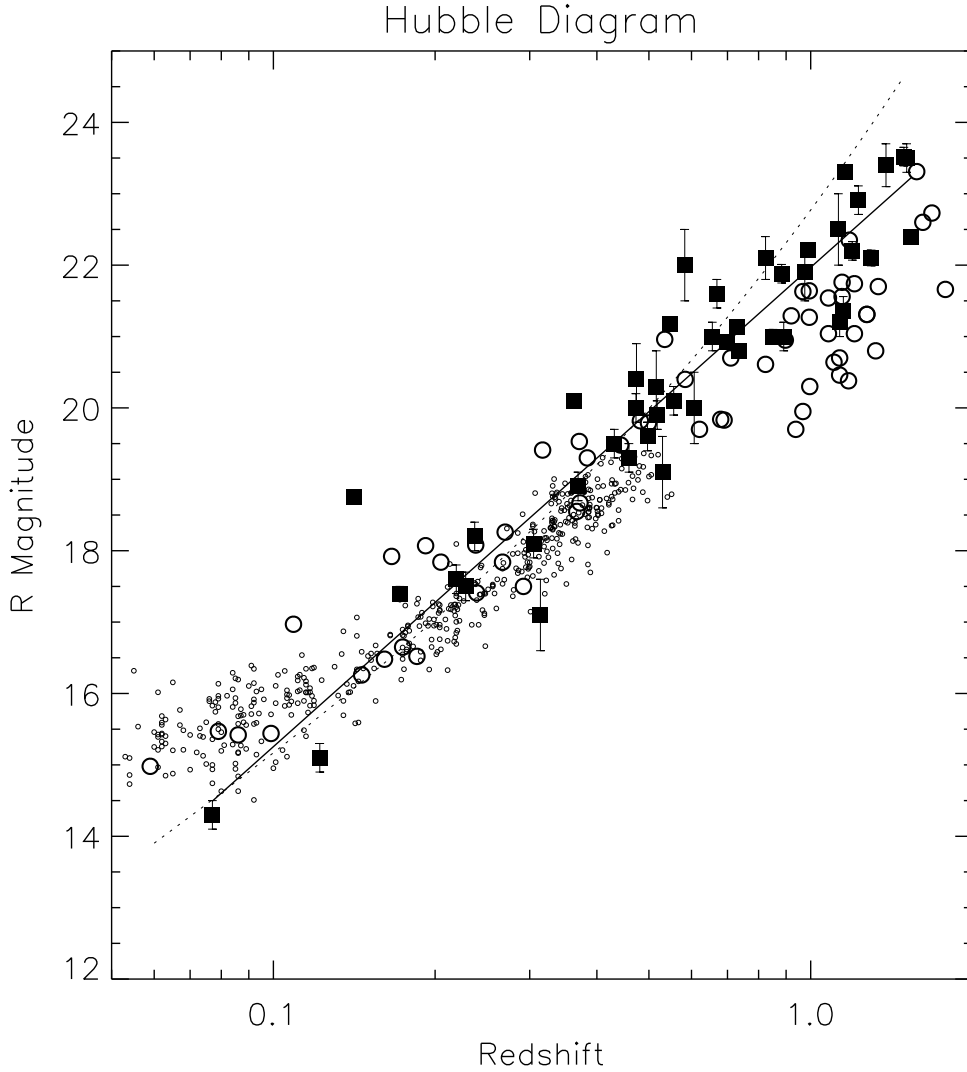


Figure 2.1: — Cousins R_C Hubble diagram of GPS galaxies (solid squares), 3C galaxies (open circles), and LRGs (small circles). The dotted line is the R -band Hubble relation as derived by Snellen et al. (1996a), the solid line is a linear least squares fit to the current data.

absorption lines, all in the range $0.474 < z < 1.539$. One spectrum (PKS J1556–0622) resulted in a tentative redshift ($z = 1.195$), based on only one line. We assumed the line to be [OII] 3727 Å, because of the resemblance between this spectrum and those of PKS J2339–0604 and PKS J2212+0152, and the absence of plausible alternatives. A further nine sources in the sample (19%) remain without redshift. The results of the spectroscopic observations are given in the appendix (Table 2.3); in column 1 the source name, in column 2 the exposure time, in column 3 the name of the telescope used, in columns 4–7 respectively the name, rest wavelength, observed wavelength and rest-frame equivalent width

of the identified spectral features, and in column 8 the derived redshift for each identified spectral feature and for each source. All spectra are also shown in the appendix (Fig. 2.4).

Table 2.1: — Details of the photometric observations.

ESO 3.6m Telescope observations			
Object name	t (s)	m_r	m_{RC}
PKS J0441–3340	600	22.8 ± 0.4	22.5 ± 0.4
PKS J0913+1454	1200	23.2 ± 0.5	22.9 ± 0.5
PKS J1044–2712	1200	23.1 ± 0.4	22.8 ± 0.4
PKS J1057+0012	1200	22.6 ± 0.3	22.3 ± 0.3
PKS J1109+1043	1200	22.9 ± 0.3	22.6 ± 0.3
PKS J1122–2742	1600	23.3 ± 0.5	23.0 ± 0.5
PKS J1135–0021	60		21.9 ± 0.4
PKS J1648+0242	1200	22.4 ± 0.3	22.1 ± 0.3
ESO VLT observations			
Object name	t (s)		m_{RC}
PKS J0401–2921	10		21.0 ± 0.2
PKS J1345–3015	10		21.2 ± 0.2
PKS J1352+1107	10		21.0 ± 0.2
ESO NTT observation			
Object name	t (s)		m_{Ks}
PKS J0210+0419	450		18.3 ± 0.2

2.3.1 R-band Hubble diagram

Now that we have significantly increased the number of GPS galaxies with known redshifts, particularly around redshift $z \sim 1$, it is interesting to review the R-band Hubble relation as previously discussed by Snellen et al. (1996a) and O’Dea et al. (1996). For this purpose we combined our southern/equatorial sample with the northern sample of GPS sources of Stanghellini et al. (1998), excluding all those objects identified with quasars. Spectroscopic observations of two sources from our sample (PKS J1203+0414 and PKS J1506–0919) reveal broad emission lines ($\sim 10^4$ km/s) and non-thermal emission. Technically these sources are now identified as quasars, and have been omitted from the sample. The resulting R-band Hubble diagram of GPS galaxies (solid squares) is shown in Fig. 2.1. For comparison, 3C radio galaxies (open circles) from a compilation of samples (Best et al. (1997), Eales (1985), and de Koff

et al. (1996)) and a subset of the ‘Luminous Red Galaxies’ (LRGs; small circles) sample (Eisenstein et al. 2001) from the Sloan Digital Sky Survey (SDSS) are shown. If necessary, the magnitudes were converted to ‘total magnitudes’ in Cousins R_C . Note the one GPS source (PKS J1604–2223, with $R_C = 18.75$ and $z = 0.141$) that is over two magnitudes fainter than the general population. This is much too faint for a typical powerful AGN host galaxy, for which a number of explanations could be given. Although the source is located in a region with high galactic extinction, it is unlikely that this is the reason for the offset, since the object is also over two magnitudes fainter in K -band (de Vries et al. in prep.) than expected from the K -band Hubble diagram (as presented by Snellen et al. 1996b). Of course there is always the possibility that a foreground galaxy is located between us and the radio source. This would also explain why the optical spectrum shows no emission lines or signs of nuclear activity. Alternatively, it could be that the source is not a typical young powerful AGN, but some other object that happens to have a similar radio spectrum. Although PKS J1604–2223 is shown in Fig. 2.1, it is left out of any further analysis.

Now that the R -band Hubble relation is better sampled at $z \sim 1$ it is clear that the new data points systematically fall below the original fit (dotted line) of Snellen et al. (1996a). Since this relation is often used to estimate redshifts of GPS galaxies for which only photometric R -band data are available, it is valuable to determine a relation that holds for a larger redshift range, out to $z \simeq 1.5$. We performed a linear least squares fit to the current data and found the relation:

$$m_{R_C} = 21.97 + 6.71 \times \log(z) \quad (2.2)$$

with a dispersion of 0.6 magnitudes. To estimate redshifts of GPS galaxies, this relation can be inverted to give:

$$z_{est} = 5.32 \cdot 10^{-4} \times (1.41)^{m_R}, \quad \sigma_z \simeq 0.21 \times z_{est} \quad (2.3)$$

with σ_z the 1- σ uncertainty in the redshift estimate.

Furthermore the new data at $z \sim 1$ confirm that GPS galaxies are on average 1.0 magnitudes fainter in this redshift range than 3C radio galaxies, as was initially claimed by Snellen et al. (1996a). This agrees with the hypothesis that GPS galaxies are redder, due to the lack of

the extra, blue light associated with the radio-optical alignment effect (Chambers, Miley & van Breugel 1987; McCarthy et al. 1987; Best, Longair & Röttgering 1997). The LRGs form a volume limited sample of the most luminous, intrinsically red galaxies out to $z \simeq 0.55$. They are selected on the basis of colors and magnitudes, and are thought to represent the most massive early type galaxies, many of which are classified as ‘Brightest Cluster Galaxies’. Fig. 2.1 shows that host galaxies of GPS radio sources have similar optical luminosities to LRGs, indicating that powerful young radio sources are hosted by the most massive early type galaxies. Note that the flattening of the distribution of LRGs at low redshift is probably due to the known problem that SDSS subtracts too high background levels for large sources, which can result in a magnitude difference of up to ~ 1 magnitude.

2.3.2 Absolute magnitudes

To study the cosmological evolution of GPS galaxies in more detail, we determined their absolute magnitudes M_{RC} as a function of redshift. These can be calculated from the apparent magnitudes m_{RC} , using (Hogg 2000):

$$\begin{aligned} m_{RC} &= M_{RC} + \mu + K \\ &= M_{RC} + 5 \log \left(\frac{D_L}{10 \text{ pc}} \right) - 2.5 \log \left[\frac{L_{\lambda/(1+z)}}{(1+z) L_{\lambda}} \right] \end{aligned} \quad (2.4)$$

with μ the distance modulus, which depends, through the luminosity distance D_L , on the redshift of the source and on the assumed cosmology (we adopted the cosmological parameters as found by WMAP; Spergel et al. 2006). The last term, K , is the ‘k-correction’, which is required to convert the absolute magnitude to rest-frame R -band. This depends on the assumed spectral energy distribution (SED) of the source and is represented by the luminosity at the intrinsic wavelength $L_{\lambda/(1+z)}$ divided by that at the observed wavelength L_{λ} .

All variables in equation (2.4) are determined in a straightforward way from the observations and adopted cosmology, except for the k-correction. We therefore determined $m_R - \mu$ for each galaxy in the sample and determined a range of possible k-corrections, depending on the age and metallicity of the stellar population. For these we used the

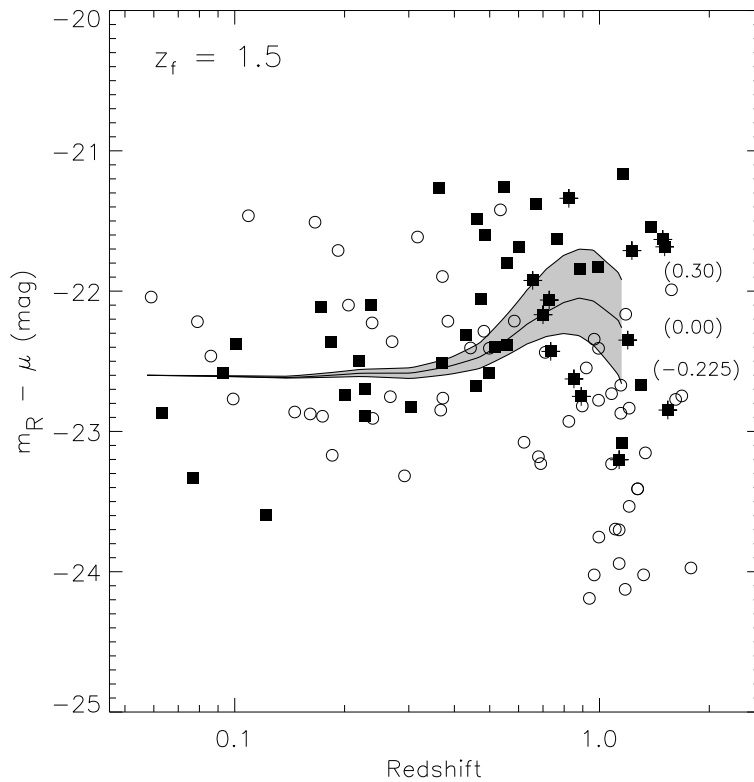
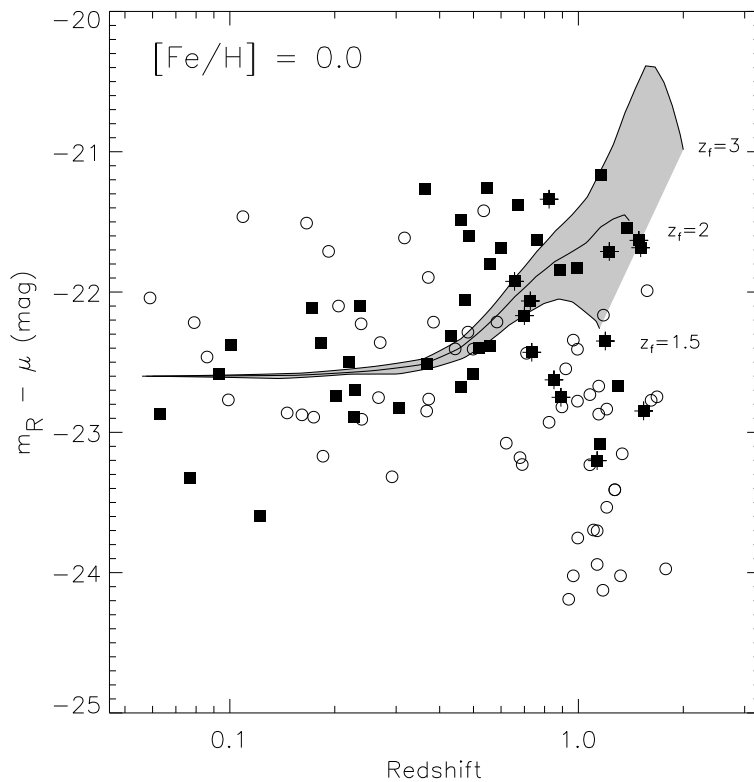


Figure 2.2 — (top) Absolute magnitudes (without k-correction, $m_R - \mu$) for the combined samples of GPS galaxies (solid squares) and 3C galaxies (open circles). The grey shaded area is the modelled evolution, assuming a formation redshift of 1.5 and a range of metallicities from -0.225 to 0.30. Evolutionary tracks for the extreme metallicities as well as one for solar metallicity are overplotted, with metallicity decreasing from the upper to the lower track.

(bottom) The same figure, except that the evolution models now vary in formation redshift and keep the metallicity fixed at solar. The evolutionary tracks are for a formation redshift of 1.5 (lower), 2 (middle) and 3 (upper).



model galaxy SEDs by Worthey (1994). In figure (2.2) we show $m_R - \mu$ of the combined samples (see Sect. 2.3.1) of GPS galaxies (solid squares) and 3C galaxies (open circles) as a function of redshift. The three solid lines show the expected trend in $m_R - \mu$ for a stellar population with a formation redshift $z_f = 1.5$ and metallicities $[\text{Fe}/\text{H}]$ of 0.3, 0.0, and -0.225 compared to solar. In figure (3) we show the same data, overplotted with the k-correction for a stellar population with solar metallicity and a range of formation redshifts of $z_f = 1.5, 2.0$, and 3.0 .

These figures show that the data are in best agreement with a recent formation redshift of $1.5 - 2.0$ (with a possible range of metallicities). However, we do not believe that the host galaxies really are that young, since GPS galaxies are always classified as early type galaxies, which are generally thought to have formed at higher redshifts ($z \sim 5$). In addition, Fig. 2.1 also indicates that GPS galaxies are old, massive, early type galaxies. Therefore we interpret this result as evidence for starburst activity and/or AGN induced light. We note that, although the optical/UV contribution from the alignment effect appears significantly smaller in GPS galaxies than for classical 3C radio galaxies, it does not exclude such AGN induced light being present at a low level. This extra blue light would brighten galaxies the most at high redshifts, where the R -band probes the rest-frame UV, and therefore could mimic a young stellar population and low formation redshifts. A thorough investigation using deep optical and infrared spectra will be needed to determine the possible contributions from the AGN and young starbursts to the overall galaxy spectrum.

Acknowledgments

This research has made use of observations collected at the ESO/Paranal Very Large Telescope and the ESO/La Silla 3.6m Telescope, and made use of the VizieR catalogue access tool, CDS, Strasbourg, France (Ochsenbein et al. 2000). This publication makes use of data products from the USNO-B1.0 Catalog and the Two Micron All Sky Survey, which is a joint project of the University of Massachusetts and the Infrared Processing and Analysis Center/California Institute of Technology, funded by the National Aeronautics and Space Administration and the National Sci-

ence Foundation.

References

- Baum S.A., O'Dea C.P., Murphy D.W., de Bruyn A.G., 1990, *A&A*, 232, 19
 Best P.N., Longair M.S., Röttgering H.J.A., 1997, *MNRAS*, 292, 758
 Biretta J.A., Schneider D.P., Gunn J.E., 1985, *AJ*, 90, 250
 Chambers K.C., Miley G.K., van Breugel W., 1987, *Nature*, 329, 604
 Drinkwater M.J. et al., 1997, *MNRAS*, 284, 85
 de Koff S., Baum S.A., Sparks W.B. et al., 1996, *ApJS*, 107, 621
 de Vries W.H., Barthel P.D., Hes R., 1995, *A&AS*, 114, 259
 de Vries W.H., Barthel P.D., O'Dea C.P., 1997, *A&A*, 321, 105
 de Vries W.H., O'Dea C.P., Barthel P.D., Thompson D.J., 2000, *A&AS*, 143, 18
 Eales S.A., 1985, *MNRAS*, 213, 899
 Eisenstein D.J. et al., 2001, *AJ*, 122, 2267
 Fugmann W., Meisenheimer K., Roeser H.-J., 1988, *A&AS*, 75, 173
 Hambly N.C. et al., 2001, *MNRAS*, 326, 1279
 Hogg, D.W., 2000, astro-ph/9905116
 Irwin M., Maddox S., McMahon R., 1994, *Spectrum*, 2, 14
 McCarthy, P.J., van Breugel, W., Spinrad, H. Djorgovski, S., 1987, *ApJ*, 321, 29
 Murgia M., 2003, *PASA*, 20, 19M
 Ochsenbein F., Bauer P., Marcout J., 2000, *A&AS* 143, 221
 O'Dea C.P., Baum S.A., Morris G.B., 1990, *A&A*, 82, 261
 O'Dea C.P., Stanghellini C., Baum S.A., Charlot S., 1996, *ApJ*, 470, 806
 Otrupcek R., Wright A., 1991, *PASA*, 9, 170
 Owsianik I., Conway J.E., 1998, *A&A*, 337, 69
 Owsianik I., Conway J.E., Polatidis A.G., 1998, *A&A*, 336, L37
 Polatidis A.G., Conway J.E., 2003, *PASA*, 20, 69P
 Schombert J.M., Wallin J.F., & Struck-Marcell, C. 1990, *AJ*, 99, 497
 Snellen I.A.G., Bremer M.N., Schilizzi R.T., Miley G.K., van Ojik R., 1996a, *MNRAS*, 279, 1294
 Snellen I.A.G., Bremer M.N., Schilizzi R.T., Miley G.K., 1996b, *MNRAS*, 283, 123
 Snellen I.A.G., Schilizzi R.T., Bremer M.N. et al., 1999, *MNRAS*, 307, 149
 Snellen I.A.G., Lehnert M.D., Bremer M.N., Schilizzi R.T., 2002, *MNRAS*, 337, 981
 Spergel D.N. et al., 2006, submitted, "Three-Year Wilkinson Microwave Anisotropy Probe (WMAP) Observations: Implications for Cosmology"
 Stanghellini C., O'Dea C.P., Baum S.A., Laurikainen E., 1993, *ApJS*, 88, 1
 Stanghellini C., O'Dea C.P., Dallacasa D. et al., 1998, *A&AS*, 131, 303
 Stanghellini C., O'Dea C.P., Murphy D.W., 1999, *A&AS*, 134, 309
 Stern D., Dey A., Spinrad H. et al., 1999, *AJ*, 117, 1122
 Tschager W., Schilizzi R.T., Röttgering H.J.A., Snellen I.A.G., Miley G.K., 2000, *A&A*, 360, 887
 Vink J., Snellen I.A.G., Mack K.-H., Schilizzi R.T., 2006, *MNRAS*, 367, 928V
 Worthey G., 1994, *ApJS*, 95, 107
 Wright A., Otrupcek R., 1990, *PKS Catalog*

2.4 Appendix

2.4.1 Comments on selected sources

PKS J0108–1201 The carbon line CIII] 1909 Å and the neon lines ([NeV] 3346 Å, [NeV] 3426 Å) are detected. By smoothing the spectrum with a boxcar of 20 pixels the MgII 2799 Å line is revealed as a broad (FWHM ~ 250 Å $\sim 10^4$ km/s) spectral feature, centered at ~ 7100 Å.

PKS J0210+0419 Neither a continuum nor emission lines were detected for this object. This is consistent with the non-detection in the *R*-band (Snellen et al. 2002).

PKS J0401–2921 The spectrum shows very strong oxygen lines, weaker neon lines and the CaII K and H absorption features with a 4000 Å break.

PKS J0407–2757 The slit was tilted 45° so that the object North Eastern of the radio source (separation $\sim 2.5''$) was included. The North Eastern object shows many strong emission lines, where the South Western object shows [OII] 3727 Å and very weak neon lines. An *R*-band image of this source is shown in Fig. 2.3.

PKS J0433–0229 The spectrum shows [OII] 3727 Å in emission and the Ca II H, G-band, H_γ , H_β and MgI features in absorption.

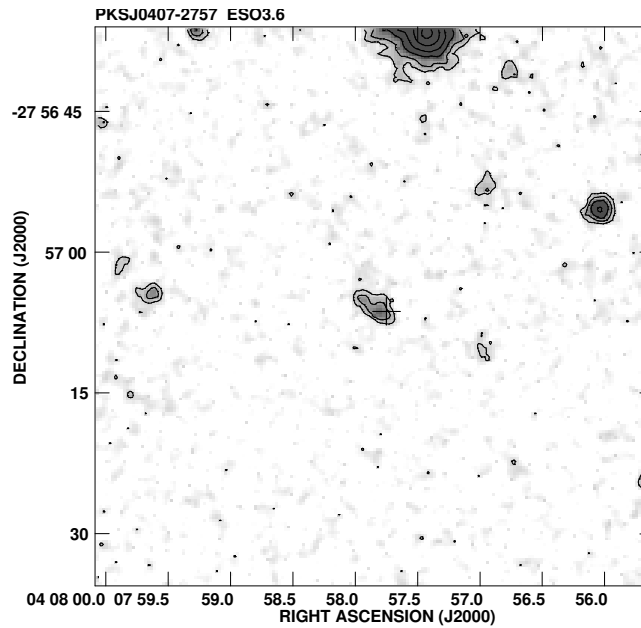


Figure 2.3: — *R*-band image of PKS J0407–2757 taken from Snellen et al. (2002). The GPS radio source is located in the South Western object, as indicated with the plus sign. Most of the line emission originates from the object North Eastern of the radio source.

PKS J1057+0012 This object was observed in photometric (1200 s) and spectroscopic (2700 s) mode on the ESO 3.6m Telescope. The images resulted in a new identification with a $m_{RC} = 22.5 \pm 0.3$ object, but the spectrum was not deep enough to determine a redshift for this source.

PKS J1109+1043 This radio source has erroneously been identified with a $m_{RC} = 20.5$ object. It was already noted (Snellen et al. 2002) that there was a large offset between the radio and optical position. Our observations resulted in an identification with a much fainter object ($m_{RC} = 22.6 \pm 0.3$) at the radio position. The S/N of the spectrum (2700 s on the 3.6m Telescope) was too low to see spectral features.

PKS J1135–0021 This radio source has erroneously been identified with a star ($m_{RC} = 16.5$). In our long slit spectrum we found, at a distance of about $2.4''$ from the typical stellar spectrum, a faint AGN spectrum from which we determined a redshift of 0.975. From the acquisition image we also estimated the magnitude of the object: $m_{RC} = 21.9 \pm 0.4$.

PKS J1203+0414 Spectroscopic observations of this object show a typical quasar spectrum with broad carbon and magnesium lines and the object should therefore be removed from the sample of GPS galaxies.

PKS J1345–3015 The spectrum shows a strong [OII] 3727 Å line, the CII] 2326 Å, [NeV] 3426 Å and [NeIII] 3869 Å lines and a very broad MgII feature.

PKS J1352+1107 The [OII] 3727 Å line, the neon emission lines and the CaII K and H absorption features are detected.

PKS J1506–0919 Spectroscopic observations of this object show a typical quasar spectrum with broad carbon and magnesium lines and the object should therefore be removed from the sample of GPS galaxies.

PKS J1556–0622 Only one emission line is detected, so only a tentative redshift could be determined. We assumed the line to be [OII] 3727 Å, because of the resemblance between this spectrum and those of PKS J2339–0604 and PKS J2212+0152, and the absence of viable alternatives.

PKS J1648+0242 The spectrum shows very weak [OII] 3727 Å and neon emission lines, but strong CaII K and H absorption features, the G-band and the 4000 Å break.

PKS J1734+0926 The [OII] 3727 Å and [NeIII] 3869 Å emission lines are weak, but the H_γ and CaII K and H absorption features, the G-band and

the 4000 Å break are strong.

PKS J2212+0152 The [OII] 3727 Å emission line is strong and the MgII 2798 Å and neon lines are weak.

PKS J2339–0604 The spectrum shows a strong [OII] 3727 Å line and weak CII] 2326 Å, MgII 2798 Å and [NeIII] 3869 Å lines.

Table 2.2: — The radio and optical properties of objects in the southern/equatorial sample of GPS galaxies.

Comments: (A) also in the sample of > 1 Jy GPS sources from Stanghellini et al. (1998); (B) also in the sample of de Vries et al. (1997) (C) also in the sample of de Vries et al. (2000); (D) near a bright star, no magnitude; (E) radio source is optically identified with a quasar; will be excluded from the sample.

References: (1) this chapter; (2) Snellen et al. (2002); (3) Snellen et al. (1996a); (4) O’Dea, Baum & Morris (1990); (5) de Vries et al. (1995); (6) de Vries et al. (2000). (7) Biretta, Schneider & Gunn (1985); (8) Stern et al. (1999); (9) Fugmann, Meisenheimer & Rooser (1988); (10) Stanghellini et al. (1993); (11) Stanghellini et al. (1998); (12) Otrupcek & Wright (1991); (13) Drinkwater et al. (1997); (14) Digitized Sky Survey II; APM catalogue (Irwin et al. 1994); SuperCosmos Sky Surveys (Hambly et al. 2001).

IAU name	Other name	Radio position (J2000)			m_{R_C} (mag)	z	$S_{2.7\text{GHz}}$ (Jy)	ν_{peak} (GHz)	S_{peak} (Jy)	Ref. m_R	Ref. z	Com.
J0022+0014	4C+00.02	00 22 25.48	+00 14 56.0	18.10 \pm 0.20	0.305	0.305	1.94	0.6	3.1	3	3	A
J0108–1201	B0105–122	01 08 13.20	–12 00 50.3	22.39 \pm 0.06	1.539	1.539	0.52	1.0	0.9	2	1	
J0206–3024	B0204–306	02 06 43.26	–30 24 58.2	21.00 \pm 0.50			0.58	0.5	0.9	14		
J0210+0419	B0208+040	02 10 44.52	+04 19 35.4	K_s 18.3 \pm 0.2			0.56	0.4	1.3	1		
J0210–2213	B0207–224	02 10 10.05	–22 13 36.6	23.52 \pm 0.13	1.491	1.491	0.86	1.5	1.1	2	1	
J0242–2132	B0240–217	02 42 35.87	–21 32 26.2	17.10 \pm 0.50	0.314	0.314	0.97	1.0	1.3	14	12	
J0323+0534	4C+05.14	03 23 20.27	+05 34 11.9	19.20 \pm 0.50			1.60	0.4	7.1	14		
J0401–2921	B0359–294	04 01 21.50	–29 21 26.1	21.00 \pm 0.20	0.656	0.656	0.58	0.4	1.0	1	1	
J0407–3924	B0405–395	04 07 34.43	–39 24 47.2	20.40 \pm 0.50	0.474	0.474	0.52	0.4	1.4	14	1	
J0407–2757	B0405–280	04 07 57.94	–27 57 05.1	21.14 \pm 0.04	0.728	0.728	0.93	1.5	1.4	2	1	
J0433–0229	4C–02.17	04 33 54.90	–02 29 56.0	19.10 \pm 0.50	0.530	0.530	1.04	0.4	3.0	14	1	
J0441–3340	B0439–337	04 41 33.80	–33 40 03.6	22.50 \pm 0.40			0.88	1.5	1.2	1		
J0457–0848	B0454–088	04 57 20.24	–08 49 05.2	20.30 \pm 0.50	0.516	0.516	0.58	0.4	1.0	14	1	
J0503+0203	B0500+019	05 03 21.20	+02 03 04.6	21.0 \pm 0.20	0.583	0.583	2.46	2.5	2.5	5	5	A
J0943–0819	B0941–080	09 43 36.86	–08 19 32.0	17.50 \pm 0.20	0.228	0.228	1.73	0.4	4.2	10	11	A
J0913+1454	B0910+151	09 13 35.00	+14 54 20.1	22.90 \pm 0.50			0.54	0.6	1.1	1		
J1044–2712	B1042–269	10 44 37.63	–27 12 18.6	22.80 \pm 0.40			0.55	1.5	0.8	1		
J1057+0012	B1054+004	10 57 15.78	+00 12 03.7	22.30 \pm 0.30			0.58	0.4	1.6	1		
J1109+1043	B1107+109	11 09 46.04	+10 43 43.4	22.60 \pm 0.30			0.80	0.5	2.4	1		
J1110–1858	B1107–187	11 10 00.45	–18 58 49.2	19.60 \pm 0.20	0.497	0.497	0.65	1.0	0.9	9	13	
J1120+1420	4C+14.41	11 20 27.81	+14 20 55.0	20.10 \pm 0.10	0.362	0.362	1.50	0.4	3.7	5	5	A
J1122–2742	B1120–274	11 22 56.41	–27 42 48.2	23.00 \pm 0.50			0.74	1.4	0.8	1		
J1135–0021	4C–00.45	11 35 12.96	–00 21 19.5	21.90 \pm 0.40	0.975	0.975	0.76	0.4	2.9	1	1	

Table 2.2: — The radio and optical properties of objects in the southern/equatorial sample of GPS galaxies, continued.

IAU name	Other name	Radio position (J2000)			m_{R_C} (mag)	z	$S_{2.7\text{GHz}}$ (Jy)	ν_{peak} (GHz)	S_{peak} (Jy)	Ref. m_R	Ref. z	Com.
J1203+0414	B1200+045	12 03 21.95	+04 14 17.7	18.80 ± 0.50	1.221	0.52	0.4	1.4	14	1	1	E
J1345−3015	B1343−300	13 45 51.52	−30 15 04.1	21.20 ± 0.20	1.132	0.56	0.4	2.5	1	1	1	
J1347+1217	4C+12.50	13 47 33.36	+12 17 24.2	15.20 ± 0.20	0.122	3.88	0.4	8.8	3	3	3	A
J1350−2204	B1347−218	13 50 14.33	−22 04 43.7	20.93 ± 0.05	0.700	0.72	0.4	1.4	2	2	1	
J1352+0232	B1349+027	13 52 30.68	+02 32 47.7	20.00 ± 0.50	0.607	0.78	0.4	2.0	14	14	1	
J1352+1107	4C+11.46	13 52 56.37	+11 07 07.7	21.00 ± 0.20	0.891	0.78	0.4	3.6	1	1	1	
J1447−3409	B1444−339	14 47 19.69	−34 09 16.2	21.00 ± 0.10	0.851	0.50	0.5	1.0	14	14	1	
J1506−0919	B1503−091	15 06 03.05	−09 19 12.5	19.70 ± 0.50	1.486	0.87	0.6	1.6	14	14	1	E
J1521+0430	4C+04.51	15 21 14.51	+04 30 20.0	22.10 ± 0.11	1.296	2.30	1.0	5.4	7	11	11	A
J1543−0757	B1540−077	15 43 01.69	−07 57 03.6	17.40 ± 0.10	0.172	1.21	0.4	1.7	6	6	6	C
J1546+0026	B1543+005	15 46 09.50	+00 26 24.6	20.10 ± 0.20	0.556	1.24	0.6	2.2	3	3	6	C
J1548−1213	B1545−120	15 48 12.97	−12 13 31.8	21.88 ± 0.13	0.883	1.45	0.4	3.7	2	2	2	
J1556−0622	4C−06.43	15 56 13.99	−06 22 37.8	22.20 ± 0.13	(1.195)	0.77	0.4	2.4	2	2	1	
J1600−0037	B1557−004	16 00 00.91	−00 37 23.3	—	—	0.54	1.0	1.2	2	2	2	D
J1604−2223	B1601−222	16 04 01.45	−22 23 41.3	18.75 ± 0.10	0.141	0.57	0.6	1.0	6	6	2	
J1640+1220	4C+12.60	16 40 47.96	+12 20 02.1	21.36 ± 0.20	1.150	1.48	0.4	3.7	2	2	2	
J1648+0242	4C+02.43	16 48 31.79	+02 42 46.0	22.10 ± 0.30	0.824	0.61	0.4	3.4	1	1	1	
J1734+0926	B1732+094	17 34 58.38	+09 26 57.8	20.80 ± 0.10	0.735	1.08	1.0	1.1	6	1	1	B
J2011−0644	B2008−068	20 11 14.22	−06 44 03.6	21.18 ± 0.04	0.547	2.09	1.4	2.6	2	2	2	A
J2058+0540	4C+05.78	20 58 28.84	+05 42 50.7	23.40 ± 0.30	1.381	0.65	0.4	3.1	8	8	8	
J2123−0112	B2121−014	21 23 39.12	−01 12 34.3	23.30 ± 0.10	1.158	0.64	0.4	2.0	4	4	3	
J2130+0502	B2128+048	21 30 32.88	+05 02 17.5	22.21 ± 0.07	0.990	3.12	1.0	4.8	2	2	11	A
J2151+0552	B2149+056	21 51 37.88	+05 52 13.0	20.20 ± 0.20	0.740	1.01	5.0	1.2	4	4	11	A,E
J2212+0152	4C+01.69	22 12 37.97	+01 52 51.7	22.0 ± 0.20	1.126	1.80	0.4	4.6	5	5	1	A
J2325−0344	B2322−040	23 25 10.23	−03 44 46.7	23.50 ± 0.20	1.509	0.91	1.4	1.2	10	10	1	B
J2339−0604	4C−06.76	23 37 11.95	−06 04 12.4	22.91 ± 0.20	1.227	0.80	0.4	3.8	2	2	1	

2.4.2 Tables and figures

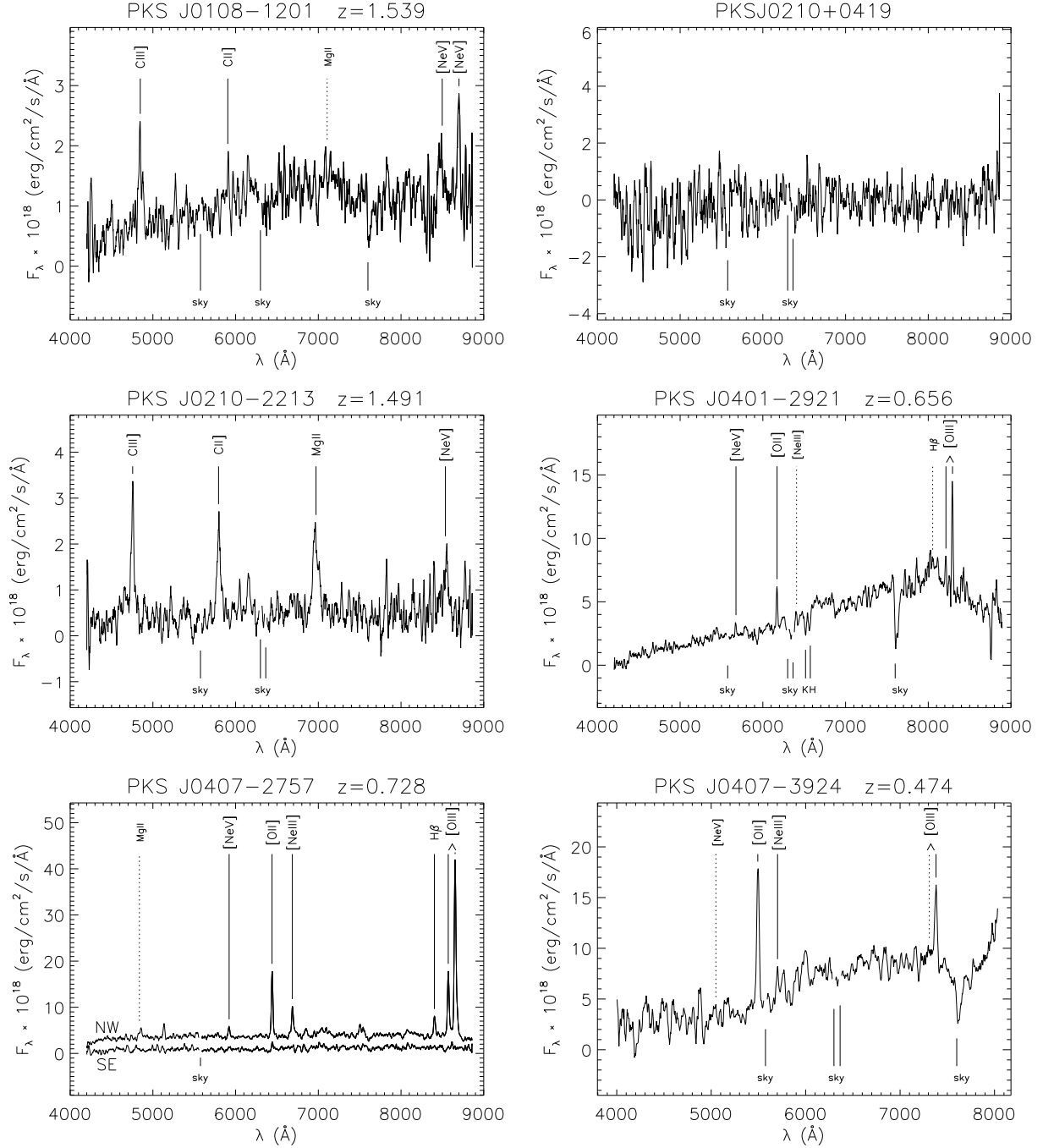


Figure 2.4: — Spectra from the ESO Very Large Telescope and ESO 3.6m Telescope of 24 objects in the sample. From 21 spectra, a redshift could be deduced, which is indicated at the top. Labeled are emission and absorption lines that were used to determine the redshift (drawn lines) and wavelengths where other common emission lines are expected (dotted lines). Regions where the night sky emission lines are strong have been omitted. These regions are indicated, as well as the 7000 \AA sky absorption feature.

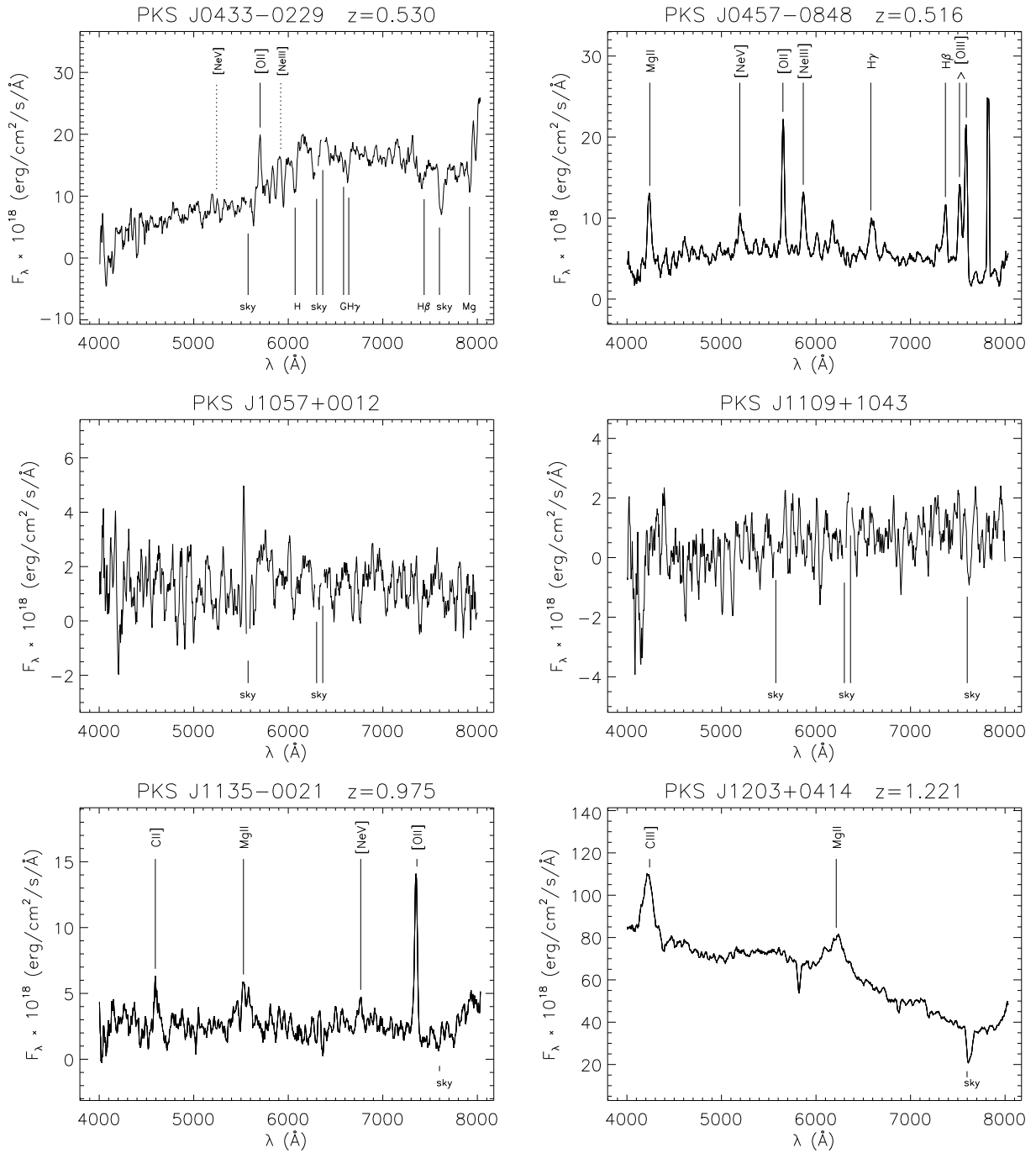
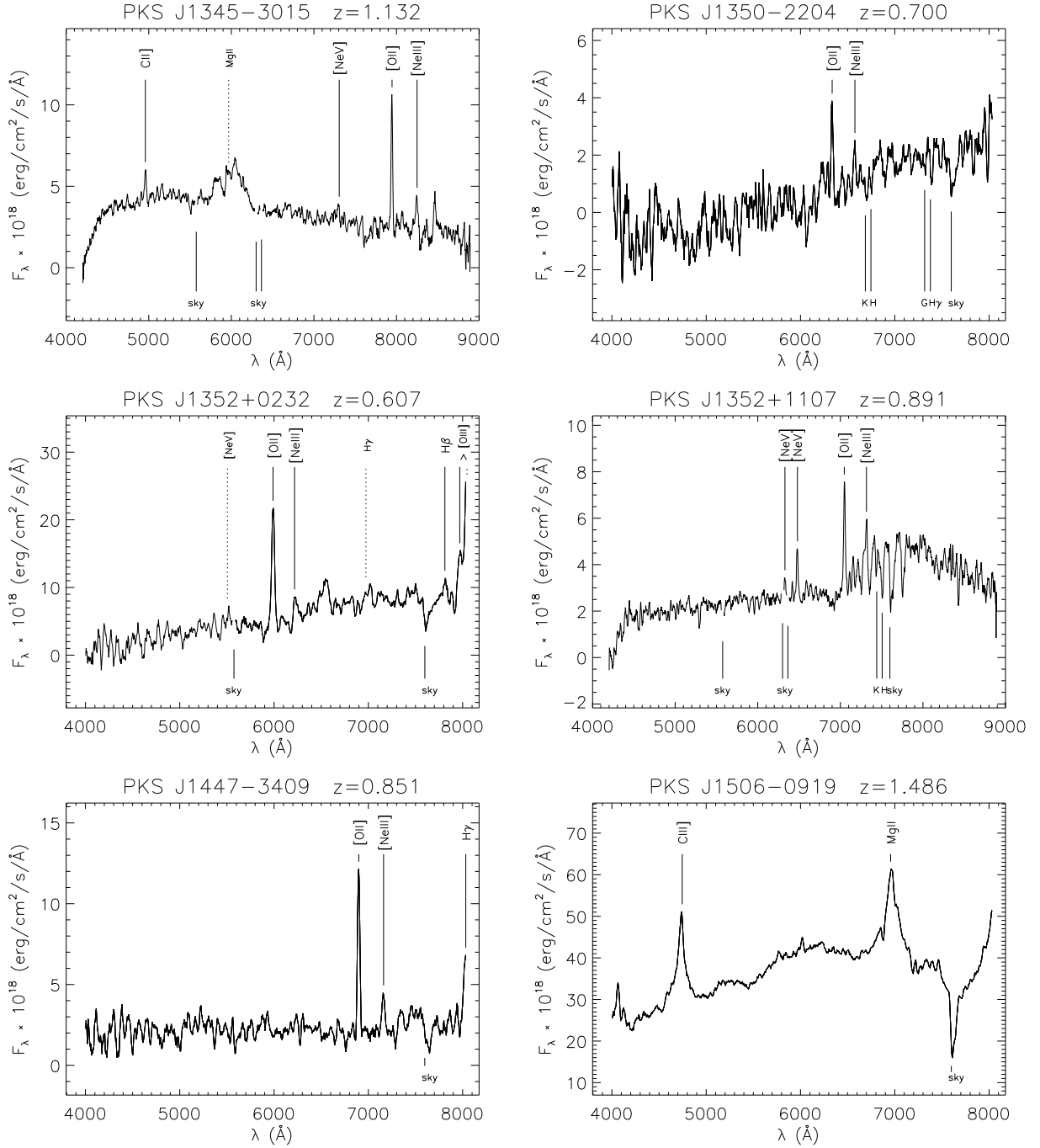


Figure 2.4: — continued

Figure 2.4: — *continued*

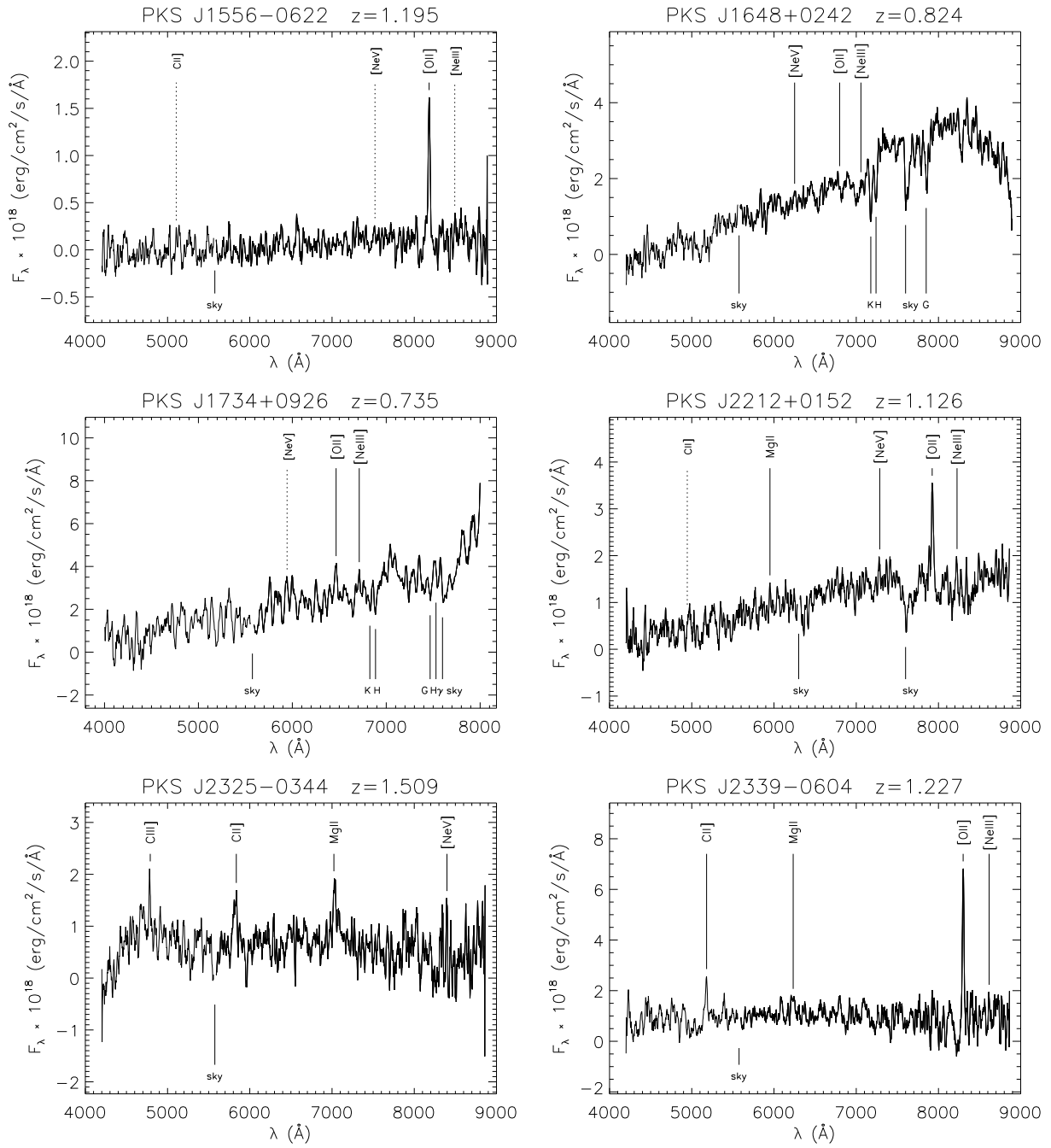


Figure 2.4: — continued

Table 2.3: — Details of the spectroscopic observations.

Object name	t (s)	Telescope	Spectral feature			z
			Species	λ_{rest} (Å)	λ_{obs} (Å)	
PKS J0108–1201	1800	ESO VLT				1.539 ± 0.001
			CIII]	1909	4845	1.538
			CII]	2326	5911	1.541
			[NeV]	3346	8488	1.537
			[NeV]	3426	8700	1.539
PKS J0210+0419	1800	ESO VLT				
PKS J0210–2213	1800	ESO VLT				1.491 ± 0.003
			CIII]	1909	4757	1.492
			CII]	2326	5799	1.493
			MgII	2798	6964	1.489
			[NeV]	3426	8553	1.497
PKS J0401–2921	1800	ESO VLT				0.656 ± 0.001
			[NeV]	3426	5672	0.656
			[OII]	3727	6170	0.656
			CaII K	3934	6518	0.657
			CaII H	3969	6562	0.653
			[OIII]	4959	8212	0.656
			[OIII]	5007	8290	0.656
PKS J0407–2756	1800	ESO VLT				0.728 ± 0.001
North West			[NeV]	3426	5920	0.728
			[OII]	3727	6442	0.728
			[NeIII]	3869	6687	0.728
			H β	4861	8404	0.729
			[OIII]	4959	8571	0.728
			[OIII]	5007	8654	0.728
PKS J0407–2756	1800	ESO VLT				0.729 ± 0.001
South East			[NeV]	3426	5929	0.731
			[OII]	3727	6442	0.729
PKS J0407–3924	2700	ESO 3.6m				0.474 ± 0.001
			[OII]	3727	5496	0.475
			[NeIII]	3869	5700	0.473
			[OIII]	5007	7379	0.474
PKS J0433–0229	1200	ESO 3.6m				0.530 ± 0.001
			[OII]	3727	5496	0.530
			CaII H $_a$	3969	6071	0.530
			G-band $_a$	4304	6584	0.530
			H γ_a	4340	6634	0.529
			H β_a	4861	7411	0.525
			MgI $_a$	5175	7921	0.531
PKS J0457–0848	2700	ESO 3.6m				0.516 ± 0.001
			MgII	2798	4238	0.515
			[NeV]	3426	5195	0.516

Table 2.3: — Details of the spectroscopic observations, continued.

Object name	t (s)	Telescope	Spectral feature		z
			Species	λ_{rest} (Å)	λ_{obs} (Å)
PKS J1057+0012	2700	ESO 3.6m	[OII]	3727	5653
			[NeIII]	3869	5865
			[SII]	4072	6174
			H γ	4340	6582
			[OIII]	4363	6618
			H β	4861	7373
			[OIII]	4959	7521
			[OIII]	5007	7589
PKS J1109+1043	2700	ESO 3.6m			
PKS J1135–0021	1800	ESO 3.6m			0.975 ± 0.002
PKS J1203+0414	1200	ESO 3.6m	CII]	2326	4593
			MgII	2798	5531
			[NeV]	3426	6769
			[OII]	3727	7351
					1.221 ± 0.004
PKS J1345–3015	1800	ESO VLT	CIII]	1909	4230
			MgII	2798	6225
					1.132 ± 0.001
			CII]	2326	4960
			[NeV]	3426	7297
PKS J1350–2204	2700	ESO 3.6m	[OII]	3727	7944
			[NeIII]	3869	8248
					0.700 ± 0.002
			[OII]	3727	6333
			[NeIII]	3869	6572
PKS J1352+0232	1800	ESO 3.6m	CaII K _a	3934	6707
			CaII H _a	3969	6752
			G-band _a	4304	7317
			H γ_a	4340	7390
					0.607 ± 0.001
PKS J1352+1107	1800	ESO VLT	[OII]	3727	5990
			[NeIII]	3869	6215
			H β	4861	7813
			[OIII]	4959	7968
					0.891 ± 0.001
PKS J1352+1107	1800	ESO VLT	[NeV]	3346	6329
			[NeV]	3426	6478
			[OII]	3727	7050
			[NeIII]	3869	7319
			CaII K	3934	7434
			CaII H	3969	7508

Table 2.3: — Details of the spectroscopic observations, continued.

Object name	t (s)	Telescope	Spectral feature		λ_{rest} (Å)	λ_{obs} (Å)	z
			Species				
PKS J1447–3409	5400	ESO 3.6m					0.851 ± 0.001
			[OII]	3727	6898	0.851	
			[NeIII]	3869	7161	0.851	
			H γ	4340	8047	0.854	
PKS J1506–0919	2700	ESO 3.6m					1.486 ± 0.003
			CIII]	1909	4740	1.483	
			MgII	2798	6966	1.490	
PKS J1556–0622	1800	ESO VLT					1.195 ± 0.001
			[OII]	3727	8182	1.195	
PKS J1648+0242	1800	ESO VLT					0.824 ± 0.001
			[NeV]	3426	6252	0.825	
			[OII]	3727	6777	0.818	
			[NeIII]	3869	7069	0.827	
			CaII K	3934	7176	0.824	
			CaII H	3969	7242	0.825	
			G-band	4305	7856	0.825	
PKS J1734+0926	5400	ESO 3.6m					0.735 ± 0.001
			[NeV]	3426	5938	0.733	
			[OII]	3727	6468	0.735	
			[NeIII]	3869	6713	0.735	
			CaII K _a	3934	6829	0.736	
			CaII H _a	3969	6884	0.735	
PKS J2212+0152	1800	ESO VLT					1.126 ± 0.001
			MgII	2798	5955	1.128	
			[NeV]	3426	7280	1.125	
			[OII]	3727	7926	1.127	
			[NeIII]	3869	8219	1.124	
PKS J2325–0344	1800	ESO VLT					1.509 ± 0.002
			CIII]	1909	4781	1.505	
			CII]	2326	5837	1.510	
			MgII	2798	7029	1.512	
			[NeV]	3346	8394	1.109	
PKS J2339–0604	3600	ESO VLT					1.227 ± 0.001
			CII]	2326	5181	1.226	
			MgII	2798	6230	1.227	
			[OII]	3727	8300	1.227	
			[NeIII]	3869	8617	1.226	

Chapter 3

VLBI observations of the CORALZ sample: young radio sources at low redshift

Abstract. Young radio-loud active galactic nuclei form an important tool to investigate the evolution of extragalactic radio sources. To study the early phases of expanding radio sources, we have constructed CORALZ, a sample of 25 compact ($\theta < 2''$) radio sources associated with nearby ($z < 0.16$) galaxies. In this chapter we determine the morphologies, linear sizes, and place first constraints on the lobe expansion speeds of the sources in the sample. We observed the radio sources from the CORALZ sample with MERLIN at 1.4 GHz or 1.6 GHz, the EVN at 1.6 GHz, and global VLBI at 1.6 GHz and/or 5.0 GHz. Radio maps, morphological classifications, and linear sizes are presented for all sources in the CORALZ sample. We have determined a first upper limit to the expansion velocity of one of the sources, which is remarkably low compared to the brighter GPS sources at higher redshifts, indicating a relation between radio luminosity and expansion speed, in agreement with analytical models. In addition we present further strong evidence that the spectral turnovers in GPS and CSS sources are caused by synchrotron self-absorption (SSA): the CORALZ sources are significantly offset from the well-known correlation between spectral peak frequency and angular size, but this correlation is recovered after correcting for the flux-density dependence, as predicted by SSA theory.

N. de Vries, I. A. G. Snellen, R. T. Schilizzi, K.-H. Mack, and C. R. Kaiser
Astronomy & Astrophysics, **498**, 641 (2009)

VLBI observations of the CORALZ sample: young radio sources at low redshift



YOUNG radio-loud active galactic nuclei (AGN) are ideal objects to study the triggering of AGN activity, and the early evolution of classical double radio sources. Young radio sources can be recognised by their small angular (physical) sizes, their inverted spectra at low frequencies, and their often compact symmetric morphologies, with jet or lobe-like structures on either side of a central core. Depending on the observed characteristics, they are called compact steep spectrum (CSS) sources (Peacock & Wall 1982; Fanti et al. 1990; O'Dea 1998), gigahertz peaked spectrum (GPS) sources (O'Dea 1998), and/or compact symmetric objects (CSO, Wilkinson et al. 1994; Conway 2002).

Samples of CSS, GPS, and CSO have been used in a statistical way to constrain the early evolution of radio sources. Relative number statistics indicated that at a young age, radio sources must have significantly higher radio luminosities than at a later stage (O'Dea & Baum 1996; Readhead et al. 1996; Fanti & Fanti 2003). This decrease in radio luminosity may be preceded by a period of luminosity increase (Snellen et al. 2000b; 2003).

Very interesting results come from multi-epoch Very Long Baseline Interferometry (VLBI) observations of individual GPS and CSO. They show, for a handful of powerful objects, the proper motions of the lobes from which their dynamical ages can be estimated (Owsianik & Conway 1998; Polatidis & Conway 2003 and references therein). Separation velocities between the opposite extremities of the sources of up to $0.4h^{-1}c$ have been measured, corresponding to dynamical ages in the range of a few hundred to a few thousand years.

The CORALZ sample: The most nearby young radio sources

Snellen et al. (2004) selected a sample of young radio sources, CORALZ (COmpact RAdio sources at Low Redshift), with the aim of obtaining an unbiased view of young radio-loud AGN in the nearby universe. The sources in the CORALZ sample are significantly closer than the archetypal CSO and GPS sources available in the literature. Proper motions should be easier to detect in these nearby sources, since similar intrinsic expansion velocities would result in significantly higher angular motion compared to previous studies. Moreover, in general these radio sources are less powerful than the archetypal CSO and GPS sources, which will allow luminosity-dependent comparison studies.

The CORALZ programme was also initiated to investigate possible selection biases in GPS and CSO samples, since CORALZ is thought to be much less biased, due to its relatively clean selection criteria. The sample has been selected based on flux density ($S_{1.4 \text{ GHz}} > 100 \text{ mJy}$) and angular size ($\theta < 2''$). Using the Very Large Array (VLA) Faint Images of the Radio Sky at Twenty-centimeters (FIRST) survey (White et al. 1997), the optical Automated Plate Measuring machine (APM) catalogue of the first Palomar Observatory Sky Survey (POSS-I) (McMahon & Irwin 1991), and follow-up observations, all radio sources identified with bright galaxies were selected (red magnitude of $e < 16.5 \text{ mag}$ or blue magnitude of $o < 19.5 \text{ mag}$). Originally, four of these 28 sources were excluded from the CORALZ sample, since the offset between the radio position and its optical counterpart was suspiciously large ($\Delta_{\text{pos}} > 2''$), suggesting that the radio source had been erroneously identified with a random foreground galaxy. In the meantime, based on the Sloan Digital Sky Survey (SDSS) Data Release 6 (Adelman-McCarthy et al. 2008), one of these identifications actually turned out to be correct (CORALZ J115000+552821 and SDSS J115000.08+552821.4, with an offset of $0.5''$), raising the number of radio sources with reliable optical identifications to 25. These 25 compact radio sources will be referred to as *the CORALZ sample*. The three sources that still show anomalously large offsets between the radio and optical position are referred to as *additional sources*. Although the CORALZ sample is statistically complete down to the flux density limit, the limit corresponds to different redshifts, since the host galaxies are selected on optical magnitude and have a range in

absolute magnitude. However, simulations show that the sample is 95% statistically complete in the redshift range $0.005 < z < 0.16$ (Snellen et al. 2004), which, including the new SDSS identification, now contains 18 sources. In the rest of this chapter we will refer to these 18 sources as *the CORALZ core sample*. A detailed description of the selection process and additional radio observations can be found in Snellen et al. (2004). Nearly all (17/18) of the sources in the CORALZ core sample are classified as GPS and CSS sources, confirming that these are likely to be young radio sources. This also confirms that the spectral shape of a radio source is a good criterion to select very young radio (GPS) sources in general.

In this chapter we present VLBI and MERLIN observations of the CORALZ sample. In Sect. 3.1 the observations and data reduction are described; the data analysis and modeling is described in Sect. 3.2. The results are presented and discussed in Sect. 3.3, and we conclude with Sect. 3.4. Throughout this chapter we adopt the cosmological parameters as found by WMAP5 (Komatsu et al. 2008; $H_0 = 70.1 \text{ km s}^{-1} \text{ Mpc}^{-1}$, $\Omega_\Lambda = 0.721$, $\Omega_m = 0.279$).

3.1 Observations and data reduction

We observed radio sources from the CORALZ sample using a range of arrays at several frequencies; MERLIN, the Multi-Element Radio Linked Interferometer Network, at 1.4 GHz or 1.6 GHz, the European VLBI Network (EVN) at 1.6 GHz, and global VLBI at 1.6 GHz and/or 5.0 GHz. The combination of telescope array and observing frequency was chosen to have a wide range in angular resolution, required to match the expected wide range in angular size of the sources in the sample. An initial guess of the angular sizes of the individual sources was obtained from the position and strength of the radio spectral peak. In this way the sample was divided into three sub-samples of expected ‘large’, ‘intermediate’, and ‘small’ size sources. Details of the different observing runs are given below.

MERLIN observations

The subsample of ‘large’ radio sources (seven sources, including four from the CORALZ core sample) was observed with MERLIN using the following six telescopes: Defford, Cambridge, Knockin, Darnhall, Jodrell Bank Mk2, and Pickmere. The observing times ranged from 9 to 17 hours, alternating between the science targets (3 min.) and the radio sources used as their phase-references (2 min.), resulting in on-source integration times ranging from 5 to 10 hours. The largest projected baselines were typically 200 km, resulting in a resolution of about 150 mas using uniform weighting. These observations were carried out between November 9, 2000, and January 2, 2001, at either 1.4 GHz or 1.6 GHz.

EVN observations at 1.6 GHz

The twelve ‘intermediate’ size CORALZ sources (including ten sources from the CORALZ core sample) were observed with the EVN at 1.6 GHz using the Effelsberg, Jodrell Bank, Medicina, Noto, Torun, Westerbork, and Onsala antennas between February 14, 2000, and May 28, 2001, except for two sources, CORALZ J134158+541524 and CORALZ J150805+342323, which were observed on February 19, 2002, using the MERLIN antenna at Cambridge instead of Noto. Each source typically was observed for 10×13 minutes, spread in time to obtain optimal *UV* coverage. The largest projected baselines were typically 1400 km, resulting in a resolution of about 20 mas using uniform weighting. J0650+6001 and J1740+5211 were observed as primary calibrators. The data correlation was performed at Socorro on the VLBA correlator. The Astronomical Image Processing System (AIPS) has been used for editing, a-priori calibration, fringe-fitting, self-calibration and imaging of the data. For fringe-fitting, the AIPS task FRING was used with a point source model, a solution interval of 6 minutes, and a standard signal-to-noise ratio cutoff of 5. Several iterations of phase (or amplitude & phase) self-calibration and imaging were performed using the AIPS tasks CALIB and IMAGR, until the image quality converged, with negligible negative structure and a low noise level.

Global VLBI observations (2000) at 5.0 GHz

The eight ‘small’ CORALZ sources (including three sources from the CORALZ core sample) were observed on March 2, 2000, with an 18 station array at a frequency of 5.0 GHz, using the EVN antennas Effelsberg, Jodrell Bank, Medicina, Noto, Torun, Westerbork, Onsala, and Shanghai and the Very Long Baseline Array (VLBA) antennas St. Croix, Hancock, North Liberty, Fort Davis, Los Alamos, Pie Town, Kitt Peak, Owens Valley, Brewster, and Mauna Kea. Each source was typically observed for 3×11 minutes, spread in time to obtain optimal *UV* coverage. The largest projected baselines were typically 9000 km, resulting in a resolution of about 2 mas using uniform weighting. J0650+6001 and J1740+5211 were observed as primary calibrators. The data correlation was performed at Socorro on the VLBA correlator. The data reduction was carried out the same way as the EVN observations.

Global VLBI observations (2004) at 1.6 GHz and 5.0 GHz

The fourteen most compact sources from the CORALZ core sample were observed for a second time on May 24, 2004, and June 5, 2004, at 5.0 GHz and/or 1.6 GHz, respectively. A similar observing strategy was used as the previous global VLBI observations, with observing times of 3×11 minutes. The largest projected baselines were typically 9000 km, resulting in a resolution of about 2 mas at 5.0 GHz, and 5 mas at 1.6 GHz, using uniform weighting. Both experiments were conducted with global VLBI, using the EVN antennas Effelsberg, Jodrell Bank, Medicina, Noto, Torun, Westerbork, and Onsala and the VLBA antennas St. Croix, Hancock, North Liberty, Fort Davis, Los Alamos, Pie Town, Kitt Peak, Owens Valley, and Brewster. J1740+5211 and 4C39.25 were observed as primary calibrators. The data correlation was performed at the Joint Institute for VLBI in Europe (JIVE). The data reduction was carried out in the same way as the EVN observations.

All details of the observations are given in the appendix in Table 3.3; in Col. 1 the IAU name of the source, in Col. 2 the figure in which the map is presented, in Cols. 3-7 the observing date, frequency, bandwidth, and array, in Col. 8 the peak flux density, in Col. 9 the r.m.s. noise level, and in Cols. 10-12 the major and minor axis and the position angle of

the restoring beam.

3.2 Data analysis

3.2.1 Source structure and angular sizes

The observed radio source structures were characterised using the AIPS task JMFIT, which fits (by least-squares) up to four Gaussian components to an image subsection. A first guess of the input parameters (position, flux density, and shape of the components) was made using the INPFIT procedure. The results for all observations of all sources are given in Table 3.4, with in Col. 1 the source IAU name, in Col. 2 the figure in which the corresponding map is presented, in Col. 3 the observation date, in Col. 4 the observing frequency, in Cols. 5-6 the relative position of the component, in Cols. 7-9 the flux density, deconvolved size and position angle of the component. The angular sizes of the radio sources were determined by measuring the distance between the outer edges of the two outermost components in the deconvolved image. In the case of unresolved components, the positions of the components were used. For unresolved or barely resolved sources the deconvolved major axis as returned by JMFIT was used as an estimate of the angular size of the radio source.

3.2.2 Morphological classification

We also made an attempt to morphologically classify the radio sources by eye, using the source structures at different frequencies. We identify five classes:

1. Unresolved (U). The source is unresolved or barely resolved.
2. Compact Double (CD). The source exhibits two components with a similar spectral index and/or flux density.
3. Compact Symmetric Object (CSO). A source with a range of components, with the most flat spectral component *not* located at one of the extremities of the source.
4. Core-Jet (CJ). A source with two or more components, significantly different in flux density and/or spectral index, with the most flat spectral component located at one of the extremities of the source.

5. Complex (CX). A source with a complex morphology, not falling in one of the above categories.

Each identification is followed by a ‘?’ if the classification is particularly uncertain. The results are shown in Table 3.1, and discussed in Sect. 3.3.2.

3.2.3 Expansion velocity

For three sources we have obtained two epochs of VLBI observations (Fig. 3.7), observed with the same telescope array at the same frequency, for which we could potentially estimate expansion velocities. One of these sources (CORALZ J073934+495438) is practically unresolved, and a second source (CORALZ J131739+411545) shows a complex morphology, making the analysis of expansion velocities for these sources impossible at this stage. The third source (CORALZ J083139+460800) on the other hand exhibits a compact double morphology with two strong, unresolved components separated by 4.4 mas. The relative positions of the two components were determined using the AIPS tasks JMFIT as well as MAXFIT, which fits a quadratic function to a selected region of the map to determine the position of an extremum. It is always difficult to obtain error estimates for component positions from VLBI observations, which are particularly important in the case of slow expansion speeds and upper limits. When three or more epochs of observations are available, positional errors are often derived from the scatter around a linear fit to the component motion (Owsianik & Conway 1998), although in this case no independent goodness-of-fit can be determined. Since we only have two epochs of observations, we use the following formula from Fomalont (1999) to derive estimates of the error in the component position:

$$\sigma_r = \frac{\sigma_{\text{rms}} d}{2 I_{\text{peak}}} \quad (3.1)$$

where σ_{rms} is the post-fit r.m.s. error of the map, and d and I_{peak} are the size and the peak intensity of the component. We have also used Monte Carlo simulations to check our error estimates, by repeatedly fitting the peak position of a Gaussian with random noise added. The error estimates from the approximating formula from Fomalont (1999) and from

the Monte Carlo simulations were very similar. We do note, however, that these error estimates only take into account the errors in the analysis of the radio maps, not the possible biases introduced during the synthesis of these maps.

3.3 Results and discussion

Table 3.1: — Source characteristics of the CORALZ sample.

IAU Name	z	$S_{1.4\text{GHz}}$ (mJy)	$L_{5.0\text{GHz}}$ (W Hz $^{-1}$)	ν_{peak} (MHz)	θ (mas)	LLS (pc)	Morph.
The CORALZ core sample							
J073328+560541	0.104	394	24.68	460	47	90	CSO
J073934+495438	0.054	107	23.63	950	2*	2*	U
J083139+460800	0.127	131	24.62	2200	9	20	CD
J083637+440109	0.054	139	23.66	< 150	1600	1700	CSO?
J090615+463618	0.085	314	24.49	680	31	49	CSO
J102618+454229	0.153	105	24.55	180	17	45	CSO
J103719+433515	0.023	129	22.96	< 150	19	9	CSO
J115000+552821	0.139	143	24.57	< 230	41	100	U
J120902+411559	0.095	147	24.26	370	20	35	CSO
J131739+411545	0.066	249	24.37	2300	4	5	CX
J140051+521606	0.116	174	24.36	< 150	150*	320*	U
J140942+360416	0.148	143	24.45	330	27	70	CJ?
J143521+505122	0.099	141	24.20	< 150	150*	270*	U
J150805+342323	0.045	130	23.35	< 230	170	150	CD?
J160246+524358	0.106	576	24.75	< 150	180	350	CSO
J161148+404020	0.152	553	25.03	< 150	1300	3400	CX
J170330+454047	0.060	119	23.54	< 150			
J171854+544148	0.147	329	24.86	480	68	175	CSO?
Other nearby sources in the CORALZ sample							
J093609+331308	0.076	55	23.84	2200	1.5*	2*	U
J101636+563926	0.232	108	24.91	< 150	240	890	CD?
J105731+405646	0.008	47	21.59	1250	0.5*	0.1*	U
J115727+431806	0.229	256	25.25	< 150	630	2300	CJ?
J132513+395552	0.074	56	23.69	1900	10	14	CSO?
J134035+444817	0.065	82	23.89	2300	3.3	4.1	CJ?
J155927+533054	0.178	182	24.67	< 150	1500	4500	CSO?
Additional sources							
J071509+452555		74		3800	1.3		CD?
J080454+433537		360		1500	24		CD?
J134158+541524		125		< 150	530		CD?

3.3.1 Source structure

Contour maps of the CORALZ sample at 1.4, 1.6, and/or 5.0 GHz, using the EVN, global VLBI, and MERLIN arrays, are shown in the appendix. Fig. 3.6 shows contour maps of those eight sources from the CORALZ core sample, observed with the EVN at 1.6 GHz in 2000/2001 (left column), and with global VLBI in 2004 at 1.6 GHz and 5.0 GHz (middle and right column, respectively). Fig. 3.7 shows contour maps of the three most compact sources in the CORALZ core sample, obtained with global VLBI at 5.0 GHz in 2000 (top row), and 2004 (bottom row). Fig. 3.5 shows radio maps of the six more extended sources in the CORALZ core sample, taken with MERLIN in 2000 at 1.4 GHz or 1.6 GHz, or with the EVN at 1.6 GHz. Fig. 3.8 shows contour maps of other sources from the CORALZ sample, that are not part of the core sample, obtained with global VLBI at 5.0 GHz or with MERLIN at 1.4 GHz or 1.6 GHz. These objects are nearby GPS/CSS radio sources, but are not included in the CORALZ core sample, because they either have slightly too low flux densities ($S_{1.4 \text{ GHz}} < 100 \text{ mJy}$), or are too distant ($z > 0.16$). Fig. 3.9 shows contour maps of the additional sources, which have been excluded from the CORALZ sample because the optical and radio positions are significantly offset, indicating that the radio sources have been erroneously identified with a random foreground galaxy. For three sources (CORALZ J073328+560541, CORALZ J103719+433515, and CORALZ J160246+524358), the S/N at 5.0 GHz on the longer baselines was too low for fringe-fitting, and we used the EVN antennas only. One source (CORALZ J140942+360416) was too weak at 5.0 GHz for self-calibration, and we were only able to produce a map at 1.6 GHz.

From these observations we have derived the largest angular size, θ , of each source, from which the (projected) largest linear size (LLS) can be calculated. Six sources (CORALZ J073934 +495438, CORALZ J115000 +552821, CORALZ J140051 +521606, CORALZ J143521 +505122, CORALZ J093609 +331308, and CORALZ J105731 +405646) were (almost) unresolved by our observations, and we have estimated θ using the deconvolved major axis. Sizes determined this way are less certain and are therefore indicated with a star. The results are given in Table 3.1, with in Col. 1 the source IAU name, in Cols. 2-5 the redshift, the flux density at 1.4 GHz, the luminosity density at 5.0 GHz, and the peak frequency

(Snellen et al. 2004), in Col. 6 the largest angular size θ , in Col. 7 the projected largest linear size, in Col. 8 a possible morphological classification (see Sect. 3.2.2 for a description of the different classes).

3.3.2 Radio morphology

For 13 out of the 18 sources from the CORALZ core sample, a morphological classification was possible. The majority of the classified CORALZ sources show a CSO or CD morphology (10/13, 77%). Only one source has been tentatively classified as a core-jet source. These results are in agreement with Stanghellini et al. (1997) and Snellen et al. (2000a), who find that GPS sources classified as core-jet are usually identified with quasars, whereas GPS sources identified with galaxies tend to exhibit CSO morphologies.

3.3.3 Spectral turnover and angular size

Following Snellen et al. (2000b) we searched for correlations between the angular sizes and spectral turnovers of the sources in the CORALZ core sample, and compared the results with those presented in the literature. Early measurements of the angular sizes of GPS and CSS sources using VLBI strongly suggested that their spectral turnovers are caused by synchrotron self-absorption (SSA, Jones, O'Dell & Stein 1974; Hodges, Mutel & Phillips 1984; Mutel, Hodges & Phillips 1985). This was further advocated by Fanti et al. (1990), who showed that the peak frequency and the largest angular size of CSS radio sources are strongly anticorrelated, as expected for SSA. For a homogeneous synchrotron self-absorbed radio source, the peak frequency, ν_p , is given approximately by (Kellermann & Pauliny-Toth 1981):

$$\nu_p \sim 8 B^{1/5} S_p^{2/5} \theta^{-4/5} (1+z)^{1/5} \text{ GHz}, \quad (3.2)$$

where B is the magnetic field in Gauss, S_p the flux density at the spectral peak in Jy, θ the largest angular size in mas, and z the redshift of the source. In contrast, Bicknell et al. (1997) argue that models where the radio source is surrounded by ionized gas can also reproduce the observed relation, and the turnover could also be caused by free-free absorption (FFA).

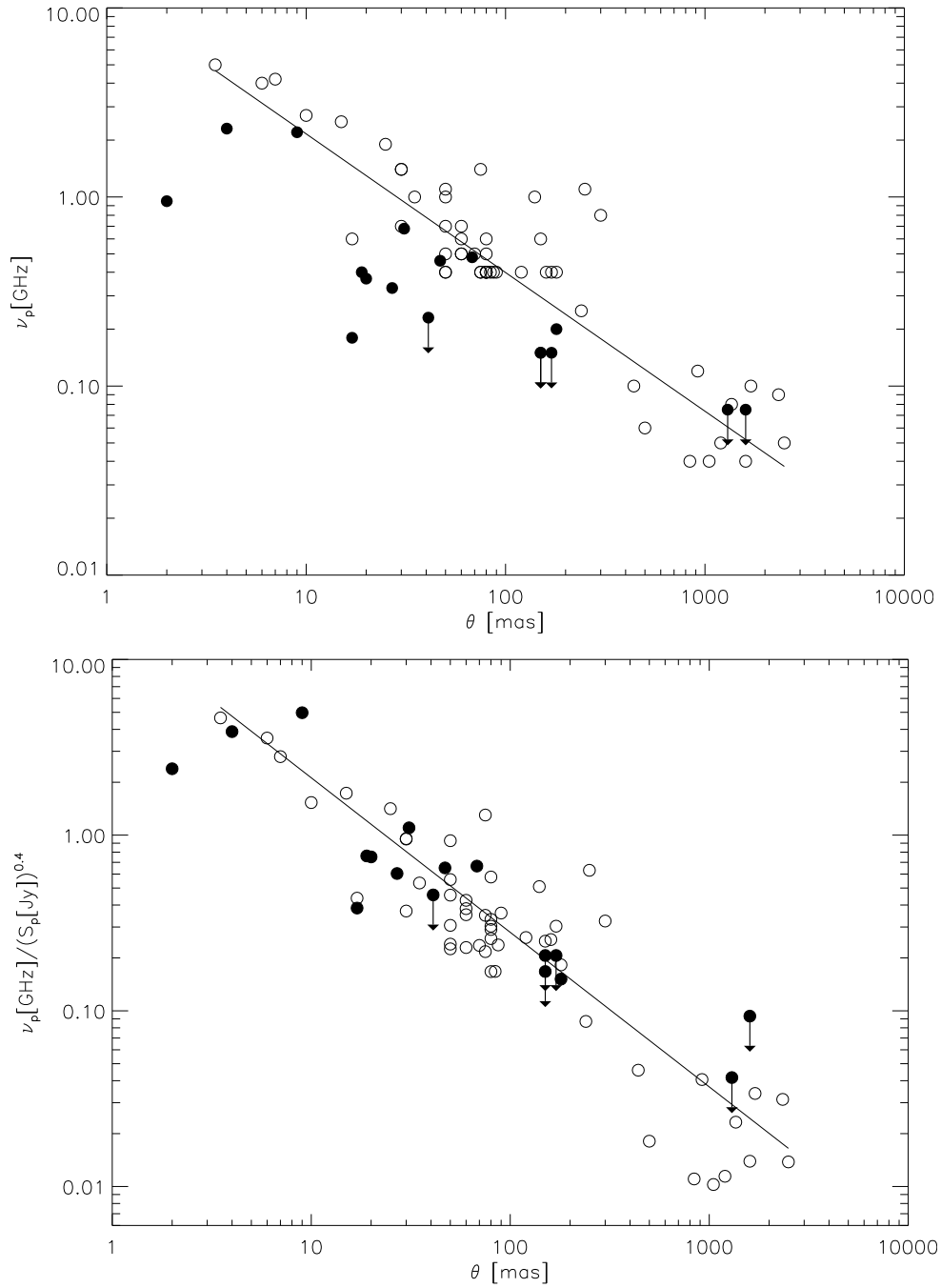


Figure 3.1: — (*top*) Largest angular sizes and peak frequencies of the CORALZ core sample (filled circles) and the bright PHJ (Snellen et al. 2002), Stanghellini (1998), and Fanti (1990) samples (open circles). Circles with arrows denote upper limits. The line is a linear least-squares fit (in log-log space) to the bright literature samples. (*bottom*) To correct for the flux density-dependence predicted by SSA, we divide the peak frequency by $S_m^{2/5}$, and show that the linear sizes and peak frequencies of the CORALZ sources are now consistent with the linear least-square fit to the bright samples.

Now that we have measured sizes and peak frequencies of the CORALZ core sample, at significantly lower redshifts and radio luminosities,

ties than the literature samples, it is interesting to see whether weak radio sources follow the same anticorrelation between θ and ν_p . We have collected angular sizes and peak frequencies of several flux density-selected samples from the literature for comparison. These included the Parkes half-Jansky (PHJ) sample of GPS galaxies (Snellen et al. 2002, with angular sizes from Liu et al. 2007), the GPS galaxies from the Stanghellini (1998) sample, and the CSS galaxies from the Fanti (1990) sample. The angular sizes for the sources in the latter two samples come from O’Dea (1998).

Fig. 3.1 (*top*) shows that the peak frequency and linear size of the CORALZ core sample (filled circles) are also anticorrelated, but they fall significantly below the relation for the brighter and more distant literature samples. However, this is expected from SSA theory. As can be seen in equation (3.2), the peak frequency of a synchrotron self-absorbed radio source scales with the flux density as: $\nu_p \propto S_p^{2/5}$, and therefore the low flux density CORALZ sample should have smaller angular sizes for similar peak frequencies. In Fig. 3.1 (*bottom*) we have corrected for this effect, and show that the linear sizes and peak frequencies of the CORALZ core sample are now consistent with the linear fit to the bright literature samples, perfectly in line with synchrotron self-absorption theory.

In Fig. 3.1 (*bottom*) we assume that GPS and CSS radio sources obey equation (3.2), although this formula in principle only applies to homogeneous synchrotron self-absorbed sources. From VLBI observations it is clear that GPS/CSS sources are not homogeneous, so the fact that the correlation between peak frequency and overall angular size is so tight suggests that the ratio of component to overall size does not change significantly over the lifetime of GPS/CSS radio sources. This fixed ratio of component to overall size is in agreement with VLBI observations and can be explained as self-similar evolution (e.g. Snellen et al. 2000b). To determine how the data constrain the correlation between turnover frequency, peak flux density and angular size to be in agreement with SSA and self-similar evolution, we fit the data using the fitting function:

$$\theta = c S_p^a \nu_p^b (1+z)^{1/4}, \quad (3.3)$$

where a , b , and c are parameters that can be varied in order to best fit the data. For $a = 1/2$, $b = -5/4$, and $c = 8^{5/4} B^{1/4}$, this expression reduces to

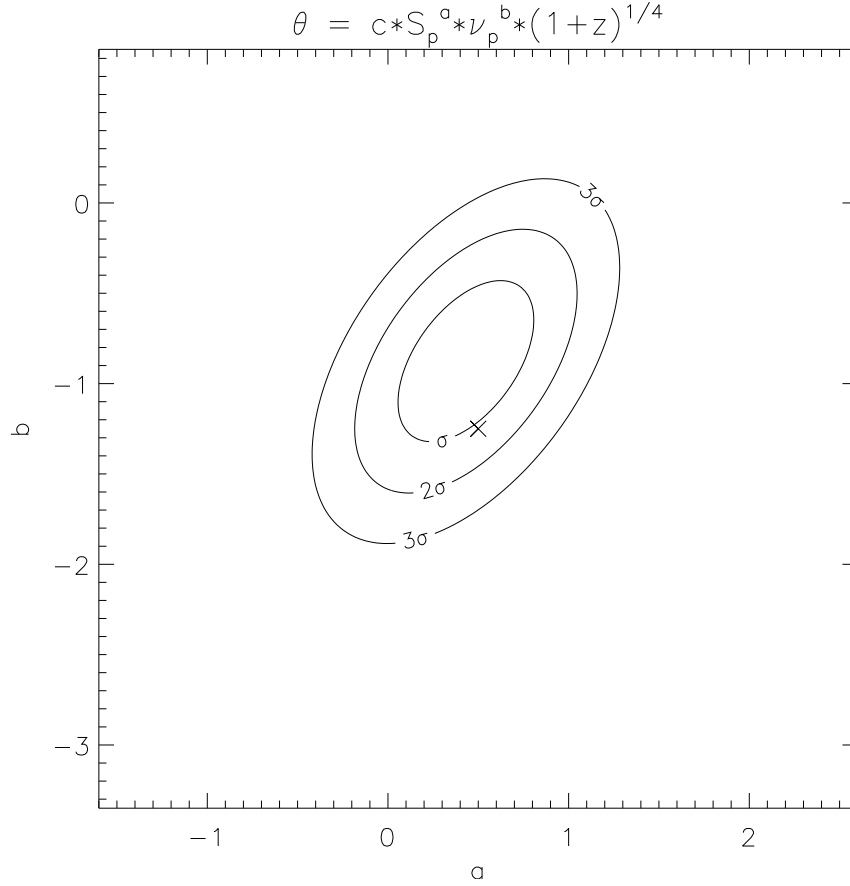


Figure 3.2: — Contour map of the goodness-of-fit parameter $\Delta\chi^2$ for the combined sample of young radio sources (the CORALZ core sample, PHJ (Snellen et al. 2002), Stanghellini (1998), Fanti (1990)). The contours are drawn at the 68.3%, 95.4% and 99.7% levels of a $\Delta\chi^2$ -distribution with two degrees of freedom. The location of the parameters expected for SSA (equation (3.2)) is indicated by the cross.

equation (3.2). In Fig. 3.2 we show a contour map of the goodness-of-fit parameter $\Delta\chi^2$, resulting from fitting the data to equation (3.3) with a range of fixed values for a and b . We again used the CORALZ core sample, and the PHJ (Snellen et al. 2002), Stanghellini (1998), and Fanti (1990) samples. Note that the five larger sources from the CORALZ core sample, which have upper limits to the turnover frequency (see Fig. 3.1), are not included in this analysis. When turnover frequencies and peak flux densities for these become available, we expect to significantly improve the constraints on the parameters in equation (3.3). The contours are drawn at the 68.3%, 95.4% and 99.7% levels of a $\Delta\chi^2$ -distribution with two degrees of freedom. The values of the parameters a and b expected for a homogeneous synchrotron self-absorbed source (equation (3.2)) are indicated by the cross. From Fig. 3.2 we conclude that the data

are in remarkably good agreement with the homogeneous SSA source model, with $a = 0.45 \pm 0.25$ and $b = -0.9 \pm 0.3$. This confirms that the spectral turnovers in GPS and CSS spectra are generally caused by SSA, and also favours self-similar evolution models of young radio sources.

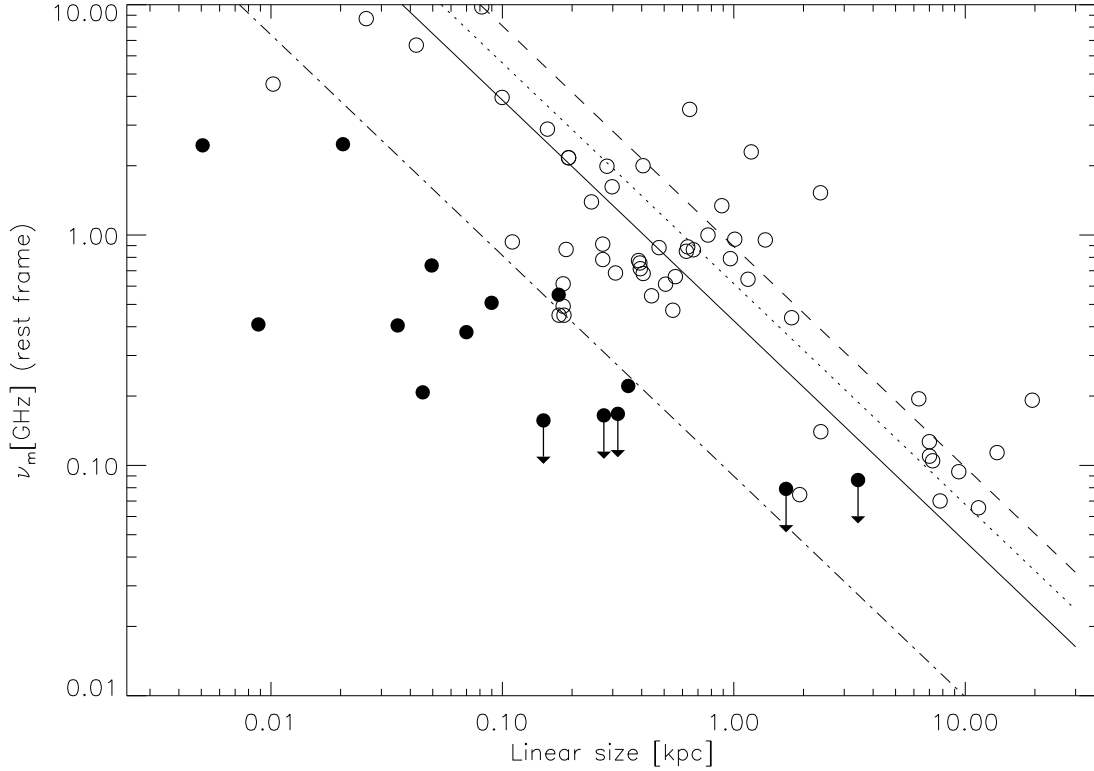


Figure 3.3: — Rest-frame turnover frequency against linear size for the CORALZ core sample (filled circles) and the PHJ (Snellen et al. 2002), Stanghellini (1998), and Fanti (1990) samples (open circles). The lines are models from Bicknell et al. (1997) for jet energy fluxes of 10^{46} , $10^{45.5}$, 10^{45} , and $10^{42.7} \text{ erg s}^{-1}$ (dashed, dotted, solid, and dot-dashed line, respectively), density power-law slope of $\beta = 2$, and number density at 1 kpc of 10 cm^{-3} .

Can FFA also explain the relations found? Bicknell et al. (1997) present radio source evolution models, where the AGN ionizes the gas surrounding the radio source by shocks and photoionization. These models predict an anticorrelation between the rest-frame peak frequency and the largest linear size of GPS and CSS radio sources, consistent with the data available at that time (the samples of Fanti et al. (1990) and Stanghellini et al. (1998)). To see whether the sizes and peak frequencies of the CORALZ core sample are also in agreement with this model, we have reproduced Fig. 7 (*top right*) from Bicknell et al. (1997) in Fig. 3.3, and added the data from the CORALZ core sample. Sources from the CORALZ core sample are represented by filled circles and sources from the

PHJ (Snellen et al. 2002), Stanghellini (1998), and Fanti (1990) samples by open circles. The lines are predictions of the radio source models from Bicknell et al. (1997) for jet energy fluxes of 10^{45} , $10^{45.5}$, and 10^{46} erg s $^{-1}$ (solid, dotted, and dashed line, respectively), density power-law slope of $\beta = 2$, and number density at 1 kpc of 10 cm^{-3} . The fact that the lines fit the literature samples fairly well is no surprise, since the model is designed to do so.

The median radio luminosity of the CORALZ core sample is a factor of 630 lower than that of the bright literature samples, meaning that the jet energy fluxes should also be a factor of 630 lower, assuming a constant fraction of the jet energy radiated as synchrotron emission (as expected from analytical models, e.g. see appendix Sect. 3.5.1), resulting in a jet energy flux of $\sim 10^{42.7}$ erg s $^{-1}$. This is indicated by the dot-dashed line in Fig. 3.3. All-but-one of the CORALZ core members with measured turnover frequency fall below this line, indicating that the model is not consistent with these data, or that, for some reason, the ratio of jet energy flux to radio luminosity is significantly lower for the CORALZ core sample. Of course, it will be possible to add extra parameters to the Bicknell model, such that it fits the peak frequency and angular size data of GPS and CSS sources. However, since the SSA self-similar evolution scenario is so straightforward and fits the data well, we believe it is scientifically more elegant.

3.3.4 Expansion velocity and radio power

Three sources have been observed twice (March 2000 and May 2004) with the same VLBI array at the same frequency, allowing investigation of possible structural changes, but only one source, CORALZ J083139+460800, is suitable for determination of the expansion velocity (see above). However, we found no change in the position (x or y) to within $18 \mu\text{as}$, which corresponds to a 3σ upper limit to the projected expansion velocity of $v_{\text{exp}} < 0.07 h^{-1}c = 0.10 c$. We noted that this upper limit is lower than the expansion velocities previously found for bright archetypal GPS/CSOs, and we therefore investigated the dependence of expansion velocity on radio luminosity. We have searched the literature for detections of and upper limits to expansion velocities in CSOs. Since the first detections of lobe proper motions in 0710+439 (Owsianik & Conway

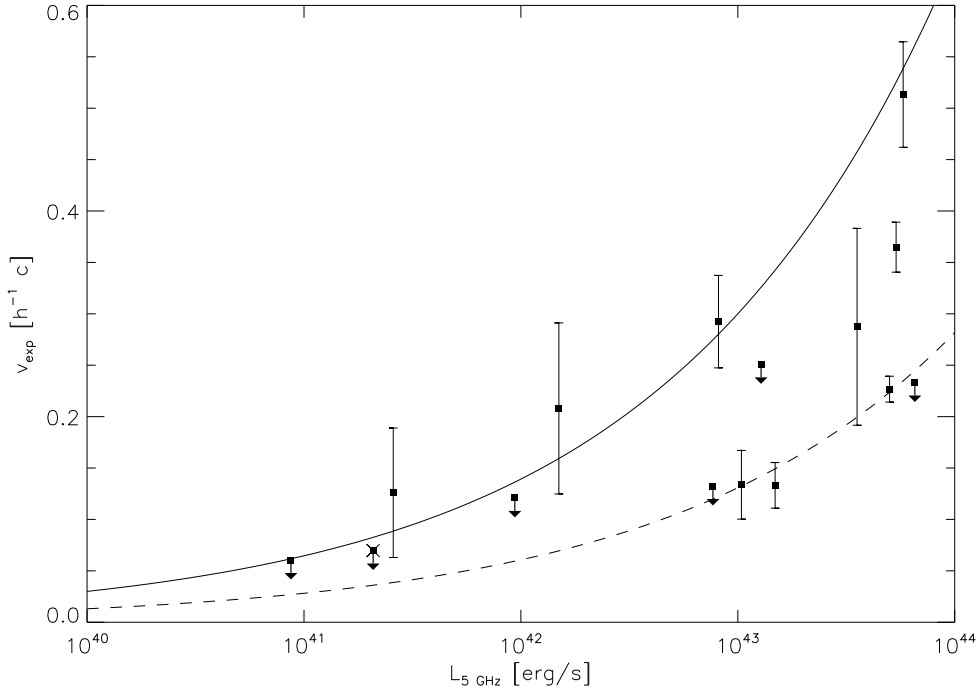


Figure 3.4: — Expansion velocities of Compact Symmetric Objects in units of $h^{-1} c$, and radio luminosities at 5 GHz in erg s^{-1} . The upper limit indicated with the cross is our 3σ upper limit to the expansion velocity of CORALZ J083139+460800, the other arrows indicate 1σ upper limits from previous studies. The solid line shows the expected relation between expansion velocity and radio luminosity, derived from an analytic radio source evolution model described in the appendix in Sect. 3.5.1, with arbitrary scaling. The dashed line represents this relation scaled down by a factor of $\sqrt{1 - 0.9^2} \simeq 0.44$, such that 90% of a sample of randomly oriented sources that intrinsically would follow the solid line, should be located above the dashed line.

1998) and 0108+388 (Owsianik, Conway & Polatidis 1998) expansion velocities have been measured for only a few other sources. In Table 3.2 we summarize these results, and also include upper limits to expansion velocities for which no significant expansion has been measured so far. Col. 1 gives the source IAU name, Col. 2 the redshift, Col. 3 the lobe-to-lobe, projected expansion velocity in units of $h^{-1}c$, converted to the adopted cosmology (WMAP5; $H_0 = 70.1 \text{ km s}^{-1} \text{ Mpc}^{-1}$, $\Omega_\Lambda = 0.721$, $\Omega_m = 0.279$), Col. 4 the number of observing epochs and the years of the first and last observations, and Col. 5 gives the reference for the expansion velocity. Note that the upper limits as presented in Gugliucci et al. (2005) were not corrected for cosmological time dilation. The values we present here have been corrected and represent rest-frame quantities.

In Fig. 3.4 we show the expansion velocities measured in GPS/CSOs as a function of radio luminosity. Both the radio luminosity and the lobe-to-lobe, projected expansion velocity have been corrected for cos-

mological effects, and represent rest-frame quantities. The upper limit indicated with the cross is our 3σ upper limit to the expansion velocity of CORALZ J083139+460800, the other arrows indicate 1σ upper limits from the literature (see Table 3.2).

Although there is a large scatter, a positive correlation with radio luminosity can be seen. A Spearman rank correlation analysis shows that, ignoring all measured upper limits to the expansion velocity, the correlation is significant at a 98% confidence level ($n = 9$, $\rho = 0.717$, one-tailed). With the upper limits included in the analysis, the correlation reaches confidence levels $> 98\%$, regardless of the precise way we treat these upper limits. Furthermore it seems that the scatter can mostly be explained in terms of projection effects, since the majority of the sources lie between the solid and dashed lines, comprising a range of 90% probability.

Note that we do expect a correlation between expansion velocity and radio luminosity from radio source evolution theory. In the appendix in Sect. 3.5.1 we present an analytic model of a young, expanding radio source with a constant jet power in a power-law density environment. This model predicts that $v_{\text{exp}} \propto L_{\text{radio}}^{1/3}$. The solid line represents such a relation, with arbitrary scaling. The dashed line represents this relation scaled down by a factor of $\sqrt{1 - 0.9^2} \simeq 0.44$, such that 90% of a sample of randomly oriented sources that intrinsically would follow the solid line, should be located above the dashed line.

3.4 Conclusions

In this chapter we present VLBI and MERLIN observations of the CORALZ sample, a nearby sample of 25 compact ($\theta < 2''$) radio sources, of which 18 form a 95% statistically complete sample in the redshift range $0.005 < z < 0.16$. We have measured the sizes of the sources, and performed a morphological classification.

The CORALZ core sample follows the well established relation between radio spectral peak frequency and angular size, but with significantly smaller sizes at any particular peak frequency, compared to more powerful and more distant GPS/CSS sources. We show that this is exactly as expected from synchrotron self-absorption theory, in which the

Table 3.2: — Expansion velocities of Compact Symmetric Objects presented in the literature. *References:* (1) Polatidis & Conway (2003); (2) Taylor et al. (2000); (3) Stanghellini et al. (2002); (4) Tschager et al. (2000); (5) Gugliucci et al. (2005); (6) Tingay et al. (2002); (7) Tzioumis et al. (1998).

IAU Name	z	v_{exp} $h^{-1}c$	No. of epochs	Ref.
0035+227	0.096	0.13 ± 0.06	2 (1998-2001)	1
0108+388	0.669	0.23 ± 0.01	5 (1982-2000)	1
0710+439	0.518	0.36 ± 0.02	7 (1980-2000)	1
1031+567	0.460	0.29 ± 0.10	2 (1995-1999)	2
OQ208	0.077	0.21 ± 0.08	6 (1993-1997)	3
1843+356	0.763	0.51 ± 0.05	2 (1993-1997)	1
1943+546	0.263	0.29 ± 0.04	4 (1993-2000)	1
2021+614	0.227	0.13 ± 0.02	3 (1982-1998)	4
2352+495	0.238	0.13 ± 0.03	6 (1983-2000)	1
J1111+1955	0.299	< 0.13	3 (1997-2002)	5
J1414+4554	0.190	< 0.12	3 (1997-2002)	5
1718-649	0.014	< 0.06	2 (1993-1999)	6
J1734+0926	0.735	< 0.23	3 (1997-2002)	5
1934-638	0.183	< 0.25	3 (1969-1988)	7

angular size is also proportional to the square root of the peak flux density. By least-squares fitting of the combined sample of CORALZ and bright literature samples, we recover the dependencies of angular size on peak frequency and peak flux density as expected for synchrotron self-absorbed radio sources evolving in a self-similar way. Current models that invoke FFA to explain the spectral turnovers in GPS and CSS sources (Bicknell et al. 1997) cannot explain the relatively small angular sizes found for the CORALZ core sample. We therefore conclude that, although FFA may play a role in some sources, the turnovers must be caused by SSA for the majority of GPS and CSS radio sources.

In addition, based on two epochs of global VLBI, we have derived a strong upper limit to the expansion velocity of CORALZ J083139+460800 ($v_{\text{exp}} < 0.07 h^{-1}c$). We show that, in comparison with more powerful young radio sources, the expansion velocity is low, indicating that the expansion speed of GPS radio sources is correlated to their radio luminosity. We show that this is expected from analytic radio source evolution modelling, which predicts $v_{\text{exp}} \propto L_{\text{radio}}^{1/3}$ (appendix Sec. 3.5.1). The scatter in the correlation is consistent with being due to projection effects.

Acknowledgments

The European VLBI Network is a joint facility of European, Chinese, South African and other radio astronomy institutes funded by their national research councils (proposal codes: ES042, GS016, GS021). The National Radio Astronomy Observatory is a facility of the National Science Foundation operated under cooperative agreement by Associated Universities, Inc (proposal codes: GS016, GS021). MERLIN is a National Facility operated by the University of Manchester at Jodrell Bank Observatory on behalf of STFC (proposal codes: MN/00B/07, ES042). This research has made use of the NASA/IPAC Extragalactic Database (NED) which is operated by the Jet Propulsion Laboratory, California Institute of Technology, under contract with the National Aeronautics and Space Administration.

References

- Adelman-McCarthy, J. K., et al. 2008, *ApJS*, 175, 297
- Bicknell, G. V., Dopita, M. A., & O'Dea, C. P. O. 1997, *ApJ*, 485, 112
- Conway, J. E. 2002, *New Astronomy Review*, 46, 263
- Fanti, R., Fanti, C., Schilizzi, R. T., Spencer, R. E., Nan Rendong, Parma, P., van Breugel, W. J. M., & Venturi, T. 1990, *A&A*, 231, 333
- Fanti, C., & Fanti, R. 2003, *Radio Astronomy at the Fringe*, ed. J. A. Zensus, M. H. Cohen, & E. Ros, 300, 81
- Fomalont, E. B. 1999, *Synthesis Imaging in Radio Astronomy II*, 180, 301
- Gugliucci, N. E., Taylor, G. B., Peck, A. B., & Giroletti, M. 2005, *ApJ*, 622, 136
- Hodges, M. W., Mutel, R. L., & Phillips, R. B. 1984, *AJ*, 89, 1327
- Jones, T. W., O'dell, S. L., & Stein, W. A. 1974, *ApJ*, 192, 261
- Kaiser, C. R., & Best, P. N. 2007, *MNRAS*, 381, 1548
- Kellermann, K. I., & Pauliny-Toth, I. I. K. 1981, *ARA&A*, 19, 373
- Komatsu, E., et al. 2008, submitted to *ApJS*, ArXiv e-prints, 803, arXiv:0803.0547
- Liu, X., Cui, L., Luo, W.-F., Shi, W.-Z., & Song, H.-G. 2007, *A&A*, 470, 97
- McMahon R. G., Irwin M. J., 1991, in *Proceedings of the conference on 'Digitised Optical Sky Surveys*, eds. H. T. MacGillivray, E. B. Thomson (Kluwer Acad. Publ., Dordrecht), p. 417
- Mutel, R. L., Hodges, M. W., & Phillips, R. B. 1985, *ApJ*, 290, 86
- O'Dea, C. P. & Baum, S. A. 1996, in *GPS and CSS radio sources*, ed. I. A. G. Snellen, R. T. Schilizzi, H. J. A. Röttgering & M. N. Bremer, 241
- O'Dea, C. P. 1998, *PASP*, 110, 493
- Owsianik, I., & Conway, J. E. 1998, *A&A*, 337, 69
- Owsianik, I., Conway, J. E., & Polatidis, A. G. 1998, *A&A*, 336, L37
- Peacock, J. A., & Wall, J. V. 1982, *MNRAS*, 198, 843
- Polatidis, A. G., & Conway, J. E. 2003, *Publications of the Astronomical Society of Australia*, 20, 69
- Readhead, A. C. S., Taylor, G. B., Xu, W., Pearson, T. J., Wilkinson, P. N., & Polatidis, A. G. 1996, *ApJ*, 460, 612
- Snellen, I. A. G., Schilizzi, R. T., & van Langevelde, H. J. 2000, *MNRAS*, 319, 429
- Snellen, I. A. G., Schilizzi, R. T., Miley, G. K., de Bruyn, A. G., Bremer, M. N., Röttgering, H. J. A. 2000, *MNRAS*, 319, 445

- Snellen, I. A. G., Lehnert, M. D., Bremer, M. N., & Schilizzi, R. T. 2002, *MNRAS*, 337, 981
- Snellen, I. A. G., Mack, K.-H., Schilizzi, R. T., & Tschager, W. 2003, *Publications of the Astronomical Society of Australia*, 20, 38
- Snellen, I. A. G., Mack, K.-H., Schilizzi, R. T., & Tschager, W. 2004, *MNRAS*, 348, 227
- Spergel, D. N., et al. 2007, *ApJS*, 170, 377
- Stanghellini, C., O'Dea, C. P., Baum, S. A., Dallacasa, D., Fanti, R., & Fanti, C. 1997, *A&A*, 325, 943
- Stanghellini, C., O'Dea, C. P., Dallacasa, D., Baum, S. A., Fanti, R., & Fanti, C. 1998, *A&AS*, 131, 303
- Stanghellini, C., Liu, X., Dallacasa, D., & Bondi, M. 2002, *New Astronomy Review*, 46, 287
- Taylor, G. B., Marr, J. M., Pearson, T. J., & Readhead, A. C. S. 2000, *ApJ*, 541, 112
- Tingay, S. J., et al. 2002, *ApJS*, 141, 311
- Tschager, W., Schilizzi, R. T., Röttgering, H. J. A., Snellen, I. A. G., & Miley, G. K. 2000, *A&A*, 360, 887
- Tzioumis, A. K., et al. 1998, *IAU Colloq. 164: Radio Emission from Galactic and Extragalactic Compact Sources*, 144, 179
- White, R. L., Becker, R. H., Helfand, D. J., & Gregg, M. D. 1997, *ApJ*, 475, 479
- Wilkinson, P. N., Polatidis, A. G., Readhead, A. C. S., Xu, W., & Pearson, T. J. 1994, *ApJ*, 432, L87

3.5 Appendix

3.5.1 Radio source evolution modelling

In this section we present analytic models predicting how the expansion velocity of young radio sources depends on radio luminosity L_{radio} , source age t , and environment. Our consideration is based on the radio source evolution models of Kaiser & Best (2007), hereafter KB. If the sources are physically small (less than a few kpc in size) and their radio luminosity is measured at a frequency where self-absorption is not important, they are in the ‘synchrotron loss dominated’ regime as discussed in KB (Sect. 2.3). In this regime we expect the radio luminosity L_{radio} to be proportional to Q , the jet power, which is assumed to be constant with time, and independent of the density of the source environment. If we assume that the density ρ in the source environment follows a power-law distribution with respect to r , the distance to the centre, then

$$\rho = \rho_0 \left(\frac{r}{a_0} \right)^{-\beta}, \quad (3.4)$$

where ρ_0 is the density at an arbitrary reference point a_0 , and β is the slope of the density profile. Note that ρ_0 and a_0 are not independent, and the model can only depend on their combination $\rho_0 a_0^\beta$. Using equation A2 from the appendix of KB, the linear size of the source, D , is given by

$$D \propto \left(\frac{Q}{\rho_0 a_0^\beta} \right)^{1/(5-\beta)} t^{3/(5-\beta)}. \quad (3.5)$$

This means that the expansion speed of the lobe is given by

$$v_{\text{exp}} = \dot{D} \propto Q^{1/(5-\beta)} t^{(\beta-2)/(5-\beta)} \left(\rho_0 a_0^\beta \right)^{-1/(5-\beta)}. \quad (3.6)$$

Assuming Q is proportional to L_{radio} , we obtain

$$v_{\text{exp}} \propto L_{\text{radio}}^{1/(5-\beta)} t^{(\beta-2)/(5-\beta)} \left(\rho_0 a_0^\beta \right)^{-1/(5-\beta)}. \quad (3.7)$$

If we take the often adopted value $\beta = 2$ (e.g. Bicknell et al. 1997), the time dependence drops out and equation (3.7) reduces to

$$v_{\text{exp}} \propto L_{\text{radio}}^{1/3} \left(\rho_0 a_0^2 \right)^{-1/3}. \quad (3.8)$$

We have used this equation for comparison with the observed expansion speeds in Sect. 3.3.4. Note that in the central part of galaxies one might expect the density profile to become less steep, even possibly resulting in a flat density profile with $\beta = 0$. In this extreme case you would expect $v_{\text{exp}} \propto L_{\text{radio}}^{1/5} t^{-2/5} \rho_0^{-1/5}$, so the slope of the correlation between expansion velocity and radio power is not extremely sensitive to the value of β , but the additional time dependence may increase the scatter around it, in addition to the scatter caused by projection effects and by variations in the density profile of the surrounding medium from source to source.

3.5.2 Observations and radio maps

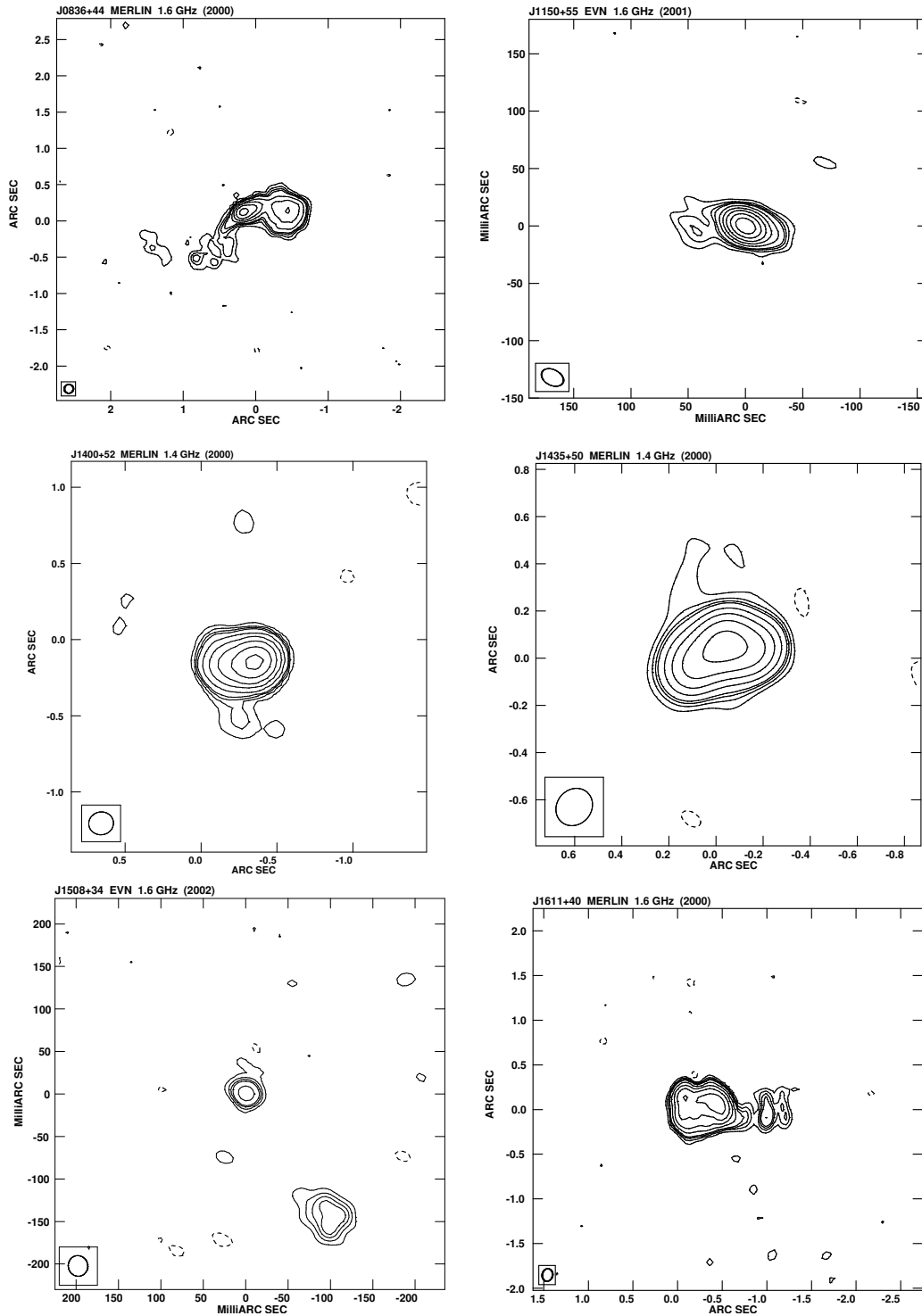


Figure 3.5: — Contour maps of the more extended sources from the CORALZ core sample taken with MERLIN at 1.4 GHz or 1.6 GHz in 2000, or with the EVN at 1.6 GHz.

Table 3.3: — Observations of the sources in the CORALZ sample. The first 18 objects form the CORALZ core sample at $0.005 < z < 0.160$, the next seven objects are other nearby radio sources in the CORALZ sample, and the final three objects are other compact radio sources located towards probably random foreground galaxies.

IAU Name	Fig.	Epoch	Freq. (GHz)	Bandw. (MHz)	Array	S_{peak} (mJy beam $^{-1}$)	rms	Beam (mas)	$^{\circ}$
The CORALZ core sample									
J073328+560541	3.6	2000/02/14	1.655	32	EVN	126	0.39	25×15	31
	3.6	2004/06/05	1.665	16	EVN+VLBA	55	0.22	7.8×2.1	-12
	3.6	2004/05/24	4.993	16	EVN+VLBA	47	0.19	9.0×7.9	-59
J073934+495438	3.7	2000/03/02	4.987	32	EVN+VLBA	22	0.06	2.8×0.8	-25
	3.7	2004/05/24	4.993	16	EVN+VLBA	25	0.06	4.1×1.3	-32
J083139+460800	3.7	2000/03/02	4.987	32	EVN+VLBA	32	0.13	2.3×0.7	-6
	3.7	2004/05/24	4.993	16	EVN+VLBA	42	0.08	3.1×0.8	-13
J083637+440109	3.5	2000/11/13	1.658	15	MERLIN	22	0.09	125×121	-75
J090615+463618	3.6	2001/05/27	1.659	16	EVN	134	0.13	22×13	59
	3.6	2004/06/05	1.665	16	EVN+VLBA	88	0.16	9.9×2.1	-4
	3.6	2004/05/24	4.993	16	EVN+VLBA	84	0.18	2.8×0.7	-14
J102618+454229	3.6	2001/05/28	1.659	16	EVN	76	0.14	22×15	69
	3.6	2004/06/05	1.665	16	EVN+VLBA	30	0.10	10×2.1	-3
	3.6	2004/05/24	4.993	16	EVN+VLBA	30	0.06	2.7×0.8	-3
J103719+433515	3.6	2001/05/27	1.659	16	EVN	61	0.23	21×13	77
	3.6	2004/06/05	1.665	16	EVN+VLBA	21	0.10	12×2.1	-7
	3.6	2004/05/24	4.993	16	EVN+VLBA	19	0.23	11×6.7	34
J115000+552821	3.5	2001/05/28	1.659	16	EVN	103	0.14	20×14	63

Table 3.3: — Observations of the sources in the CORALZ sample, continued.

IAU Name	Fig.	Epoch	Freq. (GHz)	Bandw. (MHz)	Array	S_{peak} (mJy beam $^{-1}$)	rms	Beam (mas)	Beam °
J120902+411559	3.6	2001/05/27	1.659	16	EVN	117	0.17	23×14	48
	3.6	2004/06/05	1.665	16	EVN+VLBA	54	0.05	9.5×2.1	-11
	3.6	2004/05/24	4.993	16	EVN+VLBA	73	0.54	9.1×6.1	43
J131739+411545	3.7	2000/03/02	4.987	32	EVN+VLBA	45	0.22	1.4×0.9	-25
	3.7	2004/05/24	4.993	16	EVN+VLBA	53	0.11	2.7×0.7	-3
J140051+521606	3.5	2000/12/26	1.408	15	MERLIN	101	0.20	163×150	-82
J140942+360416	3.6	2001/05/28	1.659	16	EVN	81	0.13	28×11	37
	3.6	2004/06/05	1.665	16	EVN+VLBA	30	0.06	17×2.1	-5
J143521+505122	3.5	2000/12/26	1.408	15	MERLIN	73	0.26	166×146	-41
J150805+342323	3.5	2002/02/19	1.650	16	EVN	4	0.11	24×23	16
J160246+524358	3.6	2001/05/27	1.659	16	EVN	62	0.14	21×12	59
	3.6	2004/06/05	1.665	16	EVN+VLBA	23	0.16	8.4×2.1	-19
	3.6	2004/05/24	4.993	16	EVN+VLBA	30	0.13	7.6×6.3	58
J161148+404020	3.5	2000/11/25	1.658	15	MERLIN	86	0.12	167×136	-1
J170330+454047									
J171854+544148	3.6	2000/02/14	1.655	32	EVN	119	0.33	20×13	-84
	3.6	2004/06/05	1.665	16	EVN+VLBA	90	0.19	10×2.1	-6
	3.6	2004/05/24	4.993	16	EVN+VLBA	49	0.11	8.9×6.1	16
Other nearby sources in the CORALZ sample									
J093609+331308	3.8	2000/03/02	4.987	32	EVN+VLBA	28	0.15	1.2×0.8	0
J101636+563926	3.8	2000/11/09	1.658	15	MERLIN	52	0.08	174×136	-31

Table 3.3: — Observations of the sources in the CORALZ sample, continued.

IAU Name	Fig.	Epoch	Freq. (GHz)	Bandw. (MHz)	Array	S_{peak} (mJy beam ⁻¹)	rms	Beam (mas)	Beam °
J105731+405646	3.8	2000/03/02	4.987	32	EVN+VLBA	14	0.08	1.8×0.3	13
J115727+431806	3.8	2001/01/02	1.408	15	MERLIN	41	0.09	182×173	-47
J132513+395552	3.8	2000/03/02	4.987	32	EVN+VLBA	15	0.08	0.7×0.3	-20
J134035+444817	3.8	2000/03/02	4.987	32	EVN+VLBA	76	0.13	1.4×0.9	-7
J155927+533054	3.8	2000/12/18	1.408	15	MERLIN	16	0.11	308×202	14
Additional sources									
J071509+452555	3.9	2000/03/02	4.987	32	EVN+VLBA	30	0.13	0.8×0.8	0
J080454+433537	3.9	2000/02/14	1.655	32	EVN	182	0.39	27×14	39
J134158+541524	3.9	2002/02/19	1.650	16	EVN	10	0.13	25×22	70

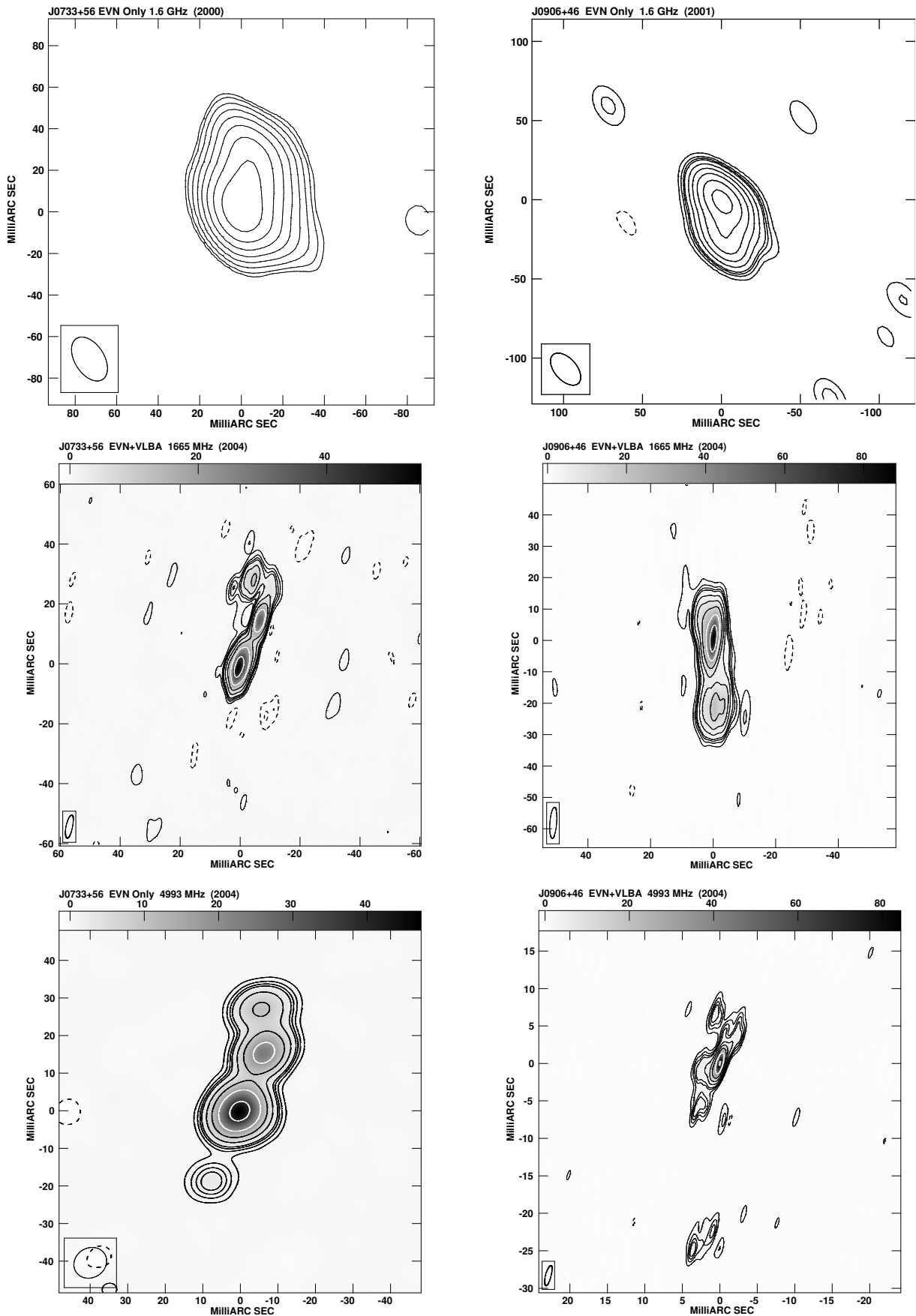


Figure 3.6: — Contour maps of sources from the CORALZ core sample observed with the EVN (1.6 GHz, 2000; first row), and global VLBI (1.6 GHz and 5.0 GHz, 2004; second and third row, respectively).

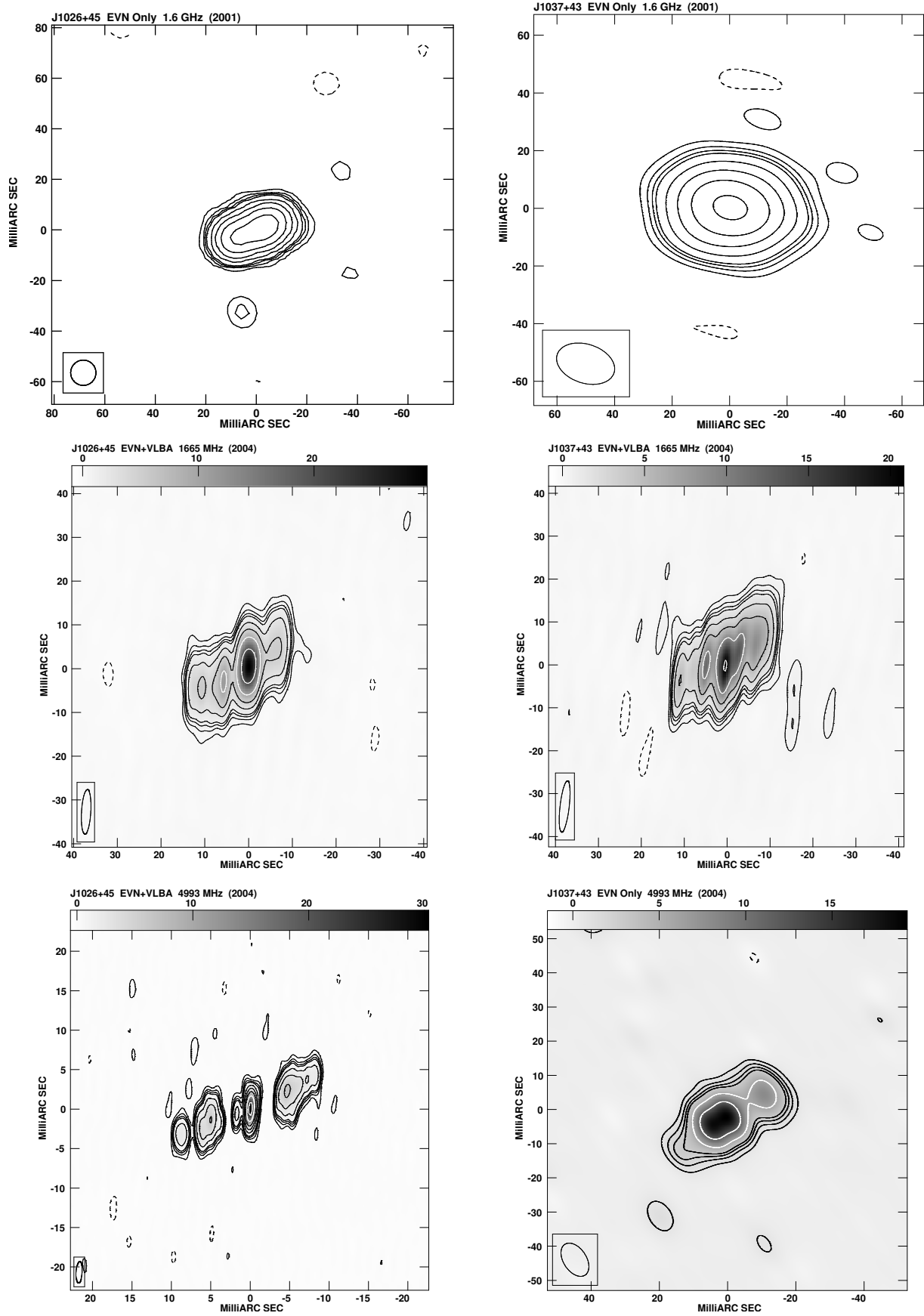


Figure 3.6: — continued.

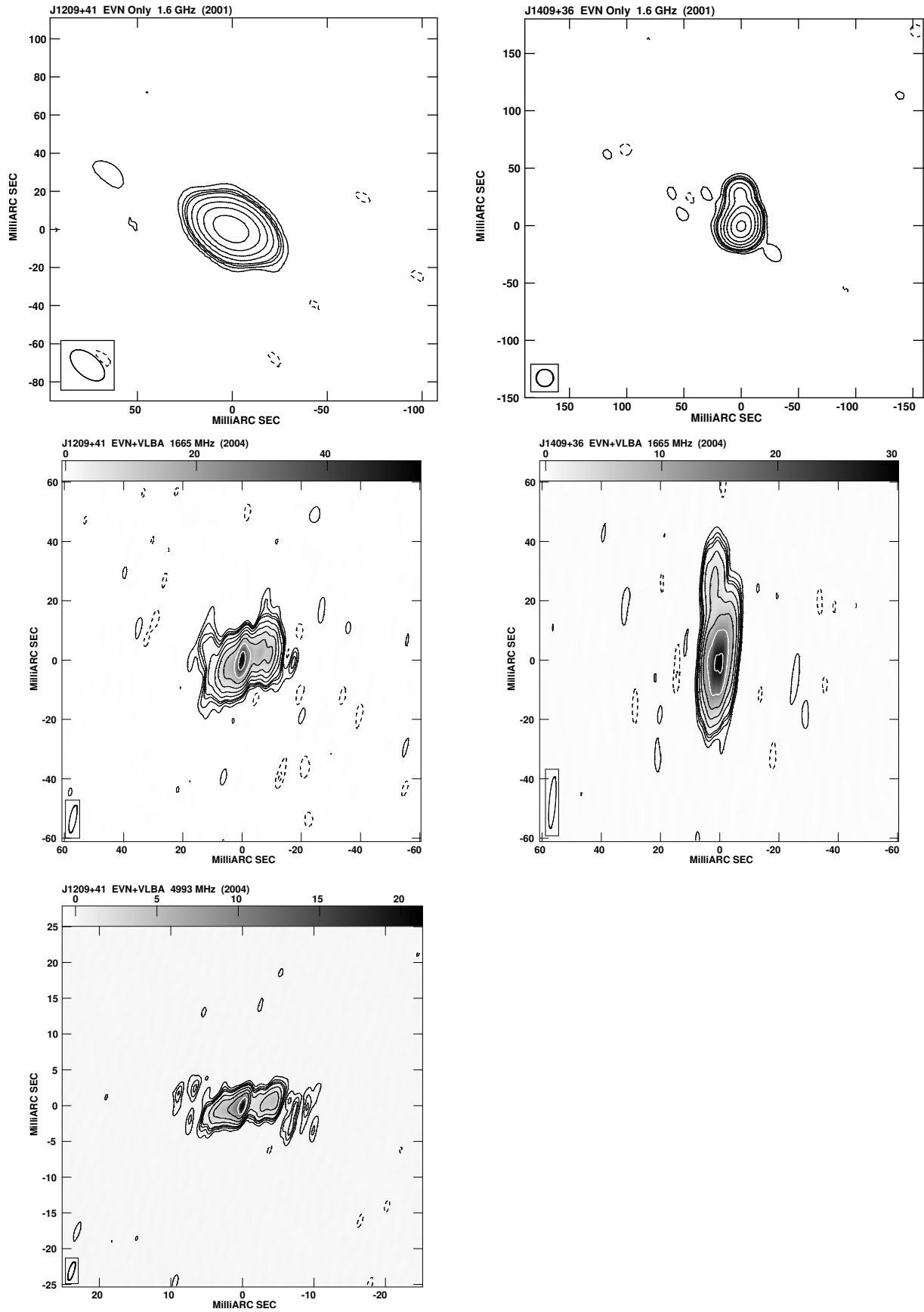


Figure 3.6: — continued.

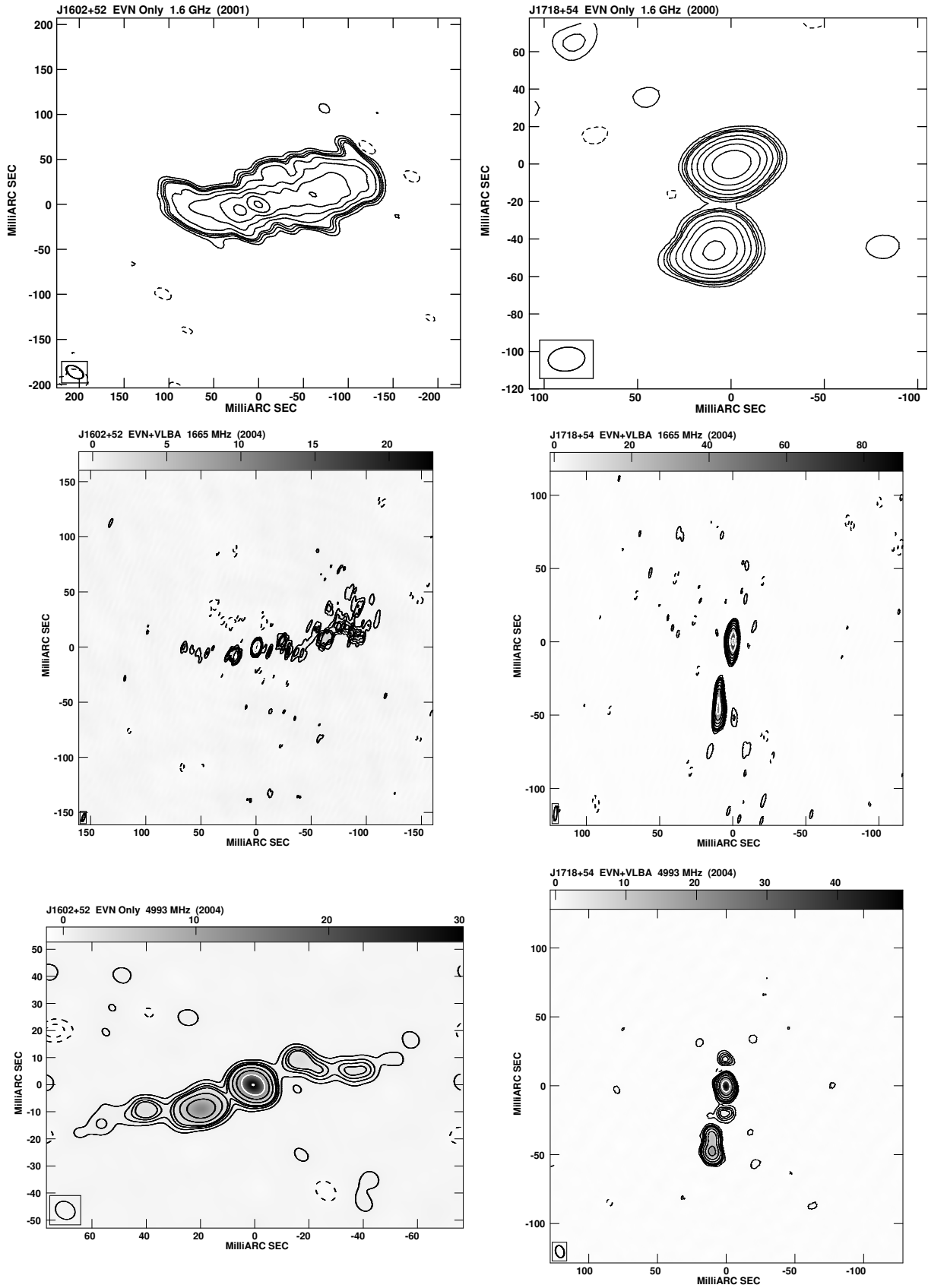


Figure 3.6: — continued.

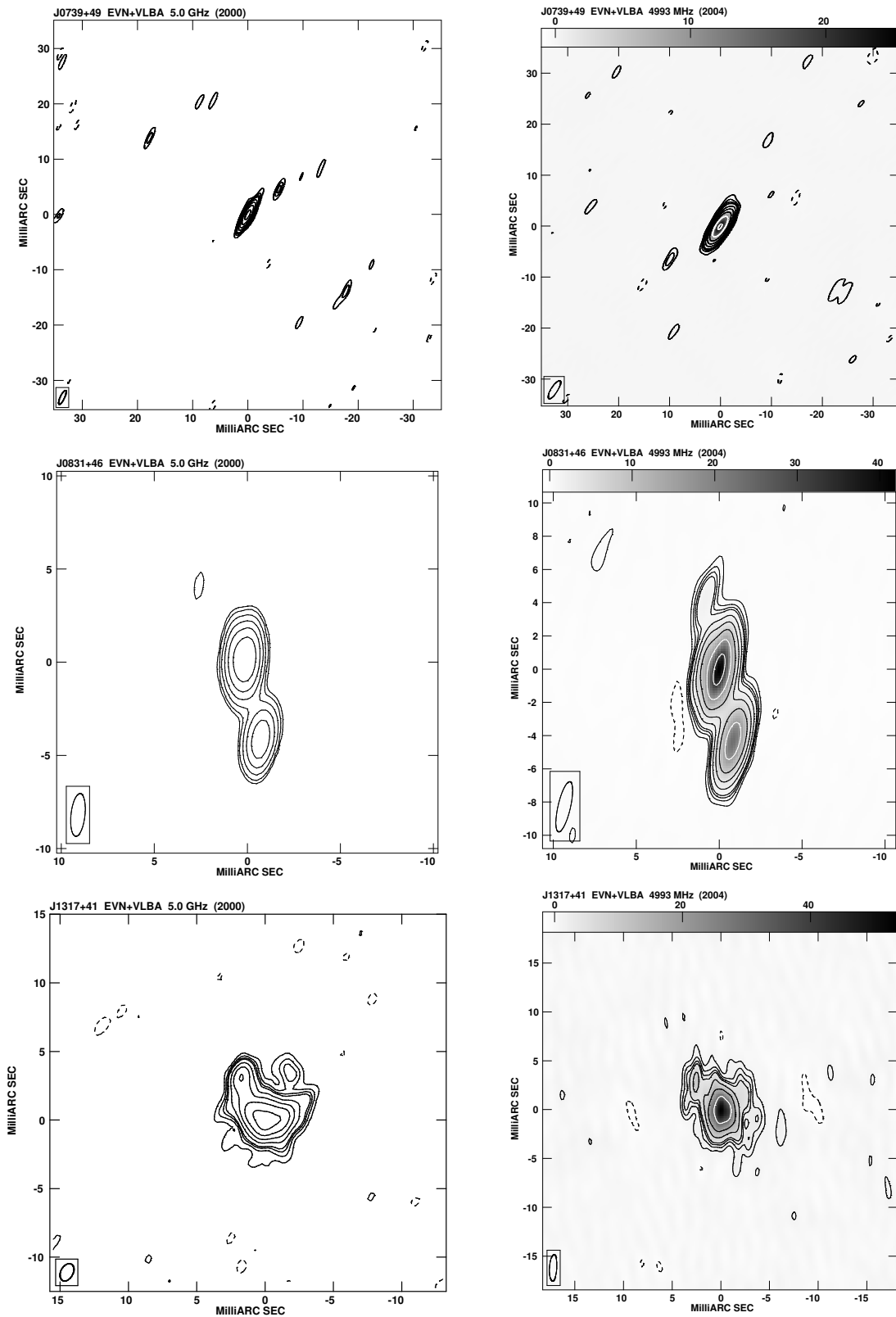


Figure 3.7: — Contour maps of the three most compact sources from the CORALZ core sample taken with global VLBI at 5.0 GHz in 2000 (first column), and 2004 (second column).

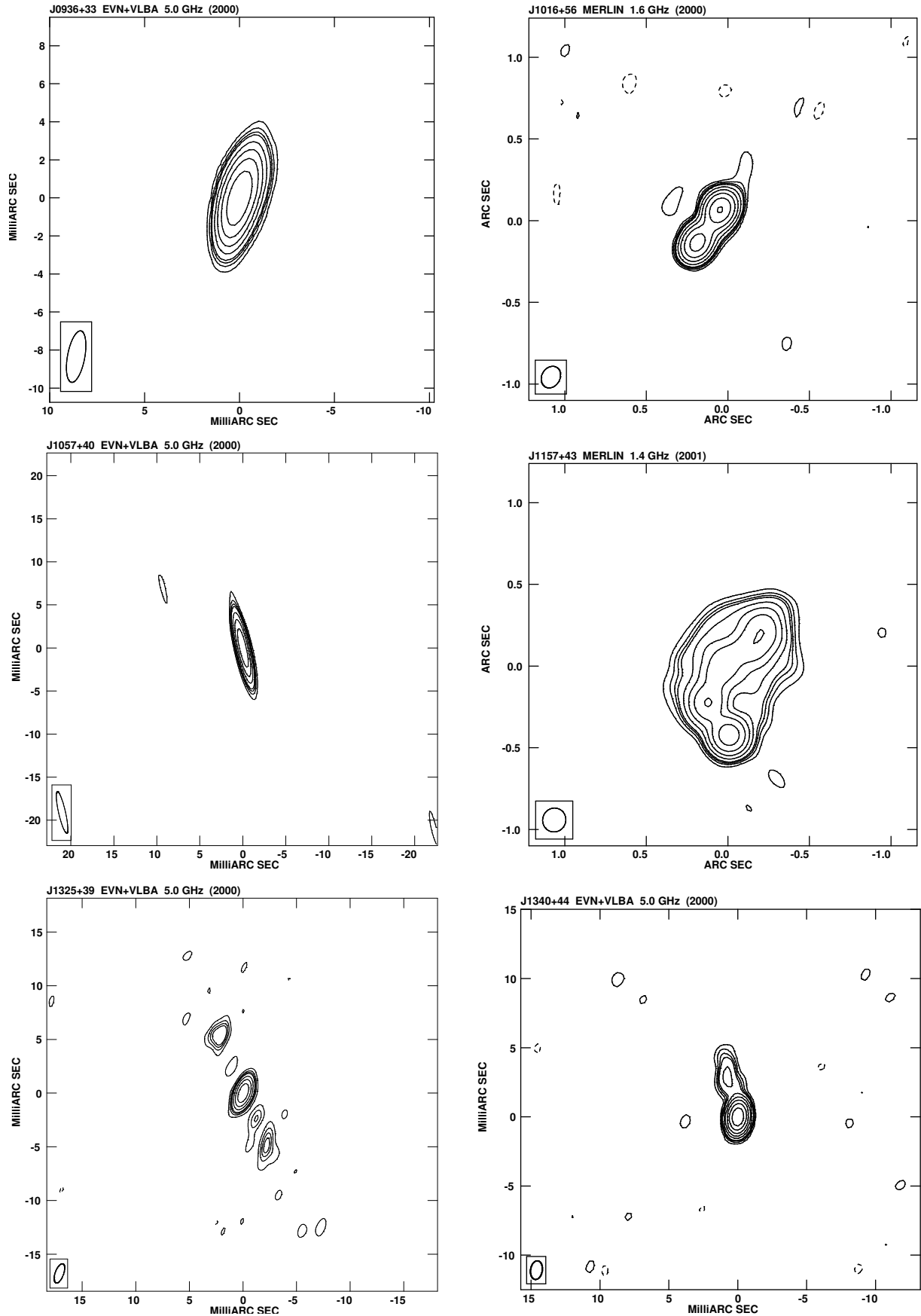


Figure 3.8: — Contour maps of other sources from the CORALZ sample taken in 2000 with global VLBI (5.0 GHz) or with MERLIN (1.4 GHz or 1.6 GHz). These sources are either slightly too faint, or too distant to be part of the CORALZ core sample.

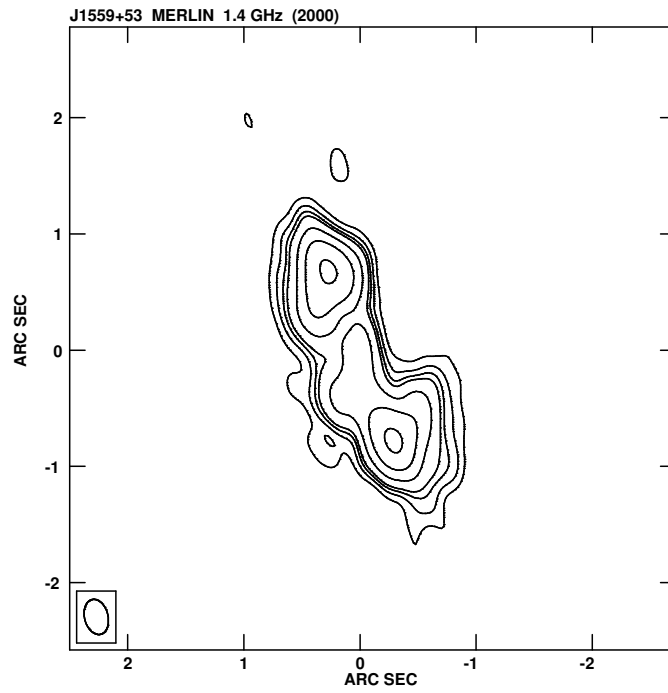


Figure 3.8: — continued.

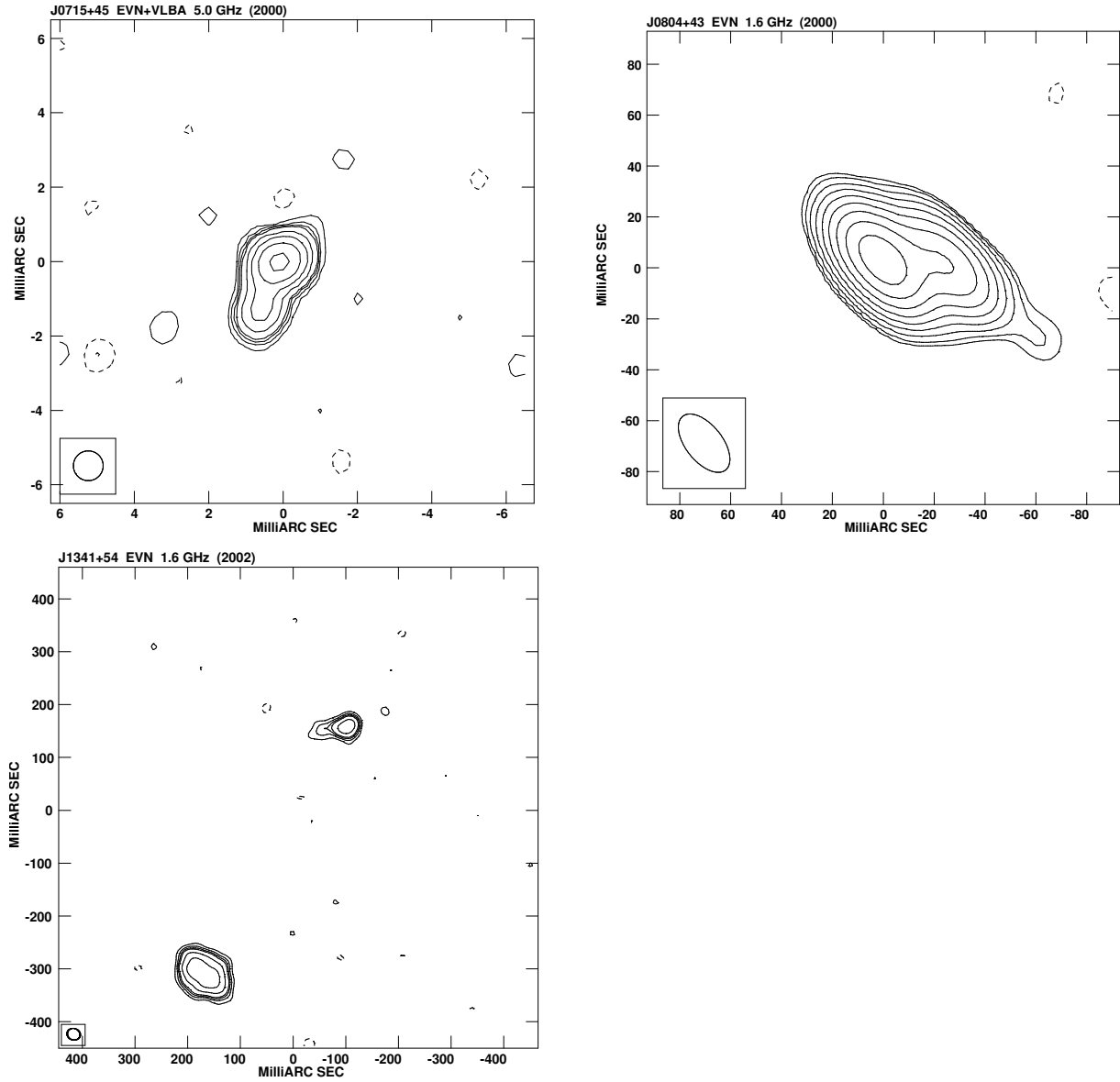


Figure 3.9: — Contour maps of the additional sources, observed with global VLBI (5.0 GHz), or with the EVN (1.6 GHz). These sources have been excluded from the CORALZ sample because the offset between the radio and optical position is large, indicating that these radio sources are located towards probably random foreground galaxies.

Table 3.4: — The fitted parameters of the observed components.

IAU name	Fig	Epoch	ν_{obs} (GHz)	Δx (mas)	Δy (mas)	Flux density (mJy)	Size (mas)	PA °
J073328+560541	3.6	2000/02/14	1.655	0.0	0.0	248.0 \pm 0.9	29.4 \times 8.4	164
	3.6	2004/06/05	1.665	0.0	0.0	150.0 \pm 0.7	7.1 \times 3.8	156
				-6.7	15.3	60.1 \pm 0.5	5.5 \times 2.2	153
				-4.3	28.9	28.6 \pm 0.7	5.9 \times 3.7	107
	3.6	2004/05/24	4.993	0.0	0.0	58.9 \pm 0.1	5.1 \times 3.4	147
				-6.4	15.5	28.1 \pm 0.1	5.3 \times 1.8	147
J073934+495438				-5.8	26.8	14.8 \pm 0.1	6.3 \times 4.8	80
				7.5	-18.6	3.1 \pm 0.1	3.1 \times 0.0	83
	3.7	2000/03/02	4.987	0.0	0.0	30.0 \pm 0.1	1.8 \times 0.4	142
J083139+460800	3.7	2004/05/24	4.993	0.0	0.0	36.7 \pm 0.1	2.0 \times 1.0	140
	3.7	2000/03/02	4.987	0.0	0.0	54.1 \pm 0.2	1.0 \times 0.8	52
				-0.9	-4.3	19.9 \pm 0.2	0.8 \times 0.1	106
	3.7	2004/05/24	4.993	0.0	0.0	65.0 \pm 0.2	1.1 \times 0.7	45
				-0.9	-4.3	35.5 \pm 0.2	0.9 \times 0.6	78
				0.8	4.2	2.3 \pm 0.2	0.6 \times 0.0	163
J083637+440109	3.5	2000/11/13	1.658	0.0	0.0	60.4 \pm 0.8	385.9 \times 295.2	76
J090615+463618				546.3	-5.4	46.7 \pm 0.3	212.6 \times 64.4	114
	3.6	2001/05/27	1.659	0.0	0.0	160.7 \pm 0.5	9.5 \times 3.3	8
				-1.3	-22.5	65.1 \pm 0.5	11.1 \times 4.2	3
	3.6	2004/06/05	1.665	0.0	0.0	160.7 \pm 0.5	9.5 \times 3.3	8
				-1.3	-22.5	65.1 \pm 0.5	11.1 \times 4.2	3

Table 3.4: — The fitted parameters of the observed components, continued.

IAU name	Fig	Epoch	ν_{obs} (GHz)	Δx (mas)	Δy (mas)	Flux density (mJy)	Size (mas)	PA °
J102618+454229	3.6	2004/05/24	4.993	0.0	0.0	105.0 ± 0.3	1.1×0.3	139
				0.4	6.4	8.5 ± 0.5	2.5×1.4	178
				2.6	-5.5	10.3 ± 0.6	2.7×1.6	150
				-0.4	-7.4	2.2 ± 0.4	2.8×0.2	171
				3.4	-24.6	6.4 ± 0.5	1.7×1.3	165
	3.6	2001/05/28	1.659	0.0	0.0	111.0 ± 0.3	17.9×2.9	112
	3.6	2004/06/05	1.665	0.0	0.0	59.0 ± 0.2	3.5×1.8	84
				5.7	-3.3	9.6 ± 0.2	1.5×0.0	152
				-6.4	4.1	13.8 ± 0.3	5.8×3.9	173
				10.4	-5.0	22.8 ± 0.4	8.7×3.4	82
J103719+433515	3.6	2004/05/24	4.993	0.0	0.0	33.7 ± 0.1	0.8×0.3	173
				5.3	-1.7	21.7 ± 0.3	3.4×1.8	159
				-4.8	2.2	26.0 ± 0.3	3.0×1.8	146
				8.8	-3.3	5.5 ± 0.2	1.4×1.1	40
				1.7	-0.6	2.2 ± 0.1	0.7×0.5	164
				-7.1	3.6	8.9 ± 0.2	2.6×1.0	133
	3.6	2001/05/27	1.659	0.0	0.0	72.0 ± 0.3	13.4×8.8	107
	3.6	2004/06/05	1.665	0.0	0.0	24.7 ± 0.2	3.0×1.6	175
				-3.0	2.9	11.7 ± 0.2	4.5×0.5	165
				4.1	0.7	24.3 ± 0.3	6.2×2.1	129
J103719+433515				-7.2	6.0	25.1 ± 0.3	6.2×4.8	140
				9.3	-2.4	10.4 ± 0.3	5.6×3.1	131

Table 3.4: — The fitted parameters of the observed components, continued.

IAU name	Fig	Epoch	ν_{obs} (GHz)	Δx (mas)	Δy (mas)	Flux density (mJy)	Size (mas)	PA °
	3.6	2004/05/24	4.993	0.0	0.0	21.0 ± 0.1	4.2×1.8	131
				5.5	-3.2	13.6 ± 0.1	1.2×0.0	75
				-10.3	6.3	12.9 ± 0.1	7.1×5.2	91
				11.4	-8.8	5.1 ± 0.1	8.6×0.0	118
J115000+552821	3.5	2001/05/28	1.659	0.0	0.0	111.9 ± 0.3	7.0×4.1	77
				40.6	0.0	5.8 ± 0.7	33.5×28.9	42
J120902+411559	3.6	2001/05/27	1.659	0.0	0.0	128.5 ± 0.2	8.1×0.0	14
3.6	2004/06/05	1.665	0.0	0.0	0.0	56.3 ± 0.1	2.6×0.0	131
				-2.7	0.5	58.9 ± 0.2	12.2×2.2	131
				-8.6	1.0	25.1 ± 0.2	4.8×0.0	171
				4.5	-2.0	33.3 ± 0.2	5.3×3.5	117
3.6	2004/05/24	4.993	0.0	0.0	0.0	19.7 ± 0.1	0.6×0.0	8
				-3.0	0.2	7.6 ± 0.2	1.5×0.8	109
				-4.5	0.8	9.3 ± 0.2	1.7×1.2	1
				1.4	-0.2	39.0 ± 0.3	4.2×1.0	105
J131739+411545	3.7	2000/03/02	4.987	0.0	0.0	126.8 ± 0.6	1.8×1.2	82
				1.6	2.1	44.0 ± 0.7	2.8×0.9	19
3.7	2004/05/24	4.993	0.0	0.0	0.0	183.8 ± 1.3	2.2×1.9	49
				2.7	2.8	23.3 ± 1.1	2.3×1.4	155
J140051+521606	3.5	2000/12/26	1.408	0.0	0.0	170.0 ± 0.5	182.3×95.9	102
J140942+360416	3.6	2001/05/28	1.659	0.0	0.0	104.1 ± 0.2	10.7×4.9	159
				-0.5	22.1	22.4 ± 0.3	22.6×5.4	16

Table 3.4: — The fitted parameters of the observed components, continued.

IAU name	Fig	Epoch	ν_{obs} (GHz)	Δx (mas)	Δy (mas)	Flux density (mJy)	Size (mas)	PA °
	3.6	2004/06/05	1.665	0.0	0.0	111.1 ± 0.3	13.0×5.8	169
				1.4	26.9	10.3 ± 0.2	6.1×4.4	148
J143521+505122	3.5	2000/12/26	1.408	0.0	0.0	75.2 ± 0.6	161.0×9.3	69
				128.8	-46.0	64.7 ± 0.6	181.5×46.6	126
J150805+342323	3.5	2002/02/19	1.650	0.0	0.0	4.0 ± 0.2	7.8×0.0	72
				-97.5	-144.4	6.1 ± 0.4	42.2×30.5	47
J160246+524358	3.6	2001/05/27	1.659	0.0	0.0	26.0 ± 0.1	0.0×0.0	0
				13.8	-2.9	200.3 ± 0.7	70.4×22.7	100
				-73.0	16.2	222.0 ± 0.8	64.0×32.8	106
	3.6	2004/06/05	1.665	0.0	0.0	41.9 ± 0.4	3.7×0.0	145
				19.1	-7.8	20.5 ± 0.6	6.1×2.8	49
				-23.5	6.2	7.4 ± 0.6	5.5×3.6	71
				-36.2	-3.3	22.1 ± 2.4	27.3×13.4	85
				-63.6	8.8	26.8 ± 1.5	15.9×8.3	132
				-104.6	43.2	2.2 ± 0.6	6.3×3.5	11
				65.7	-0.2	2.8 ± 0.5	4.9×3.6	30
	3.6	2004/05/24	4.993	0.0	0.0	37.7 ± 0.1	4.1×3.0	75
				19.1	-8.7	23.1 ± 0.2	8.5×2.6	105
				-17.5	8.9	5.1 ± 0.2	7.6×2.9	74
				-37.5	5.5	4.8 ± 0.2	13.0×2.8	92
J161148+404020	3.5	2000/11/25	1.658	0.0	0.0	227.2 ± 0.4	253.2×136.7	43
				292.8	-15.9	214.3 ± 0.5	304.5×222.0	22

Table 3.4: — The fitted parameters of the observed components, continued.

IAU name	Fig	Epoch	ν_{obs} (GHz)	Δx (mas)	Δy (mas)	Flux density (mJy)	Size (mas)	PA °
J171854+544148	3.6	2000/02/14	1.655	-591.8	-88.8	22.0 ± 0.6	329.3×263.1	134
				0.0	0.0	98.9 ± 0.8	5.3×2.7	0
	3.6	2004/06/05	1.665	10.9	-50.0	151.4 ± 1.8	19.2×5.5	169
				0.0	0.0	193.6 ± 0.5	6.7×3.0	9
	3.6	2004/05/24	4.993	9.9	-45.2	167.9 ± 0.7	17.3×2.9	180
				0.0	0.0	61.5 ± 0.2	4.7×2.1	150
				10.2	-47.4	26.0 ± 0.2	5.0×3.2	115
				9.9	-36.8	13.6 ± 0.2	3.2×1.5	155
				0.9	-19.8	3.8 ± 0.3	9.1×0.0	98
				0.4	20.0	2.3 ± 0.2	5.1×0.0	90
J093609+331308	3.8	2000/03/02	4.987	0.0	0.0	51.7 ± 0.3	1.5×0.3	142
J101636+563926	3.8	2000/11/09	1.658	0.0	0.0	57.2 ± 0.2	64.4×26.5	154
				136.9	-196.6	39.2 ± 0.1	66.5×10.7	137
J105731+405646	3.8	2000/03/02	4.987	0.0	0.0	14.8 ± 0.1	0.5×0.2	1
J115727+431806	3.8	2001/01/02	1.408	0.0	0.0	43.2 ± 0.2	55.5×44.2	76
				-185.3	604.5	59.4 ± 0.2	215.0×131.0	165
				134.8	188.5	30.4 ± 0.2	100.8×55.2	10
				41.4	423.5	58.4 ± 0.3	232.8×187.6	155
J132513+395552	3.8	2000/03/02	4.987	0.0	0.0	16.2 ± 0.1	0.4×0.0	176
				2.2	5.4	3.0 ± 0.2	1.0×0.8	86
				-2.0	-4.2	5.6 ± 0.7	6.1×2.0	15
J134035+444817	3.8	2000/03/02	4.987	0.0	0.0	78.3 ± 0.2	0.2×0.2	13

Table 3.4: — The fitted parameters of the observed components, continued.

IAU name	Fig	Epoch	ν_{obs} (GHz)	Δx (mas)	Δy (mas)	Flux density (mJy)	Size (mas)	PA °
J155927+533054	3.8	2000/12/18	1.408	0.7	3.2	5.7 ± 0.3	1.8×0.7	9
				0.0	0.0	83.0 ± 0.8	936.4×390.6	33
				560.2	1342.1	63.2 ± 0.5	555.1×367.6	4
J071509+452555	3.9	2000/03/02	4.987	0.0	0.0	39.1 ± 0.2	0.6×0.2	119
				0.5	-1.2	11.3 ± 0.2	0.8×0.1	162
J080454+433537	3.9	2000/02/14	1.655	0.0	0.0	194.1 ± 0.4	6.7×3.7	70
				-24.1	-1.8	71.3 ± 0.4	15.5×3.2	63
J134158+541524	3.9	2002/02/19	1.650	0.0	0.0	66.3 ± 0.8	67.9×40.9	50
				-270.9	467.1	10.9 ± 0.4	33.8×16.3	108

Chapter 4

The dynamical ages of two low-luminosity young radio sources

Abstract. Young radio-loud active galactic nuclei form an important tool to investigate the evolution of extragalactic radio sources. To study the early phases of expanding radio sources, we are using the CORALZ sample, which contains 25 compact ($\theta < 2''$) radio sources associated with nearby galaxies. In this chapter we aim to determine the lobe-to-lobe expansion speeds for two sources in the sample. Comparing the dynamical ages of these relatively low-luminosity objects with those of powerful sources in the literature, will serve to test radio source evolution models. We present our third epoch of VLBI observations, using the EVN+VLBA array at 5.0 GHz, four and eight years after our previous measurements. We report the detection of a lobe-to-lobe expansion speed of $0.095 \pm 0.020h^{-1}c$ for CORALZ J083139+460800, and a $1-\sigma$ upper limit to the expansion speed of CORALZ J131739+411545 of $0.074h^{-1}c$. The detected expansion speed of CORALZ J083139+460800 corresponds to a dynamical age of 245 ± 55 years. The detected expansion speed and upper limit are lower than any presented in the literature for powerful young AGN. This confirms that the expansion speeds of young radio sources are correlated with their radio luminosities.

N. de Vries, I. A. G. Snellen, R. T. Schilizzi, and K.-H. Mack
Astronomy & Astrophysics, accepted for publication

The dynamical ages of two low-luminosity young radio sources



YOUNG radio-loud active galactic nuclei (AGN) are key objects for constraining evolution models of classical double radio sources. Young radio sources can be recognised by their small sizes, their inverted spectra at low frequencies, and their often compact symmetric morphologies, with lobe-like structures on both sides of a central core. Depending on the observed characteristics, they are called compact steep spectrum (CSS) sources (Peacock & Wall 1982; Fanti et al. 1990; O'Dea 1998), gigahertz peaked spectrum (GPS) sources (O'Dea 1998), and/or compact symmetric objects (CSO, Wilkinson et al. 1994; Conway 2002).

Samples of young radio-loud AGN have been used in a statistical way to constrain the early evolution of radio sources. Relative number statistics indicated that at a young age, radio sources must have significantly higher radio luminosities than when they are older (O'Dea & Baum 1996; Readhead et al. 1996; Fanti & Fanti 2003). Some analytic models predict that this decrease in radio luminosity is preceded by a period of luminosity increase at the earliest evolutionary stages (Snellen et al. 2000; 2003).

Very important results come from multi-epoch Very Long Baseline Interferometry (VLBI) observations of individual CSOs. For a handful of powerful objects the proper motions of the lobes have been detected, from which their dynamical ages can be estimated (Owsianik & Conway 1998; Polatidis & Conway 2003 and references therein). Separation velocities between the opposite extremities of the sources of up to $0.5h^{-1}c$ have been measured, corresponding to dynamical ages in the range of a few hundred to a few thousand years.

Snellen et al. (2004) selected a sample of 25 young radio sources, CORALZ (COmpact RAdio sources at Low Redshift), with the aim of obtaining an unbiased view of young radio-loud AGN in the nearby universe. The sources in the CORALZ sample are significantly closer than

the archetypal CSO and GPS sources studied in the literature. Proper motions should be easier to detect in these nearby sources, since similar intrinsic expansion velocities would result in significantly higher angular motions compared to previous studies. Moreover, in general these radio sources are less powerful than the archetypal CSOs and GPS sources, which will allow luminosity-dependent comparison studies.

The CORALZ sample was selected on flux density ($S_{1.4 \text{ GHz}} > 100 \text{ mJy}$) and angular size ($\theta < 2''$). Using the Very Large Array (VLA) Faint Images of the Radio Sky at Twenty-centimeters (FIRST) survey (White et al. 1997), the optical Automated Plate Measuring machine (APM) catalogue of the first Palomar Observatory Sky Survey (POSS-I) (McMahon & Irwin 1991), and follow-up observations, all radio sources identified with bright galaxies were selected (red magnitude of $e < 16.5 \text{ mag}$ or blue magnitude of $o < 19.5 \text{ mag}$). A detailed description of the selection process and additional radio observations can be found in Snellen et al. (2004). Nearly all of the sources in the CORALZ sample are spectrally classified as GPS and CSS sources, and morphologically classified as CSOs, confirming that these are likely to be young radio sources.

In the previous chapter (Chapter 3; de Vries et al. 2009) we presented radio maps, morphological classifications, and linear sizes of the CORALZ sample. Furthermore we derived a remarkably low upper limit to the expansion speed of one of the sources (CORALZ J083139+460800, which is re-examined in this chapter). Since the CORALZ sample is of relatively low luminosity, we interpreted this as a hint that the expansion speeds of young radio sources are correlated with their radio luminosities. We now wish to investigate this further.

In this chapter we present a new epoch of global VLBI observations for two sources from the CORALZ sample. For these two radio sources, for which in total three epochs of VLBI observations have been obtained with the same telescope array at the same frequency, we will estimate expansion velocities. The new observations of the other sources from the CORALZ sample will be published at a later date, when sufficient data (i.e. a third epoch of observations) has been obtained for the kinematical study of those sources. In Sect. 4.1 the observations and data reduction are described; the data analysis is outlined in Sect. 4.2. The results are presented and discussed in Sect. 4.3, and we conclude with

Sect. 4.4. Throughout this chapter we adopt the cosmological parameters as found by WMAP5 (Komatsu et al. 2009; $H_0 = 70.1 \text{ km s}^{-1} \text{ Mpc}^{-1}$, $\Omega_\Lambda = 0.721$, $\Omega_m = 0.279$).

4.1 Observations and data reduction

On March 13, 2008, we observed seven radio sources from the CORALZ sample with global VLBI at 5.0 GHz with a bandwidth of 16 MHz, using the EVN (European VLBI Network) and the VLBA (Very Long Baseline Array). A similar observing strategy was used as for the previous global VLBI observations (de Vries et al. 2009), in order to minimize differences in signal-to-noise and resolution. Just like our observations in 2004, this global VLBI experiment was conducted with an array of 16 stations, using the EVN antennas Effelsberg, Jodrell Bank, Medicina, Noto, Torun, Westerbork, and Onsala, and the VLBA antennas St. Croix, Hancock, North Liberty, Fort Davis, Los Alamos, Pie Town, Kitt Peak, Owens Valley, and Brewster. The largest projected baselines were typically 9000 km, resulting in a resolution of about 2 mas. Each source was typically observed for 4×10 minutes, spread in time to obtain optimal UV coverage. 4C39.25 and J1657+5705 were observed as primary calibrators. The data correlation was performed at the Joint Institute for VLBI in Europe (JIVE). The Astronomical Image Processing System (AIPS) has been used for editing, a-priori calibration, fringe-fitting, self-calibration and imaging of the data. For fringe-fitting, the AIPS task FRING was used with a point source model, a solution interval of 6 minutes, and a standard signal-to-noise ratio cutoff of 5. Several iterations of phase (or amplitude & phase) self-calibration and imaging were performed using the AIPS tasks CALIB and IMAGR, until the image quality converged, with negligible negative structure and a low noise level of about 0.2 mJy.

4.2 Data analysis

The observed radio source structures were characterised using the AIPS task JMFIT, which fits (by least-squares) up to four Gaussian components to an image subsection. A first guess of the input parameters (position, flux density, and shape of the components) was made using the INPFIT procedure. To obtain error estimates of the component positions

we have used the formula from Fomalont (1999):

$$\sigma_r = \frac{\sigma_{\text{rms}} d}{2 I_{\text{peak}}} \quad (4.1)$$

where σ_{rms} is the post-fit r.m.s. error of the map, and d and I_{peak} are the size and the peak intensity of the component. The positional uncertainties were derived similarly in de Vries et al. (2009), where it was already noted that the error estimates only take into account the errors in the analysis of the reduced radio maps, not the possible biases introduced during the synthesis of these maps. This also applies here, and we will return to this issue in Sect. 4.3.1. The calculated hotspot separations concern the distance between the centers of the two components, not between the outer edges of the components, because the latter cannot be derived with sufficient accuracy to study the kinematics of poorly resolved components in maps with differing beam shapes.

4.3 Results and discussion

We present the third epoch of VLBI observations for two sources from the CORALZ sample, CORALZ J083139 +460800, and CORALZ J131739 +411545. These have also been observed as part of the VLBA Imaging and Polarimetry Survey (VIPS, Helmboldt et al. 2007). In Figs. 4.4 and 4.5 we show all maps of CORALZ J083139 +460800 and CORALZ J131739 +411545, respectively, including our new epoch of observations. In the following sections the results from the kinematic analyses of these sources are presented and discussed.

4.3.1 CORALZ J083139+460800

CORALZ J083139+460800 is perfectly suitable for kinematic analysis. It exhibits a compact double morphology with two strong, unresolved components separated by about 4.4 mas. We rereduced our May 2004 data for this source, since an additional (possibly spurious) component was cleaned, not detected in the other epochs, biasing the positions of the two radio lobes. The two hotspot separation measurements differ with a 3σ significance. Note that the error estimate is based on the reduced map only, and does not include possible biases introduced during the synthesis of the map, as was noted by de Vries et al. (2009).

Table 4.1: — Hotspot separation measurements and error estimates of CORALZ J083139+460800.

observation date	σ_{rms} (mJy)	separation (mas)	$\sigma_{separation}$ (mas)
2000 March 2	0.30	4.349	0.023
2004 May 24	0.38	4.416	0.021
2006 May 31	0.40	4.435	0.024
2008 March 13	0.32	4.483	0.017

In table 4.1 the measured component separations for CORALZ J083139+460800 are presented, with in Col. 1 the observation date, in Col. 2 the post-fit r.m.s. error of the map, in Col. 3 the measured hotspot separation in milliarcseconds, and in Col. 4 the $1-\sigma$ uncertainty of the hotspot separation. Fig. 4.1 shows the measured component separations in milliarcseconds for CORALZ J083139+460800 from March 2000 to March 2008, with the vertical bars indicating the $1-\sigma$ uncertainties. The data are in excellent agreement with a linear expansion.

The solid line in Fig. 4.1 is the result of a linear least-squares fit to the data, with a slope of 16 ± 3 microarcseconds per year, corresponding to a lobe-to-lobe, projected expansion rate of $0.095 \pm 0.020 h^{-1} c = 0.136 \pm 0.029 c$ at this redshift ($z = 0.127$). It is the lowest expansion speed measured in any GPS radio source so far, supporting the dependence of the expansion speeds of young radio sources on their radio luminosities. The projected expansion speed of $v_{exp} = 0.136 \pm 0.029 c$, together with the measured projected hotspot separation of 4.4 milliarcseconds, corresponding to 33 light years, yields a dynamical age for CORALZ J083139+460800 of 245 ± 55 years. This confirms that CORALZ J083139+460800 is a genuinely young radio source, with an age similar to those found for other compact symmetric objects (e.g. Polatidis & Conway 2003).

4.3.2 CORALZ J131739+411545

It is more of a challenge to analyse CORALZ J131739+411545, because of its complicated morphology. Its morphology was originally classified as complex (CX), but considering all data currently available (Fig. 4.5), we now tentatively classify this source as a compact double (CD) radio source. The problem is that the strongest component is not resolved well enough for detailed modelling of its structure, but too extended

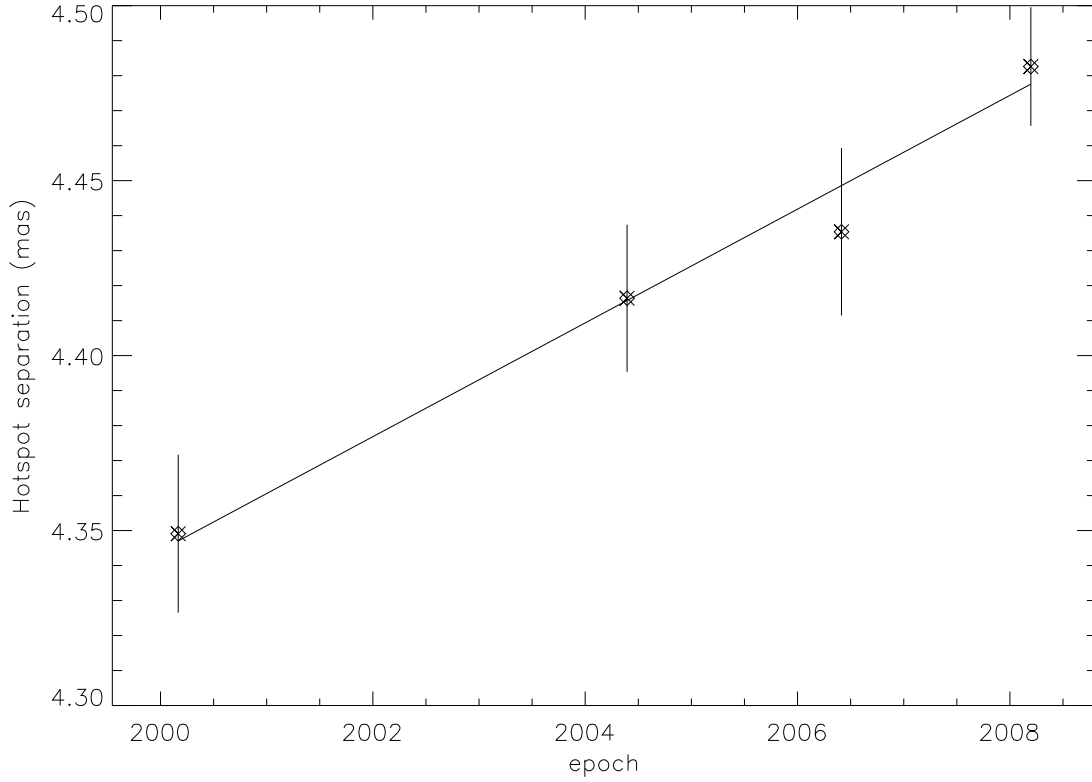


Figure 4.1: — The measured hotspot separations in milliarcseconds for CORALZ J083139+460800 from March 2000 to March 2008, with the vertical bars indicating the 1- σ uncertainties. The solid line is the result of a linear least-squares fit to the data, and has a slope of 16 microarcseconds per year.

to model it as a simple Gaussian component. Furthermore it is located relatively close to the second component, making the construction of a reliable radio map and the measurement of the component positions a challenging effort. For this source JMFIT was run on each of the two components separately, because otherwise the residuals of the strongest component made the solution for the second component diverge. The derived errors are crude estimates. On the one hand they are overestimated because we estimate the center of the components much more accurately than the values of σ_{rms} indicate, because these are dominated by symmetric residuals on either side of the component. On the other hand the errors might be underestimated, because the error estimates do not include possible biases introduced during the synthesis of the map, which might particularly arise in sources with a complex structure like this.

In table 4.2 the measured component separations for CORALZ J131739+411545 are presented, with in Col. 1 the observation date, in Col. 2 the

Table 4.2: — Hotspot separation measurements and error estimates of CORALZ J131739+411545.

observation date	$\sigma_{rms,a}$ (mJy)	$\sigma_{rms,b}$ (mJy)	separation (mas)	$\sigma_{separation}$ (mas)
2000 March 2	2.11	0.47	3.320	0.051
2004 May 24	1.79	0.33	3.265	0.046
2008 March 13	2.05	0.14	3.466	0.065

post-fit r.m.s. error of the subimage containing the strongest component, in Col. 3 the post-fit r.m.s. error of the subimage of the second component, in Col. 4 the measured hotspot separation in milliarcseconds, and in Col. 5 the $1-\sigma$ uncertainty of the hotspot separation. Fig. 4.2 shows the measured hotspot separations in milliarcseconds for CORALZ J131739+411545 from March 2000 to March 2008, with the vertical bars indicating the $1-\sigma$ uncertainties. From this figure the error estimates appear reasonable. We perform a linear least-squares fit to the data, resulting in a slope of 14 ± 10 microarcseconds per year, which corresponds to a $1-\sigma$ upper limit to the projected expansion rate of $0.074h^{-1}c = 0.106c$ at a redshift of $z = 0.066$ for CORALZ J131739+411545. This limit, together with the measured projected hotspot separation of 3.3 milliarcseconds, corresponding to 14 light years, yields a lower limit to the dynamical age of CORALZ J131739+411545 of 130 years. This result is in good agreement with the upper limit of 4300 years, derived from the spectral ageing analysis of CORALZ J131739+411545 (Mack et al. 2009).

4.3.3 Expansion velocity and radio power

The new results described above significantly increase the sparsely available data on expansion velocities of young radio sources. It is therefore important to review the correlation between expansion speed and luminosity found by de Vries et al. (2009). The expansion speed we determine here for CORALZ J083139+460800, exceeds the previously derived upper limit, but is still the lowest expansion speed measured in any GPS radio source so far. Being a relatively weak radio source ($L_{5\text{GHz}} = 10^{41.3}$ erg/s, compared to a median radio luminosity of $L_{5\text{GHz}} = 10^{43.2}$ erg/s for sources with previously determined expansion speeds), this result supports the correlation between the expansion speed and radio luminosity. Further support comes from CORALZ J131739+411545 ($L_{5\text{GHz}} = 10^{41.1}$ erg/s), with an upper limit to the expansion speed lower

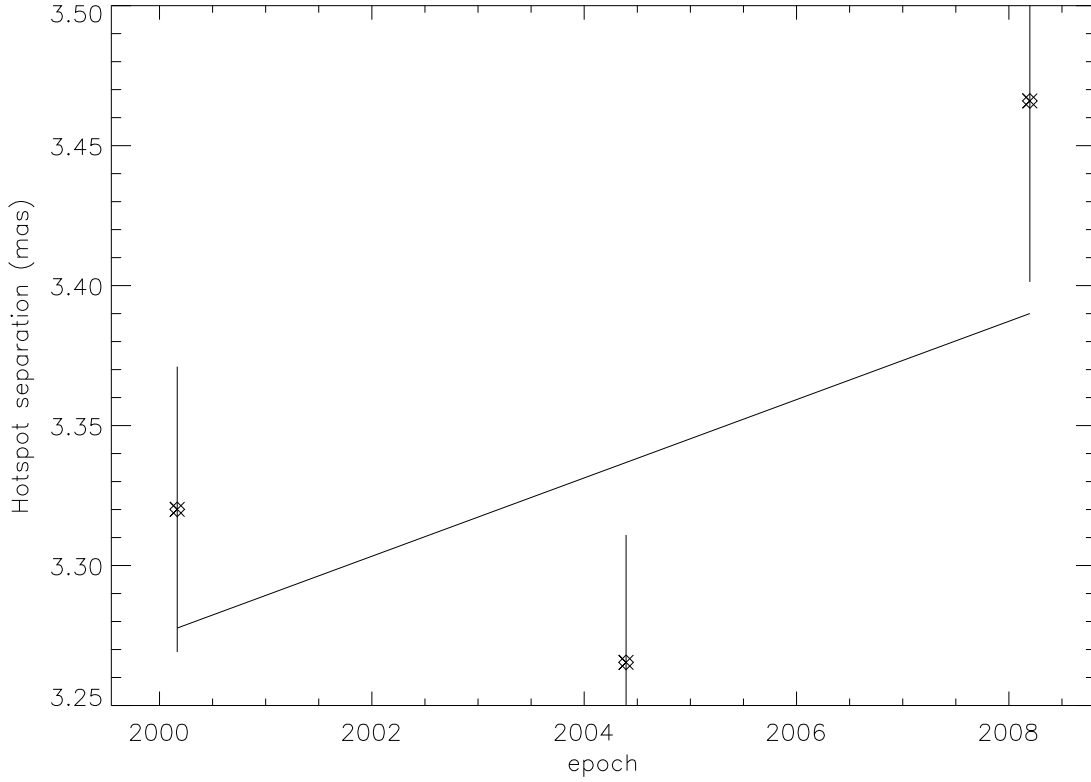


Figure 4.2: — The measured hotspot separations in milliarcseconds for CORALZ J131739+411545 from March 2000 to March 2008, with the vertical bars indicating the 1- σ uncertainties. The solid line is the result of a linear least-squares fit to the data, and has a slope of 14 ± 10 microarcseconds per year.

than the value found for any radio source with a higher radio luminosity.

In Fig. 4.3 we show the expansion velocities measured in young radio sources as a function of radio luminosity. Both the radio luminosity and the lobe-to-lobe, projected expansion velocity have been corrected for cosmological effects, and represent rest-frame quantities. The arrows indicate upper limits. The one indicated with the cross is the upper limit to the expansion velocity of CORALZ J131739+411545 presented in this chapter. In de Vries et al. (2009) we presented an analytic model of a young, expanding radio source with a constant jet power in a power-law density environment. This model predicts that $v_{\text{exp}} \propto L_{\text{radio}}^{1/3}$. The solid line represents such a relation, with arbitrary scaling. The dashed line represents this relation scaled down by a factor of $\sqrt{1 - 0.9^2} \simeq 0.44$, such that 90% of a sample of randomly oriented sources that intrinsically would follow the solid line, should be located above the dashed line. A Spearman rank correlation analysis shows that, including the measured

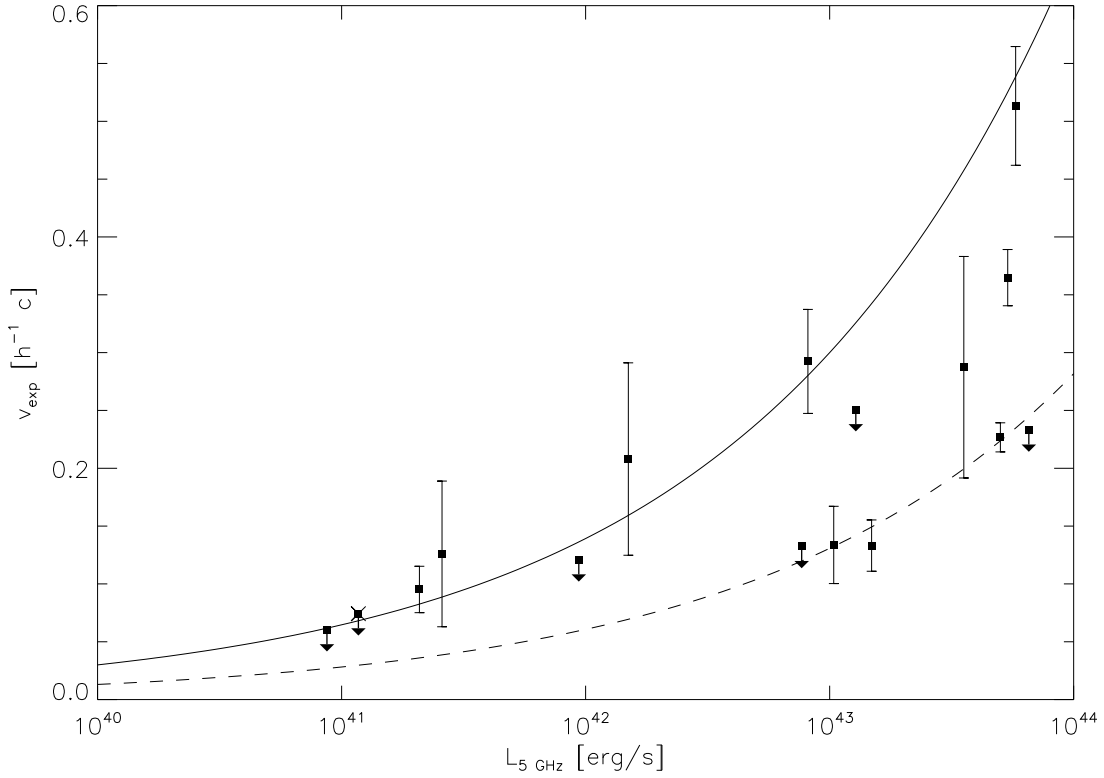
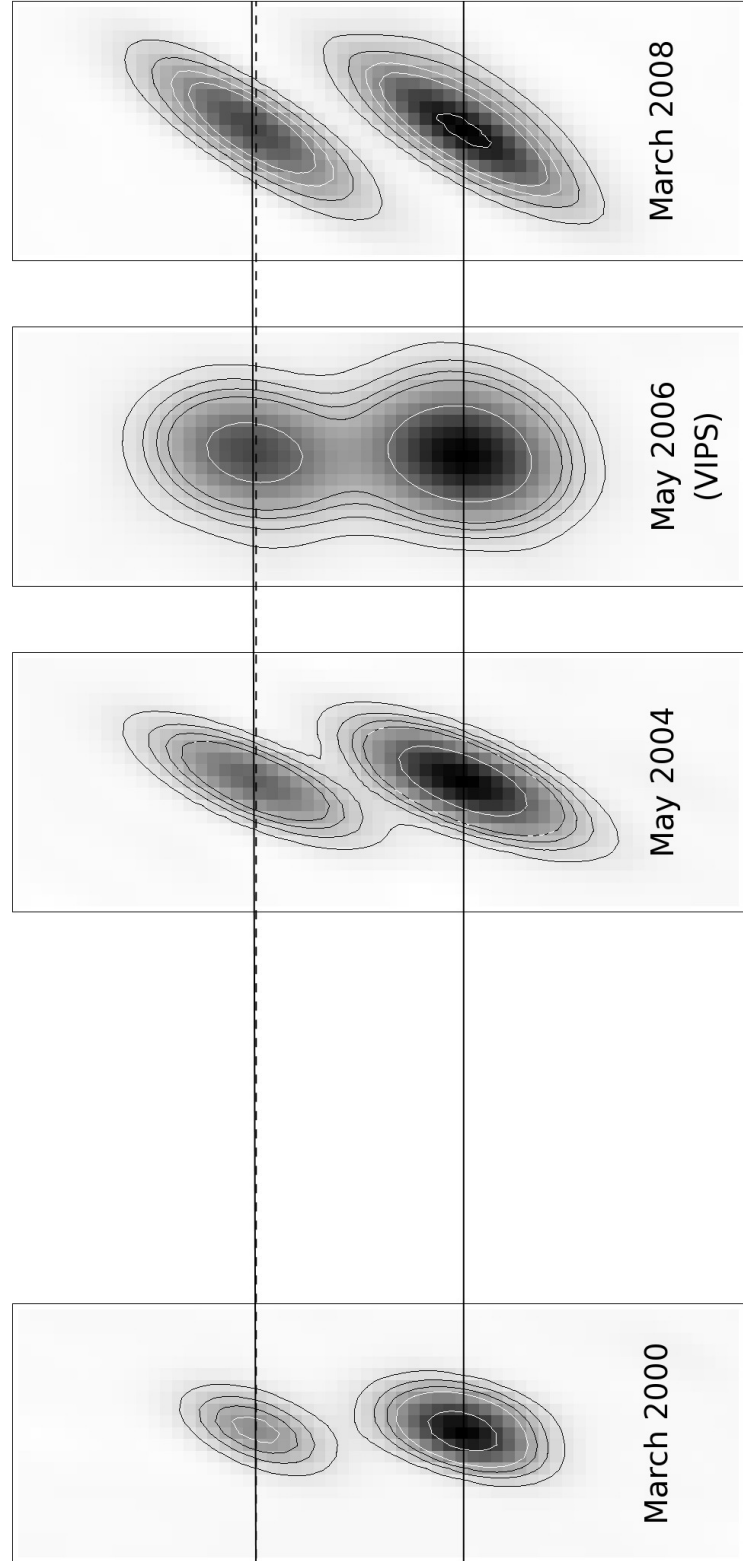


Figure 4.3: — Expansion velocities of compact symmetric objects in units of $h^{-1} c$, and radio luminosities at 5 GHz in erg s^{-1} . Arrows indicate upper limits. The one indicated with the cross is the upper limit to the expansion velocity of CORALZ J131739+411545 presented in this chapter. The solid line shows the expected relation between expansion velocity and radio luminosity, derived from analytic radio source evolution modelling (de Vries et al. 2009), with arbitrary scaling. The dashed line represents this relation scaled down by a factor of $\sqrt{1 - 0.9^2} \simeq 0.44$, such that 90% of a sample of randomly oriented sources that intrinsically would follow the solid line, should be located above the dashed line.

expansion speed presented in this chapter and ignoring all upper limits, the correlation is significant at a 99% confidence level ($n = 10$, $\rho = 0.794$). Including the upper limits in the statistical analysis tends to increase the significance of the correlation, regardless of the precise way these upper limits are treated, since the upper limits of primarily the low-luminosity radio sources are so stringent. Although it is still too early to draw definite conclusions concerning the deviations of the data from the model, it seems the data indicate a relation less steep than the analytic model, suggesting the density ρ of the radio source environment is shallower than the assumed power-law slope of $\beta = 2$ ($\rho \propto r^{-\beta}$), since the exponent of the radio luminosity L_{radio} in this relation depends on the power-law slope of the environment as $1/(5 - \beta)$ (de Vries et al. 2009).

Figure 4.4 — Contour maps of CORALZ J083139+460800, observed in March 2000, in May 2004, in May 2006 with the VLBA as part of VIPS (Helmboldt et al. 2007), and in March 2008. Peak flux densities of each map are: 31.7, 38.9, 44.4, and 26.8 mJy. The r.m.s. noise levels are: 0.14, 0.14, 0.26, and 0.06 mJy. Contours are drawn at 3, 6, 9, 12, and 24 mJy. All maps have been aligned and rotated, such that the (lower) solid line, running through the main component's center in each map, is (horizontal). The dashed line runs parallel to this line, while the (upper) solid line runs through the secondary component's center in each map. The lines slowly diverge, revealing a small but significant increase in the separation between the two components. This increase corresponds to a projected hotspot separation velocity of $0.095 \pm 0.020h^{-1}c$, yielding a dynamical age of 245 ± 55 years. Note that both components are unresolved, and therefore the varying component shapes arise from a varying clean beam shape, not from changes in the source structure.



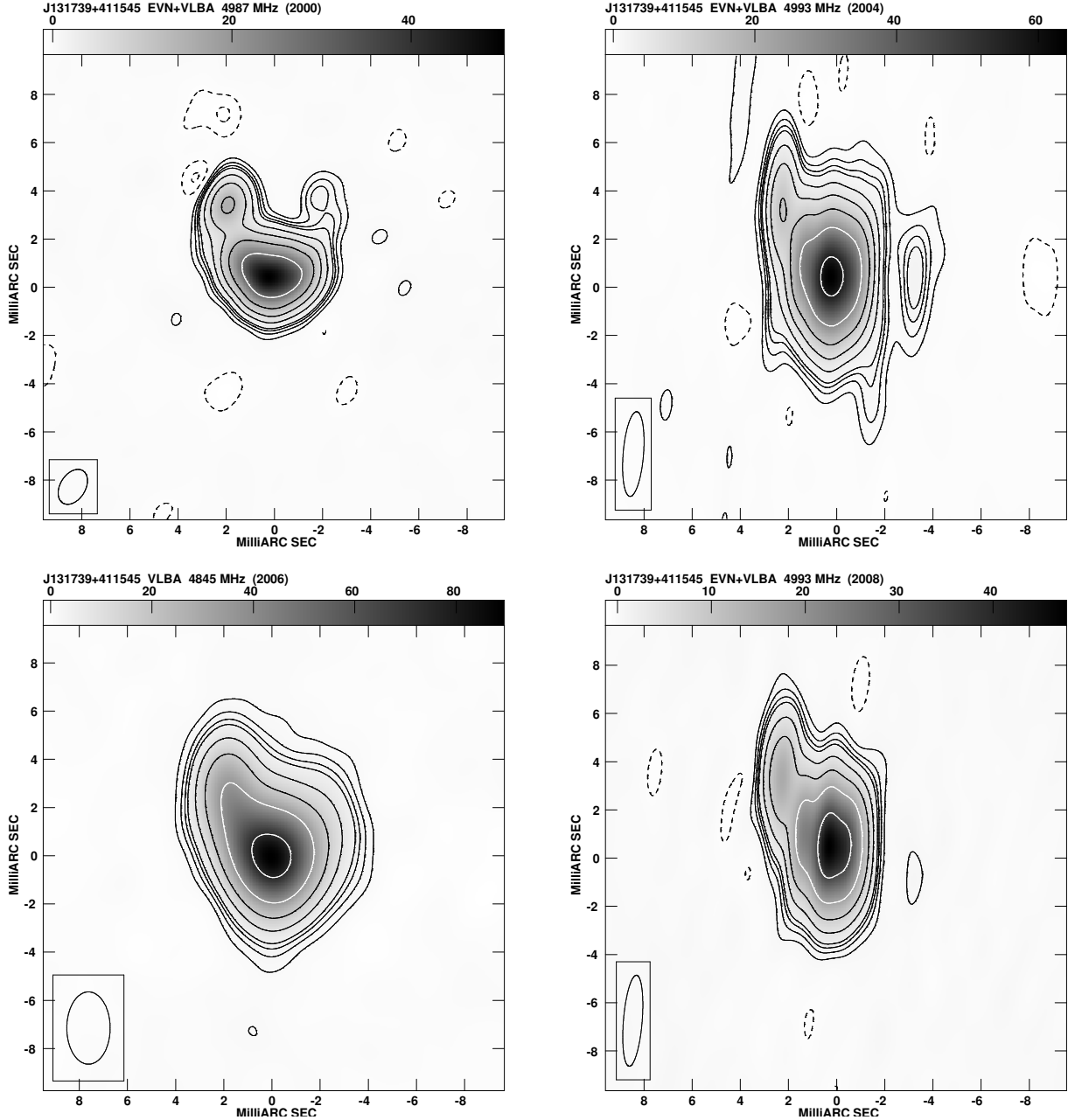


Figure 4.5: — Contour maps of CORALZ J131739+411545, observed in March 2000 (*top left*), in May 2004 (*top right*), in May 2006 with the VLBA as part of VIPS (Helmboldt et al. 2007; *bottom left*), and in March 2008 (*bottom right*). Peak flux densities of each map are: 50.3, 63.8, 89.3, and 47.7 mJy. The r.m.s. noise levels are: 0.14, 0.14, 0.37, and 0.17 mJy. Contours are drawn at (-6, -3, 3, 6, 9, 12, 24, 48, 96, 200, 400, 800, 1600) times the r.m.s. noise level of the radio map. Negative contours are indicated with dashed lines.

4.4 Conclusions

In this chapter we present a new epoch of global VLBI observations of sources from the CORALZ sample. For CORALZ J083139+460800 this resulted in the detection of its projected hotspot separation velocity of

$0.095 \pm 0.020 h^{-1}c$, representing the lowest expansion speed measured so far. This result, together with the measured hotspot separation, yields a dynamical age of 245 ± 55 years. Despite the complicated structure of the double radio source CORALZ J131739+411545, we were able to derive an upper limit to the expansion speed of this source of $0.074 h^{-1}c$, yielding a lower limit for the dynamical age of 130 years. Both expansion speeds are very low compared to CSOs with higher radio luminosities, confirming the dependence of the expansion speeds of young radio sources on their radio luminosities. These new measurements raise the significance of the correlation above 99%, and indicate the slope of this relation might be less steep than our model, suggesting the radio source environments are shallower than $\rho \propto r^{-2}$.

Acknowledgments

The European VLBI Network is a joint facility of European, Chinese, South African and other radio astronomy institutes funded by their national research councils (proposal codes: GS016, GS021, GV019). The National Radio Astronomy Observatory is a facility of the National Science Foundation operated under cooperative agreement by Associated Universities, Inc (proposal codes: GS016, GS021, GV019).

References

- Conway, J. E. 2002, *New Astronomy Review*, 46, 263
 de Vries, N., Snellen, I. A. G., Schilizzi, R. T., Mack, K.-H., & Kaiser, C. R. 2009, *A&A*, 498, 641, Chapter 3
 Fanti, R., Fanti, C., Schilizzi, R. T., Spencer, R. E., Nan Rendong, Parma, P., van Breugel, W. J. M., & Venturi, T. 1990, *A&A*, 231, 333
 Fanti, C., & Fanti, R. 2003, *Radio Astronomy at the Fringe*, ed. J. A. Zensus, M. H. Cohen, & E. Ros, 300, 81
 Fomalont, E. B. 1999, *Synthesis Imaging in Radio Astronomy II*, 180, 301
 Helmboldt, J. F., et al. 2007, *ApJ*, 658, 203
 Komatsu, E., et al. 2009, *ApJS*, 180, 330
 Mack, K.-H., Snellen, I. A. G., Schilizzi, R. T., & de Vries, N. 2009, *Astronomische Nachrichten*, 330, 217
 McMahon R. G., Irwin M. J., 1991, in *Proceedings of the conference on 'Digitised Optical Sky Surveys*, eds. H. T. MacGillivray, E. B. Thomson (Kluwer Acad. Publ., Dordrecht), p. 417
 O'Dea, C. P. & Baum, S. A. 1996, in *GPS and CSS radio sources*, ed. I. A. G. Snellen, R. T. Schilizzi, H. J. A. Röttgering & M. N. Bremer, 241
 O'Dea, C. P. 1998, *PASP*, 110, 493
 Owsianik, I., & Conway, J. E. 1998, *A&A*, 337, 69
 Peacock, J. A., & Wall, J. V. 1982, *MNRAS*, 198, 843
 Polatidis, A. G., & Conway, J. E. 2003, *Publications of the Astronomical Society of Australia*, 20, 69

- Readhead, A. C. S., Taylor, G. B., Xu, W., Pearson, T. J., Wilkinson, P. N., & Polatidis, A. G. 1996, *ApJ*, 460, 612
- Snellen, I. A. G., Schilizzi, R. T., Miley, G. K., de Bruyn, A. G., Bremer, M. N., Röttgering, H. J. A. 2000, *MNRAS*, 319, 445
- Snellen, I. A. G., Mack, K.-H., Schilizzi, R. T., & Tschager, W. 2003, *Publications of the Astronomical Society of Australia*, 20, 38
- Snellen, I. A. G., Mack, K.-H., Schilizzi, R. T., & Tschager, W. 2004, *MNRAS*, 348, 227
- White, R. L., Becker, R. H., Helfand, D. J., & Gregg, M. D. 1997, *ApJ*, 475, 479
- Wilkinson, P. N., Polatidis, A. G., Readhead, A. C. S., Xu, W., & Pearson, T. J. 1994, *ApJ*, 432, L87

Chapter 5

Infrared properties of radio sources in the Boötes field: evidence for evolution of the dust-torus over AGN-lifetime

Abstract. Active galactic nuclei (AGN) can have a wide range of observational characteristics. However, the precise relation between the many different classes of AGN remains unclear. In particular, orientation based unification scenarios so far fail to explain the differences between radio-quiet and radio-loud AGN. Recently the idea emerged that low-luminosity radio AGN and optical AGN have different accretion modes. Additionally, the temporal evolution of individual AGN may also play an important role in AGN unification. In this chapter we investigate the evolution of radio-loud AGN in the context of current unification theories, by determining whether radio sources have (cold) circumnuclear tori, or whether they are fueled by (hot) Bondi accretion through cooling flows. We exploited the large data sets available for the 9 deg² Boötes field, in particular deep multi-frequency radio observations obtained with the WSRT and NRAO's VLA, the optical NOAO Deep Wide-Field Survey, the near-infrared FLAMINGOS Extragalactic Survey and Spitzer Deep Wide-Field Survey, and mid-infrared MIPS observations from the Spitzer Space Telescope. For a sample of 334 radio sources down to $S_{325\text{ MHz}} > 0.75$ mJy the photometric redshifts and stellar masses were determined from the optical and near-infrared data. Radio source angular sizes were determined from the 325 MHz data, and converted to projected linear size using the photometric redshifts. These were subsequently used as a proxy for radio source age. Finally, the sample was positionally matched to the mid-infrared 24 μm catalog. We detect a significant decrease of 24 μm detection rate with projected linear source size, while a similar but weaker trend is seen at 8 μm . We suggest this fits an evolution scenario, in which young radio-loud AGN contain a circumnuclear torus, while older AGN consumed most of the circumnuclear material. The results contradict the hypothesis that low-luminosity radio-loud AGN are fueled through Bondi accretion. If the radio size-infrared relation was caused by orientation, we would expect a stronger trend at 8 μm than at 24 μm , while the opposite is seen. We argue that radio AGN may still be powered through cooling flows, but with the accreted material probably settling in a (standard unification theory) disk, and not being continuously replenished.

Infrared properties of radio sources in the Boötes field: evidence for evolution of the dust-torus over AGN-lifetime



ACTIVE galactic nuclei (AGN) can have a wide range of observational characteristics, for example in their emission line properties, in their optical to X-ray continuum emission, in their thermal infrared emission, and in the properties of their radio jets and lobes, if present. Over the years this has led to the definition of an enormous number of AGN classes. The first attempts to link in this wide range of observational phenomena into a single model, involved the orientation of the AGN. These theories are based on a spherically asymmetric AGN model, where the central object is surrounded by a torus of gas and dust, which, when viewed from the side, blocks off the most central part of the AGN, which would be visible from other viewing angles (Antonucci 1984; Barthel 1989). Despite the success of this unification theory many issues remain unresolved. For example it does not explain the relation between radio-loud and radio-quiet AGN, the different radio morphologies, and the differences in optical properties between radio galaxies with low and high radio luminosities.

Inspired by studies of X-ray binaries (XRBs; Fender, Belloni, & Gallo 2004), which also produce radio jets under certain circumstances, the idea emerged that low luminosity radio AGN have a different mode of accretion than optical AGN (Merloni, Heinz, & di Matteo 2003). XRBs with high accretion rates are found to have luminous accretion disks (high-soft state) and do not produce jets, while low accretion rates result in radiatively inefficient accretion flows (low-hard state) and weak jets (Fender, Belloni, & Gallo 2004). Strong radio jets are produced during the transition from the low-hard to the high-soft state. Merloni, Heinz, & di Matteo (2003) suggest the disk-jet systems of AGN are scaled versions of those in XRBs, based on XRBs and AGN sharing a common “Fundamental Plane of black hole activity”, correlating their radio and X-ray luminosity with the mass of the accreting black hole. Körding,

E. G., Jester, S., & Fender (2006) generalize the hardness intensity diagram of XRBs, in which low-hard, high-soft, and intermediate XRBs occupy similar regions to low-luminosity radio AGN, optical quasars, and powerful radio AGN, respectively. Kaiser & Best (2007) estimate that for AGN the transition timescale from the low-hard to the high-soft state would roughly correspond to the lifetime of powerful radio AGN.

In this dual-mode scenario the relevant parameter, causing the differences between several classes of AGN, is argued to be the accretion rate or accretion mode (e.g. Hardcastle, Evans, & Croston 2007; Merloni & Heinz 2008). In this scenario optical (or *quasar-mode*) AGN are expected to be powered by gas rich mergers or disk instabilities, driving large amounts of cold gas to the nucleus, needed to form a radiatively efficient accretion flow surrounded by an extinguishing torus, such as predicted in the original orientation-based unified models. Low luminosity radio AGN (*radio-mode*) on the other hand are expected to be fueled by steady cooling flows of hot gas from the intracluster medium in this scenario, and to have radiatively inefficient accretion flows. Several authors have found results in agreement with this dual-mode scenario (e.g. Best et al. 2005; Tasse et al. 2008; Ogle, Whyson & Antonucci 2006; Hickox et al. 2009).

Another effect, however, may also play an important role in AGN unification, and that is evolution. Since AGN are active for a limited amount of time only, and the observed AGN characteristics are not expected to disappear all at once, different classes of AGN may represent an evolutionary sequence. In this chapter we wish to investigate this possible evolution of AGN in the context of current unification theories, and aim to find out whether (1) radio-loud AGN do have a radiatively efficient accretion disk with circumnuclear gas and dust, and if so (2) whether the torus evolves over the lifetime of the radio source. For this purpose we exploit the wealth of data available for the Boötes field, and study the infrared properties for a sample of 334 radio sources.

We describe the relevant data available for the Boötes field in Sect. 5.1. The relevant properties of the radio sources and their host galaxies are derived from these in Sect. 5.2. In Sect. 5.3 the sample selection is described. The results are presented in Sect. 5.4, discussed in Sect. 5.5, and we conclude with Sect. 5.6. Throughout this chapter we adopt

the cosmological parameters as found by WMAP5 (Komatsu et al. 2009; $H_0 = 70.1 \text{ km s}^{-1} \text{ Mpc}^{-1}$, $\Omega_\Lambda = 0.721$, $\Omega_m = 0.279$).

5.1 Surveys in the Boötes field

The Boötes field is a region of $\sim 9 \text{ deg}^2$, centered at approximately $14^h 32^m 06^s + 34^\circ 16' 47''$ (J2000), located at high Galactic and ecliptic latitude in the constellation of Boötes. In this section we briefly describe the available data for the Boötes field that are relevant to our study of the mid-infrared properties of radio-loud AGN. We describe the deep radio observations in Sect. 5.1.1. In the next section we outline the optical and near-infrared surveys (Sect. 5.1.2) that are used to determine the properties and photometric redshifts of the host galaxies of the radio sources. Finally we describe the available mid-infrared data (Sect. 5.1.3) for studying the thermal emission from dust around AGN.

5.1.1 Radio observations

Our sample is based on the 1.4 GHz and 325 MHz observations of the Boötes field. At 1.4 GHz a region of $\sim 7 \text{ deg}^2$ of this field has been observed with the Westerbork Synthesis Radio Telescope (WSRT). From these deep observations 3172 radio sources were detected down to a 5σ detection threshold of $140 \mu\text{Jy}$ (de Vries et al. 2002). Most of these sources are unresolved by the $13'' \times 27''$ restored beam. A region of 4.9 deg^2 within the Boötes field, completely overlapped by the WSRT 1.4 GHz observations, has also been observed with the Very Large Array (VLA) in A-configuration at 325 MHz. The resulting map has an angular resolution of $5''$ FWHM (Croft et al., in preparation). Using a 5σ detection threshold of 0.75 mJy , 652 radio sources are detected at 325 MHz. Since we required the $5''$ resolution 325 MHz data to measure the angular sizes for most sources, our sample is based on the 652 radio sources detected at both 325 MHz and 1.4 GHz. As described in Sect. 5.2.2, all these sources were examined by eye, to check the results of the automated source component association routine used to generate the 1.4 GHz catalog. This resulted in a radio catalog containing 613 distinct sources. Although the 1.4 GHz WSRT catalog reaches much lower flux densities, and contains many more sources, we will use this radio cata-

log of 613 sources also detected at 325 MHz as the basis for our sample selection (Sect. 5.3), because we need the $5''$ resolution of the 325 MHz VLA map to measure the angular sizes that are vital for this study.

We will also make use of the deep 150 MHz radio map of the Boötes field (Intema et al. 2009). With a resolution of $26'' \times 22''$, a region of about 11.3 deg^2 , fully covering the NDWFS Boötes field, is imaged down to a noise level of $\sim 1 \text{ mJy beam}^{-1}$. These low frequency observations form an important complementary dataset, to trace the extended structure of steep spectrum radio sources.

5.1.2 Optical and near-infrared surveys

The Boötes field was initially selected for observation as one of the two 9 deg^2 regions of the NOAO Deep Wide-Field Survey (NDWFS; Jannuzi & Dey 1999). The NDWFS is a deep optical photometric survey (B_W , R , and I). The near-infrared surveys FLAMEX (FLAMINGOS Extragalactic Survey; Elston et al. 2006) and ISS (IRAC Shallow Survey; Eisenhardt et al 2004) were performed, complementing the optical data for the calculation of reliable photometric redshifts.

An aperture of $5''$ was used for all optical and near-infrared photometry, because this matches the ISS resolution better, allowing an unbiased derivation of photometric redshifts (Sect. 5.2.5). With this aperture the limiting magnitudes of the NDWFS are $B_W = 25.3$, $R = 24.1$, and $I = 23.6$ (Vega). FLAMEX provides J and K_S mosaics of 4.7 deg^2 of the NDWFS Boötes field down to $K_S = 19.4$ (Vega). The ISS covered 8.5 deg^2 of the NDWFS field, and reaches limiting magnitudes of 18.6, 17.8, 15.4, and 14.9 (Vega) at 3.6, 4.5, 5.8, and $8.0 \mu\text{m}$, respectively. The ISS field has since been reimaged three times to the same depth as the initial ISS, allowing studies of variability. The total dataset is publicly available as the Spitzer Deep Wide-Field Survey (SDWFS; Ashby et al. 2009), including co-adds of the four epochs, significantly improving the sensitivity relative to the ISS (see table 5.1).

5.1.3 Mid-infrared survey

The radio catalog was positionally matched to the mid-infrared MIPS Boötes survey (Jannuzi et al., in preparation). This survey was conducted with the Multiband Imaging Photometer for Spitzer (MIPS), us-

Table 5.1: — SDWFS limiting magnitudes (Vega) and number of sources in the catalog for each of the four IRAC channels. The limiting magnitudes of the ISS are indicated for comparison.

Wavelength	m_{lim} (ISS)	m_{lim} (SDWFS)	Sources
3.6 μm	18.6	19.77	677,522
4.5 μm	17.8	18.83	523,350
5.8 μm	15.4	16.50	120,259
8.0 μm	14.9	15.85	96,176

ing each of its three photometric bands. At 24 μm , a detection limit of 0.3 mJy is reached, with a resolution of 6". Using a matching radius of 5", 24 μm counterparts to our radio catalog were identified. Since the survey depth is far from the confusion limit, the probability of spurious matches is negligible. The MIPS Boötes catalog contains 28391 sources detected at 24 μm . In the radio catalog 38% (235 out of 613) of the sources have a detected counterpart at 24 μm .

5.2 Properties of the radio sources

For each source in the radio catalog we measured the largest angular size of the radio source (Sect. 5.2.2), and determined the position of the central compact component, assumed to be the radio core (Sect. 5.2.3). The radio core positions are used to identify the host galaxies of the radio sources in the optical and near-infrared images (Sect. 5.2.4). The photometric data on the optical counterparts are used to derive stellar masses and photometric redshifts of the host galaxies (Sect. 5.2.5), and to subsequently deduce projected linear radio source sizes and radio luminosities (Sect. 5.2.6).

5.2.1 Visual examination

Because of the great depth, combined with the relatively large beam size, the WSRT 1.4 GHz map has a high source density and is very crowded. This makes it particularly difficult to produce a reliable source list from the list of individually detected source components. It was therefore no real surprise that many pairs of detections, listed as one radio source in the 1.4 GHz radio catalog, proved to be unassociated after examination in the VLA map. Therefore all 652 radio sources detected at both 1.4 GHz and 325 MHz were examined by eye to decide which components

are associated and make up double, triple, or more complicated sources. If this was for some reason difficult, we took advantage of the available SDWFS $3.6 \mu\text{m}$ image. If there were no IR counterparts at the positions of the islands, but instead an IR counterpart was found somewhere in between the islands, with a reasonable arm-length ratio and opening angle, we assumed the islands to be associated, together making up a double radio source hosted by this specific IR counterpart. If no obvious host galaxy was found in between the islands, but each radio island was located at the same position of a $3.6 \mu\text{m}$ source instead, we assumed each radio island to be a separate radio source, hosted by their corresponding $3.6 \mu\text{m}$ counterparts. Although the source density in the SDWFS $3.6 \mu\text{m}$ image is quite high, this simple prescription led to a clear solution in virtually all cases.

5.2.2 Angular size

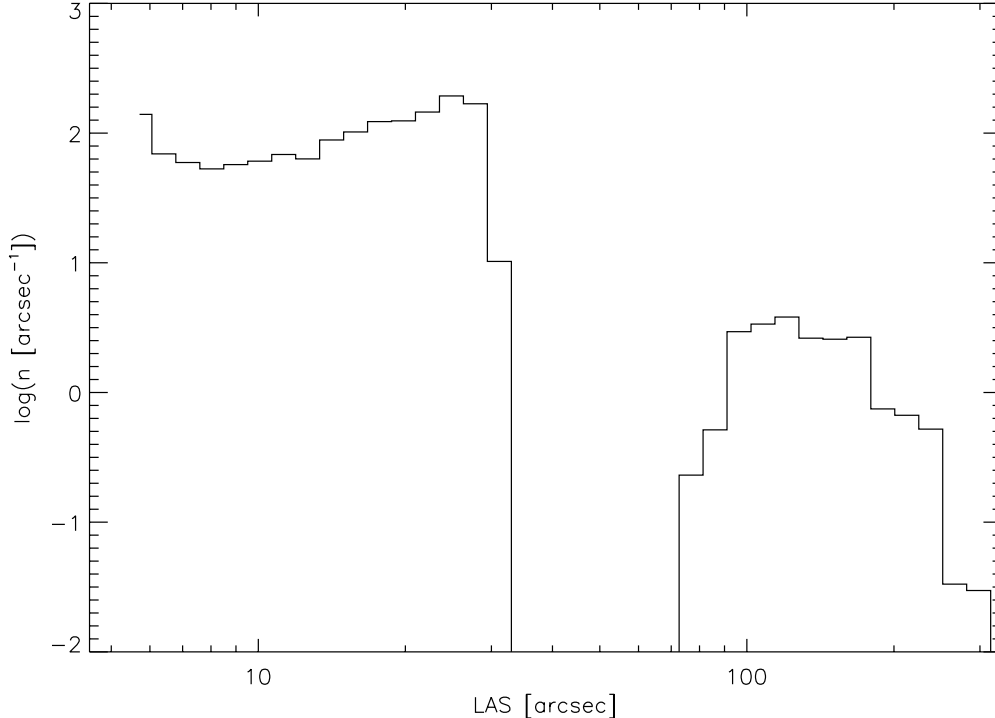


Figure 5.1: — Angular size distribution of the 3172 radio sources in the 1.4 GHz WSRT catalog (de Vries et al. 2002), shown here for comparison. The 1.4 GHz radio map was restored with a beam of $13'' \times 27''$. This distribution indicates the need for more accurate LAS measurements, using the high-resolution VLA 325 MHz radio map.

The 1.4 GHz catalog (de Vries et al. 2002), which is publicly available through anonymous ftp¹, includes measurements of the largest angular size (LAS) of each radio source. These were derived using automated routines, originally developed for the Westerbork Northern Sky Survey (WENSS), described in detail by Rengelink et al. (1997). To indicate that the LAS measurements from the WSRT 1.4 GHz map are of insufficient quality for our analyses, we show the distribution of the LAS of all 3172 radio sources in the 1.4 GHz WSRT catalog in Fig. 5.1. It shows a clear bimodal distribution. The vacuous region between 25'' and 70'' is caused by a difference in treatment of islands of radio emission with one local maximum only, and islands with multiple local maxima. Angular sizes of islands with multiple components are derived from the deconvolved components. However, for islands with only one local maximum, angular sizes are estimated using a formula based solely on the SNR, not on the actual structure of the source (de Vries et al. 2002). In addition, the 1.4 GHz radio map, restored with a beam of 13'' \times 27'', has a much poorer resolution than the VLA 325 MHz map, which we will use.

To characterize the structure of the radio sources we have applied the Blob Detection and Source Measurement (BDSM) source extraction program² on the 325 MHz radio map. BDSM is a software package currently being developed for the LOFAR project. It identifies islands of contiguous emission, and fits multiple Gaussians to each island (after convolving the Gaussians with the beam of the radio map). We used the default values of 5σ and 3σ for the initial pixel threshold and for the threshold for the contiguous pixels, respectively.

The largest angular size (LAS) of each radio source was subsequently measured between the (FWHM) outer edges of the two outermost Gaussians. For a few sources we found extended structure with low surface brightness, sometimes only detected at low frequencies in the 150 MHz map (e.g. J142923+352851, Fig. 5.11), or in the very deep 1.4 GHz map (e.g. J142842+342445, Fig. 5.11), but clearly associated with a detected radio source in its vicinity. In these cases we measured the largest angular size manually. For radio sources characterized with only one Gaussian the angular size of the radio source was estimated using the decon-

¹ftp://ftp.nfra.nl/pub/Bootes

²version 2.1, available through <http://www.strw.leidenuniv.nl/~mohan/anaamika>

volved major axis of that Gaussian.

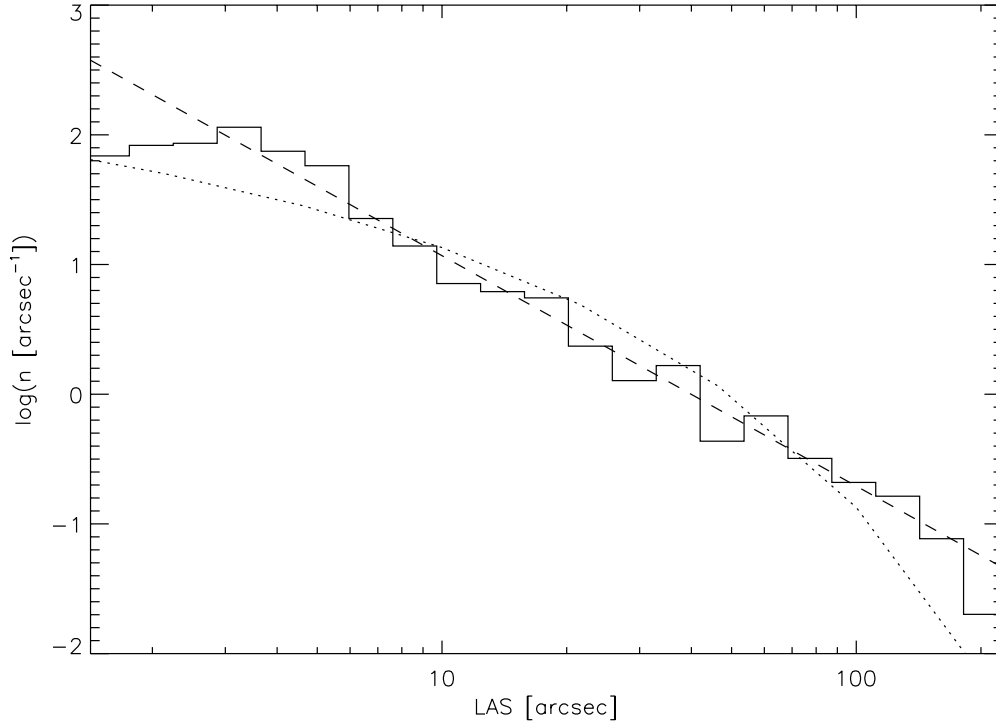


Figure 5.2: — Distribution of the measured angular sizes for the 613 radio sources in the Boötes field detected at 325 MHz. The error bars indicate 1σ Poissonian errors. The CLEAN beam of the 325 MHz radio map has a FWHM of $5''$, indicated with the vertical dashed line. The dotted line corresponds to the distribution function of Windhorst et al. (1990), the dashed line is a linear fit to the distribution in log-log space.

In Fig. 5.2 we show the distribution of the angular sizes we determined for the 613 radio sources in the Boötes field detected at 325 MHz. The vertical axis shows the number of radio sources in each LAS bin, divided by the bin size. The error bars indicate 1σ Poissonian errors. The CLEAN beam of the 325 MHz radio map has a FWHM of $5''$, indicated with the vertical dashed line, causing the distribution to turn over below a few arcseconds. The dotted line corresponds to the distribution function as described by Windhorst et al. (1990):

$$h(\theta) = \frac{N(> \theta)}{N_{\text{total}}} = \exp [-\ln 2 (\theta/\theta_{\text{med}})^{0.62}] \quad (5.1)$$

where $N(> \theta)$ is the number of sources with LAS greater than θ , N_{total} is the total number of sources, and θ_{med} is the median LAS of the sample. The dashed line is a linear least-squares fit to the distribution in

log-log space, excluding angular sizes smaller than $5''$. It has a slope of -1.76 ± 0.04 , meaning that the LAS density function (the number of radio sources in each LAS bin, divided by the bin size in arcseconds) n scales as:

$$n = \frac{dN(< \theta)}{d\theta} \propto \theta^{-1.76}, \quad (5.2)$$

where $N(< \theta)$ is the number of radio sources with LAS less than θ . The distribution of the measured angular sizes generally agrees very well with the prediction from the Windhorst relation. The deviations from the distribution below a size of $\sim 5''$ are due to the resolution of the 325 MHz map. Discrepancies at the highest LAS bins can be attributed to small-number statistics.

5.2.3 Radio positions

We used the radio positions from the 1.4 GHz catalog. However, the simple flux-weighted average positions presented in the 1.4 GHz catalog do not have the accuracy to be matched with optical/IR catalogs, especially in the case of radio sources with arcminute-scale sizes. Therefore, during the process of visually inspecting the component associations, we also refined the radio positions. For each extended source for which we identified a radio core or a $3.6 \mu\text{m}$ identification (see Sect. 5.2.1), we used the position of these when matching with other catalogs.

5.2.4 Host galaxies

All radio sources in the catalog were positionally matched with the SD-WFS+NDWFS catalog (version 0.1; Brodwin & Brown in preparation). This catalog was produced using SExtractor on the full-depth NDWFS and SDWFS (Ashby et al. 2009) mosaics, selecting at $4.5 \mu\text{m}$ and photometry in all bands.

We used the likelihood ratio (LR) method as described by Sutherland & Saunders (1992), which is based on earlier versions (Richter 1975; de Ruiter, Willis & Arp 1977; Prestage & Peacock 1983; Wolstencroft et al. 1986), but incorporates the a priori probability that a radio source has no detected optical counterpart and deals with the identification reliability of multiple candidates in a self-consistent way. The likelihood ratio LR

is defined by

$$LR(r, m_{\text{lim}}) = \frac{\theta(m_{\text{lim}}) \exp(-r^2/2)}{2\pi\sigma_\alpha\sigma_\delta\rho(m_{\text{lim}})}, \quad (5.3)$$

where $\theta(m_{\text{lim}})$ is the *a priori* probability that a radio source has a detected optical counterpart with magnitude $m < m_{\text{lim}}$, $\rho(m_{\text{lim}})$ is the surface number density of galaxies with magnitude $m < m_{\text{lim}}$, and σ_α and σ_δ are the positional uncertainties (the quadratic sum of the uncertainties in the optical and radio positions) for right ascension and declination, respectively. The uncertainty-normalized angular distance r between the radio core and the optical host candidate is defined as

$$r = \sqrt{(\Delta_\alpha/\sigma_\alpha)^2 + (\Delta_\delta/\sigma_\delta)^2}, \quad (5.4)$$

with Δ_α and Δ_δ the positional differences between the radio source and the optical candidate in right ascension and declination, respectively. Using this technique, the expected number of true identifications can now be calculated by summing the identification probabilities of all prime candidates. This way we found that for 545 out of the 613 radio sources (89%) the prime identification candidate is the true optical counterpart, brighter than the 5σ limiting magnitude of the SDWFS $4.5 \mu\text{m}$ image of $m_{\text{lim}} = 19.12$. Adopting a LR cutoff of 0.5, host galaxies are identified for 537 out of the 613 radio sources, with a completeness of 97% and a reliability of 99%. A LR cutoff of 1.0 would result in 520 identifications, a completeness of 94%, and a reliability of 99%.

For sources with large angular sizes identifications might be more uncertain than for more compact objects. To show that this effect is only marginal, we present image cutouts for identified radio galaxies with angular sizes larger than one arcminute in Fig. 5.11. For each radio source six panels are shown, to provide the reader with all relevant information (325 MHz VLA map, SDWFS $3.6 \mu\text{m}$, $4.5 \mu\text{m}$, and $8.0 \mu\text{m}$, with 150 MHz, 325 MHz, and 1380 MHz contours overlaid). Careful inspection shows that identifying the host galaxy is quite obvious for most sources, with some uncertainty about the true host in only two out of twelve cases (17%, J143223+332852 and J143653+341657). There is another galaxy located between the two radio lobes of J143223+332852, but at a more unusual arm-length ratio. For J143653+341657, although its arm-length ratio is somewhat unusual, we assume this galaxy to be the radio source

host, because it basically is the only candidate. Since there are no other $24\ \mu\text{m}$ detections in the area, identifying the radio source with a different galaxy could only strengthen the results described in Sect. 5.4.1.

We note that in the image cutouts of some radio sources a second (unrelated) radio source is visible (J142759+345513, J142842+342445, J142911+332637, J143223+332852). Naturally, the secondary sources were not included as components of the main sources in the LAS measurement.

5.2.5 Photometric redshifts and stellar masses

We use the photometric redshifts of galaxies in the Boötes field derived by Brodwin et al. (2006) using a hybrid algorithm incorporating neural-net and template-fitting techniques. The photometric redshifts are based on the available NDWFS+FLAMEX+ISS photometry from B_W -band to $4.5\ \mu\text{m}$. Using the same broadband photometry, stellar masses of the radio host galaxies were estimated with the IDL code `kcorrect` (version v4.1.4; Blanton et al. 2003; Blanton & Roweis 2007). This IDL code fits a superposition of a few carefully chosen spectral energy distribution (SED) models to the galaxy photometry. The SED models used by `kcorrect` are based on the Bruzual-Charlot stellar evolution synthesis code (Bruzual & Charlot 2003). The `kcorrect` SED fits are also used for an independent goodness-of-fit analysis of the photometric redshifts.

In Fig. 5.3 we show the photometric redshift distribution of the 334 radio sources in the Boötes field with reliable optical identification, and a photometric redshift estimate based on at least four photometric detections, with a reduced χ^2 of the template fit less than 2.0. The hashed bars indicate the redshift distribution of those radio sources detected at $24\ \mu\text{m}$. Although the redshift distribution falls off steeply beyond $z \sim 1$, still a significant number of radio sources have photometric redshift estimates $z > 1.2$. These estimates are very uncertain, because beyond this redshift the peak of the stellar continuum at $1.6\ \mu\text{m}$ shifts out of the photometric bands used for SED fitting. This means that any monotonically increasing SED will be pushed out to $z > 1.2$ and be poorly constrained beyond this redshift. Furthermore the spectroscopic data, used to calibrate and verify the photometric redshifts, go out to $z = 1.2$ (Brodwin et al. 2006). Also indicated in this figure is a (scaled) model redshift distribution (dotted histogram), which is based on the SKA Simulated Skies

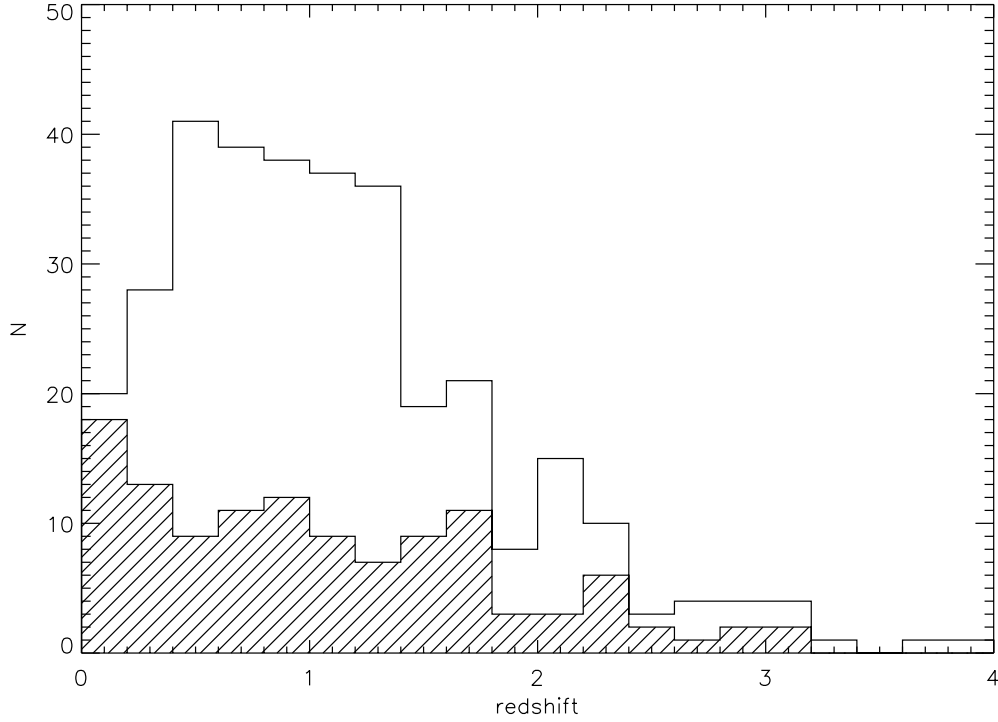


Figure 5.3: — Photometric redshift distribution of the 334 radio sources in the Boötes field with reliable optical identification, and a photometric redshift estimate based on at least four photometric detections, with a reduced χ^2 of the template fit less than 2.0. The hashed bars indicate the redshift distribution of those radio sources detected at $24\ \mu\text{m}$. The dotted histogram indicates the modeled redshift distribution (scaled).

(S^3), a set of computer simulations of the radio and (sub)millimeter universe³. These simulations were performed as part of the Square Kilometer Array Design Studies (SKADS), primarily with the aim to aid the preparation of the Square Kilometer Array (SKA). The redshift distribution presented here was obtained by querying the S^3 semi-empirical extragalactic Database (S^3 -SEX; Wilman et al. 2008), using the same flux density criterion as used for the radio source sample presented here ($S_{325\ \text{MHz}} > 0.75\ \text{mJy}$). Comparing the redshift distribution to this model distribution reveals that, besides the uncertainties of the photometric redshift estimates at $z > 1.2$ mentioned above, the sample also starts to suffer from incompleteness not far beyond this redshift. For these reasons we choose to restrict our analyses to the redshift range $z < 1.2$, as described in Sect. 5.3.

In Fig. 5.4 the stellar mass is plotted as a function of redshift. At the

³<http://s-cubed.physics.ox.ac.uk/>

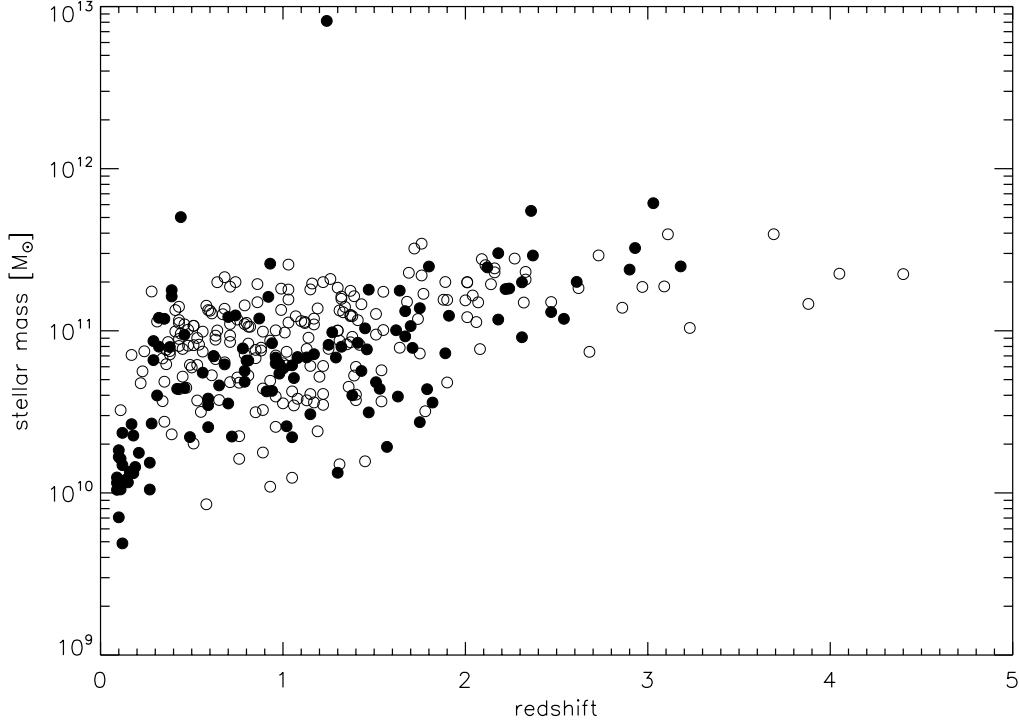


Figure 5.4: — Stellar mass vs. redshift of the 334 identified radio source host galaxies with photometric redshift, based on at least four photometric detections, with a reduced χ^2 of the template fit less than 2.0. Filled circles are radio sources detected at $24\ \mu\text{m}$, and open circles have no detected $24\ \mu\text{m}$ counterpart.

lower left of this plot a number of low-redshift galaxies can be distinguished, all detected at $24\ \mu\text{m}$ and with stellar masses rather low for radio galaxies. These are most likely star-forming galaxies, where both the radio and infrared emission may be due to star formation. For this reason these galaxies will be excluded from our analyses (see Sect. 5.3).

In Fig. 5.5 the distribution of stellar mass is shown, after selecting out the population of star-forming galaxies, with redshift $z < 0.3$ and stellar mass $M_* < 3 \cdot 10^{10}$. The hashed bars again indicate the distribution of the subsample detected at $24\ \mu\text{m}$. The bulk of the radio host galaxies have stellar masses of the order of $10^{11}\ M_\odot$, as expected for radio galaxies. The stellar mass estimate of $10^{13}\ M_\odot$ is probably an outlier with an overestimated photometric redshift.

This figure indicates that the fraction of $24\ \mu\text{m}$ detected radio sources is not correlated with the stellar mass of the host galaxy. Also, after selecting out the star-forming galaxies, the $24\ \mu\text{m}$ detection rate does not depend on redshift for $z < 1.2$. This is important, because the correla-

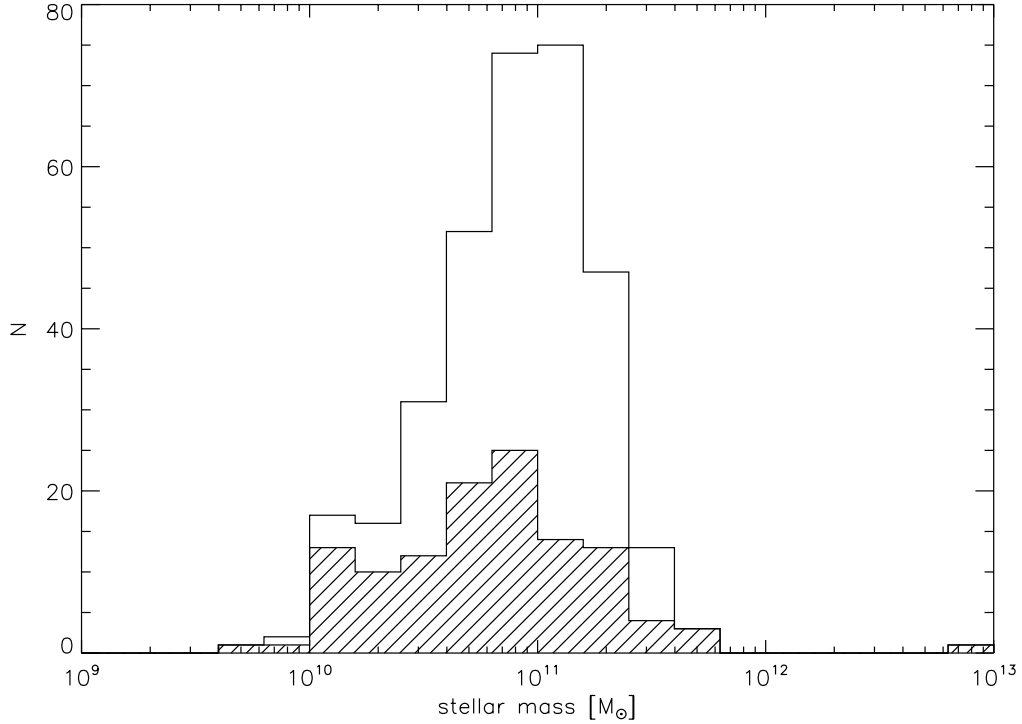


Figure 5.5: — Stellar mass distribution of the 312 identified radio AGN (low-redshift star-forming galaxies excluded) with photometric redshift, based on at least four photometric detections, with a reduced χ^2 of the template fit less than 2.0. The hashed bars indicate the distribution of radio sources detected at $24\ \mu\text{m}$.

tions we study in Sect. 5.4.1 could otherwise be caused via dependencies on stellar mass and redshift.

5.2.6 Radio luminosities and physical sizes

Using the photometric redshifts of the radio source host, flux densities can be converted into luminosities, and angular sizes into physical sizes. In Fig. 5.6 the distribution of 1.4 GHz radio luminosities is shown. The radio luminosity distribution spans a wide range in radio luminosity, but is dominated by radio sources with $10^{24.5}\ \text{W Hz}^{-1} < P_{1.4\ \text{GHz}} < 10^{26}\ \text{W Hz}^{-1}$, the low-luminosity regime of radio-loud AGN.

In Fig. 5.7 we show the distribution of (projected) physical sizes of the radio sources, usually referred to as largest linear sizes (LLSs), in kiloparsecs. The size distribution of these radio galaxies spans a wide range, and we have good number statistics over more than an order of magnitude in LLS. Below about 30 kpc the distribution bends down,

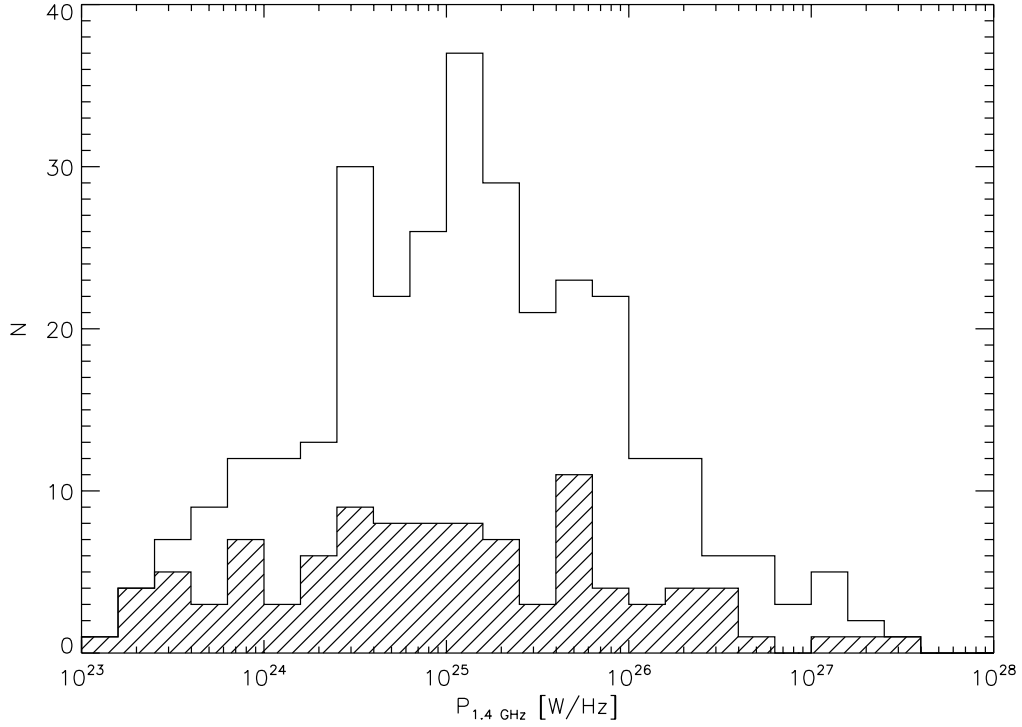


Figure 5.6: — Distribution of 1.4 GHz radio luminosities of the 312 radio galaxies with reliable photometric redshift. The hashed bars indicate the distribution of those sources detected at $24\ \mu\text{m}$.

probably due to resolution effects (the FWHM of the VLA radio map of $5''$ corresponds roughly to 40 kpc at $z = 1$).

5.3 Sample selection

The basis of our sample are the 613 radio sources that are detected to 5σ (0.75 mJy) at 325 MHz. With the smooth LAS distribution presented in Sect. 5.2.2, which is in good agreement with the previously derived LAS distribution of Windhorst et al. (1990), we feel confident that our LAS measurements are reliable. For our analyses we also need reliable optical identifications and photometric redshifts. Therefore we choose to restrict our analysis to radio sources with optical identification candidates with a LR of 0.5 or higher, resulting in a sample of 537 radio galaxies with an identification fraction of 84%, a completeness of 97%, and a reliability of 99%. In order to avoid biases arising from erroneous redshifts, we excluded from our analyses all radio source's hosts detected at fewer than four photometric bands, or with a reduced χ^2 of the template

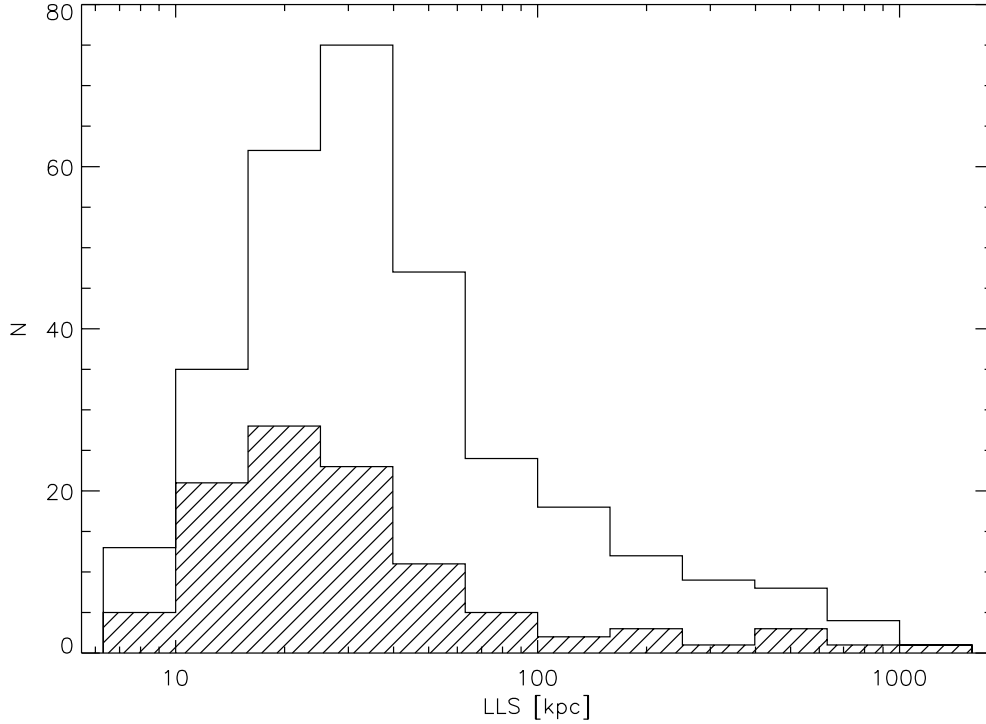


Figure 5.7: — Distribution of LLS (projected physical size) of the 312 radio galaxies with reliable photometric redshift. The hashed bars indicate the LLS distribution of the sources detected at $24\ \mu\text{m}$.

fit greater than 2.0, leaving 334 radio galaxies. We also excluded radio galaxies with photometric redshift estimates $z > 1.2$, because of the uncertainties described in Sect. 5.2.5, and an additional 22 objects that are likely to be star-forming galaxies (see Sect. 5.2.5), leaving a final sample of 203 radio galaxies with reliable optical identification and photometric redshift in the range $0 < z < 1.2$.

5.4 Results

We have selected a sample of radio sources in the Boötes field, for which we identified the host galaxies. The available optical and near-infrared photometry, dominated by stellar light, has been used for photometric redshift estimates. We use the mid-infrared photometry, tracing thermal emission from warm dust, to study the material surrounding the nucleus of radio-loud AGN. We have measured the LAS of each radio source, and converted these to LLSs using the photometric redshifts.

We used the LLS of the radio sources as a proxy of radio source age,

to determine whether the infrared properties of radio sources change over their lifetimes. In Sect. 5.4.1 and Sect. 5.4.2 we present our results concerning the evolution of the mid-infrared emission of radio sources at $24\ \mu\text{m}$ and $8.0\ \mu\text{m}$, respectively, which will be discussed in Sect. 5.5.2. Finally, in Sect. 5.4.3 we present the IRAC colors of those radio sources detected in all four IRAC bands.

5.4.1 Evolution of $24\ \mu\text{m}$ emission

Since the MIPS $24\ \mu\text{m}$ survey of the Boötes field is rather shallow, and only about a third of the radio sources are detected, we cannot analyse the relation between $24\ \mu\text{m}$ luminosity and LLS directly, so we calculate the $24\ \mu\text{m}$ detection rate as a function of LLS instead. The results are presented in Fig. 5.8, with the ordinate showing the fraction of radio sources that are detected at $24\ \mu\text{m}$ in each LLS bin. The vertical bars indicate the 1σ uncertainties corresponding to a binomial distribution. We have selected radio sources with host galaxies in the redshift ranges $0.0 < z < 0.7$ (top) and $0.7 < z < 1.2$ (bottom). We chose two separate ranges in order to limit redshift effects, as well as biases introduced by cosmological evolution.

There is a clear decreasing trend of the detection rate with LLS in both redshift ranges, starting out at about 40% for the smallest, barely resolved radio sources (the FWHM of the VLA 325 MHz radio map of $5''$ corresponds to 30 to 40 kpc in this redshift range), decreasing to about 10% for radio sources larger than 100 kpc. A non-evolving detection rate is rejected at a level of 99.94% and 99.97% for the redshift ranges $0.0 < z < 0.7$ and $0.7 < z < 1.2$, respectively.

5.4.2 Evolution of $8.0\ \mu\text{m}$ emission

The SDWFS $8.0\ \mu\text{m}$ image reaches a much deeper sensitivity than the Boötes $24\ \mu\text{m}$ survey, so we could perform the same analysis on these data, but the Rayleigh-Jeans tail of the stellar continuum will be significant at this wavelength. Therefore we study the $8.0\ \mu\text{m}$ infrared excess, Δ_{IR} , defined as:

$$\Delta_{IR} = \log(F_\nu(8.0\mu\text{m})/F_\nu^{\text{model}}(8.0\mu\text{m})), \quad (5.5)$$

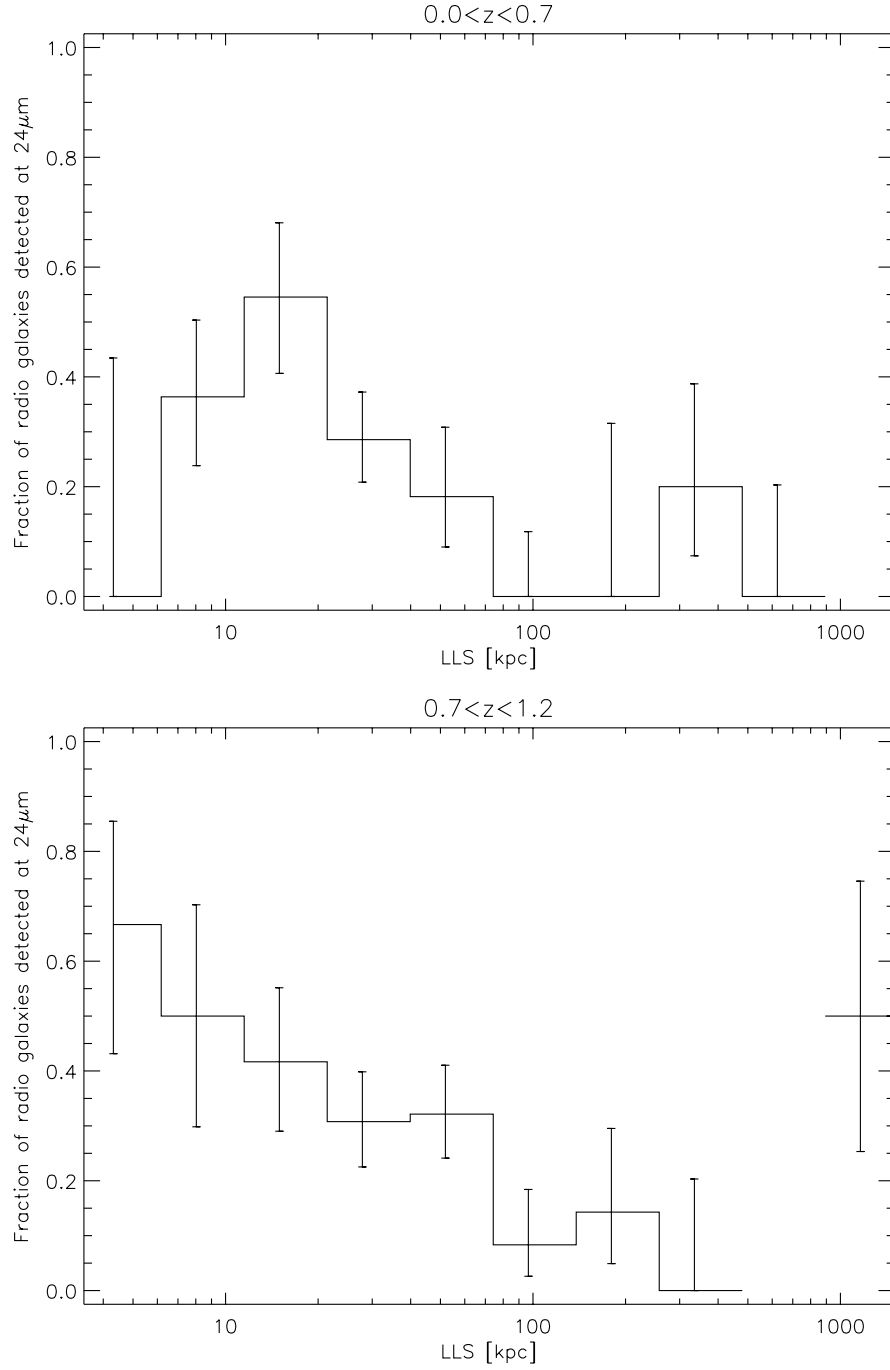


Figure 5.8: — Fraction of radio sources detected at $24\ \mu\text{m}$ as a function of LLS. Only radio sources with reliable optical identification and photometric redshift, in the range $0.0 < z < 0.7$ (top) and $0.7 < z < 1.2$ (bottom) are shown.

where $F_\nu(8.0\ \mu\text{m})$ is the observed $8.0\ \mu\text{m}$ flux density, and $F_\nu^{\text{model}}(8.0\ \mu\text{m})$ is the (observer's frame) $8.0\ \mu\text{m}$ flux density derived from the model SED fitted to the broadband photometry by kcorrect in order to check

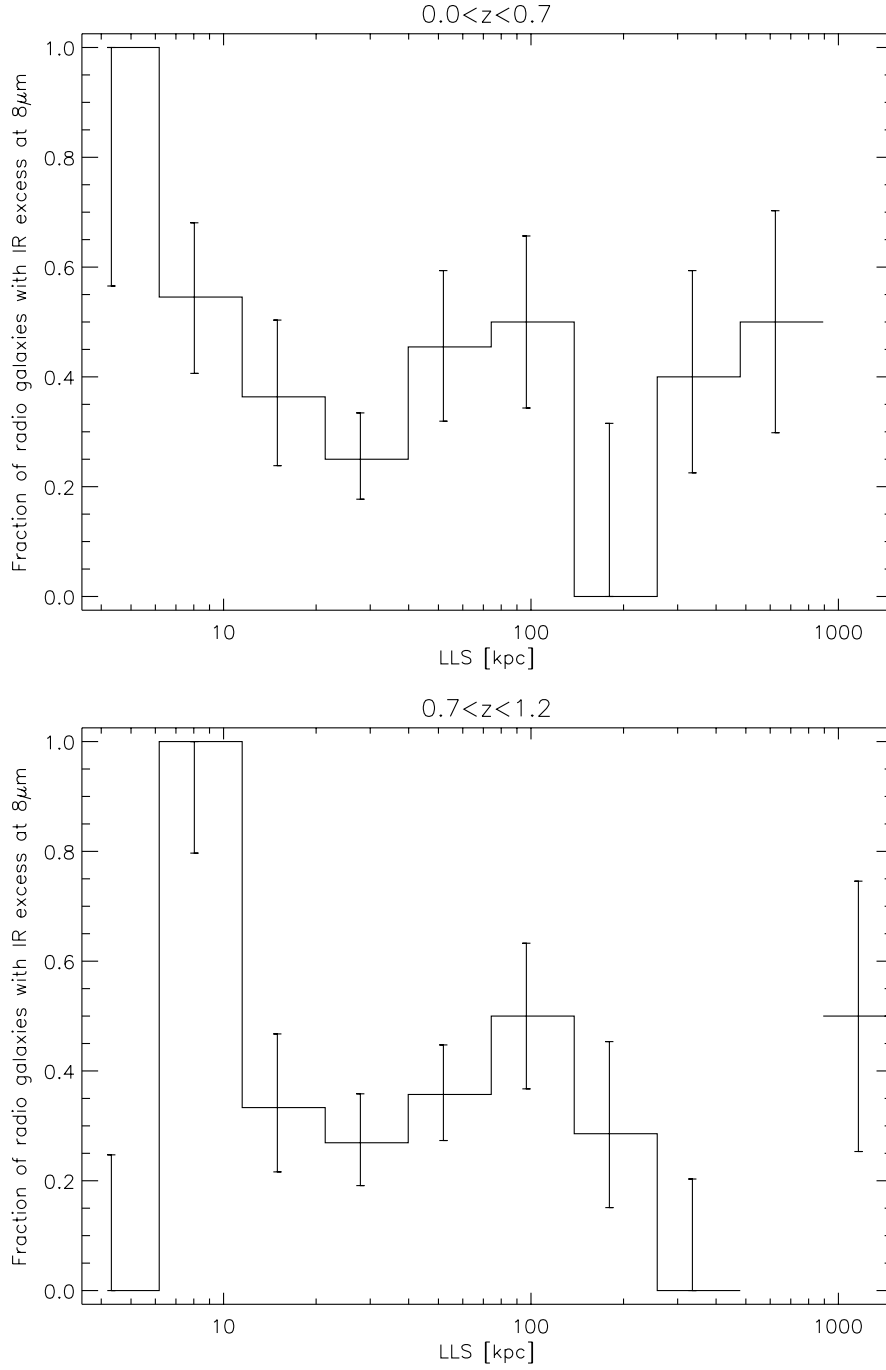


Figure 5.9: — Fraction of radio sources with a significant ($> 4\sigma$) infrared excess at $8\ \mu\text{m}$ as a function of LLS. The infrared excess was derived by comparing the actual flux density measurement with the SED template the photometric redshift was based on. Only radio sources with reliable optical identification and photometric redshift, in the range $0.1 < z < 0.7$ (top) and $0.7 < z < 1.2$ (bottom) are shown.

the photometric redshifts and estimate stellar masses (see Sect. 5.2.5).

In Fig. 5.9 we show the fraction of radio sources with a significant infrared excess at $8\ \mu\text{m}$ as a function of LLS. We chose a relatively con-

servative significance cutoff of 4σ , to account for the fact that not only the measurement errors play a role, but also the uncertainties of the extrapolated SEDs of the underlying stellar population. We find that the fraction of radio galaxies with a significant $8.0\ \mu\text{m}$ excess shows a decreasing trend with LLS somewhat similar to, but less significant than the decrease in $24\ \mu\text{m}$ detection rate, at a level of 78% and 90%.

5.4.3 IRAC colors

In Fig. 5.10 we show IRAC color-color diagrams, where the horizontal and vertical axes indicate the magnitude differences $[5.8\ \mu\text{m}] - [8.0\ \mu\text{m}]$ and $[3.6\ \mu\text{m}] - [4.5\ \mu\text{m}]$, respectively. Only radio sources detected in all IRAC bands with less than 0.4 magnitude uncertainty are shown. Filled squares are radio sources with a detected infrared counterpart in the MIPS $24\ \mu\text{m}$ catalog, while open squares denote radio sources that have not been detected at $24\ \mu\text{m}$. The sources have been divided in two different redshift bins: $0.1 < z < 0.7$ (left) and $0.7 < z < 1.2$ (right). The region indicated with the drawn line segments is the Stern wedge (Stern et al. 2005), an empirically defined region in which type 1 AGN tend to reside. Galaxies in the lower left part of the diagrams, where both colors are approximately zero, are dominated by old stellar populations at these wavelengths. The lower right part of the spectrum is also of particular importance. Low-redshift galaxies occupying this region are usually star-forming galaxies, since young stars excite polycyclic aromatic hydrocarbons (PAHs), producing a strong feature around (rest-frame) $8\ \mu\text{m}$. However, for the redshift range of our sample the IRAC $8.0\ \mu\text{m}$ band generally does not trace the rest-frame PAH bands. These red $[5.8\ \mu\text{m}] - [8.0\ \mu\text{m}]$ colors thus indicate excess infrared emission caused by heated dust. In principle young stars could be responsible for heating this dust, but since these galaxies are AGN, the most simple explanation is that the $8\ \mu\text{m}$ excess is caused by circumnuclear dust heated by the AGN.

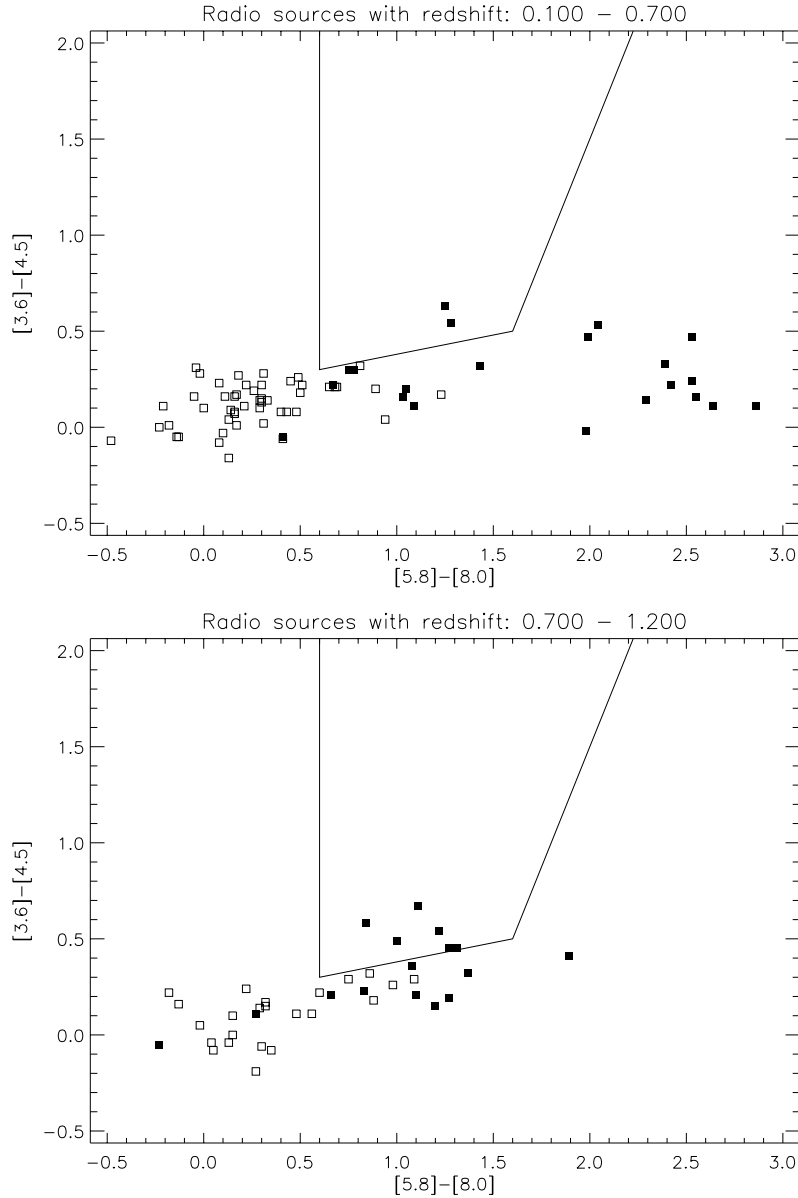


Figure 5.10: — IRAC color-color diagram for radio sources detected in all IRAC bands. Filled squares are radio sources with a detected infrared counterpart in the MIPS 24 μm catalog, while open squares denote radio sources that have not been detected at 24 μm . The region indicated with the drawn line segments is the Stern wedge (Stern et al. 2005) in which type 1 AGN tend to reside. The sources have been divided in two different redshift bins: $0.1 < z < 0.7$ (left) and $0.7 < z < 1.2$ (right).

5.5 Discussion

5.5.1 AGN unification

It is generally accepted that all AGN classes are powered by the same physical process: the accretion of matter on a supermassive black hole. The orientation of the AGN with respect to the line of sight has been

shown to explain some of the differences between AGN classes, but not all. Another hypothesis in AGN unification theory that recently gained popularity is that there is a critical accretion rate (relative to the Eddington accretion rate) that determines whether the accretion flow is radiatively efficient or not. In this dual-mode scenario high accretion rates ($\dot{M} \gtrsim 0.1 \dot{M}_{\text{Edd}}$, where \dot{M}_{Edd} is the Eddington accretion rate) result in optical (or *quasar-mode*) AGN, which are therefore expected to be powered by gas rich mergers or disk instabilities. Low accretion rates produce low luminosity radio AGN (*radio-mode*), which are expected to be fueled by steady cooling flows of hot gas from the intracluster medium.

Since cooling flows can only occur in very massive galaxy haloes, an interesting result is that Best et al. (2005), using a large sample of radio-loud AGN selected from the Sloan Digital Sky Survey (SDSS), find that the fraction of galaxies hosting a radio-loud AGN strongly depends on stellar mass, as $M_*^{2.5}$. Furthermore they show that the probability for a galaxy to host a (low luminosity) radio AGN is independent of optical signs of AGN activity, and suggest that optical and radio AGN are distinct phenomena, triggered by different accretion processes.

Support for this hypothesis was found by Tasse et al. (2008), who studied radio source host galaxies and their environment. The radio galaxies with lower stellar masses ($\lesssim 10^{10.5} M_\odot$), lie in regions underdense at large scales, but overdense at small scales, indicative of merging systems. These galaxies show excess mid-infrared emission consistent with a hidden (radiatively efficient) AGN. Massive elliptical radio galaxies on the other hand, lying in galaxy groups or clusters, do not show a significant mid-infrared excess, suggesting these radio sources are powered by a radiatively inefficient accretion flow.

Hickox et al. (2009) compare samples of radio, X-ray, and infrared AGN, selected from the AGN and Galaxy Evolution Survey (AGES). They find that radio-loud AGN are hosted by luminous elliptical galaxies, are strongly clustered (with $M_{\text{halo}} \sim 3 \cdot 10^{13} M_\odot$), and have very low Eddington ratios ($L_{\text{bolometric}} \lesssim 10^{-3} L_{\text{Edd}}$). They conclude that radio-loud AGN activity corresponds to a later phase in the evolution of galaxies than X-ray and infrared AGN.

Other recent mid-infrared studies include that of Ogle, Whyson & Antonucci (2006), who observed a sample of 42 powerful radio sources

with the Spitzer IRS, and found that 55% of the NLRGs are weak at $15\ \mu\text{m}$. They suggest that, while the other 45% of the NLRGs and all BLRGs/quasars, being luminous in the infrared, possess powerful (hidden) quasar nuclei (quasar-mode AGN activity), these $15\ \mu\text{m}$ weak NLRGs have radiatively inefficient accretion flows (radio-mode AGN activity).

However, some of these results can also be explained in terms of evolution. Since radio emission generally comes from regions hundreds of kpc from the nucleus, it may be that the nuclear object merely has faded somewhere during the past millions of years. This could explain for example the findings of Ogle, Whyson & Antonucci (2006), because in this evolutionary scenario all mid-infrared weak radio galaxies, which presumably do not have a powerful quasar nucleus anymore, indeed should not emit broad line emission anymore. The fact that some of them still emit narrow lines emission is expected, since this emission originates from a much larger region and will therefore fade much later and slower. Summarizing, for evolving AGN we expect the luminosity decrease to start on small scales, slowly moving to larger scales. These are in sequence: the broad line region, the warm ($\sim 200\text{K}$) heated dust primarily located close to the nucleus, the more extended narrow line region, and in the end also the radio source. Note that from an observational viewpoint this sequence may be softened due to differing physical timescales of each of the emission processes, and further complicated by orientation effects.

In Sect. 5.4 we determined the infrared properties of radio AGN, in order to determine whether radio AGN do have a radiatively efficient accretion disk with circumnuclear gas and dust, and whether the central object evolves over the lifetime of the radio source. We found that many radio-loud AGN do show excess emission at mid-infrared wavelengths, indicative of large amounts of circumnuclear gas and dust, and that this mid-infrared emission of radio AGN decreases with radio source size. This is in line with the evolution scenario suggested above, as will be discussed in the following section.

5.5.2 Evolution of mid-infrared emission

In Sect. 5.4.1 we show that the $24\ \mu\text{m}$ detection rate of radio sources decreases with LLS. A decrease in detection rate with LLS is exactly what would be expected if radio sources are powered by accretion from a circumnuclear torus: while the radio source grows, the gas and dust supply surrounding the SMBH is slowly consumed, causing the initially intense thermal infrared emission to fade. However, a purely orientation-based unification scenario might possibly produce a similar trend. In this scenario the radio AGN that are seen face-on will be brighter at optical wavelengths, and their radio structures will appear smaller on average due to projection effects. For edge-on radio AGN projection effects are relatively unimportant, but these will be fainter at optical wavelengths due to the extinction from the obscuring torus. Therefore a lower optical luminosity for larger radio sources would be expected from orientation-based unification theories. Note that this reasoning relies on the anisotropy of the *optical* emission of AGN. Infrared emission, especially at long wavelengths like $24\ \mu\text{m}$, is expected to be much more isotropic compared to optical emission, since the infrared emission is much less affected by extinction, and because it traces warm dust, which occupies a less centralized region. This is also confirmed by recent observations of a complete and well-studied sample (Dicken et al. 2009). Previous publications present contradicting results, some in favour of anisotropic infrared emission (Heckman et al. 1994; Hes et al. 1995; Shi et al. 2005; Cleary et al. 2007), others favouring isotropy (Meisenheimer et al. 2001; Haas et al. 2004), but these earlier studies were based on samples that were heterogeneous and/or incomplete in terms of far-infrared detections.

If the trend of decreasing $24\ \mu\text{m}$ emission with LLS was actually caused by orientation, and not by evolution, a much stronger effect is expected for the $8.0\ \mu\text{m}$ excess, because infrared emission at $8.0\ \mu\text{m}$ is more affected by extinction than emission at $24\ \mu\text{m}$. The fact that the fraction of radio galaxies with a significant $8.0\ \mu\text{m}$ excess shows a decreasing trend with LLS similar to, but less significant than the results at $24\ \mu\text{m}$, suggests that the trend of decreasing detection rate at $24\ \mu\text{m}$ is not a result of orientation effects, and therefore (at least a large fraction of) radio AGN are powered by the consumption of large amounts of circumnuclear gas

and dust.

Note that a decrease in infrared emission with LLS could also mean that the intrinsic power of the heating source, the AGN, fades with age. We argue that this may play an additional role, but that the consumption of the torus is the main effect, because otherwise we would expect the hotter dust, emitting at $8\ \mu\text{m}$, to fade faster, and cooler dust, emitting at $24\ \mu\text{m}$, to fade later on, but we don't see any evidence for this when comparing Fig. 5.9 and Fig. 5.8.

5.5.3 IRAC colors

There are a few interesting things to learn from Fig. 5.10. Firstly, although these galaxies are all radio-loud AGN, they have no tendency to lie in the Stern wedge. This means that their near-infrared photometry is not dominated by direct emission from type 1 AGN. This is in agreement with the recent finding that there is little overlap between samples of radio-loud AGN and IRAC selected AGN (Hickox et al. 2009). Secondly, there is no significant difference between the two redshift bins, except that for the lower redshift bin the colors can reach more extreme values. This is probably caused by redshifting of the strongest dust emission to longer wavelengths at higher redshifts, but in general we can conclude that no important redshift effects seem to play a role. Thirdly, the probability that a radio source has a MIPS $24\ \mu\text{m}$ detection is strongly correlated with its position on the color-color diagram. A red $[5.8\ \mu\text{m}] - [8.0\ \mu\text{m}]$ color significantly increases the chance to be detected with MIPS, indicating that 8.0 and $24\ \mu\text{m}$ emission are caused by the same physical mechanism (thermal emission from dust).

Finally, radio source host galaxies mostly have IRAC colors consistent with old stellar populations, but a significant fraction has much redder $[5.8\ \mu\text{m}] - [8.0\ \mu\text{m}]$ colors, indicating excess infrared emission caused by heated dust. Interestingly, the host galaxies with red and blue $[5.8\ \mu\text{m}] - [8.0\ \mu\text{m}]$ colors do not seem to form two separate populations, but rather form a continuous stream from heated dust dominated mid-infrared colors at the lower right, to (stellar) Rayleigh-Jeans dominated galaxies in the lower left region. This suggests, but does not prove, radio galaxies evolve from the right to the lower left of the IRAC color-color diagram, favouring the scenario where radio sources evolve from in-

frared luminous to weak while growing. This result can only be united with the decrease in 8 and 24 μm emission with LLS being due to orientation, if the anisotropy of the infrared emission at these wavelengths would be the same. Since this is unlikely, we deduce that radio AGN consume their circumnuclear material over their lifetimes.

5.6 Conclusions

We investigated the evolution of radio-loud AGN in the context of current unification theories, by determining whether radio sources have (cold) circumnuclear tori, or whether they are fueled by (hot) Bondi accretion (Bondi 1952) through cooling flows. We exploited the large data sets available for the 9 deg² Boötes field, in particular deep multi-frequency radio observations obtained with the WSRT and VLA, the optical NDWFS, the near-infrared FLAMEX and SDWFS, and mid-infrared MIPS observations from the Spitzer Space Telescope. For a sample of 334 radio sources down to $S_{325 \text{ MHz}} > 0.75 \text{ mJy}$ the photometric redshifts and stellar masses were determined from the optical and near-infrared data. Radio source angular sizes were determined from the 325 MHz data, and converted to projected linear size using the photometric redshifts. These were subsequently used as a proxy for radio source age. The mid-infrared properties were determined for all sources in the sample.

We detect a significant decrease of 24 μm detection rate with projected linear source size, while a similar but weaker trend is seen at 8 μm . We suggest this fits an evolution scenario, in which young radio-loud AGN contain a circumnuclear torus, while older AGN consumed most of the circumnuclear material. The results contradict the hypothesis that radio-loud AGN are fueled through Bondi accretion. If the radio size-infrared relation was caused by orientation, we would expect a stronger trend at 8 μm than at 24 μm , while the opposite is seen. We argue that radio AGN may still be powered through cooling flows, but with the accreted material probably settling in a (standard unification theory) disk, and not being continuously replenished.

Acknowledgments

This work is based on observations made with the *Spitzer Space Telescope*, which is operated by the Jet Propulsion Laboratory, California Institute of Technology under contract with NASA. Support for this work was provided by NASA through an award issued by JPL/Caltech. We gratefully acknowledge the Boötes MIPS team for allowing us early access to those data for this analysis. This work made use of images and/or data products provided by the NOAO Deep Wide-Field Survey (Jannuzi & Dey 1999), which is supported by the National Optical Astronomy Observatory (NOAO). NOAO is operated by AURA, Inc., under a cooperative agreement with the National Science Foundation.

References

- Antonucci, R. R. J. 1984, *ApJ*, 278, 499
Ashby, M. L. N., et al. 2009, *ApJ*, 701, 428
Barthel, P. D. 1989, *ApJ*, 336, 606
Best, P. N., Kauffmann, G., Heckman, T. M., Brinchmann, J., Charlot, S., Ivezić, Ž., & White, S. D. M. 2005, *MNRAS*, 362, 25
Blanton, M. R., et al. 2003, *AJ*, 125, 2348
Blanton, M. R., & Roweis, S. 2007, *AJ*, 133, 734
Bondi, H. 1952, *MNRAS*, 112, 195
Brodwin, M., et al. 2006, *ApJ*, 651, 791
Bruzual, G., & Charlot, S. 2003, *MNRAS*, 344, 1000
Cleary, K., Lawrence, C. R., Marshall, J. A., Hao, L., & Meier, D. 2007, *ApJ*, 660, 117
de Ruiter, H. R., Arp, H. C., & Willis, A. G. 1977, *A&AS*, 28, 211
de Vries, W. H., Morganti, R., Röttgering, H. J. A., Vermeulen, R., van Breugel, W., Rengelink, R., & Jarvis, M. J. 2002, *AJ*, 123, 1784
Dicken, D., Tadhunter, C., Axon, D., Morganti, R., Inskip, K. J., Holt, J., Delgado, R. G., & Groves, B. 2009, *ApJ*, 694, 268
Eisenhardt, P. R., et al. 2004, *ApJS*, 154, 48
Elston, R. J., et al. 2006, *ApJ*, 639, 816
Fender, R. P., Belloni, T. M., & Gallo, E. 2004, *MNRAS*, 355, 1105
Haas, M., et al. 2004, *A&A*, 424, 531
Hardcastle, M. J., Evans, D. A., & Croston, J. H. 2007, *MNRAS*, 376, 1849
Heckman, T. M., O'Dea, C. P., Baum, S. A., & Laurikainen, E. 1994, *ApJ*, 428, 65
Hes, R., Barthel, P. D., & Hoekstra, H. 1995, *A&A*, 303, 8
Hickox, R. C., et al. 2009, *ApJ*, 696, 891
Intema, H. T., van Weeren, R. J., Röttgering, H. J. A., Lal, D. V., & Mohan, N. R. 2009, *A&A*, submitted
Jannuzi, B. T. & Dey, A., 1999, *ASP Conference Series*, Vol. 191, 111, ed. R. Weymann, L. Storrie-Lombardi, M. Sawicki, and R. Brunner
Kaiser, C. R., & Best, P. N. 2007, *MNRAS*, 381, 1548
Komatsu, E., et al. 2009, *ApJS*, 180, 330
Körding, E. G., Jester, S., & Fender, R. 2006, *MNRAS*, 372, 1366
Meisenheimer, K., Haas, M., Müller, S. A. H., Chini, R., Klaas, U., & Lemke, D. 2001, *A&A*, 372, 719
Merloni, A., Heinz, S., & di Matteo, T. 2003, *MNRAS*, 345, 1057
Merloni, A., & Heinz, S. 2008, *MNRAS*, 388, 1011

- Ogle, P., Whyson, D., & Antonucci, R. 2006, *ApJ*, 647, 161
- Prestage, R. M., & Peacock, J. A. 1983, *MNRAS*, 204, 355
- Rengelink, R. B., Tang, Y., de Bruyn, A. G., Miley, G. K., Bremer, M. N., Röttgering, H. J. A., & Bremer, M. A. R. 1997, *A&AS*, 124, 259
- Richter, G. A. 1975, *Astronomische Nachrichten*, 296, 65
- Shi, Y., et al. 2005, *ApJ*, 629, 88
- Stern, D., et al. 2005, *ApJ*, 631, 163
- Sutherland, W., & Saunders, W. 1992, *MNRAS*, 259, 413
- Tasse, C., Best, P. N., Röttgering, H., & Le Borgne, D. 2008, *A&A*, 490, 893
- Wilman, R. J., et al. 2008, *MNRAS*, 388, 1335
- Windhorst, R., Mathis, D., & Neuschaefer, L. 1990, *ASP Conference Series*, 10, 389
- Wolstencroft, R. D., et al. 1986, *MNRAS*, 223, 279

5.7 Appendix

5.7.1 Overlays

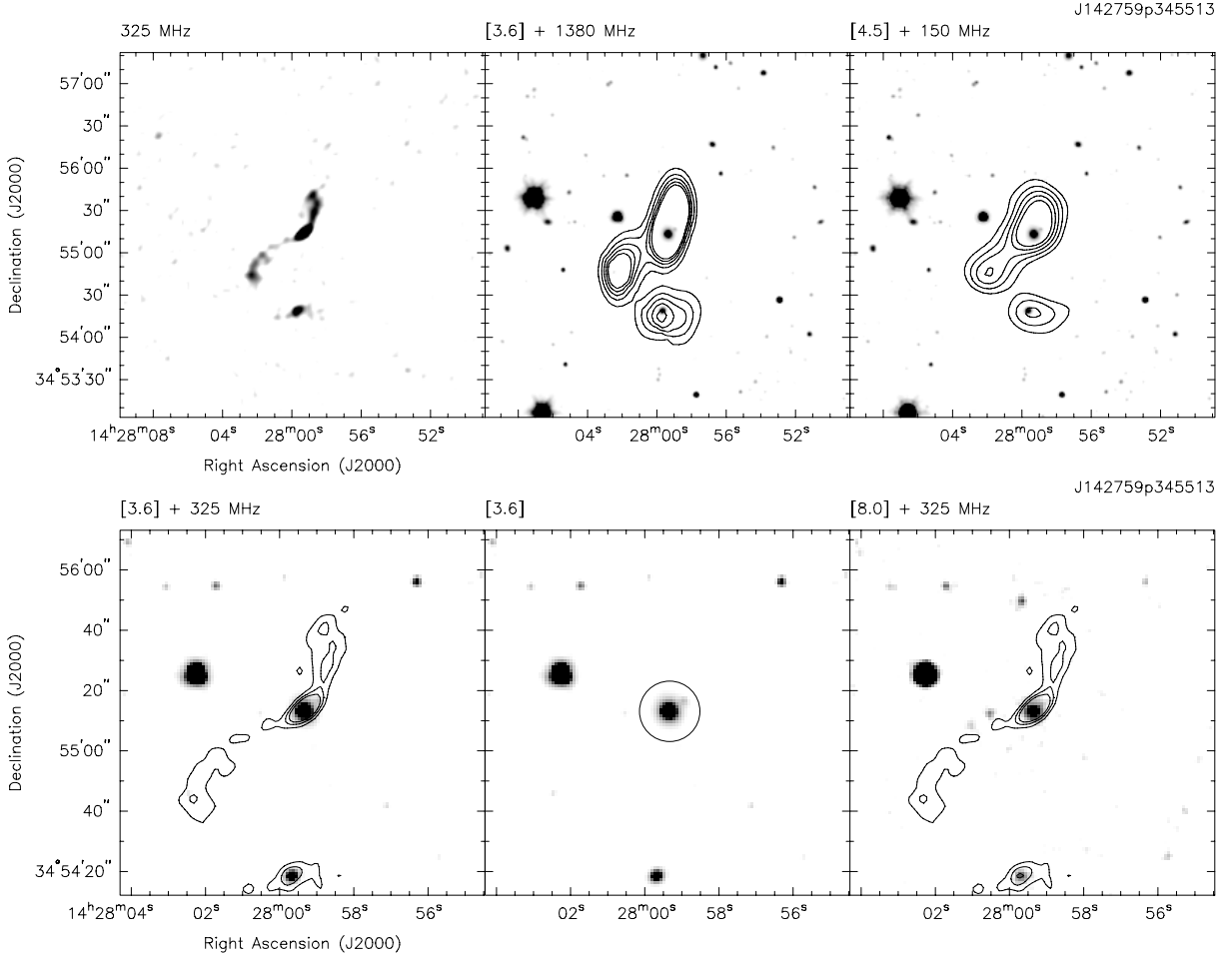
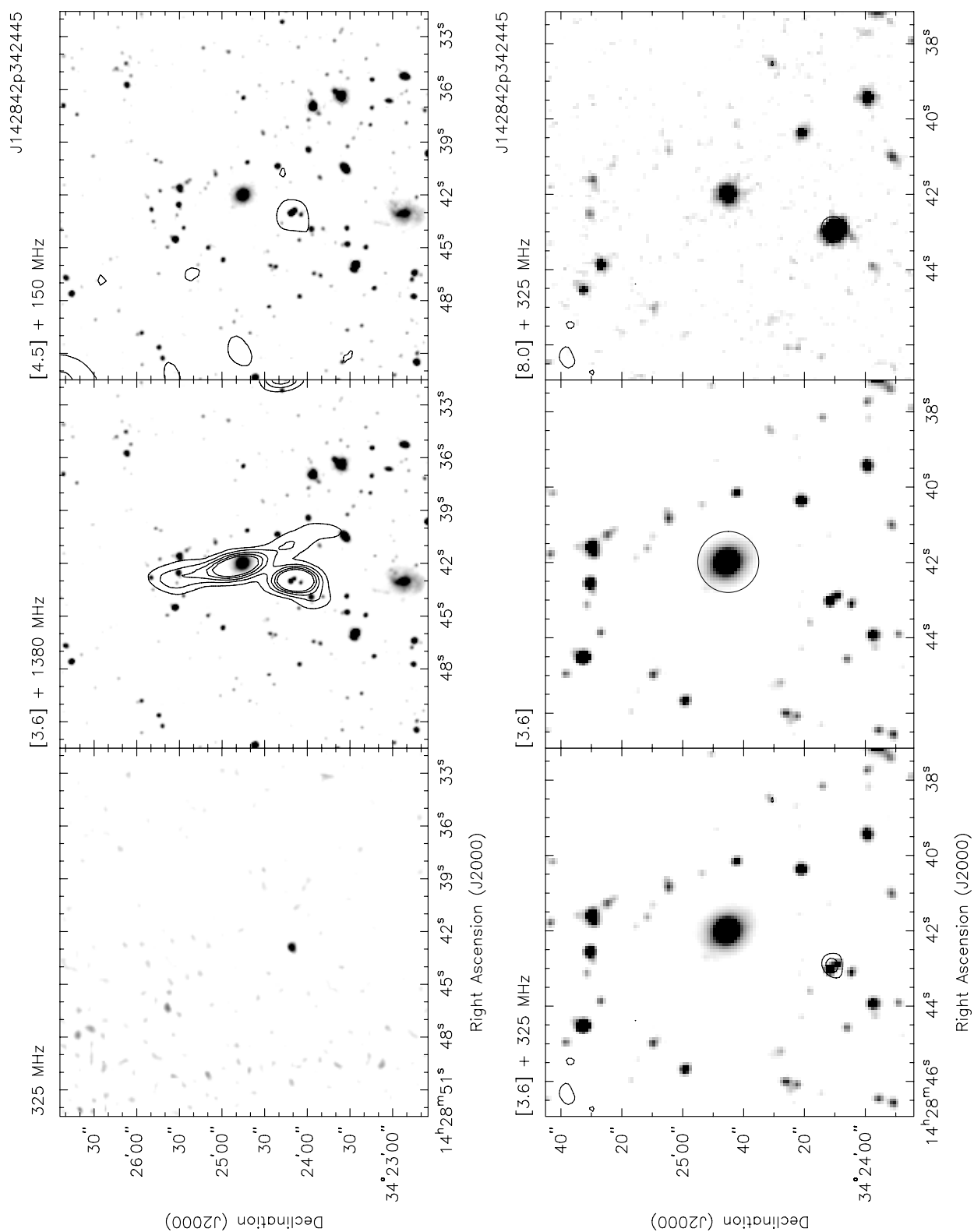
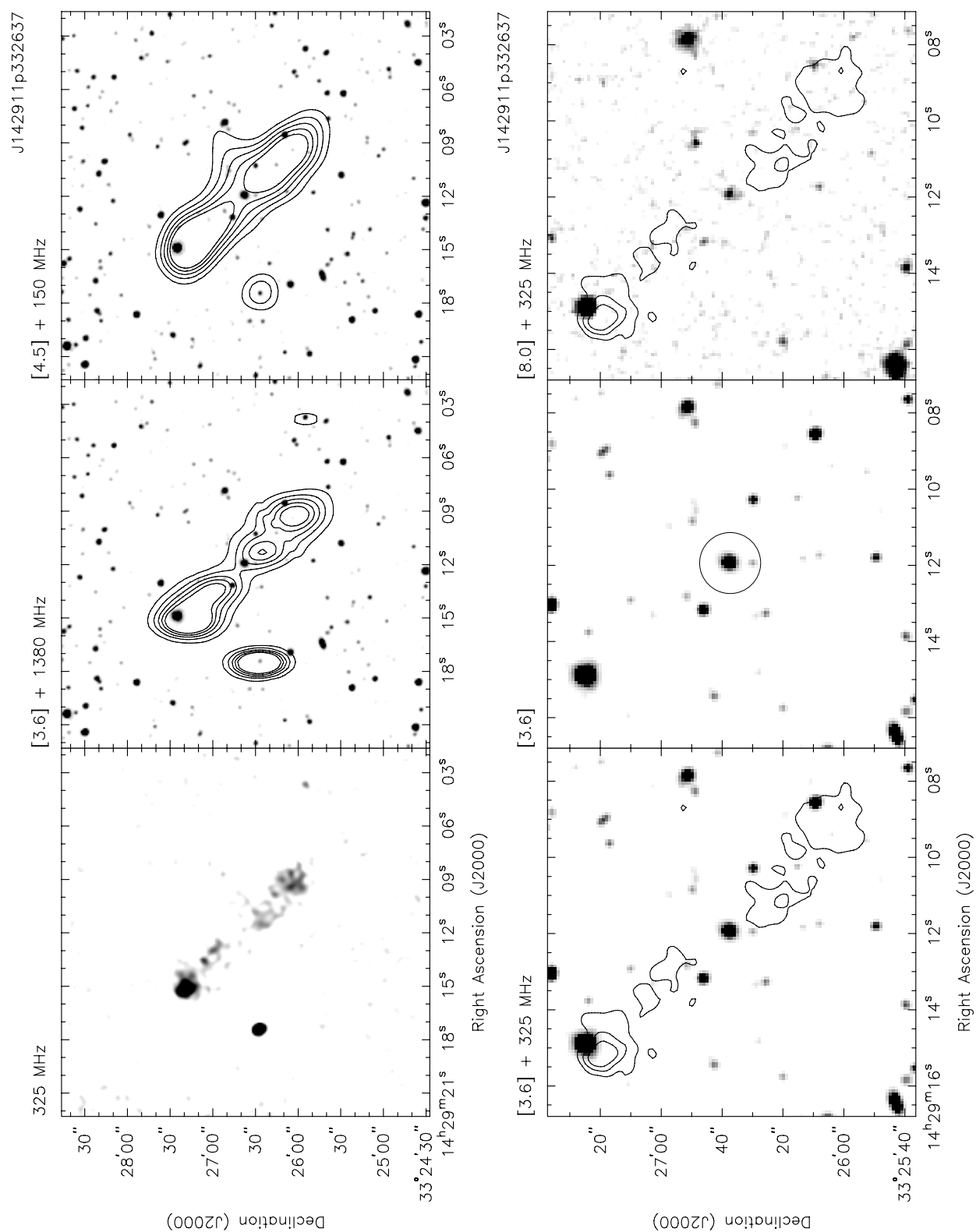
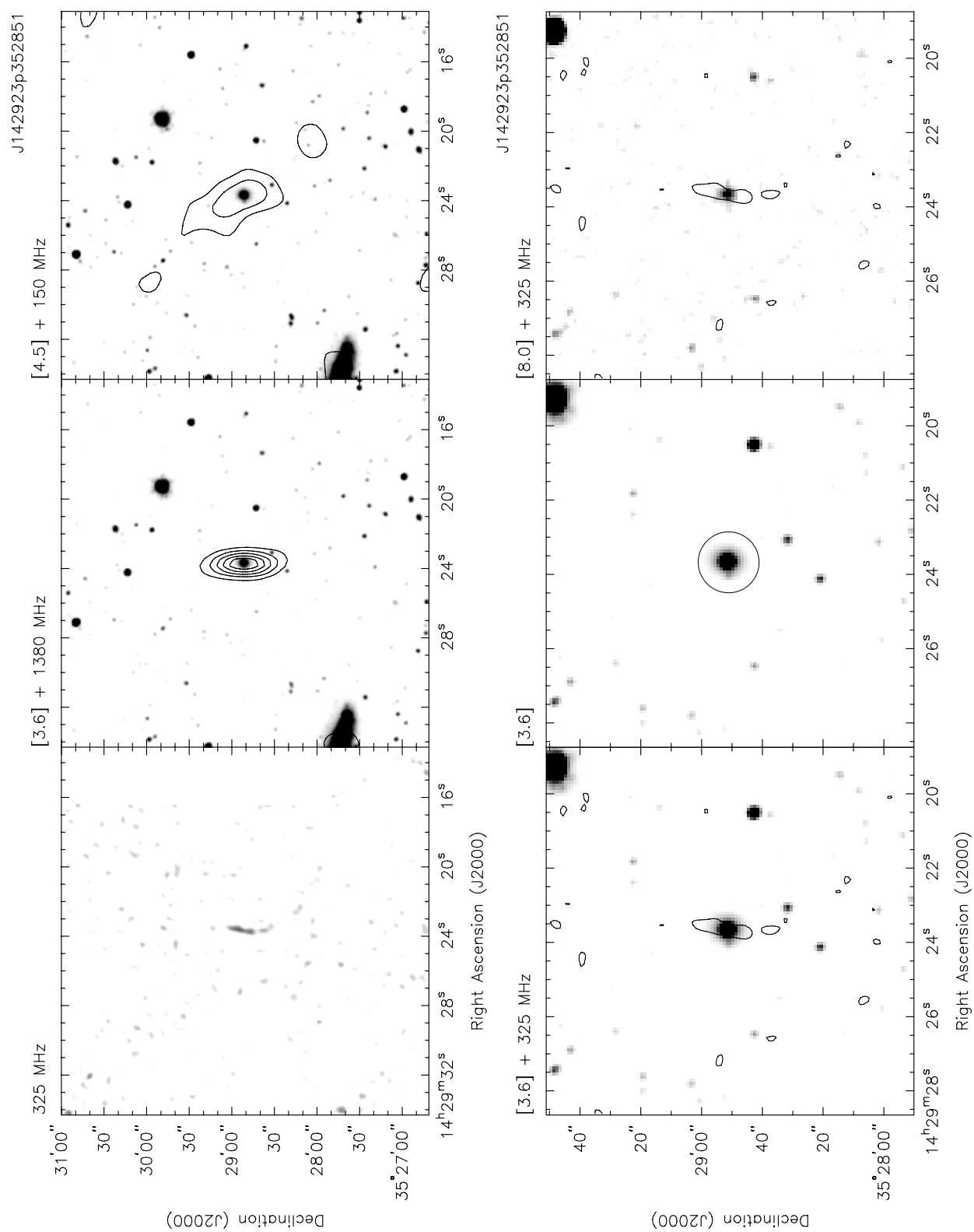
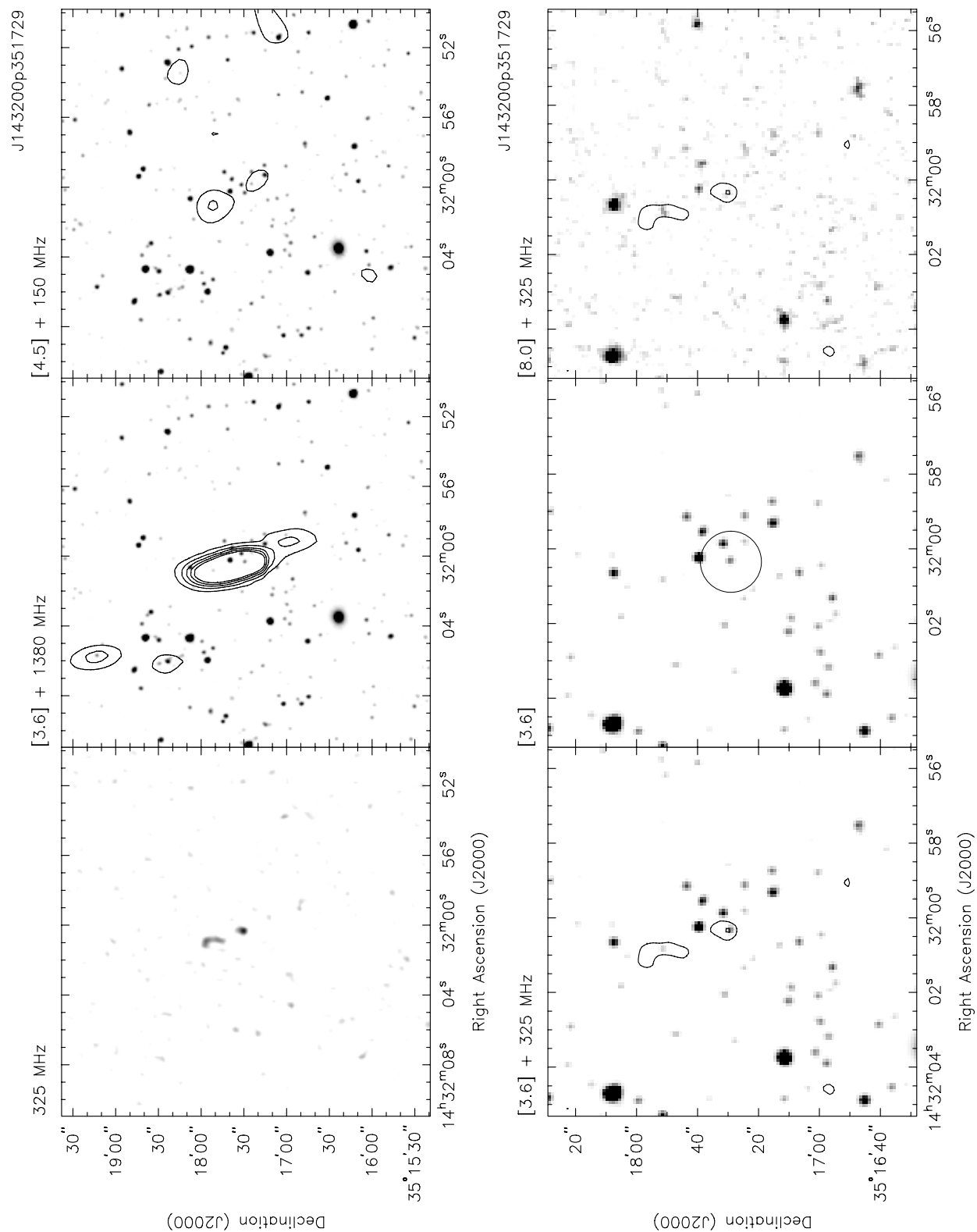


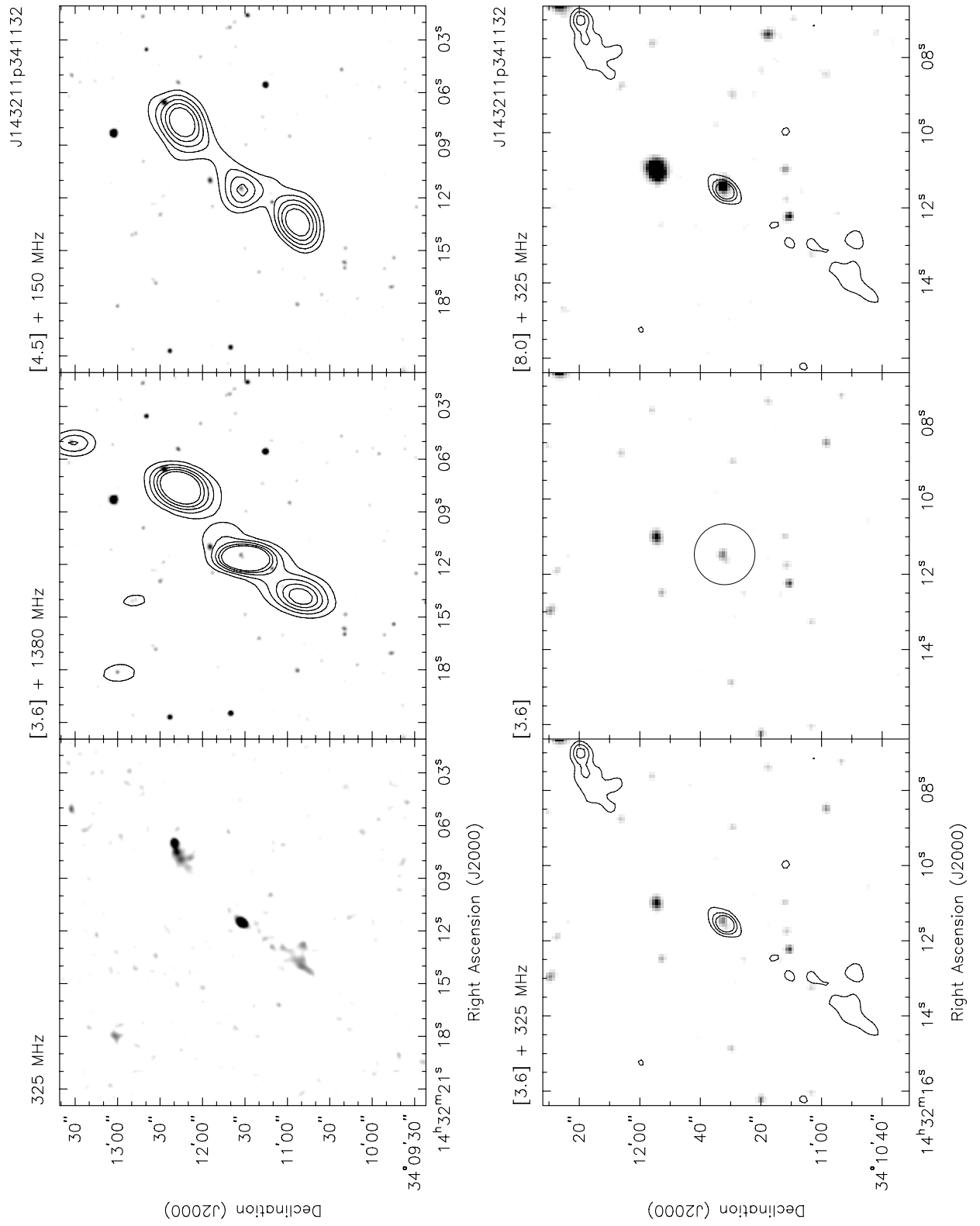
Figure 5.11: — Image cutouts overlaid with radio contours for identified radio galaxies with angular sizes larger than one arcminute. For each radio source six panels are shown, to provide the reader with all relevant information. The first panel shows the 325 MHz VLA map with greyscale intensity ranging from 2σ to 7σ . The second top panel shows the SDWFS $3.6\ \mu\text{m}$ image of the region, with 1.4 GHz WSRT contours overlaid. The greyscale intensity for this panel, as well as for the remaining four panels, ranges from 1σ to 7σ above the median pixel value of the SDWFS cutout, and the WSRT contours range from 3σ to 15σ in five levels. The third panel shows the SDWFS $4.5\ \mu\text{m}$ image, overlaid with the 150 MHz radio map, with five contours ranging from 2.5σ to 10σ . The lower panels show a zoom-in on the central region, with the first two panels again showing the SDWFS $3.6\ \mu\text{m}$ image, this time (1) with three VLA 325 MHz radio contours overlaid and (2) with the identified host galaxy indicated with a circle. The last panel shows the SDWFS $8.0\ \mu\text{m}$ image, with three VLA 325 MHz radio contours ranging from 3σ to 10σ .

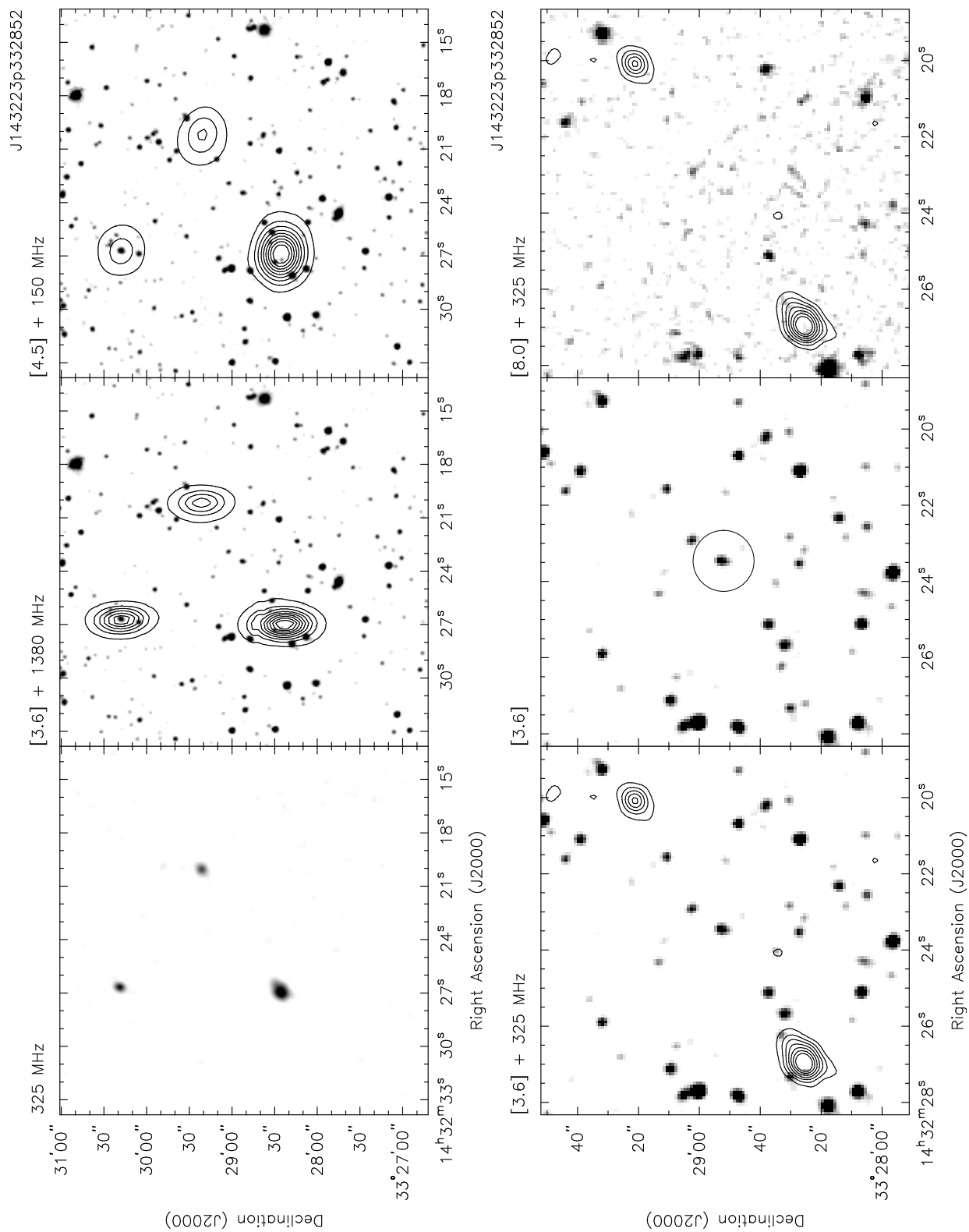
Figure 5.11: — *continued.*

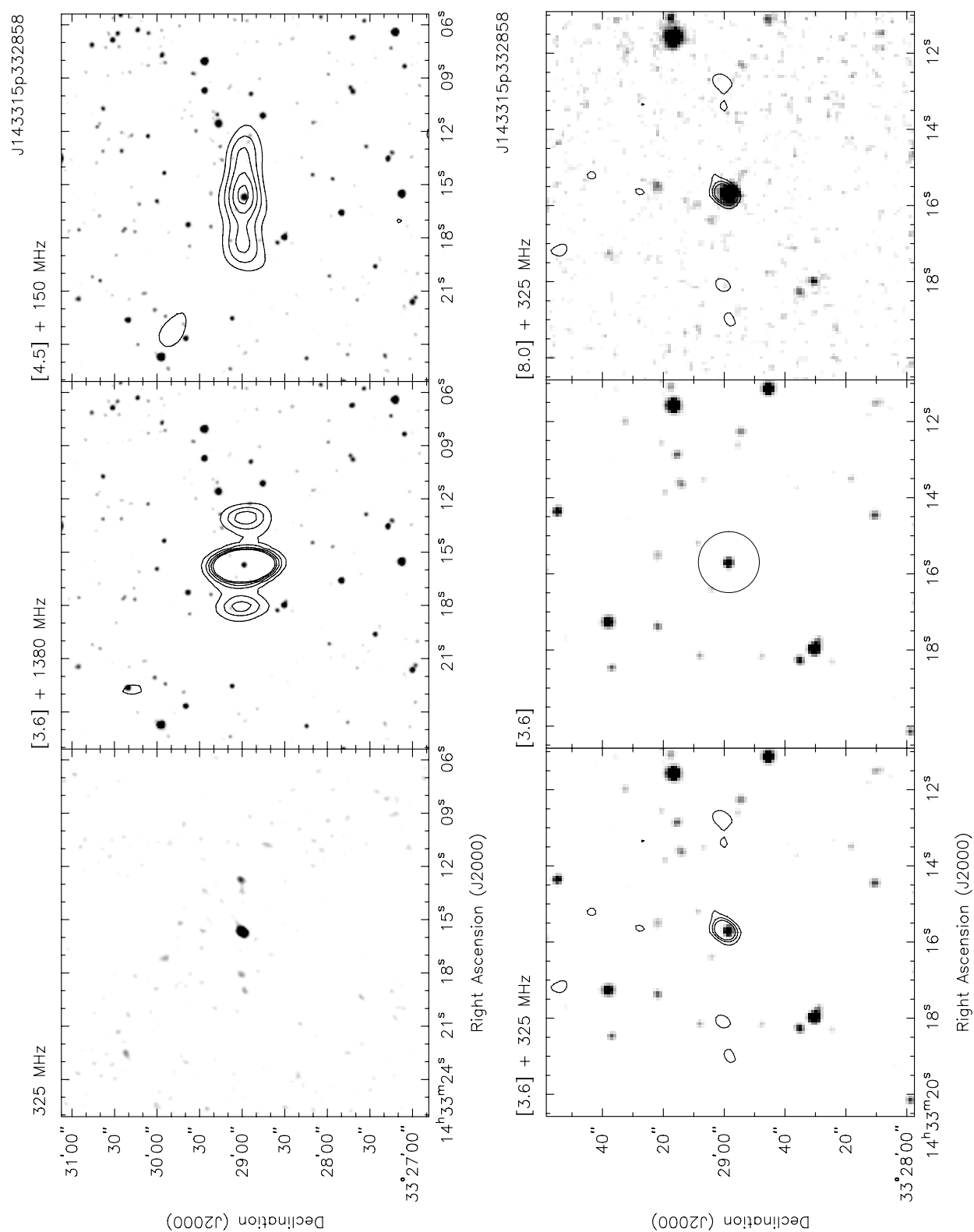
Figure 5.11: — *continued.*

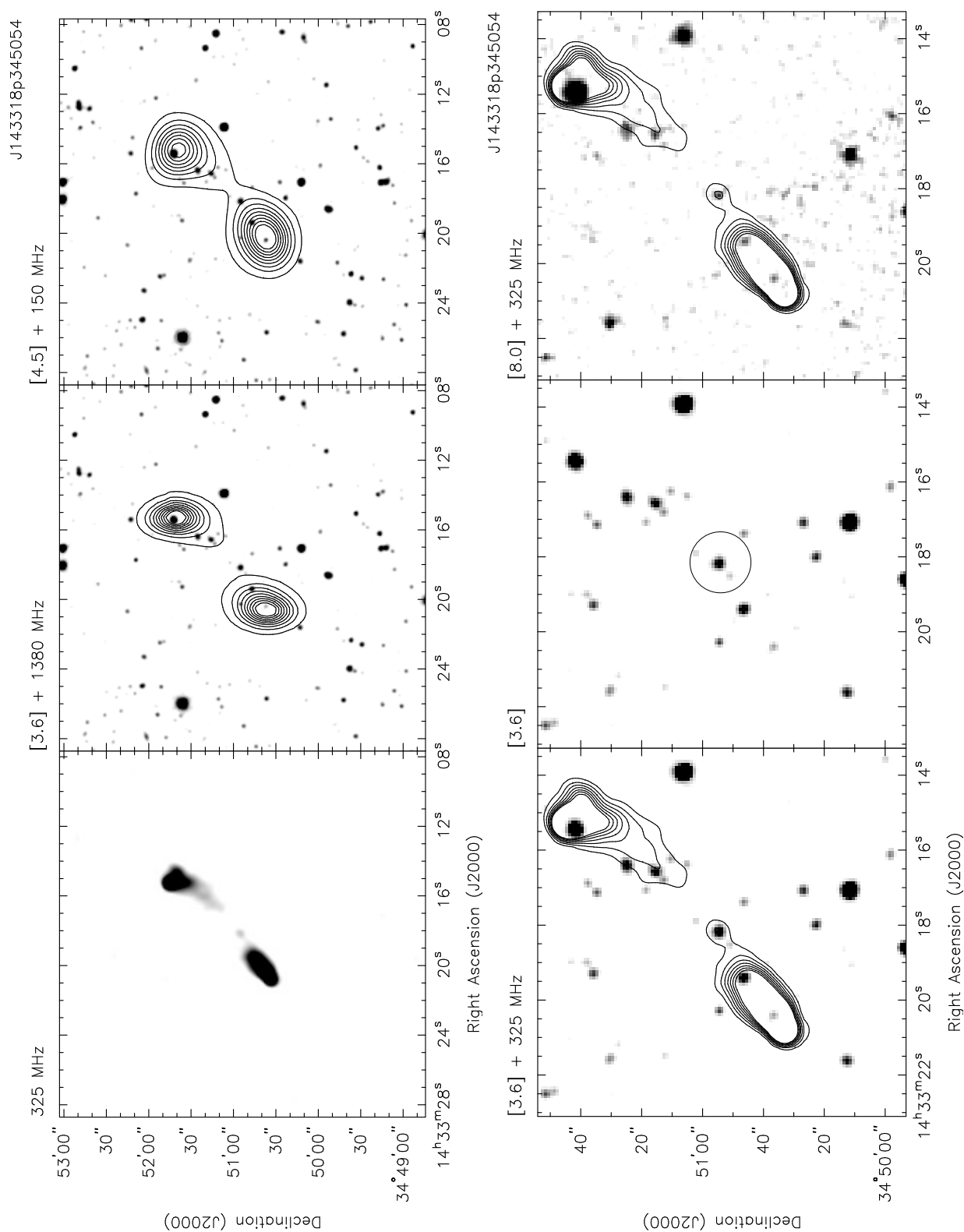
Figure 5.11: — *continued.*

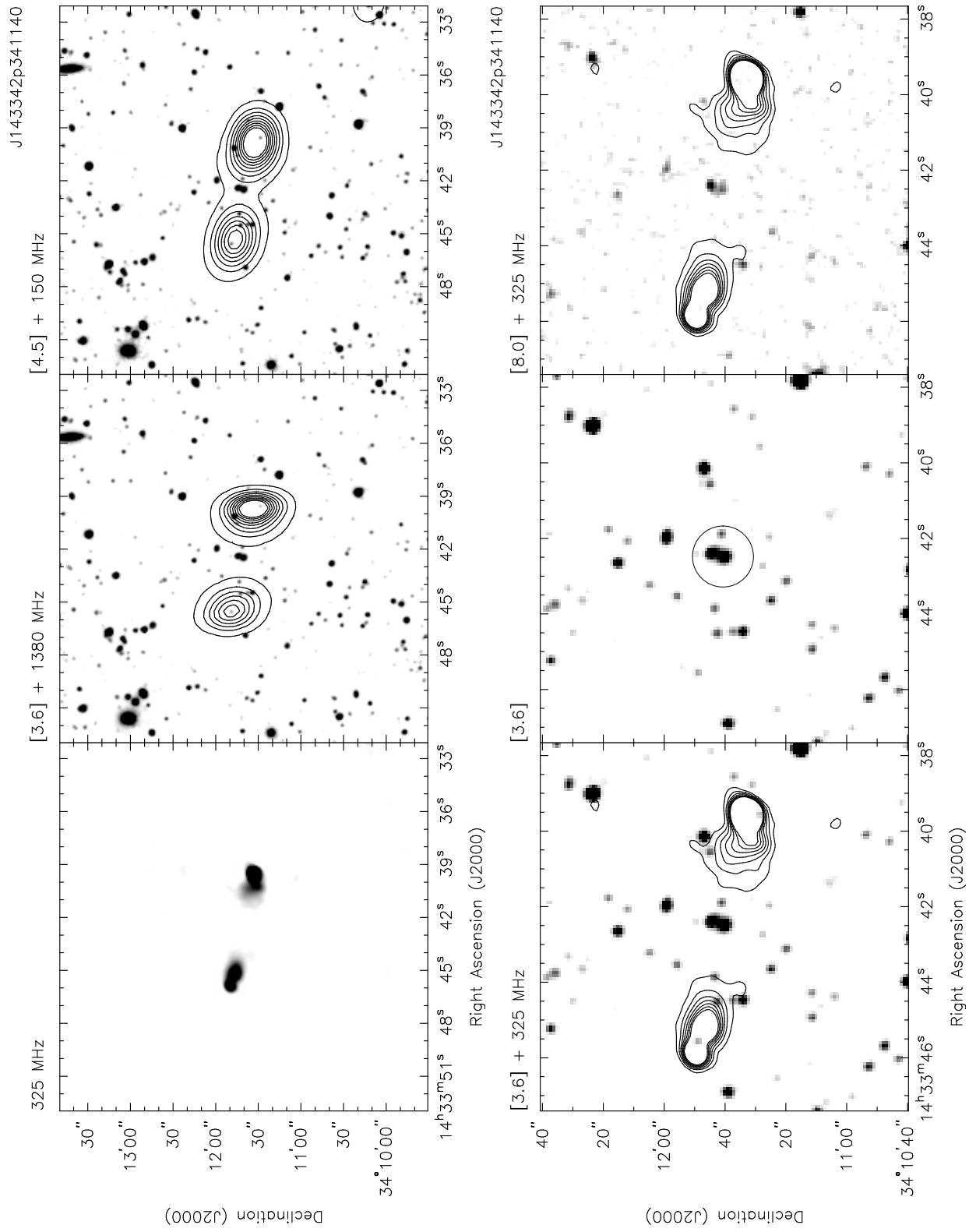
Figure 5.11: — *continued*.

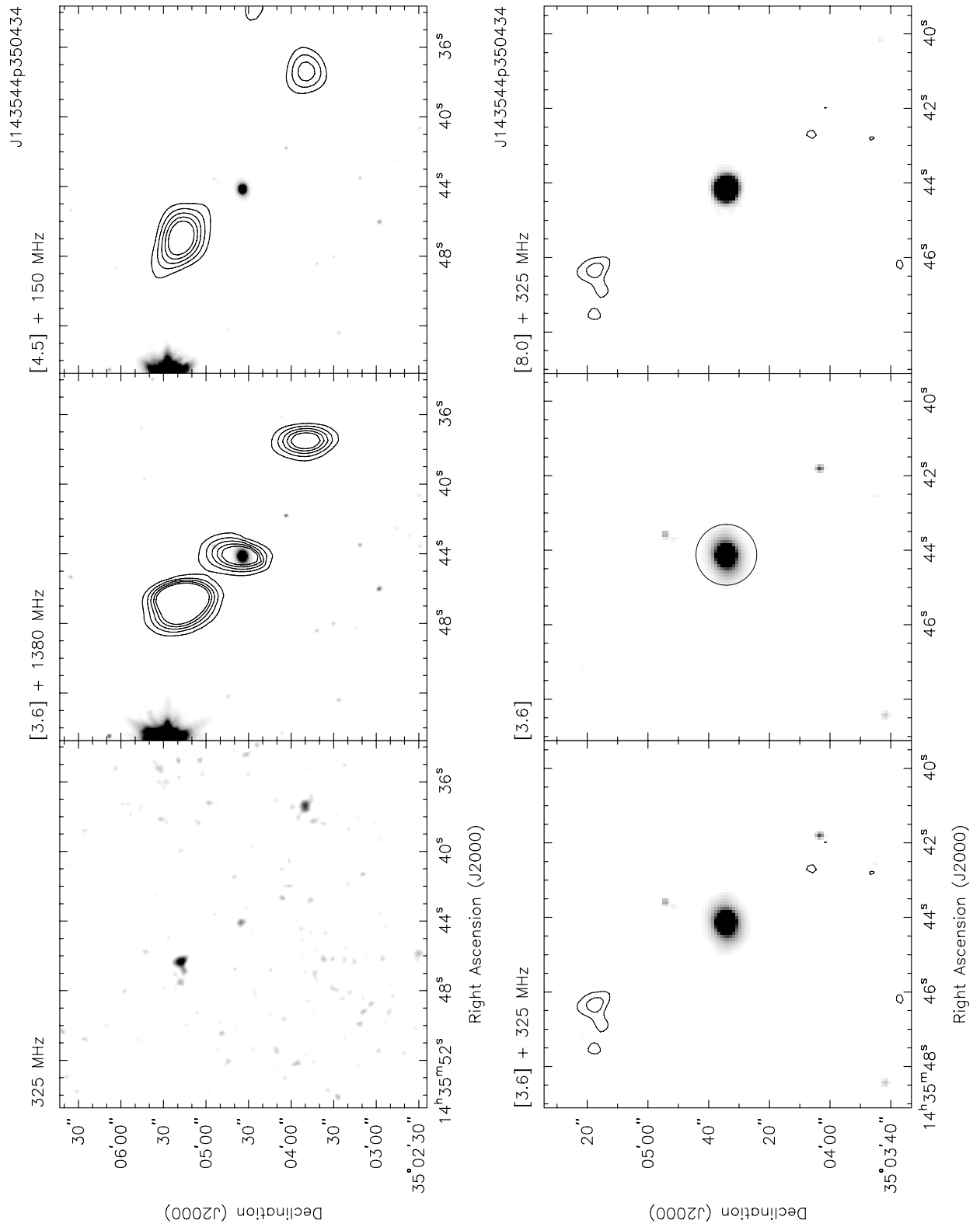
Figure 5.11: — *continued.*

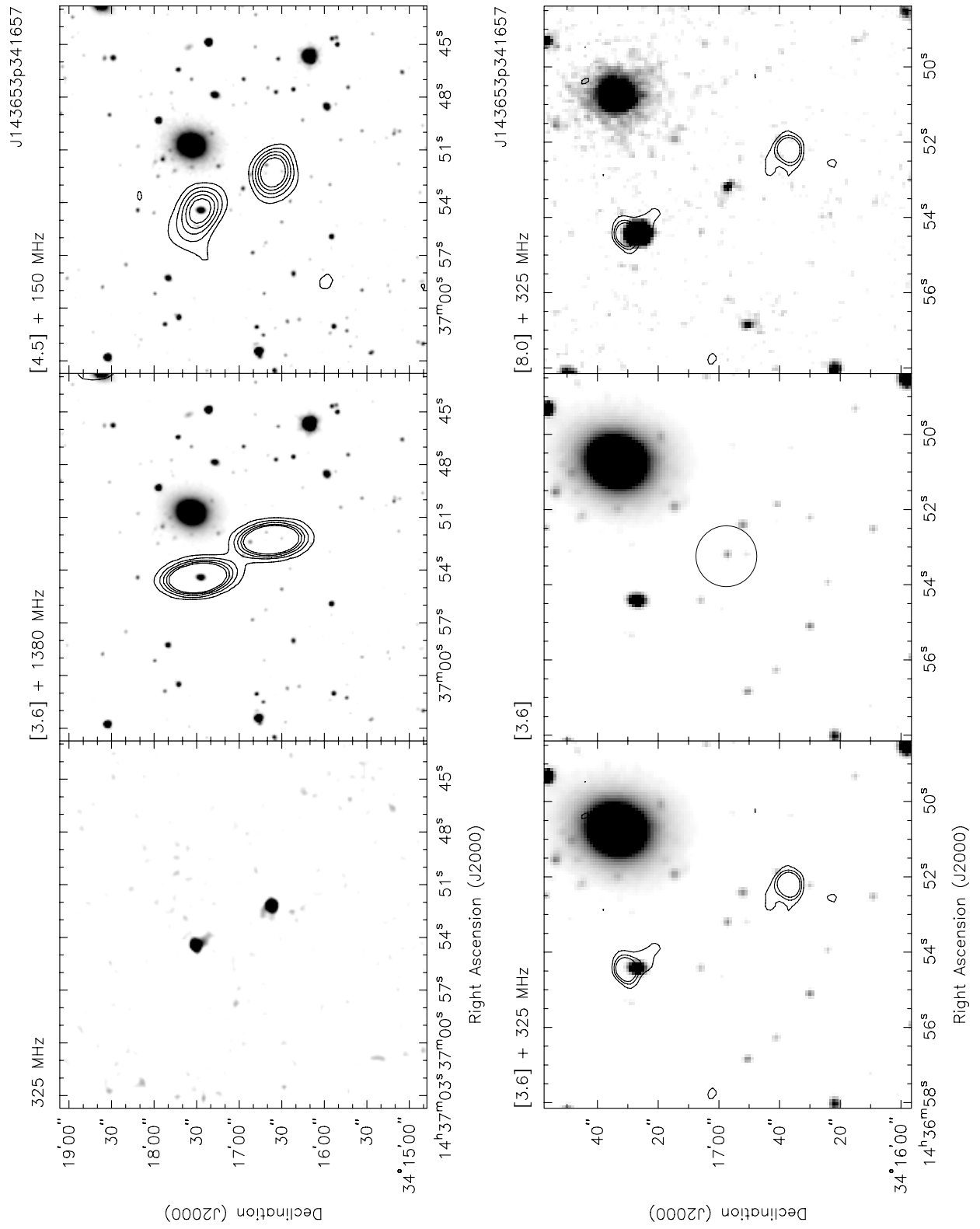
Figure 5.11: — *continued.*

Figure 5.11: — *continued*.

Figure 5.11: — *continued*.

Figure 5.11: — *continued*.

Figure 5.11: — *continued.*

Figure 5.11: — *continued*.

Chapter 6

Survival rates of young radio-loud AGN and their environments

Abstract. Young radio-loud active galactic nuclei can be used to investigate the evolution of extragalactic radio sources. In these studies a common assumption is that *all* young radio sources eventually evolve into extended FR II and/or FR I radio sources. However, not much observational evidence is currently available to support this hypothesis, and it could well be that a significant population shuts down early. We investigate this assumption by comparing the observed characteristics of the CORALZ core sample of compact radio sources at low redshift with mock populations of radio sources. The simulations are based on the analytic radio source models of Kaiser & Best (2007), fully taking into account size and luminosity evolution. From this comparison we find that the distributions of redshift and radio luminosity of the mock radio source populations are in agreement with being drawn from the same distribution as the CORALZ core sample. The size distribution of the CORALZ core sample on the other hand differs from those of the simulated radio sources in being smaller on average, and strongly favors a steep density profile of the external medium. In order to explain the size distribution of the CORALZ core sample, a significant fraction ($\sim 80\%$ for preferred parameter values) of the *most compact* CORALZ sources must shut down and fade before they could evolve into FR I/II radio sources. However, a comparison with the predicted sample sizes shows that a large fraction of the *total* number of CORALZ sources cannot suffer an early death, otherwise an unreasonably long lifetime for typical radio-loud AGN activity would be implied.

N. de Vries, I. A. G. Snellen, R. T. Schilizzi, and K.-H. Mack
to be submitted

Survival rates of young radio-loud AGN and their environments



OMPACT steep spectrum (CSS) and gigahertz peaked spectrum (GPS) radio sources have very similar structures to FR I/II (Fanaroff & Riley 1974) radio sources, but on a much smaller angular scale with physical sizes of $\lesssim 20$ kpc and $\lesssim 1$ kpc (e.g. O'Dea 1998), respectively. Long after the discoveries of CSS (Conway, Kellermann & Long 1963) and GPS (Bolton, Gardener & Mackey 1963) radio sources, detailed studies only began during the early 1980s, when more observations at higher frequencies became available. At 2.7 GHz CSS and GPS sources start to make up a significant proportion of the bright flux density-selected samples (e.g. Peacock & Wall 1982). To explain the relatively small sizes of these sources two scenarios were proposed, (1) that GPS radio sources are very young radio-loud active galactic nuclei (AGN) which may evolve into CSS sources and eventually grow to become extended FR I/II (Fanaroff & Riley 1974) radio sources, or (2) that they are 'frustrated' radio sources, millions of years old, but confined by a dense interstellar medium (Baum et al. 1990). In recent years compelling evidence has accumulated in favour of the youth scenario. VLBI monitoring of the archetype GPS sources, that began in the early 1980s, has now conclusively shown these sources expand in size, implying source ages of 10^{2-3} years only (Owsianik et al. 1998; Owsianik & Conway 1998; Tschager et al. 2000; Polatidis & Conway 2003), in good agreement with spectral age estimates (Murgia 2003). In Chapter 4 we for the first time detect expansion for a low-luminosity GPS radio source, although at a significantly slower speed (de Vries et al. 2009b), indicating a correlation between expansion speed and radio luminosity. The measured expansion rates so far suggest that at least the brightest GPS radio sources eventually evolve into extended radio sources.

Samples of young radio-loud AGN have been used in a statistical way to constrain the luminosity evolution of radio sources. Relative number

statistics indicated that at a young age, radio sources must have significantly higher radio luminosities than when they are older (O’Dea & Baum 1996; Readhead et al. 1996; Fanti & Fanti 2003). The basic assumption of these, and many other, studies is the general belief that *all* GPS and CSS radio sources eventually evolve into FR II and/or FR I radio sources (e.g. Woltjer 2003). However, not much observational evidence is currently available to support this hypothesis. In this chapter we wish to investigate this assumption by comparing the sample size and observed characteristics of the CORALZ sample of compact radio sources at low redshift with mock populations of radio sources. The properties of these simulated radio sources are based on the analytic radio source models of Kaiser & Best (2007), fully taking into account size and luminosity evolution.

We describe the selection criteria and further details of the CORALZ sample in Sect. 6.1. The analytic radio source evolution model and its application is set out in Sect. 6.2. The results are presented in Sect. 6.3, discussed in Sect. 6.4, and we conclude with Sect. 6.5. Throughout this chapter we adopt the cosmological parameters from WMAP5 (Komatsu et al. 2009; $H_0 = 70.1 \text{ km s}^{-1} \text{ Mpc}^{-1}$, $\Omega_\Lambda = 0.721$, $\Omega_m = 0.279$).

6.1 CORALZ sample

Snellen et al. (2004) selected a sample of compact radio sources, CORALZ (COmpact RAdio sources at Low Redshift), with the aim of obtaining an unbiased view of young radio-loud AGN in the local universe. The sources in the CORALZ sample are significantly closer than the archetypal CSO and GPS sources available in the literature. Therefore these radio sources are in general less powerful than the archetypal CSO and GPS sources, and represent the population of more common, low-luminosity radio galaxies more closely.

The sample was selected on flux density ($S_{1.4 \text{ GHz}} > 100 \text{ mJy}$) and angular size ($\theta < 2''$) criteria. Using the Very Large Array (VLA) Faint Images of the Radio Sky at Twenty-centimeters survey (FIRST; White et al. 1997), the optical Automated Plate Measuring machine (APM) catalogue of the first Palomar Observatory Sky Survey (POSS-I) (McMahon & Irwin 1991), and follow-up observations, all radio sources identified

with bright galaxies were selected (red magnitude of $e < 16.5$ mag or blue magnitude of $o < 19.5$ mag). Simulations show that the sample is 95% statistically complete in the redshift range $0.005 < z < 0.16$, which contains 18 sources, and is referred to as the CORALZ core sample. A detailed description of the selection process can be found in Snellen et al. (2004), of which a summary is repeated here.

Nearly all (17/18) of the sources in the CORALZ core sample are classified as GPS and CSS sources, confirming that these are likely to be young radio sources. Also in line with their supposed youth, very long baseline interferometry (VLBI) observations reveal that the majority has compact symmetric morphologies (Chapter 3; de Vries et al. 2009a). At least one of the sources, CORALZ J083139+460800, is indisputably young, with a dynamical age of 245 ± 55 years, as reported in Chapter 4. Compared to the more extreme GPS and CSS sources from extensively studied flux density selected samples (e.g. Stanghellini et al. 1998; Fanti et al. 1990; Snellen et al. 2002), they have relatively low radio luminosities of $L_{1.4 \text{ GHz}} \sim 10^{24} \text{ W Hz}^{-1}$, in particular just below the break in the radio luminosity function.

6.2 Mock radio source populations

To investigate whether GPS and CSS radio sources eventually evolve into FR II and/or FR I radio sources, or whether there is a significant population of young sources that shut down early, we generate mock radio source populations, based on analytic radio source evolution models (Kaiser & Alexander 1997; Kaiser, Dennett-Thorpe & Alexander 1997; Kaiser & Best 2007). Subsequently the selection criteria of the CORALZ sample are applied to the mock radio sources, and the statistical properties of the resulting sample are compared to those of the CORALZ sample. In Sect. 6.2.1 the radio source evolution model is outlined, and in Sect. 6.2.2 the default values of the fixed input parameters are described. The properties that are randomly assigned to each radio source according to certain probability distributions are discussed in Sect. 6.2.3. Finally, the procedure to generate mock radio source populations and normalize the number density to the observed radio luminosity function (RLF) are described in Sects. 6.2.4 and 6.2.5, respectively.

6.2.1 Radio source evolution model

To generate mock radio source populations we used the radio source evolution model of Kaiser & Best (2007), which is based on the dynamical evolution model of Kaiser & Alexander (1997), and the evolution model for the radio emission of Kaiser, Dennett-Thorpe & Alexander (1997). The model assumes a relativistic jet with a constant jet power, which interacts with its surrounding medium, described by a power-law density distribution ρ ,

$$\rho = \rho_0 \left(\frac{r}{a_0} \right)^{-\beta}, \quad (6.1)$$

with a_0 a scale length, ρ_0 the density at this scale length, r the radial distance, and β the slope of the density distribution. The jet is assumed to remain laminar, due to a re-confinement shock, until it collides with the hot spot. With these assumptions, dimensional arguments give for the radio source size D ,

$$D = 2 c_1 \left(\frac{Q}{\rho_0 a_0^\beta} \right)^{1/(5-\beta)} t^{3/(5-\beta)}, \quad (6.2)$$

where c_1 is a constant, the value of which follows from the input parameters discussed in next section, t is the age of the radio source, and Q is the jet power.

Deriving a reliable estimate for the radio luminosity L_ν is more complicated, since many different physical processes are involved. In the Kaiser & Best (2007) model, electrons are accelerated at the hotspot such that their Lorentz factors γ initially follow a power law distribution,

$$n(\gamma) d\gamma = n_0(t_i) \gamma^{-m} d\gamma, \quad (6.3)$$

for $\gamma_{\min} < \gamma < \gamma_{\max}$, and with m the injection index, and n_0 the normalization at the injection time t_i . Subsequently the spectrum evolves due to synchrotron radiation energy losses, inverse Compton scattering of the electrons off cosmic microwave background (CMB) photons, and the adiabatic expansion of the lobe. Not included in the model is synchrotron self-absorption (SSA), which causes radio spectra, particularly those of young radio sources, to turn over at low frequencies. The derived radio luminosity estimates are therefore only valid at frequencies

higher than the turnover frequency. The effect of SSA on the total energy budget is expected to be negligible.

The expression for the radio luminosity L_ν is given by eqn. A19 (Kaiser & Best 2007):

$$L_\nu = f_L Q p^{(m+1)/4} t \int_{x_{\min}}^1 x^\epsilon [1 - \gamma g(x, t)]^{m-2} dx, \quad (6.4)$$

where f_L and ϵ are constants, the values of which follow from the input parameters discussed in next section, p is the pressure inside the lobe, and $g(x, t)$ is a function depending on the different energy loss processes. The integral sums the contributions to the luminosity from electrons that were injected into the lobe at different times. The integration variable $x = t_i/t$ runs from $x = x_{\min}$ up to $x = 1$, corresponding to material injected in the lobe over a range in time up to the current age t of the radio source. The lower integration limit x_{\min} corresponds to the specific injection time at which the injected material does not emit at the current age t of the radio source anymore.

For complete details of the model we refer the reader to Kaiser & Best (2007), and the reader should note that there also is an erratum to the paper (Kaiser & Best 2008).

6.2.2 Default model parameters

Table 6.1: — Model parameters. Other values are used only when clearly stated in the text.

Parameter	Value	Description
a_0	$6.2 \cdot 10^{19} \text{ m (2 kpc)}$	scale length of the density distribution
ρ_0	$7.2 \cdot 10^{-22} \text{ kg m}^{-3}$	density at scale length a_0
β	1.9	slope of the density distribution
Γ_{lobe}	4/3	adiabatic index of the material inside the lobe
Γ_{ext}	5/3	adiabatic index of the external material
Γ_B	4/3	adiabatic index of the magnetic field energy density
A	4.0	ratio of lobe length to lobe radius
m	2.14	injection index

In table 6.1 all model parameters, their values, and a short description of their meaning is given. We have used the same values as Bird, Martini & Kaiser (2008), in order to ensure the applicability of their estimates of

the maximum lifetime of radio-loud AGN. Since the density is described by a power law, it is scale invariant, so ρ_0 and a_0 are not independent parameters. The model only depends on their combination $\rho_0 a_0^\beta$. The material inside and outside the lobe are assumed to obey, respectively, relativistic and nonrelativistic equations of state, setting the values of the corresponding adiabatic indices to $\Gamma_{\text{lobe}} = 4/3$ and $\Gamma_{\text{ext}} = 5/3$.

6.2.3 Randomly assigned radio source properties

Upon creation, each radio source is assigned a random orientation, jet power, age, and redshift. The assumed probability distribution of each of these properties is outlined in this section. The angle ϕ between the radio source axis and the line of sight is assumed to be isotropically distributed. This means that $\cos(\phi)$ follows a uniform distribution. Radio source ages are drawn from a uniform distribution between $t_{\min} = 0$ and $t_{\max} = 1.5 \cdot 10^7$ yrs. This radio-loud AGN lifetime of ~ 15 million years is based on the study by Bird, Martini & Kaiser (2008), comparing the length distributions of FR II radio sources with mock radio source populations, using the same analytic models as used here.

We used the observed local radio luminosity function (RLF) to constrain the distribution of jet powers Q . Similar to Bird, Martini & Kaiser (2008), we assumed a power-law distribution of Q , which is based on the RLF derived by Sadler et al. 2002,

$$p(Q)dQ = \begin{cases} c_Q Q^{-1.62} dQ & Q_{\min} \leq Q \leq Q_{\max} \\ 0 & \text{otherwise} \end{cases}, \quad (6.5)$$

with c_Q a normalization constant. We adopt limits to the jet power distribution of $Q_{\min} = 5.0 \cdot 10^{33}$ W and $Q_{\max} = 1.0 \cdot 10^{37}$ W. A limit of $Q_{\max} = 1.0 \cdot 10^{39}$ W is used by Bird, Martini & Kaiser (2008). Although the Kaiser & Best (2007) model explains the break in the RLF qualitatively, we could not reproduce the steeper slope at high radio luminosities using this value. Therefore we adopted a lower value for Q_{\max} in order not to overpredict the number of very bright sources. Since the CORALZ core sample has typical radio luminosities below the break in the RLF, and the derived maximum AGN lifetimes of Bird, Martini & Kaiser (2008) are not very sensitive to the jet power distribution, we do not expect this difference to influence our results.

We assumed a uniform spatial distribution of radio sources, corresponding to a normalized redshift distribution of

$$\begin{aligned} n(z)dz &= \frac{1}{V_{total}} dV \\ &= \frac{4\pi D_c^2(z)}{4/3 \pi D_c^3(z=0.16) - 4/3 \pi D_c^3(z=0.005)} dD_c, \end{aligned} \quad (6.6)$$

with $D_c(z)$ the comoving distance to redshift z .

6.2.4 Generating mock radio source populations

Once a radio source has been assigned values for ϕ , Q , t , and z , its linear size is calculated from eqn. 6.2, projected on the plane of the sky using the orientation ϕ , and converted into an angular size through division by the angular diameter distance $D_A(z)$. We now proceed in calculating the flux density $S_{1.4 \text{ GHz}}$ of the radio source. First we solve for the lower integration limit x_{\min} , corresponding to the oldest material that at the current age t still contributes to the radio luminosity of the source. Subsequently eqn. 6.4 is evaluated to find $L_{(1+z)1.4 \text{ GHz}}$, which is then converted to the flux density $S_{1.4 \text{ GHz}}$ using the luminosity distance $D_L(z)$.

We produced 10^5 radio sources per simulation this way. All generated radio sources were used to determine the space density of powerful radio sources, by normalizing to the observed RLF (see Sect. 6.2.5). Only those sources satisfying the CORALZ angular size selection criterion, $\theta < 2''$, and the flux density criterion, $S_{1.4 \text{ GHz}} > 100 \text{ mJy}$, are selected for further analysis. We compare their statistical properties in Sect. 6.3 to those of the CORALZ core sample.

6.2.5 Normalization to the radio luminosity function

In order to determine the space density of the simulated radio sources, we need to normalize our mock populations to the observed local radio luminosity function (RLF). The RLF of radio-loud AGN in general is described by a broken power law,

$$\Phi(L_\nu) = C \left[\left(\frac{L_\nu}{L_*} \right)^{\zeta_{\text{low}}} + \left(\frac{L_\nu}{L_*} \right)^{\zeta_{\text{high}}} \right]^{-1}, \quad (6.7)$$

where $C = 2\Phi(L_*)$ is a normalisation constant, and ζ_{low} and ζ_{high} are the slopes of the distribution below and above the break luminosity, L_* , respectively. Note that the RLF has dimensions of number density per unit *logarithm* of radio luminosity. Mauch & Sadler (2007) found best fitting values for the local RLF at 1.4 GHz of:

$$\begin{aligned} C &= 10^{-5.50 \pm 0.25} \text{ mag}^{-1} \text{ Mpc}^{-3} \\ L_* &= 10^{24.59 \pm 0.30} \text{ W Hz}^{-1} \\ \zeta_{\text{low}} &= 0.49 \pm 0.04 \\ \zeta_{\text{high}} &= 1.27 \pm 0.18 \end{aligned} \tag{6.8}$$

We now scale the RLF of the mock radio source population to match the observed RLF of Mauch & Sadler (2007). This way we get an estimate of n_{AGN} , the number of powerful (with jet powers in the range described in Sect. 6.2.3) radio sources per Mpc^3 . The value we derive for n_{AGN} only depends very weakly on our assumed parameters, except for the lower limit of the jet power distribution Q_{min} , as expected (the number of radio sources one detects in a given volume likewise depends on the survey depth in flux density). We will therefore need to calculate n_{AGN} for every set of input parameters and jet power distributions.

In Fig. 6.1 the RLF of the mock radio source population is shown (drawn histogram), along with the best fit to the observed local RLF of Mauch & Sadler (2007) as described by eqns. 6.7 and 6.8.

By normalizing to the observed local RLF, we derived a value for the number density of powerful radio sources of $n_{\text{AGN}} = 1.3 \cdot 10^{-4}$, for the default model parameters.

6.3 Results

6.3.1 Predicted CORALZ sample sizes

Using the fraction of radio sources that satisfy the CORALZ selection criteria, we can predict the sample size of the CORALZ core sample and compare the result with the real size of the CORALZ core sample, 18 radio sources. Since the CORALZ core sample is 95% complete within the redshift range $0.005 < z < 0.16$, the predicted sample size N_{pred} of the CORALZ core sample is

$$N_{\text{pred}} = f_{\text{CORALZ}} \cdot n_{\text{AGN}} \cdot 0.95 \cdot V_{\text{CORALZ}}, \tag{6.9}$$

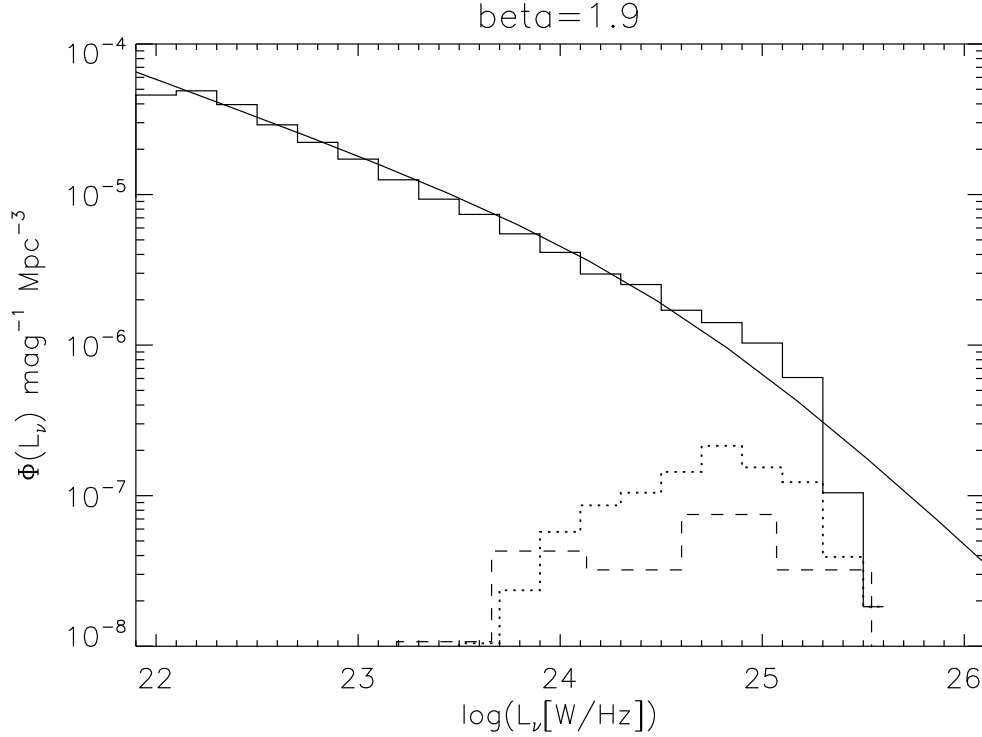


Figure 6.1: — The RLF of the mock radio source population (drawn histogram), and the best fit to the observed local RLF of Mauch & Sadler (2007; drawn line). The subsample of radio sources satisfying the CORALZ selection criteria is also indicated (dotted histogram), as well as the actual RLF of the CORALZ core sample (dashed histogram). The RLF is in units of number of sources per magnitude in radio luminosity, per Mpc^3 .

where f_{CORALZ} is the fraction of simulated radio sources satisfying the CORALZ selection criteria, and V_{CORALZ} is the comoving volume integrated over the redshift range $0.005 < z < 0.16$ and the solid angle of the sky area from which the CORALZ sample was selected. The resulting predicted sample sizes are presented in table 6.2. The first value is for the default model parameters, with the slope of the density distribution $\beta = 1.9$. The following values are for different values of β , ranging from a flat to an extremely steep density distribution.

Table 6.2: — Predicted sample size N_{pred} of the CORALZ core sample for a range of values for β .

β	1.9	0.1	0.5	1.0	1.5	2.5	3.0
N_{pred}	40	27	28	30	33	57	94

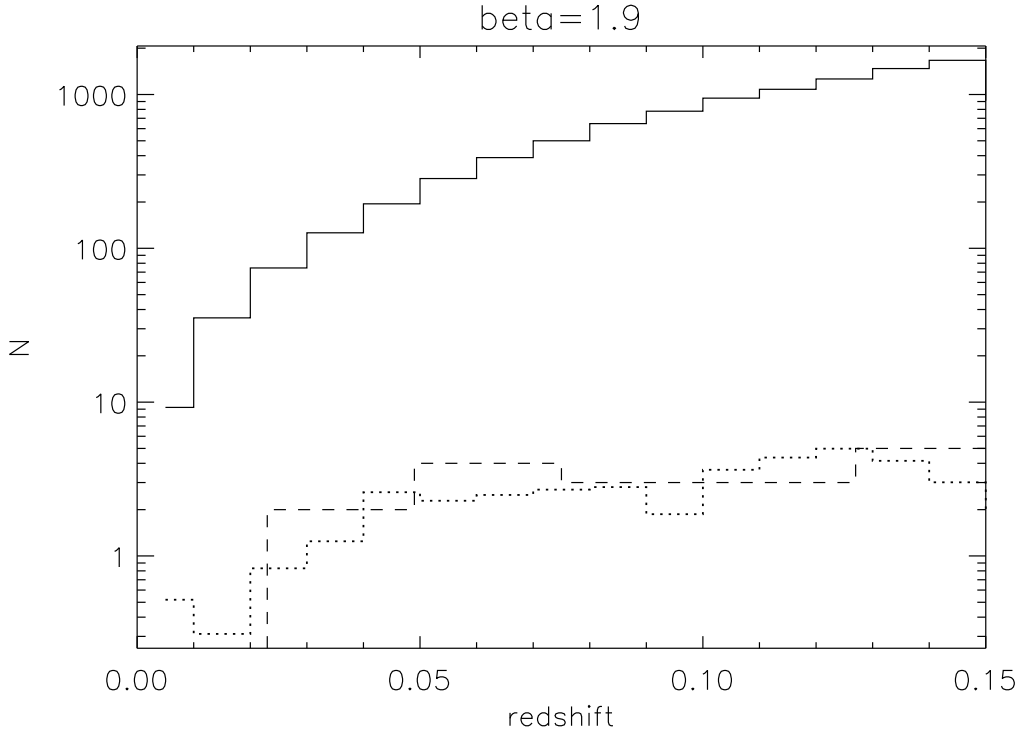


Figure 6.2: — The redshift distribution of all simulated radio sources (drawn histogram), of those simulated sources that satisfy the CORALZ selection criteria (dotted histogram), and of the observed CORALZ core sample (dashed histogram). The default model parameters were used, and the distribution is normalized to the volume of the CORALZ core sample.

6.3.2 Distributions of radio source properties

In Fig. 6.1 we presented the RLF of the mock radio source population (drawn histogram), along with the best fit to the observed local RLF of Mauch & Sadler (2007). In this figure, the subsample of radio sources satisfying the CORALZ selection criteria is also indicated (dotted histogram), as well as the actual RLF of the CORALZ core sample (dashed histogram). The RLF of the CORALZ core sample agrees well with the RLF of simulated sources satisfying the CORALZ selection criteria. In Fig. 6.2 we show the redshift distribution of all simulated radio sources (drawn histogram), of those simulated sources that satisfy the CORALZ selection criteria (dotted histogram), and of the observed CORALZ core sample (dashed histogram). The redshift distribution of the mock radio source population also nicely agrees with the observed redshift distribution of the CORALZ sample.

In Fig. 6.3 we present the distribution of projected linear sizes for the default model parameters, normalized to the total number of simu-

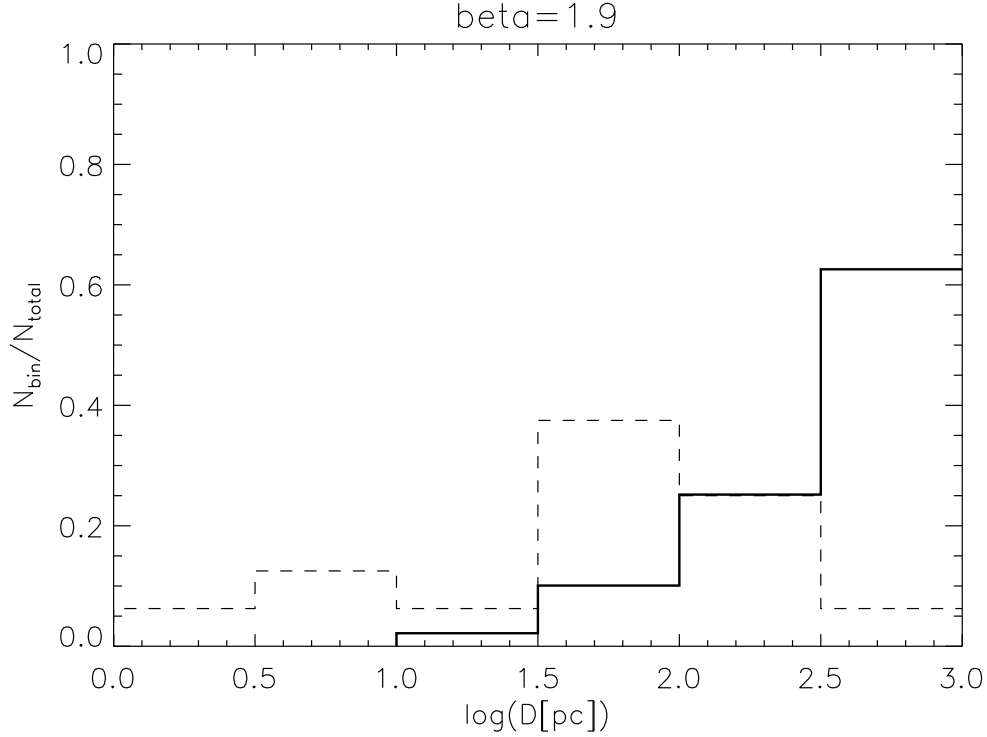


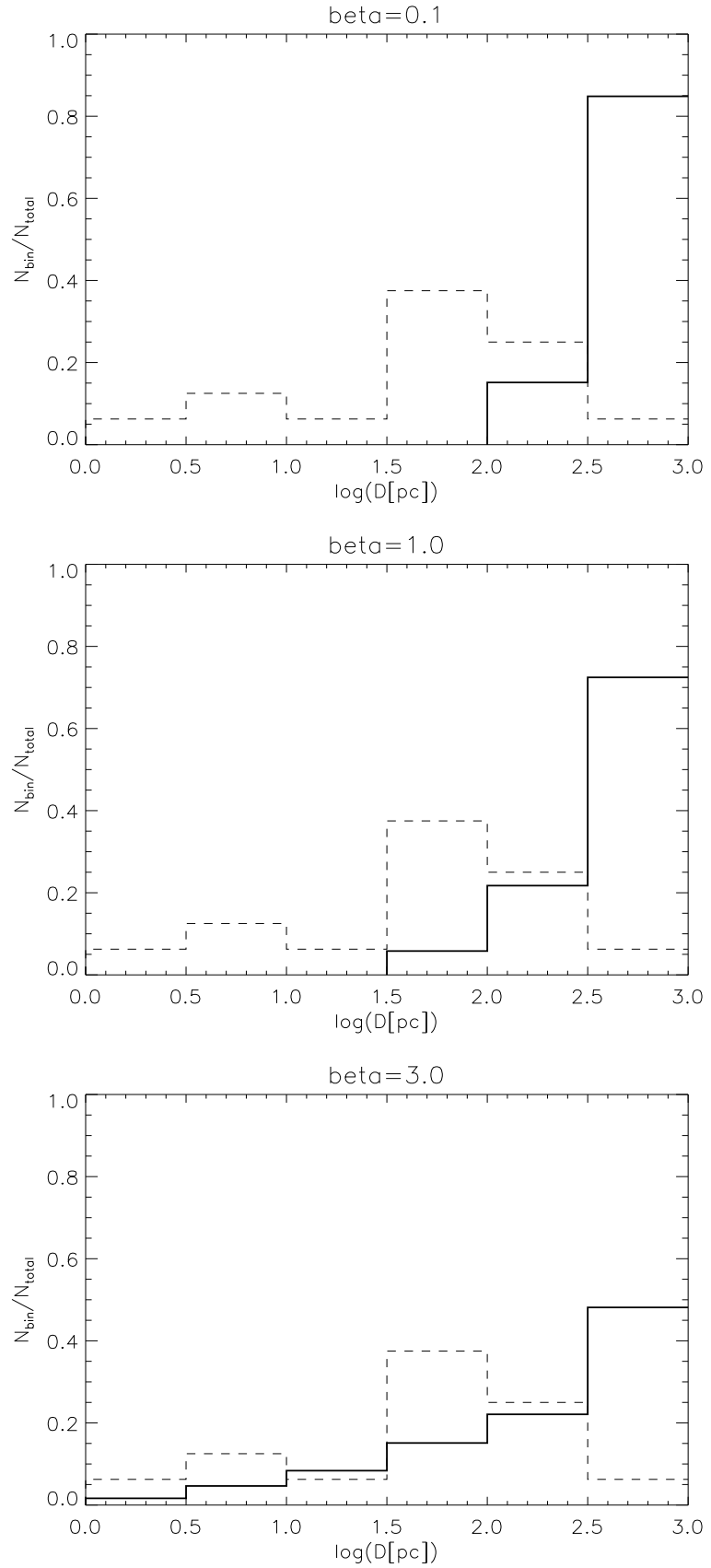
Figure 6.3: — The distribution of projected linear sizes for the default model parameters, normalized to the total number of simulated radio sources. The dashed histogram is the size distribution of the CORALZ core sample from Chapter 3 (de Vries et al. 2009a). Projected sizes range from 1 pc to 1 kpc.

lated radio sources (10^5). The dashed histogram is the size distribution of the CORALZ core sample from Chapter 3 (de Vries et al. 2009a). The projected sizes of the CORALZ core sample span a wide range from ~ 1 pc to ~ 1 kpc. Note that the number statistics of the simulated radio sources are much better than for the CORALZ core sample of 18 radio sources. The size distribution of the latter is therefore expected to be noisier. However, it is clear that the size distribution of the CORALZ core sample is remarkably flat in logarithmic space.

In Fig. 6.4 we present similar size distributions as in Fig. 6.3, but now for a range of different slopes of the density profile β . The dashed histogram again is the size distribution of the CORALZ core sample. The size distribution becomes flatter, and more similar to that of the CORALZ core sample, for increasing values of β .

We compare the distributions of the redshift z , the size D , and the luminosity L_ν of the mock radio source populations with those of the CORALZ core sample. For this purpose we used the Mann-Whitney test on the simulated populations, with a range of values for the slope of

Figure 6.4 — The normalized distribution of projected linear sizes for different slopes of the density profile β . The dashed histogram is the size distribution of the CORALZ core sample. The used value of β is indicated at the top of each figure.



the density profile β . Table 6.3 shows the results, indicating the Z -value and the corresponding probability that the simulated sources are drawn from the same population as the CORALZ sources. For large sample sizes, the Z -value of the Mann-Whitney test should follow a standard normal distribution, and its absolute value can therefore be regarded as the significance σ that the distributions are different. A positive Z -value means the simulated values are significantly higher than the observations and vice versa. For example $Z = 5.05$ for the size distribution with $\beta = 1.9$ means that the simulated radio sources on average have larger sizes to a $5\text{-}\sigma$ level of significance. We find that while the redshift and luminosity distributions are in agreement with being drawn from the same distribution for basically all values of β , the simulated size distributions are always significantly different, but favor a steep density profile.

Table 6.3: — Results of the Mann-Whitney test. The distributions of the redshift z , the size D , and the luminosity L_ν of the mock radio source populations are compared with those of the CORALZ core sample. The assumed slope of the density profile β is indicated.

β		Z -value	$p(\text{same distribution})$
0.1	z	0.44	$3.29 \cdot 10^{-1}$
	D	6.09	0.0
	L_ν	0.96	$1.68 \cdot 10^{-1}$
0.5	z	-0.18	$4.28 \cdot 10^{-1}$
	D	5.41	$5.96 \cdot 10^{-8}$
	L_ν	0.05	$4.80 \cdot 10^{-1}$
1.0	z	0.00	$4.98 \cdot 10^{-1}$
	D	5.81	0.0
	L_ν	0.61	$2.69 \cdot 10^{-1}$
1.5	z	-0.20	$4.19 \cdot 10^{-1}$
	D	5.19	$1.19 \cdot 10^{-7}$
	L_ν	0.08	$4.67 \cdot 10^{-1}$
1.9	z	-0.57	$2.84 \cdot 10^{-1}$
	D	5.05	$2.38 \cdot 10^{-7}$
	L_ν	0.35	$3.65 \cdot 10^{-1}$
2.5	z	-0.73	$2.32 \cdot 10^{-1}$
	D	4.24	$1.12 \cdot 10^{-5}$
	L_ν	0.01	$4.96 \cdot 10^{-1}$
3.0	z	-1.07	$1.42 \cdot 10^{-1}$
	D	3.33	$4.37 \cdot 10^{-4}$
	L_ν	-0.25	$4.01 \cdot 10^{-1}$

6.4 Discussion

The predicted sample sizes are in reasonable agreement with the actual number of sources in the CORALZ core sample, although they are higher for all values of the density slope β . Except for the extremely steep density profiles, the sample sizes agree within a factor of two (see Sect. 6.3.1), which can easily be accounted for by a somewhat longer lifetime of radio-loud AGN, $t_{max} \simeq 3 \cdot 10^7$ years. The fact that the predicted sample sizes are on the large side, does constrain the fraction of GPS and CSS sources that eventually evolves into extended FR I/II radio sources. If the majority of the GPS and CSS sources were to shut down and fade before growing to larger scales, the maximum lifetime of radio-loud AGN would have to be much larger than 10^8 years, which is unlikely. Thus early deaths of GPS and CSS sources may occur, but not for the majority of the sources.

In Sect. 6.3.2 we compared the distributions in redshift, luminosity, and size for the CORALZ core sample and mock radio source populations, using the Mann-Whitney test. We found that the distributions in redshift and luminosity are in good agreement with being drawn from the same population as the mock radio sources, for all density profiles. On the other hand, the distributions of the projected physical sizes are significantly different for any value of the density slope, within a reasonable range of $0.0 \leq \beta \leq 3.0$. Although usually the density profile is assumed to flatten out in the center (e.g. Kaiser & Best 2007), observations do show high amounts of gas and dust towards the nuclei of young radio sources (Mack et al. 2009), suggesting that the density profiles of young radio-loud AGN could remain steep near the center. Indeed, for steeper density profiles ($\beta \gtrsim 2$) the distributions are more similar than for a flat profile. This means that either the density profile in the center must be very steep, or many of the most compact radio sources in the CORALZ core sample must shut down and fade before they grow larger than ~ 100 pc. If we assume for example $\beta = 1.0$, and require the size distribution to be (marginally) consistent with the CORALZ core sample, this requires that over 95% of the CORALZ sources with sizes less than 100 pc must disappear before they grow larger than this limit. However, this is in contradiction with the results on predicted sample sizes, as this would require the typical lifetime of a radio source to be

much larger than 10^8 years. Using the fiducial value of Bird, Martini & Kaiser (2008) and Kaiser, Dennett-Thorpe & Alexander (1997) of $\beta = 1.9$, about 80% of the CORALZ sources smaller than 100 pc must shut down early. This would correspond to a more realistic typical AGN lifetime of $t_{max} \simeq 6 \cdot 10^7$ years. We therefore conclude that the density profile of the external medium in GPS and CSS host galaxies remains steep near the center.

6.5 Conclusions

We have generated mock radio source populations and compared their properties with the CORALZ core sample. The results show that:

- The distributions of redshift and radio luminosity of the mock radio source populations are in agreement with being drawn from the same distribution as the CORALZ core sample.
- The size distribution of the CORALZ core sample differs from those of the simulated radio sources, and strongly favors a steep density profile.
- In order to explain the size distribution of the CORALZ core sample, a significant fraction ($\sim 80\%$ for preferred parameter values) of the most compact CORALZ sources must shut down and fade before evolving into FR I/II radio sources.
- On the other hand, comparison with the predicted sample sizes shows that a large fraction of the total number of CORALZ sources cannot suffer an early death, otherwise an unreasonably long maximum lifetime of radio-loud AGN activity would be required.
- To match both the sample size and the radio source size distribution of the CORALZ core sample, the density profile of the external medium in GPS and CSS host galaxies must remain steep near the center.

References

- Allen, L. R., Hanbury Brown, R., & Palmer, H. P. 1962, MNRAS, 125, 57
 Baade, W., & Minkowski, R. 1954, ApJ, 119, 206
 Baum S.A., O'Dea C.P., Murphy D.W., de Bruyn A.G., 1990, A&A, 232, 19
 Bennett, A. S. 1962, MNRAS, 125, 75
 Bird, J., Martini, P., & Kaiser, C. 2008, ApJ, 676, 147
 Bolton, J. G., Gardner, F. F., & Mackey, M. B. 1963, Nature, 199, 682

- Conway, R. G., Kellermann, K. I., & Long, R. J. 1963, MNRAS, 125, 261
- de Vries, N., Snellen, I. A. G., Schilizzi, R. T., Mack, K.-H., & Kaiser, C. R. 2009, A&A, 498, 641, Chapter 3
- de Vries, N., Snellen, I. A. G., Schilizzi, R. T., & Mack, K.-H. 2009, A&A, accepted, Chapter 4
- Edge, D. O., Shakeshaft, J. R., McAdam, W. B., Baldwin, J. E., & Archer, S. 1959, MmRAS, 68, 37
- Fanaroff, B. L., & Riley, J. M. 1974, MNRAS, 167, 31P
- Fanti, R., Fanti, C., Schilizzi, R. T., Spencer, R. E., Nan Rendong, Parma, P., van Breugel, W. J. M., & Venturi, T. 1990, A&A, 231, 333
- Fanti, C., & Fanti, R. 2003, Radio Astronomy at the Fringe, ed. J. A. Zensus, M. H. Cohen, & E. Ros, 300, 81
- Jansky, K. G. 1933, Nature, 132, 66
- Kaiser, C. R., & Alexander, P. 1997, MNRAS, 286, 215
- Kaiser, C. R., Dennett-Thorpe, J., & Alexander, P. 1997, MNRAS, 292, 723
- Kaiser, C. R., & Best, P. N. 2007, MNRAS, 381, 1548
- Kaiser, C. R., & Best, P. N. 2008, MNRAS, 384, 1742
- Komatsu, E., et al. 2009, ApJS, 180, 330
- Laing, R. A., Riley, J. M., & Longair, M. S. 1983, MNRAS, 204, 151
- Mack, K.-H., Snellen, I. A. G., Schilizzi, R. T., & de Vries, N. 2009, Astronomische Nachrichten, 330, 217
- Mauch, T., & Sadler, E. M. 2007, MNRAS, 375, 931
- McMahon R. G., Irwin M. J., 1991, in Proceedings of the conference on 'Digitised Optical Sky Surveys', eds. H. T. MacGillivray, E. B. Thomson (Kluwer Acad. Publ., Dordrecht), p. 417
- Murgia M., 2003, PASA, 20, 19M
- O'Dea, C. P. & Baum, S. A. 1996, in GPS and CSS radio sources, ed. I. A. G. Snellen, R. T. Schilizzi, H. J. A. Röttgering & M. N. Bremer, 241
- O'Dea, C. P. 1998, PASP, 110, 493
- Owsianik I., Conway J.E., 1998, A&A, 337, 69
- Owsianik I., Conway J.E., Polatidis A.G., 1998, A&A, 336, L37
- Peacock, J. A., & Wall, J. V. 1982, MNRAS, 198, 843
- Polatidis A.G., Conway J.E., 2003, PASA, 20, 69P
- Readhead, A. C. S., Taylor, G. B., Xu, W., Pearson, T. J., Wilkinson, P. N., & Polatidis, A. G. 1996, ApJ, 460, 612
- Sadler, E. M., et al. 2002, MNRAS, 329, 227
- Snellen, I. A. G., Lehnert, M. D., Bremer, M. N., & Schilizzi, R. T. 2002, MNRAS, 337, 981
- Snellen, I. A. G., Mack, K.-H., Schilizzi, R. T., & Tschager, W. 2004, MNRAS, 348, 227
- Stanghellini, C., O'Dea, C. P., Dallacasa, D., Baum, S. A., Fanti, R., & Fanti, C. 1998, A&AS, 131, 303
- Tschager W., Schilizzi R.T., Röttgering H.J.A., Snellen I.A.G., Miley G.K., 2000, A&A, 360, 887
- White, R. L., Becker, R. H., Helfand, D. J., & Gregg, M. D. 1997, ApJ, 475, 479
- Woltjer, L. 2003, Publications of the Astronomical Society of Australia, 20, 157

Nederlandse samenvatting

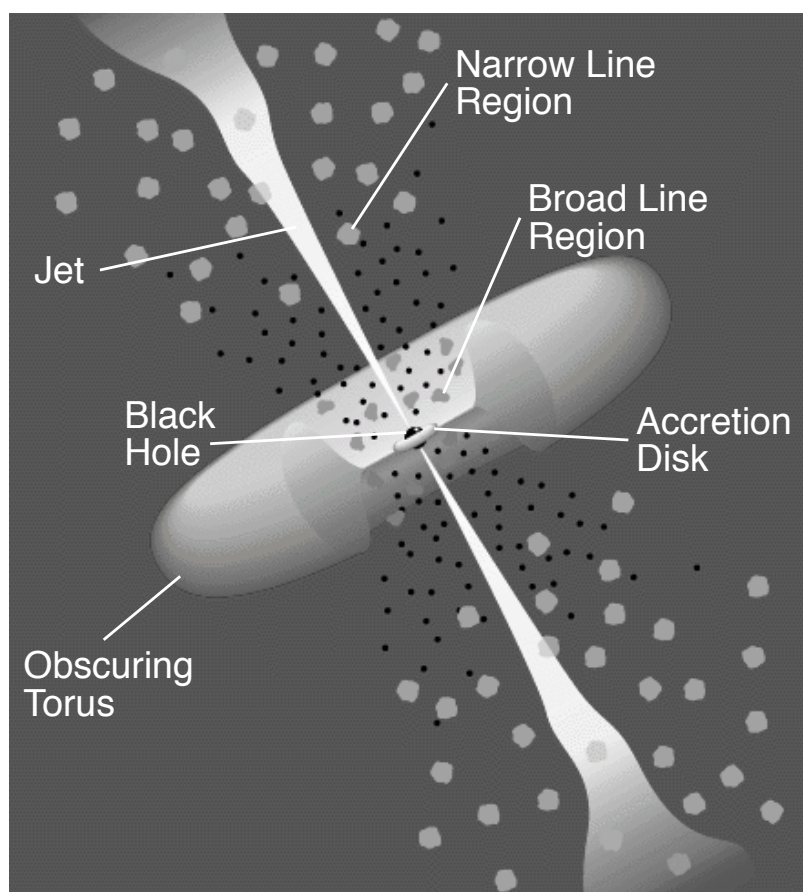


TERRENSTELSLS, enorme hoeveelheden sterren die om hun gezamenlijke massa-middelpunt bewegen, behoren tot de prachtigste objecten in het heelal. Vanaf de aarde zijn er vier sterrenstelsels met het blote oog te zien. Ten eerste natuurlijk de Melkweg, ons eigen sterrenstelsel, waarin de zon slechts een onopvallend sterretje is tussen de andere circa 300 miljard sterren. Vlakbij de Melkweg, op een afstand van minder dan 200 000 lichtjaar, zweven twee dwergsterrenstelsels die binnen een paar miljard jaar zullen worden verscheurd en opgeslokt door de Melkweg met haar veel sterkere aantrekkingskracht. De vierde is het sterrenstelsel Andromeda, onze naaste buur die ongeveer even zwaar is als de Melkweg, maar toch aanzienlijk meer sterren bevat (circa een triljoen).

Hoewel deze vier sterrenstelsels met het blote oog zichtbaar zijn, heeft de mens lange tijd niet geweten dat die lichtvlekken daadwerkelijk aparte sterrenstelsels zijn, net als de Melkweg. Dit komt doordat het bijzonder moeilijk is om de duizelingwekkende afstanden in het heelal te meten. Daardoor dacht men tot het begin van de twintigste eeuw dat deze nevels zich binnen de Melkweg bevonden en dus al veroorzaakt konden worden door een sterrenhoopje of wat oplichtend gas. Pas nadat Heber D. Curtis in 1917 ontdekte dat de Andromeda-nevel een 'eiland-heelal' (een apart sterrenstelsel buiten de Melkweg) was, realiseerde men zich dat vele nevels in feite sterrenstelsels waren, bestaande uit ontzagwekkende hoeveelheden sterren. Met behulp van de telescoop, die dit jaar zijn 400^{ste} verjaardag viert, hebben sterrenkundigen nog miljarden sterrenstelsels ontdekt, elk bestaande uit enkele tientallen miljoenen tot triljoenen sterren.

Sterrenstelsels bestaan uit meer dan alleen sterren. Tussen de sterren bevinden zich grote hoeveelheden gas en stof, waaruit nieuwe sterren gevormd kunnen worden. Bovendien bevindt zich in het centrum van vrijwel alle grote sterrenstelsels een superzwaar zwart gat. Meestal houdt het zich stil, maar af en toe wordt dit gretige monster gevoed met

vers gas, hetgeen gepaard gaat met heftige verschijnselen, een toestand die sterrenkundigen 'actief' noemen.



Figuur 1 — Het standaard unificatiemodel voor actieve galactische kernen (niet op schaal). Het centrale zwarte gat (*black hole*) en de daar omheen draaiende accretieschijf (*accretion disk*) zijn aangegeven. Brede emissielijnen worden alleen uitgezonden door gaswolken nabij het zwarte gat en zijn daardoor alleen van bovenaf zichtbaar. Zien we een AGN van de zijkant, dan worden de brede emissielijnen en warmtestraling van de accretieschijf geabsorbeerd door een ring van gas en stof, de torus. De verder weg gelegen gaswolken zenden smalle emissielijnen uit, die altijd zichtbaar zijn. Loodrecht op de accretieschijf kan in beide richtingen een straalstroom (*jet*) ontstaan. Credit: C. M. Urry & P. Padovani (1995).

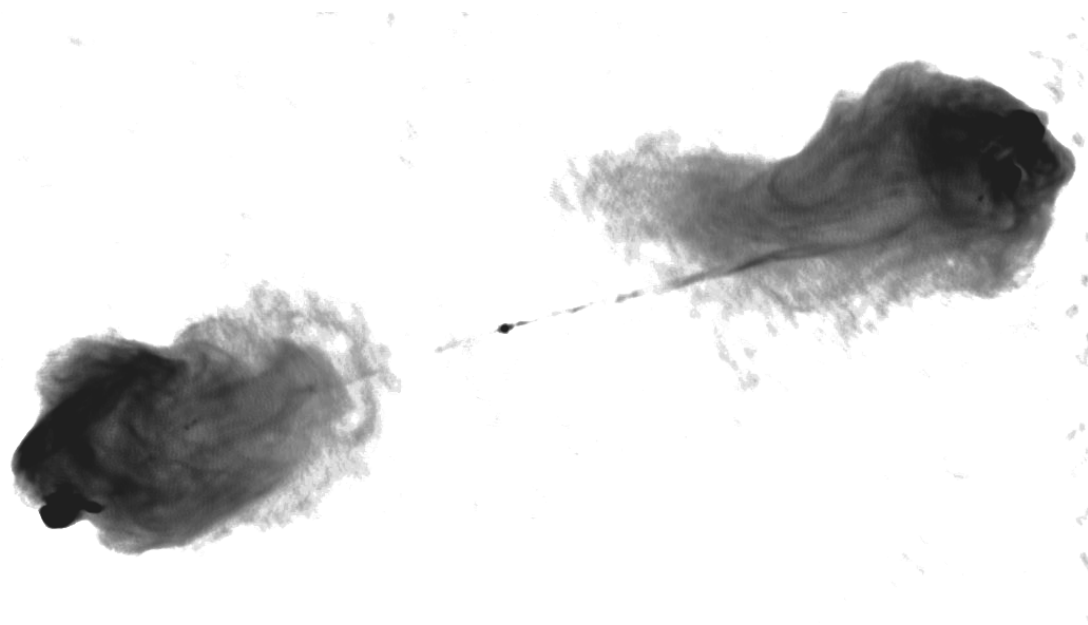
Actieve sterrenstelsels

Er is een scala aan kenmerkende eigenschappen die erop kunnen duiden dat een sterrenstelsel actief is. Al deze verschijnselen ontstaan vanuit een klein gebied, dat de actieve galactische nucleus (AGN) genoemd

wordt en gelegen is rondom het superzware zwarte gat in het centrum van het sterrenstelsel (zie figuur 1). In de optische spectra van de meeste AGN zijn smalle emissielijnen zichtbaar, met lijnbreedtes die overeenkomen met snelheden van een paar honderd kilometer per seconde. Sommige AGN hebben ook brede emissielijnen, met lijnbreedtes van een paar duizend kilometer per seconde. De helderste actieve sterrenstelsels, quasars genaamd, produceren zóveel licht in hun kern dat het sterrenstelsel zelf niet of nauwelijks meer zichtbaar is. Deze enorme lichtkracht wordt opgewekt door gas dat met hoge snelheid naar het superzware zwart gat valt, hier omheen gaat draaien en zo een accretieschijf vormt, die door wrijving extreem verhit raakt. Via allerlei natuurkundige processen kunnen AGN licht uitzenden in elk gedeelte van het elektromagnetische spectrum.



Figuur 2 — Very Large Array (VLA) radiokaart van 3C31, een radiobron van het type FR I. De woelige straalstromen waaieren uit en worden zwakker naarmate ze zich verder van de AGN verwijderen. De radiobron heeft een grootte van ongeveer 1,3 miljoen lichtjaar. Credit: NRAO.



Figuur 3 — Cygnus A, de kosmische radiobron die als eerste ontdekt werd. Cygnus A is een typisch voorbeeld van een FR II radiobron, met twee grote radiolobben en aan de uiteinden heldere *hotspots*. Tevens is de actieve galactische kern zichtbaar, waaruit de twee kleine straalstromen ontspruiten. Cygnus A is van vergelijkbare grootte als 3C31 in figuur 2. Credit: NRAO.

De structuur van AGN valt met het scheidend vermogen van huidige astronomische observatoria niet bloot te leggen. De radiostraling die door de AGN uitgezonden wordt, is vaak wel spatiëel oplosbaar en strekt zich uit over enorme afstanden, zelfs voorbij de buitenste delen van het sterrenstelsel. Deze radiostraling wordt veroorzaakt door elektronen die met bijna de lichtsnelheid rond magnetische veldlijnen draaien en zo synchrotron straling produceren. De elektronen die deze straling uitzenden worden vanuit de AGN via twee straalstromen, die in beide richtingen loodrecht staan op de accretieschijf, over duizelingwekkende afstanden aangevoerd. Sommige straalstromen hebben een woelige structuur en worden lichtzwakker naarmate ze verder van de AGN af bewegen. Deze radiobronnen worden Fanaroff & Riley type I (FR I) genoemd. Bij radiobronnen van het Fanaroff & Riley type II (FR II) blijven de straalstromen smal en gestroomlijnd, totdat ze bij de heldere uiteinden, de *hotspots*, in botsing komen met interstellair of intragalactisch gas. Het relativistische plasma dat tijdens deze botsing wordt geproduceerd, vult enorme lobben achter het schokfront. Hier verliest het

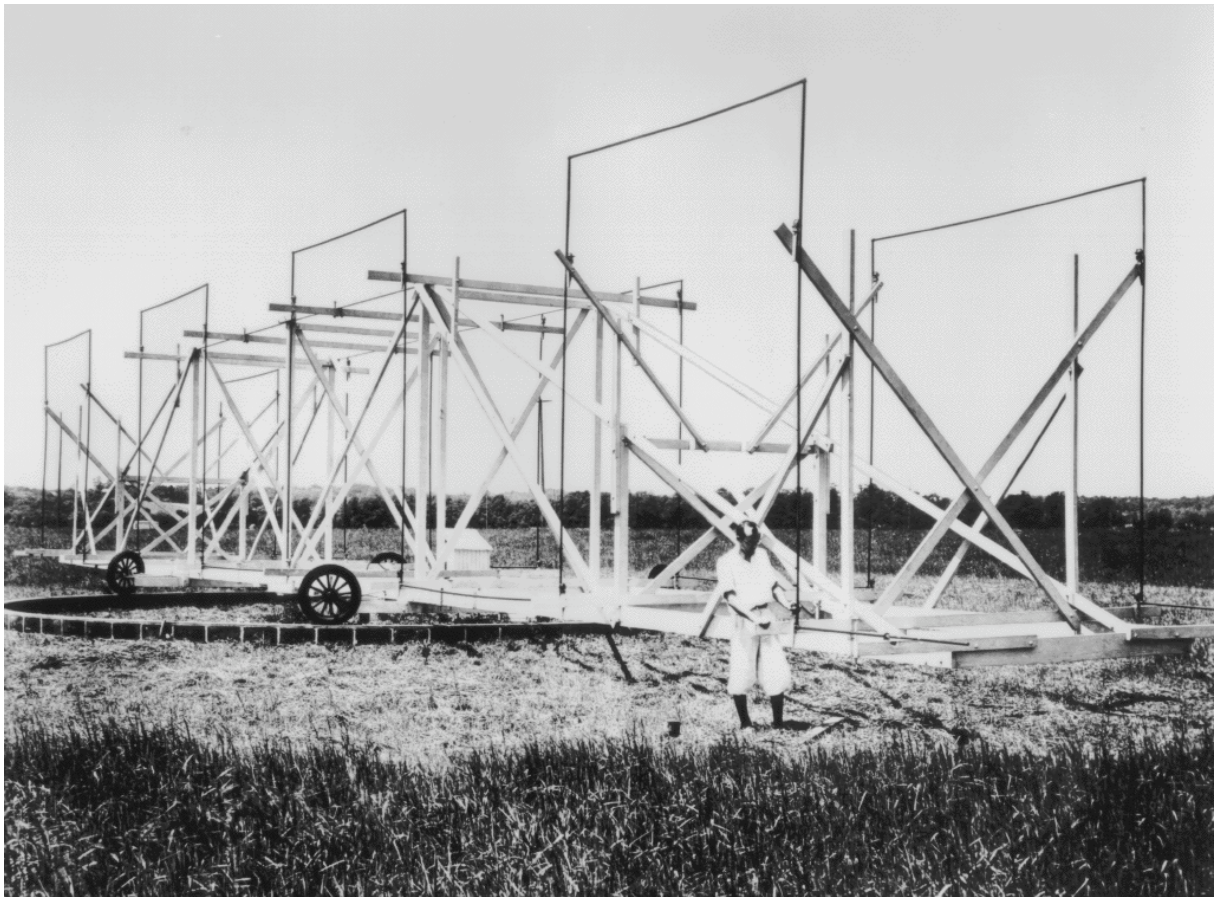
langzaam zijn energie door synchrotron radiostraling uit te zenden. In figuur 2 en 3 zijn voorbeelden van radiobronnen van type FR I en FR II weergegeven. Deze twee klassen van AGN die sterke radiostraling uitzenden, bevinden zich vrijwel altijd in hele zware elliptische sterrenstelsels. Aan de andere kant produceren veel AGN, vooral AGN die in het centrum van (minder zware) spiraalstelsels te vinden zijn, geen straalstromen of sterke radiostraling.

Deze variëteit aan kenmerken van AGN heeft geleid tot de definitie van een grote hoeveelheid AGN klassen. Aangezien algemeen aangenomen wordt dat alle AGN door hetzelfde natuurkundige mechanisme worden aangedreven - het verslinden van materie door een zwart gat - is het opmerkelijk dat AGN er zo verschillend uit kunnen zien. De eerste pogingen om de verscheidenheid aan verschijnselen met één model te beschrijven, hadden betrekking op de oriëntatie van de AGN. Deze overkoepelende theorieën waren gebaseerd op een cilindrisch-symmetrisch model, waarin het centrale object omgeven wordt door een torus (de vorm van een donut) van gas en stof (zie figuur 1). Als we de torus vanaf de zijkant zien, blijven de centrale delen van de AGN, zoals het zwarte gat met de accretieschijf, verborgen. Als een AGN zo georiënteerd is dat we de torus van de bovenkant zien, zijn deze delen wel zichtbaar. Ondanks het succes in het verklaren van een aantal eigenschappen van AGN, blijven nog veel zaken onopgelost. De theorie verklaart bijvoorbeeld niet waarom sommige AGN krachtige radiostraling uitzenden, terwijl andere dat niet doen.

Radio uit de ruimte?

De studie naar radiobronnen uit de ruimte vindt zijn oorsprong in een toevallige ontdekking van de natuurkundige en radio-technicus Karl Jansky. In 1928, toen de radio-communicatie nog in zijn kinderschoenen stond, werd Karl Jansky aangesteld door Bell Laboratories om diverse vormen van ruis in 'korte-golf' radiostraling te onderzoeken. Hij bouwde hiervoor een antenne van meer dan dertig meter, die rondgedraaid kon worden om radio straling uit alle richtingen op te kunnen vangen (zie figuur 4). Jansky ontdekte drie bronnen van ruis: nabije onweersbuien, verder weg gelegen onweersbuien waarvan het signaal

door een hoge laag in de atmosfeer wordt weerkaatst, en een derde, mysterieuze bron van radiostraling, waarvan hij pas na ruim een jaar, in 1933, kon vaststellen dat deze straling uit het centrum van de melkweg afkomstig was.



Figuur 4 — Karl Jansky met zijn radio antenne, waarmee hij in 1933 radio-straling uit de ruimte ontdekte. Credit: NRAO.

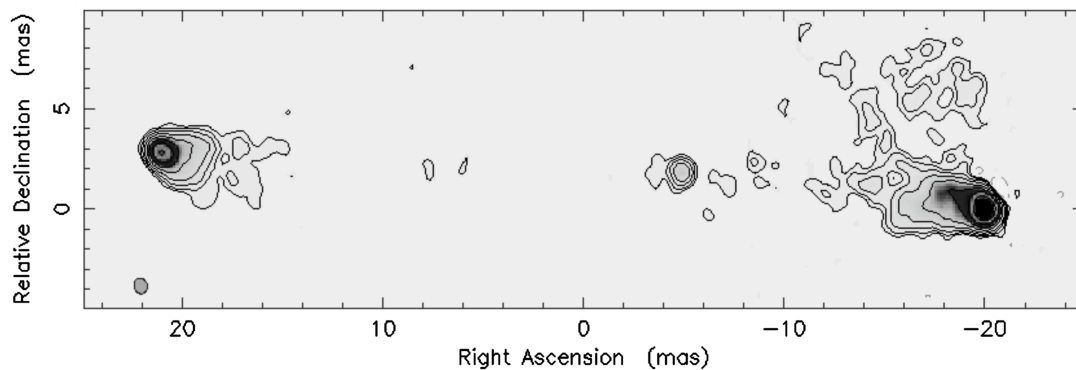
Kunstmatige radiostraling wordt vaak opgewekt met behulp van een antenne. Met wisselstroom is het mogelijk om elektronen snel langs de antenne op en neer te laten bewegen, zodat de elektronen radiogolven gaan uitzenden. Door de intensiteit of de frequentie van de radiogolven te variëren kunnen radiogolven gebruikt worden om signalen over te brengen. Voor de ontdekking van Jansky werd al wel gespeculeerd over radiostraling vanuit de ruimte, met name warmtestraling op radiofrequenties, afkomstig van de zon. Aangezien dit proces extreem zwakke

radiogolven op zou wekken, was Jansky's ontdekking toch tamelijk onverwacht. De radiogolven die hij detecteerde waren veel sterker dan verwacht, doordat ze veroorzaakt werden door razendsnel cirkelende elektronen, enigszins te vergelijken met het op en neer dansen van elektronen in een radioantenne.

Twintig jaar na de ontdekking van Karl Jansky werd de eerste radiobron buiten de Melkweg ontdekt door de astronomen Baade en Minowski. Zij identificeerden de sterkste radiobron in het sterrenbeeld Zwaan, Cygnus A, met het centrum van twee samensmeltende sterrenstelsels. Na deze ontdekking ontwikkelde de radio-sterrenkunde zich snel, hetgeen resulteerde in de publicatie van de 3C radio catalogus en zijn opvolgers. Snel werd ontdekt dat het merendeel van deze heldere radiobronnen grote, tweevoudige structuren hadden (zie figuur 3), vaak groter dan het sterrenstelsel waarin het zich bevond. De radiobronnen waarvan de structuur met het scheidend vermogen van de eerste radiotelescopen niet kon worden ontrafeld, werden geclassificeerd op basis van hun radio spectra. Dit leidde tot de ontdekking van *compact steep spectrum* (CSS) en *gigahertz peaked spectrum* (GPS) radiobronnen in 1963. Later werd het wel mogelijk de structuur van deze compacte radiobronnen te bestuderen, met behulp van *very long baseline interferometry* (VLBI). Met deze techniek worden de signalen van een aantal radiotelescopen gecombineerd om zo het scheidend vermogen van één radiotelescoop, ter grootte van de langste afstand tussen de afzonderlijke telescopen, te simuleren. De structuur van CSS en GPS radiobronnen bleek vergelijkbaar met die van de uitgestrekte radiobronnen (zie figuur 5), maar met veel kleinere afmetingen van respectievelijk $\lesssim 65\,000$ lichtjaar en $\lesssim 3\,000$ lichtjaar.

Jonge radiobronnen

Gedetailleerdere studies van CSS en GPS radiobronnen begonnen pas aan het begin van de jaren tachtig, toen radiowaarnemingen op hogere frequenties beschikbaar werden. Op een frequentie van 2,7 GHz beginnen deze compacte radiobronnen een belangrijk deel van de heldere radiobron-populatie uit te maken (ongeveer 30% CSS en 10% GPS radio-



Figuur 5 — De GPS radiobron 1943+546, waarvoor een leeftijd van ongeveer 1000 jaar is bepaald. Het heeft een grootte van slechts 500 lichtjaar. Merk de gelijkenis in structuur met Cygnus A op (figuur 3). Credit: Polatidis et al. 1999.

bronnen). Om de kleine afmetingen te verklaren werden twee scenario's voorgesteld, (1) dat GPS radiobronnen hele jonge radiobronnen zijn, die evolueren in CSS bronnen en vervolgens uitgroeien tot uitgestrekte FR I of FR II radiobronnen, of (2) dat het 'gefrustreerde' radiobronnen zijn die, ondanks hun hoge leeftijd, beperkt zijn in hun groei door omliggend gas met hoge dichtheid. Rond het begin van deze eeuw stapelde overtuigend bewijs zich op ten gunste van het 'jeugd-scenario'. Door vanaf de jaren tachtig de structuur van enkele GPS bronnen regelmatig in kaart te brengen met behulp van VLBI, werd aangetoond dat deze bronnen uitdijen met hoge snelheden. Deze snelheden komen overeen met leeftijden van slechts enkele honderden tot duizenden jaren, kloppend met de geschatte leeftijden op basis van modellen voor radio spectra.

Nu vaststaat dat GPS en CSS radiobronnen inderdaad jonge tegenhangers van de uitgestrekte FR I en FR II zijn, is het duidelijk dat ze een sleutelrol spelen in het onderzoek naar radio-krachtige AGN. In dit proefschrift worden selecties van (jonge) radio-krachtige AGN bestudeerd, met als doel:

- het mechanisme dat radio-krachtige AGN teweegbrengt te bepalen: *Waarom zijn sommige AGN radio-krachtig, terwijl andere geen sterke radiostraling produceren?*
- te bestuderen hoe radio-krachtige AGN gedurende hun levensloop evolueren: *Blijft de absorberende torus bestaan, of wordt het gas en*

stof door het zwarte gat geconsumeerd gedurende de levensloop van de radiobron?

- het bepalen van de typische levensduur van radio-krachtige AGN: *the typical lifetime of radio-loud AGN: Worden alle radio-krachtige AGN oud, of wacht een groot gedeelte van de jonge radiobronnen een vroegtijdige dood?*
- de effecten van radio-krachtige AGN op het omliggende sterrenstelsel in kaart te brengen: *Beheersen radio-krachtige AGN de ster-
vorming van het omliggende sterrenstelsel?*

Dit proefschrift

Hoofdstuk 2

In dit Hoofdstuk bestuderen we het Parkes half-Jansky sample van GPS radio-sterrenstelsels. We identificeren de gastheer-sterrenstelsels van alle radiobronnen en bepalen voor 80% van deze sterrenstelsels de roodverschuivingen, die in afstanden vertaald kunnen worden. Door de absolute helderheden van de sterrenstelsels te vergelijken met sterevolutiemodellen, vinden we dat deze zware elliptische sterrenstelsels helderder zijn dan verwacht in ultraviolet licht. Dit zou veroorzaakt kunnen worden door een kleine populatie van jonge sterren, of door straling van de AGN.

Hoofdstuk 3

Dit hoofdstuk presenteert VLBI waarnemingen van het CORALZ sample van compacte radiobronnen op lage roodverschuiving. Radiobronnen in het CORALZ sample hebben doorgaans een relatief lage radio-lichtkracht in vergelijking met voorheen bestudeerde jonge radio-krachtige AGN. We presenteren hoge resolutie radiokaarten van alle bronnen, en bepalen hoekafmetingen en morfologieën. De relatie tussen hoekafmeting, de frequentie van de spectrale piek, en de radio flux-dichtheid van het CORALZ sample leveren aanvullend, overtuigend bewijs dat de helderheidsafname op lage frequenties in de spectra van jonge radio-krachtige AGN wordt veroorzaakt door synchrotron zelf-absorptie.

Hoofdstuk 4

We detecteren de eerste uitdijings-snelheid van een lichtzwakke GPS radiobron, en bepalen een sterke bovenlimiet voor een tweede bron. De expansiesnelheid van $13\% \pm 3\%$ van de lichtsnelheid voor CORALZ J083139+460800 correspondeert met een leeftijd van 245 ± 55 jaar. Dit resultaat bevestigt de jonge leeftijd van deze radio-krachtige AGN. Toch is de expansiesnelheid significant lager dan verwacht vanuit studies van helderdere GPS radiobronnen. Dit duidt sterk op een relatie tussen de uitdijingssnelheid van radiobronnen en hun radio-lichtkracht.

Hoofdstuk 5

We onderzoeken het mechanisme dat radio-krachtige AGN veroorzaakt en de evolutie van radio-krachtige AGN in de context van huidige overkoepelende theorieën voor AGN. Hiervoor hebben we gebruik gemaakt van de grote gegevensverzamelingen die beschikbaar zijn voor het Boötes-veld van ongeveer 9 vierkante graad. Dit waren met name diepe opnames in zichtbaar licht, nabij- en middel-infrarood en radio-straling. Voor een statistisch complete selectie van 334 radiobronnen tot een radiofluxlimiet van $S_{325 \text{ MHz}} > 0.75 \text{ mJy}$, bepaalden we de fotometrische roodverschuivingen, ster massa's, (geprojecteerde) grootten van de radiobronnen en middel-infrarode eigenschappen. We detecteren een significante afname van op $24 \mu\text{m}$ gedetecteerde radiobronnen met radio-brongrootte. Op $8 \mu\text{m}$ is een vergelijkbaar, maar minder sterk effect te zien. We stellen dat dit past binnen een evolutionair scenario, waarin jonge radio-krachtige AGN een torus rond het zwarte gat hebben, terwijl oudere AGN het grootste deel van de torus hebben verslonden. Dit is in tegenspraak met de hypothese dat radio-krachtige AGN van brandstof worden voorzien via sferisch-symmetrische Bondi-accretie. We beredeneren dat *cooling flows* (afkoelend, naar het centrum samenstromend heet gas) alsnog de drijfkracht van radio-krachtige AGN kunnen verschaffen, maar dat het aangevoerde materiaal tot rust komt en een schijf vormt, die niet continu wordt aangevuld, alvorens door het zwarte gat te worden geconsumeerd.

Hoofdstuk 6

We onderzoeken de standaard aanname dat *alle* jonge radiobronnen uiteindelijk evolueren tot FR I of FR II radiobronnen, door de waargenomen kenmerken van het CORALZ core sample te vergelijken met gesimuleerde populaties van radiobronnen. De simulaties zijn gebaseerd op de analytische modellen voor de evolutie van radiobronnen van Kaiser & Best (2007), die de evolutie van zowel de grootte als de radio-lichtkracht beschrijven. We vinden dat de grootte-verdeling van het CORALZ core sample significant verschilt van de gesimuleerde radiobronnen en een steil dichtheidsprofiel van de externe gasverdeling vereist. Om de grootte-verdeling van het CORALZ core sample te kunnen verklaren, moet ongeveer 80% van de *meest compacte* CORALZ bronnen vroegtijdig sterven en vervagen, voordat ze uit zouden groeien tot uitgestrekte FR I of FR II radiobronnen. Aan de andere kant kan maar een beperkt gedeelte van het *totale* aantal CORALZ radiobronnen vroegtijdig eindigen. Een vergelijking met het door de simulaties voorspelde aantal radiobronnen in het CORALZ sample zou anders een onwaarschijnlijk lange typische levensduur voor radio-krachtige AGN vereisen.

Conclusies en vooruitblik

Veel van de grote vragen in de studie van jonge radiobronnen zijn in dit proefschrift aan bod gekomen. We hebben vastgesteld dat de spectrale piek, die de radio-spectra van jonge radiobronnen kenmerkt, wordt veroorzaakt door synchrotron zelf-absorptie. Binnenkort zal het mogelijk worden om de spectra van jonge radiobronnen tot op nog lagere frequenties te verkennen met behulp van LOFAR (low frequency array). LOFAR is een nieuwe Nederlandse radio telescoop voor lage frequenties, bestaande uit ongeveer 10 000 kleine radioantennes die elektronisch aan elkaar worden gekoppeld. Met LOFAR kan straks bekeken worden of absorptie door vrije elektronen - tot voor kort een mogelijk alternatief voor synchrotron zelf-absorptie - op lagere frequenties alsnog een rol gaat spelen. Dit zou belangrijke informatie geven over de directe omgeving van radiobronnen en met name de fysica die zich rond het schokfront afspeelt.

We zullen de structuur van de CORALZ radiobronnen regelmatig in

kaart blijven brengen met het wereldwijde netwerk van radiotelescopen door middel van VLBI. Zodoende zullen we van steeds meer radiobronnen de expansiesnelheid en leeftijd kunnen bepalen. Ook de radiobronnen waar al een expansiesnelheid van gemeten is, blijven we in de gaten houden, om te onderzoeken of de snelheden constant blijven of dat er ook versnelling of vertraging plaatsvindt. Zo kunnen we de huidige radiobron-evolutiemodellen verder verbeteren.

Eén van de belangrijkste vragen blijft waarom sommige AGN radiokrachtig zijn, terwijl andere geen sterke radiostraling produceren. In hoofdstuk 5 vonden we dat ook radio-krachtige AGN, net als AGN zonder sterke radiostraling, een torus hebben. Het verschil zit dus waarschijnlijk niet in de manier waarop materie door het zwarte gat verslonden wordt. Andere studies duiden wel op een groot verschil in de relatieve hoeveelheid materie die per seconde geconsumeerd wordt: radio-krachtige AGN blijken een stuk rustiger te eten. Momenteel wordt hard gewerkt om met behulp van computersimulaties te onderzoeken of dit het antwoord is op de vraag waarom sommige AGN sterke radiostraling produceren. Hier ligt nog wel een grote uitdaging, aangezien in deze extreme situaties allerlei natuurkundige theorieën tegelijkertijd een rol gaan spelen, bijvoorbeeld de hydrodynamica (de beweging van gasstromen), elektromagnetisme en de algemene relativiteitstheorie (de kromming van de ruimte door zware voorwerpen).

Curriculum vitae



P 27 april 1982 werd ik geboren in Haarlem. Al vroeg geboeid door de wetenschap maakte ik op zevenjarige leeftijd mijn eerste werkstuk over de schijngestalten van de maan. Enkele jaren later kende ik de nachtelijke hemel als mijn broekzak. In 1994 begon ik met atheneum aan het Adriaen Pauw te Heemstede, maar stapte later over op gymnasium op het Eerste Christelijke Lyceum te Haarlem.

In september 2000 begon ik aan de studie sterrenkunde in Leiden. Onder begeleiding van Dr. W.J. Jaffe zocht ik naar een derde behouden grootheid in axisymmetrische potentialen. Tijdens mijn afstudeeronderzoek, onder begeleiding van Prof. dr. V. Icke en Dr. I. Pelupessy, analyseerde ik verschillende implementaties van supernovae in dwergsterrenstelselsimulaties, waarna ik in juli 2005 slaagde voor het doctoraal-examen.

Het onderzoek smaakte naar meer en geboeid door actieve galactische kernen ging ik mij verdiepen in jonge radio-krachtige actieve sterrenstelsels. Dit proefschrift beschrijft de resultaten van mijn onderzoek, uitgevoerd onder begeleiding van Prof. dr. R.T. Schilizzi, Dr. I.A.G. Snelten en Prof. dr. H.J.A. Röttgering. Gedurende de afgelopen vier jaar nam ik deel aan conferenties in Leiden, Potsdam (Duitsland), Veldhoven, Oxford (Verenigd Koninkrijk) en Riccione (Italië), waar ik tevens resultaten van mijn onderzoek presenteerde. In de zomer van 2008 bracht ik een werkbezoek aan NASA's Jet Propulsion Laboratory en het Spitzer Science Center van Caltech (Pasadena, California). Ik gaf werkcolleges Sterrenstelsels en Kosmologie, Speciale Relativiteitstheorie en Klassieke Mechanica. Als commissielid Publiekscontacten van de Sterrewacht beantwoordde ik vragen van scholieren, de pers, en vele anderen. Ook was ik commissielid van de Oort Lezing 2007 en organiseerde bovendien in datzelfde jaar de eerste Nederlandse Sterrenkunde Olympiade. Nu, bij de voltooiing van mijn proefschrift, kan ik tevreden terugkijken op vier jaren vol afwisseling, uitdaging en nieuwe ervaringen.

Nawoord



IS VERBIS SCRIPTIS, wil ik voordat de laatste bladzijde omgeslagen wordt, mij nog richten tot een ieder die op zijn of haar manier bijgedragen heeft aan de totstandkoming van dit proefschrift.

Allereerst Bianca, mijn lieve vrouw, bedankt voor je begrip, wanneer mijn gedachten zich weer eens buiten dit sterrenstelsel bevonden. Voor de afgelopen maanden, waar een groot deel van de zorg voor onze kinderen op jouw schouders lag. Maar bovenal dat je er altijd voor me was.

Jisk en Fimme, bedankt voor alle nachten dat jullie wèl sliepen, maar ook voor de tijd dat jullie wakker waren; mijn inspiratie en motivatie dank ik aan jullie. Mama en Rita, voor jullie hulp bij het combineren van werk en gezin.

Anne-Marie, Maarten, Eveline, Marcel en Ignas, samen organiseerden we de eerste Nederlandse Sterrenkunde Olympiade in 2007. Het was een drukke, maar leuke tijd en ik wil jullie bij deze nog bedanken voor een bijzondere en leerzame ervaring. Ook Jan-Pieter, Chael, Patrick, Susanne, George, Laura, Merijn, Stefan, bedankt voor de gezelligheid tijdens de pauzes.

Bij de commissie Publiekscontacten van de Sterrewacht hebben we heel wat beleefd, Maaike en Freeke. Eenvoudige, lastige, interessante en vooral bijzondere vragen en verzoeken, maar samen zijn we er toch altijd weer uitgekomen. To my fellow roommates, Cat and Aleksandar, thanks for the good atmosphere in room 463. David, Tycho, Erik, Aart, Kirsten, Jeanne, Liesbeth en Anita, voor alle praktische zaken die door jullie zo goed afgehandeld worden, dat je er vaak niet eens bij stil staat wat er achter de schermen allemaal gebeurt.

Daniel, Steve, Mark, thanks for sharing much more than data alone. Many thanks to Thomas, Tanya, Nick, Lexi, David, Else, Bill, Monica, and Job, for making me and my family feel so welcome in Pasadena.

